

CT-PET Guided Target Delineation in Head and Neck Cancer and Implications for Improved Outcome

Author:

Russell Norman Moule

University College Hospital, London and Mount Vernon Cancer Centre, Middlesex

Submitted to University College, London for the degree of: Doctor of Medicine MD(Res)

Date 19th March 2010

Authors Declaration

I, Russell Norman Moule confirm that the work presented in this thesis is my own. Where information has been derived from other sources, I confirm that this has been indicated in the thesis.

.....

Acknowledgements

I would firstly like to thank Professor M I Saunders for her continued help and encouragement, and for providing me with the opportunities to develop and broaden my knowledge of Head and Neck Cancer. The support of Professor P J Hoskin has been invaluable over the past two years.

Professor Peter Ell, Dr Wendy Waddington, Dr Irfan Kayani, Dr Tryphon Lambrou, Dr John Dickson, and Caroline Townsend in the Nuclear Medicine department at UCLH have helped with this project, and dedicated their time to its success; I am very grateful.

The Head and Neck team at UCLH supported the studies and provided a platform for patient recruitment. The Radiotherapy Physics Department, and especially Derek D'Souza, and Chris Stacey provided extremely useful help and advice for IMRT planning.

The Pathology Department at UCLH, and especially Dr Amrita Jay supported the project with advice on Histo-pathology and macroscopic dissection of specimens. Also, Mark Jitlal and Alan Hackshaw from the MRC Clinical Trials Centre at UCLH gave helpful statistical advice prior to the analysis of the data.

Dr Rowena Paul worked throughout the night to produce the ^{64}Cu at St Thomas' Hospital. Dr Mike O'Doherty, Dr Phil Blower and Dr Paul Marsden supported the work with ^{64}Cu -ATSM and provided excellent advice and encouragement.

Prior to the closure of the Gray Laboratory at Mount Vernon Cancer Centre, Dr Francis Daley helped me to develop my skills in immuno-histochemistry. Dr Paul Barber, and Dr Boris Vojnovic provided the camera, and software for the digitisation of histology images.

I would lastly like to especially thank my parents and brother for their continued support during my career, and my partner Simon, who has carried me through, and helped me realise my ambitions and achieve my goals.

Table of Contents

	Page
Title	1
Acknowledgements	2
List of Figures	8
List of Tables	14
List of Abbreviations	18
Abstract	22

Chapter 1

Squamous Cell Carcinoma of the Head and Neck

<i>1.1 Incidence</i>	24
<i>1.2 Aetiology</i>	25
<i>1.3 Development of second primary cancers</i>	28
<i>1.4 Anatomical sites of the Head and Neck</i>	29
<i>1.5 Lymphatic drainage</i>	32
<i>1.6 Staging</i>	35
<i>1.7 Pathology</i>	36
<i>1.8 Presentation</i>	39
<i>1.9 Clinical examination and investigations</i>	40
<i>1.10 Imaging</i>	40
<i>1.11 Guidance to improve outcomes</i>	45
<i>1.12 Management options</i>	45
<i>1.13 Metastatic disease</i>	52
<i>1.14 Survival and outcome</i>	52
<i>1.15 Aims of thesis</i>	53
<i>1.16 References</i>	55

Chapter 2

¹⁸Fluoro-2-deoxyglucose CT-PET Functional Imaging and Target Volume Delineation in Squamous Cell Cancer of the Head and Neck

2.1	<i>Positron emission tomography</i>	65
2.2	<i>Radio-pharmaceutical properties of fluorine</i>	70
2.3	<i>¹⁸Fluoro-2-deoxyglucose</i>	71
2.4	<i>Radio-nuclide quantification</i>	73
2.5	<i>Physiological uptake of ¹⁸Fluoro-2-deoxyglucose</i>	79
2.6	<i>Methods to delineate ¹⁸Fluoro-2-deoxyglucose CT-PET guided target volumes for radiotherapy planning</i>	80
2.7	<i>Aims of ¹⁸Fluoro-2-deoxyglucose CT-PET guided target volume delineation studies</i>	86
2.8	<i>References</i>	88

Chapter 3

Hypoxia and Hypoxic Functional Imaging using ⁶⁴Cu-ATSM in Squamous Cell Carcinoma of the Head and Neck

3.1	<i>Radiation induced cell death</i>	96
3.2	<i>Hypoxia</i>	97
3.3	<i>Intra-cellular effects of hypoxia</i>	97
3.4	<i>Detection and quantification of hypoxia</i>	98
3.5	<i>Hypoxia and outcome in squamous cell carcinoma of the head and neck</i>	105
3.6	<i>Methods to overcome the effects of hypoxia</i>	105
3.7	<i>Perfusion imaging</i>	109
3.8	<i>Hypoxia imaging with CT-PET</i>	112
3.9	<i>Copper bis(thiosemicarbazone)</i>	116
3.10	<i>Aims of ⁶⁴Cu-ATSM CT-PET functional imaging</i>	124
3.11	<i>References</i>	126

Chapter 4

¹⁸Fluoro-2-deoxyglucose CT-PET Functional Imaging and Target

Volume Delineation Study

4.1	<i>Materials and methods</i>	142
4.2	<i>Statistical analysis</i>	150
4.3	<i>Results</i>	152
4.4	<i>Discussion</i>	198
4.5	<i>Conclusions</i>	222
4.6	<i>References</i>	224

Chapter 5

Hypoxic Imaging in Squamous Cell Carcinoma of the Head and Neck with ⁶⁴Cu-ATSM

5.1	<i>Materials and methods</i>	228
5.2	<i>Statistical analysis</i>	255
5.3	<i>Results</i>	257
5.4	<i>Discussion</i>	297
5.5	<i>Conclusions</i>	320
5.6	<i>References</i>	322

Chapter 6

Conclusion from CT-PET Delineation Studies

6.1	<i>Conclusions</i>	332
6.2	<i>Future directions and applications to clinical practise</i>	337
6.3	<i>Conclusion</i>	345
6.4	<i>References</i>	346

Appendix 1

<i>Supplementary Tables</i>	348
-----------------------------	-----

Appendix 2

Supplementary Figures 363

Appendix 3

Supplementary Equations 393

Appendix 4

^{64}Cu -ATSM production 397

List of Figures

Chapter 1

- 1.1 Age specific incidence rates for men and women with Head and Neck cancer per 100,000 population in the United Kingdom in 2005
- 1.2 Sagittal view of the anatomical Head and Neck
- 1.3 Anterior view of the oral cavity
- 1.4 Anterior view of the larynx
- 1.5 Nodal classification of cervical lymph node groups defined according to CT and MRI modalities
- 1.6 Haematoxylin and eosin stained section of non-dysplastic pharyngeal squamous mucosa
- 1.7 Cytological appearance of squamous cell carcinoma from a cervical lymph node
- 1.8 Squamous cell carcinoma of the oral cavity
- 1.9 European age standardised mortality rates in men and women with Head and Neck cancer between 1971 and 2006

Chapter 2

- 2.1 The structure of ^{18}F fluoro-2-deoxyglucose
- 2.2 The transport of glucose from the extra-cellular to intra-cellular environment, and its intra-cellular metabolic pathway
- 2.3 The transport of ^{18}F FDG from the extra-cellular to the intra cellular environment, and its intra-cellular metabolic pathway
- 2.4 Clinician thresholded CT-PET images by visual interpretation

Chapter 3

- 3.1 The reduction of pimonidazole in the intra-cellular environment
- 3.2 The chemical structure of copper bis(thiosemicarbazone)

Chapter 4

- 4.1 The co-registered CT-PET data sets

- 4.2 Graphical representation of the individualised adaptive threshold functional volume definition
- 4.3 The mean ^{18}F FDG primary functional volume defined by the SUV Cut Off thresholds
- 4.4 The pre-treatment functional volume defined by the SUV Cut Off threshold of 2.5bwg/ml for patient 6: a) Axial fused CT-PET, and b) Coronal CT-PET image
- 4.5 The CT-PET primary functional volume for patient 6 defined by the 3.5bwg/ml SUV Cut Off threshold at 0Gy a), 18Gy b), 40Gy c), and 66Gy d)
- 4.6 The negative correlation between the radiation dose and the primary functional volume delineated by the 4.0bwg/ml SUV Cut Off threshold
- 4.7 The mean ^{18}F FDG defined primary functional volume by the percentage of the SUVmax method
- 4.8 The ^{18}F FDG primary functional volume delineated by the 30% of the SUVmax threshold in patient 6 at a) 0Gy, b) 18Gy, c) 40Gy, and d) 66Gy
- 4.9 Simple linear regression between the radiation dose and the primary functional volume delineated by the 30% of the SUVmax threshold
- 4.10 The mean ^{18}F FDG primary functional volume delineated by the individualised adaptive threshold
- 4.11 The median ^{18}F FDG lymph node functional volume delineated by the 2.5bwg/ml SUV Cut Off threshold
- 4.12 The ^{18}F FDG lymph node functional volume delineated by the SUV Cut Off threshold of 3.5bwg/ml in patient 6 at 0Gy a), 10Gy b), 40Gy c), and 66Gy d)
- 4.13 The median ^{18}F FDG lymph node functional volume delineated by the 45% threshold of the SUVmax
- 4.14 The ^{18}F FDG lymph node functional volume delineated by the 30% of the SUVmax threshold in patient 6 at 0Gy a), 10Gy b), 40Gy c), and 66Gy d)
- 4.15 The median ^{18}F FDG lymph node functional volume delineated by the individualised adaptive threshold
- 4.16 The SUVmax within the primary functional volume delineated by the SUV Cut Off thresholds

- 4.17 Simple linear regression relationship between the SUVmax within the primary functional volume delineated at SUV Cut Off threshold of 3.0bwg/ml and the radiation dose
- 4.18 The SUVmax within the primary functional volume delineated by the individualised adaptive threshold
- 4.19 Simple linear regression relationship between the SUVmax within the primary functional volume delineated by the individualised adaptive threshold and the radiation dose
- 4.20 The SUVmax within the lymph node functional volume delineated by the 3.0bwg/ml SUV Cut Off threshold
- 4.21 Simple linear regression relationship between the SUVmax within the lymph node functional volume delineated by the SUV Cut Off threshold of 2.5bwg/ml and the radiation dose
- 4.22 The SUVmax within the lymph node functional volume delineated by the percentage of the SUVmax method
- 4.23 The mean background SUV within the reference region delineated by the SUV Cut Off and percentage threshold of the SUVmax methods
- 4.24 The mean background SUV within the reference region delineated by the individualised adaptive threshold
- 4.25 The actual SUV used to define the edge of the primary functional volume for each percentage of the SUVmax threshold
- 4.26 Simple linear regression relationship between the SUVmax and the primary functional volume delineated by the 30% threshold of the SUVmax
- 4.27 Simple linear regression relationship between the SUVmax and the primary functional volume delineated by the SUV Cut Off threshold of 3.0bwg/ml
- 4.28 The definition of the functional volume by the individualised adaptive threshold method. Well defined volume a), and poorly defined volume b)
- 4.29 Edge definition by the individualised adaptive threshold according to the gradient of the slope
- 4.30 The mean pre-treatment primary functional volume delineated at each threshold for all the investigated methods

Chapter 5

- 5.1** Surgical template for neck dissection specimens
- 5.2** Fresh macroscopic larynx a), formalin fixed larynx b), axially sectioned formalin fixed larynx c)
- 5.3** Wax embedded laryngeal specimen
- 5.4** Haematoxylin and eosin stained specimen from patient 1 a), and GLUT1 immuno-histochemical stained specimen with folded tissue secondary to antigen retrieval
- 5.5** The immuno-histochemically stained specimen with pimonidazole from patient 1 a), the image with mask applied b), the unmixed pre-thresholded image c), and the final thresholded unmixed image for pimonidazole staining d)
- 5.6** The unmixed and thresholded immuno-histochemical stained specimen for patient 1 for pimonidazole a), the corresponding grayscale image with grid placement b), the unmixed and thresholded image for GLUT1 c), and the corresponding grayscale image d)
- 5.7** The screen capture from the Xeleris software indicating the delineation panel and outlined regions of interest
- 5.8** Fused coronal CT-PET frame at 1 minute with ^{64}Cu -ATSM activity in the bilateral vasculature of the neck
- 5.9** The coronal a), and axial b) image of the fused CT-PET with the spheres sequentially numbered and delineated in red
- 5.10** Pimonidazole stained grayscale image with grid placement a), and the grayscale fused CT-PET image at 40 to 60 minutes b)
- 5.11** Aligned axial fused CT-PET a), corresponding grayscale b), blood flow c), corresponding grayscale image d), grayscale blood flow image aligned with grid e), and grayscale CT-PET image aligned with grid f) for ROI 5
- 5.12** The macroscopic pathological dissection of the specimen from patient 1. a) formalin fixed, b) dissected, and c) wax embedded specimen
- 5.13** Uptake of ^{64}Cu -ATSM within the tumour and other defined regions in patient 1

- 5.14** The uptake of ^{64}Cu -ATSM within the tumour, salivary glands, and necrotic regions at 5 to 20 minutes a), 40 to 60 minutes b), and 18 hours after injection c)
- 5.15** Fused CT-PET axial image with increased ^{64}Cu -ATSM uptake within the left mandible at 5 to 20 minutes a), reduced uptake at 18 hours after injection b), and no uptake on ^{18}F FDG CT-PET c)
- 5.16** The increased uptake of ^{64}Cu -ATSM within the right shoulder at 5 to 20 minutes a), and 40 to 60 minutes after injection b)
- 5.17** The wax embedded tissue block a), H+E stained sections b), corresponding pimonidazole immuno-histochemistry c), and fused CT-PET d)
- 5.18** The relationship between pimonidazole and GLUT1 staining per grid
- 5.19** Axial CT of patient 4 with the streak artefact through the tumour region of interest
- 5.20** Delineated region of interest a), maximum enhancement b), and permeability c) using the WinFun software
- 5.21** Axial images for region of interest 9 defined by the CT Perfusion 4 GE Healthcare software. The colour maps are: contrast enhanced CT a), blood flow b), blood volume c), mean transit time d), and x permeability surface area d)
- 5.22** The mean grayscale intensity correlation of pimonidazole staining and ^{64}Cu -ATSM uptake at 5 to 20 minutes a), 40 to 60 minutes b), and 18 hours c) after injection
- 5.23** ^{64}Cu -ATSM defined hypoxic functional volume for patient 5 according to the tumour to muscle ratio
- 5.24** The delineated hypoxic functional volume and the reference region at 5 to 20 minutes a) and 40 to 60 minutes b) after the injection of ^{64}Cu -ATSM
- 5.25** The axial images of ^{64}Cu -ATSM a), and ^{18}F FDG b) representing the uptake differences of the two radio-nuclides

Chapter 6

- 6.1** Colour washed axial image of standard Head and Neck IMRT plan

6.2 Dose escalated ^{18}F FDG CT-PET guided target volume with lower threshold set at 62Gy a), and lower threshold at 70.78Gy

List of Tables

Chapter 1

- 1.1 New cases of Head and Neck Cancer in the United Kingdom in 2004
- 1.2 Anatomical boundaries of the lymph node groups within the neck
- 1.3 Generic TNM/AJCC 2002 6th Edition Classification for oropharyngeal and hypopharyngeal cancers
- 1.4 TNM (2002) 6th Edition Overall Stage Grouping for Head and Neck cancer

Chapter 2

- 2.1 The physical properties of Lutetium Oxyorthosilicate and Bismuth Germanium Oxide
- 2.2 The parameters affecting radio-nuclide uptake
- 2.3 Factors affecting the SUV calculation

Chapter 3

- 3.1 The radio-active properties of copper isotopes

Chapter 4

- 4.1 The thresholds used to define each ¹⁸FDG functional volume
- 4.2 Definition of parameters used to assess the ¹⁸FDG functional volume prior to and during treatment
- 4.3 The characteristics of study patients
- 4.4 The mean and standard error of the mean for the delineated primary functional volumes by the SUV Cut Off method
- 4.5 The mean percentage, actual reduction, p-values, and 95% confidence intervals for the primary functional volume delineated by the SUV Cut Off method at each imaging point
- 4.6 The mean percentage, actual reduction, p-values and 95% confidence intervals between the imaging points for the primary functional volume delineated at each SUV Cut Off threshold

- 4.7** The mean and standard error of the mean for the delineated primary functional volumes by the percentage threshold of the SUVmax method
- 4.8** The mean percentage, actual reduction, p-values, and 95% confidence interval for the primary functional volume delineated by the percentage of the SUVmax method between each imaging point
- 4.9** The mean percentage, actual primary functional volume change, p-values and 95% confidence intervals between the imaging points at each percentage of the SUVmax delineation threshold
- 4.10** The median and inter-quartile range for the lymph node functional volumes delineated by the SUV Cut Off thresholds
- 4.11** The median and inter-quartile range for the lymph node functional volumes delineated by the percentage thresholds of the SUVmax
- 4.12** The mean and standard error of the mean for the SUVmax within the primary functional volume delineated by the SUV Cut Off thresholds
- 4.13** The mean percentage, actual reduction, p-values, and 95% confidence intervals for the SUVmax within the primary functional volume delineated by the SUV Cut Off thresholds at each imaging point
- 4.14** The mean percentage, actual reduction, p-values and 95% confidence intervals for the SUVmax within the primary functional volume delineated by the SUV Cut Off thresholds between the imaging points
- 4.15** The median and inter-quartile range for the SUVmax within the lymph node functional volume delineated by the SUV Cut Off thresholds
- 4.16** The mean difference, p-values, and 95% confidence intervals for the SUV used to define the primary functional volume and the background SUV at each imaging time point by the percentage thresholds of the SUVmax
- 4.17** The median and inter-quartile range for the SUV used to define the lymph node functional volume delineated by the percentage thresholds of the SUVmax
- 4.18** The median difference, p-values, and 95% confidence intervals for the SUV used to define the lymph node functional volume and the background SUV at each imaging point by the percentage thresholds of the SUVmax
- 4.19** Delineation volumes compared from UCLH and the reported study by Schinagl et al

- 4.20** The calculated tumour edge to background ratios for the primary and lymph functional volumes delineated by the percentage threshold of the SUV_{max}

Chapter 5

- 5.1** Inclusion and exclusion criteria
- 5.2** Imaging protocols for the study. Immediate 3D dynamic Head and Neck CT-PET a), 3D static Head and Neck CT-PET 18 hours after injection b), and dynamic contrast-enhanced CT c)
- 5.3** Patient characteristics
- 5.4** The presenting symptoms, smoking and alcohol history
- 5.5** The ratio of ⁶⁴Cu-ATSM uptake compared to that within the other regions of interest at 5 to 20 minutes a), 40 to 60 minutes b), and 18 hours c) after injection of ⁶⁴Cu-ATSM
- 5.6** Statistical results for the paired t-test comparing the uptake ratio at 40 to minutes a), and 18 hours after injection b) to the uptake ratio at 5 to 20 minutes after injection, and c) 18 hours compared to 40 to 60 minutes
- 5.7** Mean hypoxic area fraction per block calculated from the linear unmixed image
- 5.8** Median percentage immuno-histochemical staining within each grid for each patient, and the corresponding inter-quartile range a), and combined patient data b)
- 5.9** The correlation of GLUT1, CAIX and HIF1a immuno-histochemical stains of all block from the 4 patients
- 5.10** Difference in percentage staining per correlated grid
- 5.11** Physiological parameters within the region of interest calculated by the WinFun software
- 5.12** Physiological parameters within the region of interest calculated by the CT Perfusion 4 GE Healthcare software
- 5.13** The correlation between the hypoxic immuno-histochemical staining and the ⁶⁴Cu-ATSM uptake and retention
- 5.14** The hypoxic functional volume defined by the tumour to muscle ratio after the injection of ⁶⁴Cu-ATSM

- 5.15** The hypoxic functional volume defined by the tumour to blood ratio after the injection of ^{64}Cu -ATSM
- 5.16** The hypoxic functional volume defined by the tumour to background ratio after the injection of ^{64}Cu -ATSM
- 5.17** Perfusion parameters in patients with squamous cell carcinoma of the Head and Neck from DCE-CT images measured using the CT Perfusion application from GE Healthcare

List of Abbreviations

UK	United Kingdom
HN	Head and Neck
SCCHN	Squamous Cell Carcinoma of the Head and Neck
BMI	Body Mass Index
SCC	Squamous Cell Carcinoma
HPV	Human Papilloma Virus
HIV	Human Immunodeficiency Virus
AJCC	American Joint Committee on Cancer
LN	Lymph Node
RT	External Beam Radiotherapy
CRT	Chemo-radiotherapy
SCM	Sternocleidomastoid Muscle
CT	Computed Tomography
MRI	Magnetic Resonance Imaging
TNM	Tumour Node Metastasis
H+E	Haematoxylin and Eosin
FNA	Fine Needle Aspiration
USS	Ultrasound Scan
CT-PET	Computed Tomography-Positron Emission Tomography
3D	3 Dimensional
2D	2 Dimensional
HU	Hounsfield Units
IGRT	Image Guided Radiotherapy
TPS	Treatment Planning System
TV	Target Volume
¹⁸ FDG	¹⁸ Fluoro-2-deoxyglucose
GTV	Gross Tumour Volume
NSCLC	Non-Small Cell Lung Cancer
IMRT	Intensity Modulated Radiotherapy
NICE	National Institute of Clinical Excellence
ND	Neck Dissection

LINAC	Linear Accelerator
3DCRT	3D Conformal Radiotherapy
CTV	Clinical Target Volume
PTV	Planning Target Volume
ICRU	International Commission of Radiation Units
RTOG	Radiation Therapy Oncology Group
Gy	Gray
MV	Mega-Voltage
PORT	Post-Operative Radiotherapy
IL	Ipsi-Lateral
CL	Contra-Lateral
mg/m ²	milligram per meter squared
EGFR	Epidermal Growth Factor Receptor
TK	Tyrosine Kinase
MAB	Mono-Clonal Antibody
⁶⁴ Cu-ATSM	⁶⁴ Cu (II) diacetyl-bis(N ⁴ methylthiosemicarbazone)
DNA	Deoxyribonucleic acid
PET	Positron Emission Tomography
KeV	Kilo Electron Volt
ROI	Region Of Interest
DCE-CT	Dynamic Contrast Enhanced Computed Tomography
AC	Attenuation Corrected
mm	Millimeters
t _{1/2}	Half-life
GLUT	Glucose Transporter
NADH	Nicotine Adenine Dinucleotide Reduced Form
ATP	Adenosine Tri-Phosphate
NAD	Nicotine Adenine Dinucleotide
GLUT1	Glucose Transporter 1
mRNA	Messenger RiboNucleic Acid
SUV	Standardised Uptake Value
TLG	Total Lesion Glycolysis
bw	Body Weight
MBq	Mega Becquerel

MBq/g/ml	Mega Bequerel per gram per millilitre
SUV _{max}	Maximum SUV within the voxel
SUV _{mean}	Mean SUV within all voxels of the region of interest
lbm	Lean Body Mass
BSA	Body Surface Area
SUV _{gluc}	SUV normalised to blood glucose
FV	Functional Volume
SUVCO	SUV Cut Off
PTSUV _{max}	Percentage Threshold of the SUV _{max}
cm ³	Centimetres cubed
IAT	Individualised Adaptive Threshold
OER	Oxygen Enhancement Ratio
mmHg	Millimetres of Mercury
pO ₂	Partial Pressure of Oxygen
µm	Micro Metres
IHC	Immuno-Histochemistry
HRP	Horseradish Peroxidase
NADP	Nicotine Adenine Dinucleotide Phosphate
NADPH	Nicotine Adenine Dinucleotide Phosphate Reduced Form
HIF1α	Hypoxia Inducible Factor 1 alpha
CAIX	Carbonic Anhydrase IX
VHL	Von Hippel Lindau
¹⁸ F-MISO	¹⁸ Fluoro-Misonidazole
BV	Blood Volume
CP	Capillary Permeability
DCE-MRI	Dynamic Contrast Enhanced MRI
BF	Blood Flow
MTT	Mean Transit Time
PS	Permeability Surface Area
¹⁸ F-FAZA	¹⁸ Fluoro-Azomycin Arabinoside
¹⁸ F-FETNIM	¹⁸ Fluoro-Erythronitroimidazole
¹⁸ F-FETA	¹⁸ Fluoro-Etanidazole
¹⁸ F-EF3	Tri- ¹⁸ Fluorinated Etanidazole

¹⁸ F-EF5	Pent- ¹⁸ Fluorinated Etanidazole
Cu	Copper
Cu-PTSM	Cu(II)-pyruvaldehyde bis(N ⁴ methylthiosemicarbazone
SIB	Simultaneous Integrated Boost
UCLH	University College Hospital, London
GCP	Good Clinical Practice
ECOG	Eastern Co-operative Oncology Group
PETVCAR	Positron Emission Tomography Volume Computerised Assisted Reading
bwg/ml	Body weight in grams per millilitre
RTSS	Radiotherapy Structure Set
SLR	Simple Linear Regression
SEM	Standard Error of Mean
WCSRT	Wilcoxon Summed Rank Test
IQR	Inter-Quartile Range
CI	Confidence Interval
M	Molar
Anti-FITC	Anti-fluorescein isothiocyanate
DAB	3,3-diaminobenzidine
TBS	Tris Buffered Saline
DICOM	Digital Imaging and Communications in Medicine
NRES	National Research Ethics Service

Abstract

Aim

Fifty percent of patients with squamous cell carcinoma of the Head and Neck develop loco-regional recurrence after treatment. Factors leading to this failure are most likely altered intra-tumoural glucose metabolism and increased hypoxia. Tissue glucose utilisation and the degree of hypoxia can be visualised by CT-PET imaging with ^{18}F FDG and hypoxic radio-nuclides.

This thesis has investigated ^{18}F FDG CT-PET guided target volume delineation methods and attempted to validate ^{64}Cu -ATSM as a hypoxic radio-nuclide in patients with squamous cell carcinoma of the Head and Neck.

Materials and Methods

Eight patients with locally advanced disease underwent ^{18}F FDG CT-PET imaging before and during curative radiotherapy or chemo-radiotherapy. Fixed (SUV cut off and percentage threshold of the SUVmax) and adaptive thresholds were investigated. The functional volumes automatically delineated by these methods and SUVmax were compared at each point, and between thresholds.

Four patients with locally advanced disease, two to seven days prior to surgery, underwent 3D dynamic CT-PET imaging immediately after injection of ^{64}Cu -ATSM. Two patients were also imaged 18 hours after injection, and two underwent a dynamic contrast-enhanced CT to evaluate intra-tumoural perfusion. All patients received pimonidazole before surgery. The pimonidazole, GLUT1, CAIX, and HIF1 α immuno-histochemical hypoxic fractions were defined. Staining was correlated with the retention pattern of ^{64}Cu -ATSM at 3 time points. Hypoxic target volumes were delineated according to tumour to muscle, blood and background ratios.

Results

^{18}F FDG primary and lymph node target volumes significantly reduced with radiation dose by the SUV cut off method and correlated with the reduction in the SUVmax within the volume. Volume reduction was also found between thresholds by the same delineation method. The volumes delineated by the other methods were not significantly reduced (except the lymph node functional volume when defined by the adaptive threshold).

^{64}Cu -ATSM correlated with hypoxic immuno-histochemical staining but not with blood flow. Tumour ratios increased with time after injection, which influenced the delineated hypoxic target volume.

Conclusion

Dose-escalated image-guided radiotherapy strategies using these CT-PET guided functional volumes have the potential to improve loco-regional control in patients with squamous cell carcinoma of the Head and Neck.

CT-PET ^{18}F FDG volume delineation is intricately linked to the method and threshold of delineation and the timing of the imaging.

^{64}Cu -ATSM is promising as a hypoxic radio-nuclide and warrants further investigation.

Chapter 1

Squamous Cell Carcinoma of the Head and Neck

1.1 Incidence of Head and Neck Cancer

In 2004, in the United Kingdom (UK), 284,560 people were diagnosed with cancer. The four commonest sites included: breast (16%), lung (13%), colorectal (13%), and prostate (12%) [1-3].

Carcinoma of the Head and Neck (HN) is relatively rare. In 2004, 6,963 people were diagnosed with HN cancer (larynx, oral cavity, oropharynx, hypopharynx, and para-nasal sinuses, excluding nasopharynx) equalling 2.8% of all cancer diagnoses in 0.014% of the total adult population [4]. The commonest sites were: the larynx (31.5%), oral cavity (21.6%), tongue (20.1%), and pharynx (oropharynx and hypopharynx 19.2%). Table 1.1 shows the number of new cases by site in the UK in 2004.

Table 1.1 New Cases of Head and Neck Cancer in the United Kingdom in 2004

Site	Male (%)	Female (%)
Larynx	1800 (25.8)	394 (5.7)
Oral Cavity	904 (13.0)	601 (8.6)
Tongue	889 (12.8)	513 (7.4)
Oropharynx	649 (9.3)	242 (3.5)
Hypopharynx	348 (5.0)	100 (1.4)
Lip	193 (2.8)	91 (1.3)
Other sites	166 (2.4)	73 (1.0)
TOTAL	4949 (71.07)	2014 (28.93)

Eighty-six percent of HN cancers are diagnosed in patients over 50 years of age [1-3]. The incidence has doubled in younger adults over the past 30 years (3.6 to 8.8 per 100,000 men aged 40 to 49; and 11.5 to 24.9 per 100,000 men aged 50 to 59) [5,6]. Figure 1.1 illustrates the age-specific incidence rates for HN in men and women in the UK in 2005. The rate was 52 to 56 per 100,000 population in men, and 10 to 24 per 100,000 women aged 50 to 85.

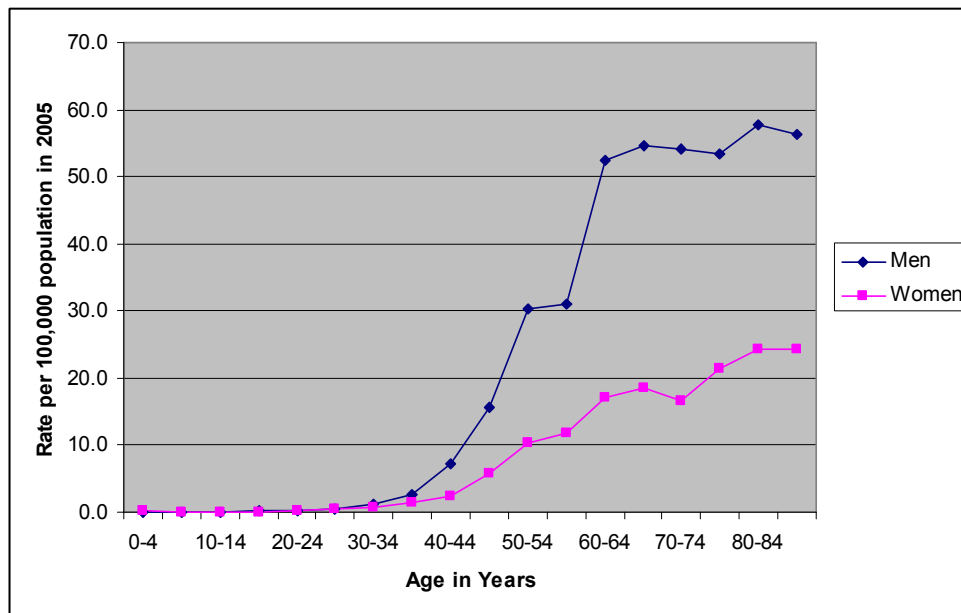


Figure 1.1: Age specific incidence rates for men and women with Head and Neck cancer per 100,000 population in the United Kingdom in 2005

1.2 Aetiology

1.2.1 Tobacco

Approximately 28% of the adult population in the UK smoke [7] (mainly cigarettes). Smoking and alcohol consumption are the commonest factors implicated in the aetiology of Squamous Cell Carcinoma of the HN (SCCHN). There is a dose response and synergistic effect [8]. Patients have a 35 fold increased risk when more than 4 alcoholic drinks are consumed with 20 to 40 cigarettes smoked per day.

The risk associated with smoking depends on the tobacco type and mode of inhalation of the smoke. Betel nut (oriental palm seed) chewing increases the risk of developing oral cavity cancer, especially in patients from Bangladesh. This is dependent on the amount chewed and the duration of use or exposure [9].

Smoking cessation significantly reduces the risk of developing SCCHN by 50% 3 to 5 years after stopping [10]. Ten years later, the risk equals that of non-smokers [11].

1.2.2 Alcohol

The risk of SCCHN increases with the amount, and type of alcohol consumed, especially beer and spirits [8]. Alcohol consumption has nearly doubled in the UK over the past century, especially among 16 to 24 year olds. In 2002, 18% of adult men and 30% of women exceeded the recommended weekly intake (21 units in men, and 18 units in women), compared to 10% and 26% respectively in 1988 [12].

Alcohol intake has increased in young adults aged 16 to 24 in the UK. In 1996 35% of men, and 21% of women in this age group drank more than the Government's weekly recommended alcohol intake [13]. This increased to 37% of men and 26% of women in 2003.

In the 11 to 15 year old group, 47% of boys and 36% of girls in England drank alcohol on a weekly basis [14], and this was typically binge drinking. In young non-smokers, more than 3.75 units of alcohol per day was the most important risk factor for SCCHN [15], and was associated with a linear increase in risk.

1.2.3 Diet and Nutrition

A low intake of fruit and vegetables has been associated with an increased incidence of SCCHN [16]. There is an inverse association between total intake of fruit and vegetables, and development of this cancer [17]. Deficiency in vitamins A and C, as well as iron, selenium and folate are all associated with an increased risk [18,19].

Heavy alcohol consumption and malnutrition are linked lifestyle factors. A low body mass index (BMI) has been associated with an increased risk of squamous cell carcinomas (SCC) of the larynx [20] and was highest in men. Poor survival following treatment was especially associated with a BMI less than 22.8 kg/m² [21].

1.2.4 Viral

Human papilloma virus (HPV) has been implicated in the pathogenesis of SCC's of the oropharynx, and to a lesser extent oral cavity. HPV-16 is the commonest serotype, and the tonsil the commonest site associated with HPV positive SCCHN. HPV positive patients are less likely to be heavy smokers, drinkers, or have p53 mutations. A positive HPV-16 serotype is associated with an improved disease-specific survival [22].

The largest review from the Surveillance, Epidemiology and End Results database reported the incidence rate increased each year by 3% between 1998 and 2003. The rate of HPV positive SCCHN was 43.6% for the tonsil, and 38.4% for the posterior third of tongue sites [23].

1.2.5 Immuno-Suppression

Immuno-suppression may be either primary or acquired. The most commonly acquired forms are due to viral disease, and drugs. There have been reports of oral SCC following allogenic haemopoietic bone marrow transplantation [24], on a background of chronic graft-versus-host disease, suggesting a mechanism of persistent, prolonged inflammation.

Human Immunodeficiency Virus (HIV) is increasing in incidence, and 33.2 million people worldwide were infected in 2007 [25]. The risk of HN cancer is increased in patients with HIV. Only Kaposi's Sarcoma is classified as an Acquired Immune Deficiency Syndrome defining disease. Hodgkin's Disease was associated with a 11.5 fold greater risk, oropharyngeal SCC 6 fold greater, SCC's of the oral cavity and pharynx 2.7 fold greater, and SCC of the larynx 2.8 greater risk [26] compared to the non-HIV positive population.

1.2.8 Pre-malignant Conditions (Leucoplakia and Erythroplakia)

Oral leucoplakia is the commonest pre-malignant condition leading to SCCHN. The incidence in the UK is between 0.2 and 11.7% [27], and depends on the minimum degree of whiteness of the mucosa taken to define the lesion. The annual rate of malignant transformation is 4.4 to 17.5% [28,29].

Erythroplakia is less common with an incidence of 0.09%, and the rate of malignant transformation is less than 1% [30]. Oral submucosal fibrosis and lichen planus are less common, and associated with an even lower rate of transformation.

1.2.3 Marijuana

There are a number of conflicting reports in the literature of the association with SCCHN. These include a dose response relationship in patients under the age of 55 with the amount and duration of marijuana smoked per day [31]. Further studies are required to confirm or refute an association of marijuana and SCCHN.

1.3 Development of Second Primary Cancers

Second primary cancers in patients with SCCHN are either synchronous, or metachronous, and develop at a median interval of 2 years after the primary diagnosis.

Synchronous cancers are geographically distinct, separated from the first primary lesion by more than or equal to 2cm of normal (squamous) epithelium. These are diagnosed at the same time or within 6 months of the first cancer. Metachronous cancers are diagnosed at least 6 months after the first cancer.

The cumulative risk has been reported as 26% at 10 years, and 47% at 20 years [32]. The overall rate of development was 17.6%, and lung was the commonest second site. Up to 40% of these are synchronous, and 60% metachronous [33].

1.4 Anatomical Sites of the Head and Neck

The extra-cranial HN extends from the base of skull to the thoracic inlet, and includes the oral cavity, oropharynx, nasopharynx, larynx, and hypopharynx, as well as the nasal vestibule, nasal cavity and para-nasal sinuses. Other sites include the orbit and orbital contents, salivary and thyroid gland. Figure 1.2 illustrates the main anatomical sites within the HN. These sites are divided according to the International Union against Cancer/American Joint Committee on Cancer (UICC/AJCC) 2002 staging system [34], and have been detailed and illustrated by Henry Gray [35] as shown in the figures 1.2 to 1.4.

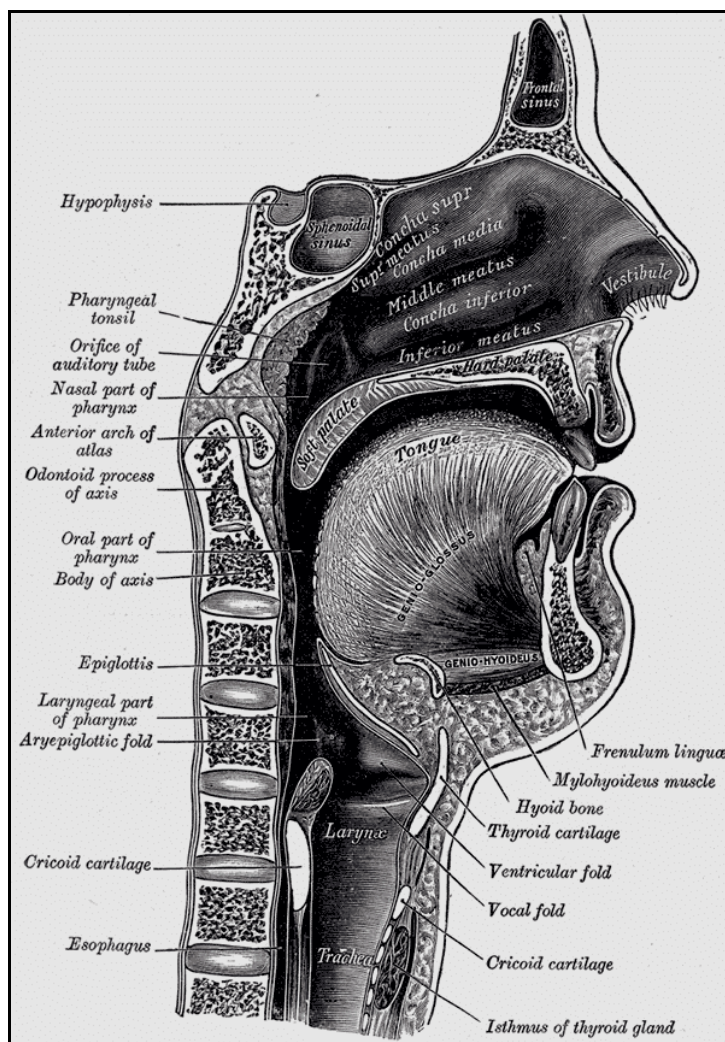


Figure 1.2: Sagittal view of the anatomical Head and Neck

1.4.1 Oral Cavity

The oral cavity extends anteriorly from the vermilion border of the lips to the junction of the hard and soft palate postero-superiorly, and the circumvallate papillae postero-inferiorly. The structures within this site include: the buccal mucosa, upper and lower alveolus and gingivae, hard palate, the anterior two-thirds of the tongue, and the floor of mouth. Figure 1.3 illustrates the anterior view of the oral cavity.

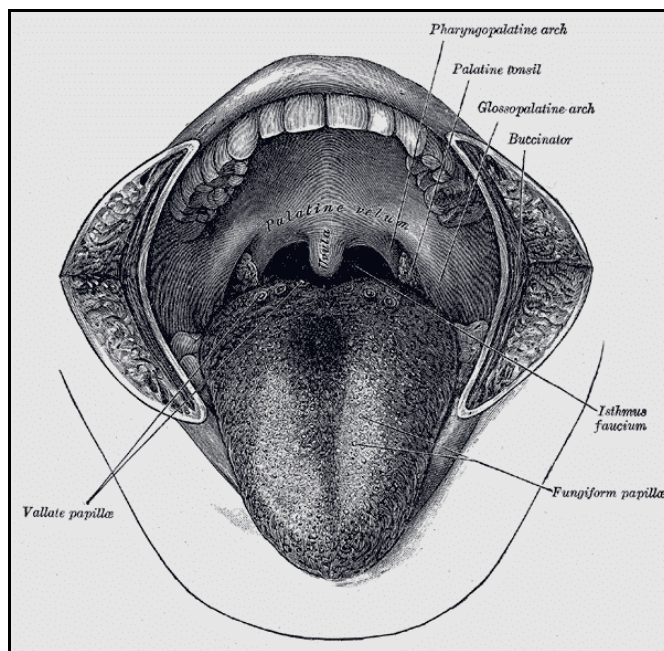


Figure 1.3: Anterior view of the oral cavity

1.4.2 Oropharynx

The oropharynx extends from the anterior tonsillar pillar and circumvallate papillae anteriorly to the pharyngeal wall posteriorly. The superior border is the level of the hard palate, and the inferior border is the hyoid bone. The lateral wall consists of the anterior and posterior tonsillar pillars, and the pharyngeal palatine tonsil. At the level of the hyoid, the oropharynx becomes the hypopharynx. The structures contained within the oropharynx include: the posterior one-third of the tongue, valleculae, lingual surface of the epiglottis, posterior pharyngeal wall, and soft palate.

1.4.3 Hypopharynx

The hypopharynx starts superiorly at the level of the hyoid and epiglottis, and extends inferiorly to the lower border of the cricoid cartilage. The larynx is anterior to the hypopharynx and indents its lateral aspect forming the potential pyriform fossa spaces. The hypopharynx is divided into three sub-sites: the pyriform fossae, post-cricoid, and the posterior pharyngeal wall.

1.4.4 Larynx

The larynx consists of three sub-sites: the supraglottis, glottis, and subglottis. The supraglottis is divided into the epiglottis, false vocal cords, ventricles, aryepiglottic folds and arytenoids. The glottis contains the true vocal cords, along with the anterior and posterior commissure. Figure 1.4 illustrates the anterior view of the larynx.

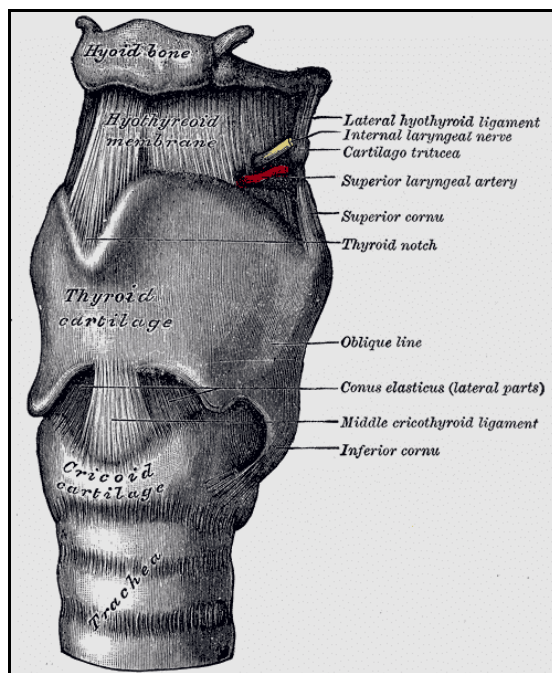


Figure 1.4: Anterior view of the larynx

1.4.5 Nasopharynx

The nasopharynx is the most superior portion of the pharynx and is in continuation with the oropharynx at the superior surface of the soft palate. The superior border is the body of the sphenoid bone, and the basilar part of the occipital bone. The anterior wall is the posterior nasal choanae. The posterior

wall is the clivus, 1st and 2nd cervical vertebrae, and the posterior wall of the pharynx.

1.4.6 Rare Sites of Squamous Cell Carcinoma Development

These include the: nasal cavity and para-nasal sinuses, ear, and the salivary glands.

1.5 Lymphatic Drainage

Within the HN, anatomical sites drain to regional lymph nodes (LN), which in turn drain into the thoracic duct. LN enlargement may be due to a variety of benign and malignant causes.

Benign causes commonly include: bacterial, viral, fungal infections for example β haemolytic streptococcal tonsillar infections. Malignant causes include primary cancers: such as Non-Hodgkin's lymphoma, Hodgkin's disease, leukaemias, or metastatic disease.

Primary SCCHN can develop loco-regional metastatic cervical lymphadenopathy, but supra-clavicular nodal involvement is rare.

1.5.1 Lymph Node Disease in Primary Squamous Cell Cancers of the Head and Neck

Microscopic and macroscopic cervical LN metastases develop due to loco-regional spread from the primary site. Surgery, external beam radiotherapy (RT) or chemo-radiotherapy (CRT), and post-operative indications for RT and CRT for the eradication of microscopic and macroscopic LN disease are all tailored to this level of risk. The neck traditionally has been divided into anterior and posterior triangles separated by the sternocleidomastoid muscle (SCM). Six major anatomical groups exist shown in Table 1.2, and levels II to V further are subdivided by imaging.

Table 1.2: Anatomical boundaries of the lymph node groups within the neck

Level	Anatomical Region
I	a) Submental b) Submandibular triangles
II	Upper jugular chain Nodes lie deep to the upper third of the sternocleidomastoid muscle. Extend from base of skull to hyoid.
III	Middle jugular chain Nodes lie deep to the middle third of sternocleidomastoid. Extend from hyoid to cricoid.
IV	Lower jugular chain Nodes lie deep to the lower third of sternocleidomastoid. Extends from omohyoid muscle to clavicle.
V	Posterior triangle Behind the posterior border of the sternocleidomastoid muscle.
VI	Anterior compartment Around the midline visceral structures of the neck from the hyoid bone to the suprasternal notch.

The risk of LN spread is dependent on: primary site, lateralisation, size, and histology (lympho-vascular invasion, peri-neural invasion, and grade). The first LN's to be infiltrated by metastatic SCC receive venous tributaries from the adjacent organ (primary site), as well as organs in other areas.

Lindberg [36] reported the topographical distribution, and incidence of cervical LN disease in patients with SCCHN, and this was consolidated by computed tomography (CT), and magnetic resonance imaging (MRI) [37,38] definition of

LN sites. Figure 1.5 shows the regional cervical LN groups relative to the anatomical structures of the HN.

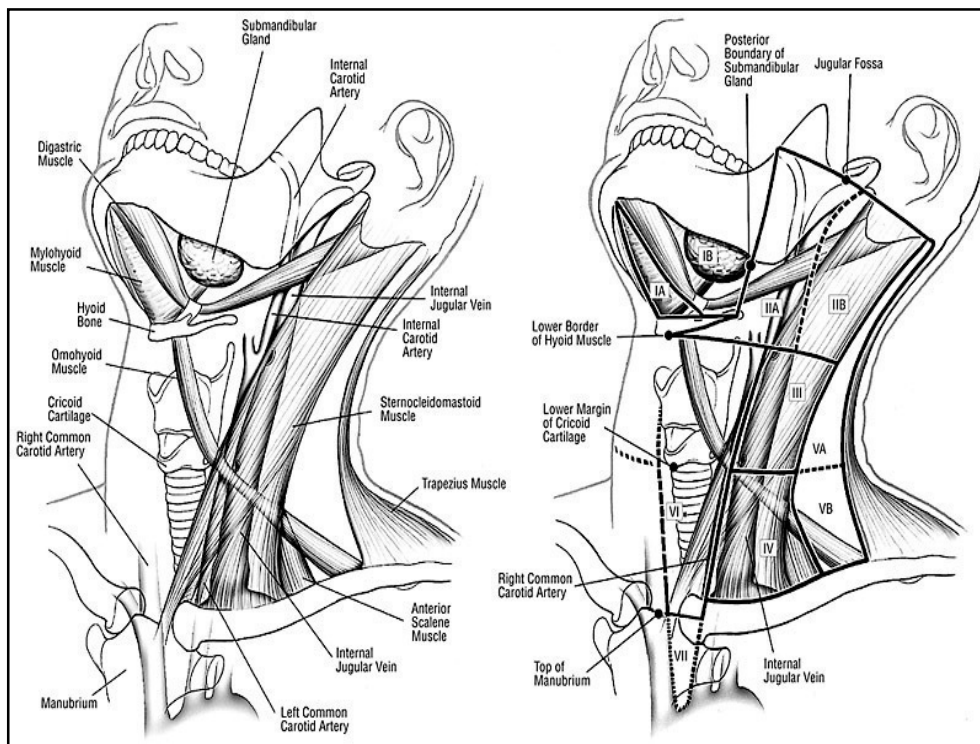


Figure 1.5: Nodal classification of cervical lymph node groups defined according to CT and MRI modalities (left anterior neck position) [38]

For early T1 SCCs the risk of LN metastases is low. Similarly, glottic and subglottic laryngeal SCCs have a low risk because these sites are relatively avascular.

The incidence of LN disease is highest for oropharyngeal primary SCCs. For example: the incidence of LN involvement on imaging was 39% in those with a clinical LN negative neck, and 61% in those with clinical LN positive disease. The incidence of a particular LN level being positive for metastatic oropharyngeal SCC was for example 55% for level II ipsi-lateral LNs, and 13% for the contra-lateral level. The incidence of LN disease has been defined [39-42], and increased rates are also associated with midline lesions.

1.6 Staging

HN cancers are staged according to the TNM (Tumour Node Metastasis)/AJCC 2002 6th Edition [34]. The staging is clinical, pathological, and primary site dependent. The LN stage is identical for all primary sites except nasopharynx and thyroid. Table 1.3 shows an example of the TNM staging for cancers of the pharynx, and 1.4 the overall stage grouping.

Table 1.3: Generic TNM/AJCC 2002 6th Edition Classification for oropharyngeal and hypopharyngeal cancers

Tumour (T)	Node (N)	Metastasis (M)
T(is) Carcinoma in-situ		
T1 <2cm	N1 Ipsi-lateral single < 3 cm	M1 Presence of metastatic disease
T2 2 to 4cm	N2a Ipsi-lateral single > 3 to 6 cm N2b Ipsi-lateral multiple < 6 cm N2c Bilateral, contra-lateral < 6 cm	

T3 >4 cm	N3 > 6 cm	
T4 Invasion into surrounding structures a. Superficial b. Deep structures		

Table 1.4: TNM (2002) 6th Edition Overall Stage Grouping for Head and Neck cancer

Stage	TNM		
0	Tis	N0	M0
I	T1	N0	M0
II	T2	N0	M0
III	T3	N0	M0
	T1-3	N1	M0
IVA	T4a	N0-1	M0
	T1-4a	N2	M0
IVB	Any T	N3	M0
	T4b	Any N	M0
IVC	Any T	Any N	M1

1.7 Pathology

1.7.1 Squamous Epithelium

Squamous epithelium lines the mucosal surfaces of the HN. It consists of layers of either keratinising or non-keratinising squamous cells depending on location and function. For example: keratinising epithelium is found on the hard palate, lateral anterior two thirds of the tongue and the external lips, and prevents cellular dehydration. Squamous cells are irregular, flat and scale like, and

constitute simple or stratified epithelium [43]. Figure 1.6 shows the haematoxylin and eosin (H+E) stained section of normal pharyngeal mucosa.

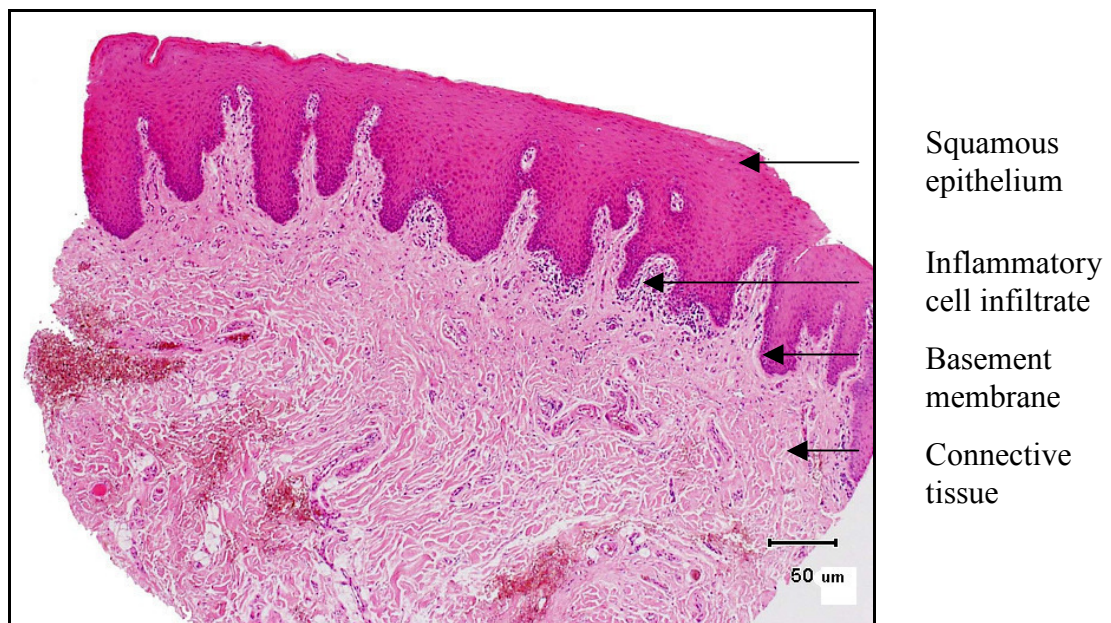


Figure 1.6: Haematoxylin and eosin stained section (magnification x 20) of non-dysplastic pharyngeal squamous mucosa

1.7.2 Squamous Cell Carcinomas

SCCs are the commonest carcinomas of the HN in over 90% of cases [44]. Variants include: papillary, verrucous, basaloid, undifferentiated, lympho-epithelial, adenosquamous, spindle cell and anaplastic types. SCCs arise within normal squamous epithelium, or glandular epithelium with squamous metaplasia.

Non-SCCs include: lymphoma (Non-Hodgkin's), sarcoma, small cell (neuroendocrine), melanoma, adenocarcinomas, and merkel-cell carcinomas.

1.7.3 Pathological Assessment

1.7.3.1 Cytology

Specimens are obtained either by fine needle aspiration (FNA) of a palpable or ultrasound (USS) detected LN, or by lavage, or brushings for example. The cytological appearance following FNA from a cervical LN is illustrated in figure 1.7. Cytological diagnosis is operator dependent.

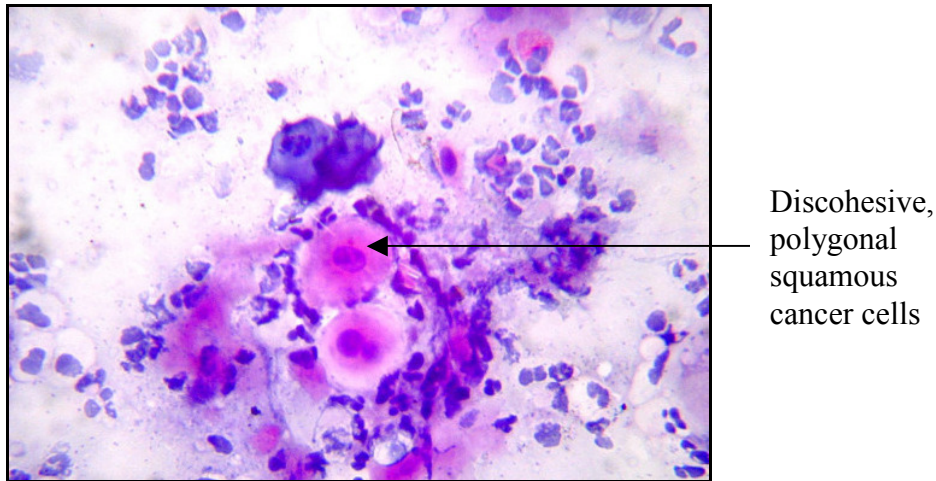


Figure 1.7: Cytological appearance of squamous cell carcinoma from a cervical lymph node

Keratinising SCCs are discohesive, dense cell populations. Cells features include: polygonal shape, varying size, hyper-chromatic nuclei and epithelial pearls.

Well-differentiated SCCs are mature squamous cells with irregular or hyper-chromatic nuclei. Moderately or poorly differentiated SCCs have large nuclei, clumped chromatin, and prominent nucleoli.

1.7.3.2 Macroscopic Pathology

SCCs are ulcerative with raised, rolled margins, and an indurated base. With time, lesions infiltrate deeply, become nodular, and develop central necrosis.

After fixation in 10% neutral buffered formalin features include: cut white, or pale grey surfaces, with irregular margins, and central gelatinous necrosis.

1.7.3.3 Microscopic Pathology

SCCs are histologically invasive. Cells breach the basement membrane, and invade along tissue planes.

The characteristic features on H+E staining include: inter-cellular bridges, and keratin pearls (kerato-hyaline granules). Prickle cells are keratinocytes, and are artefacts of processing. Squamous cancer cells are atypical, with cellular

pleomorphism, increased mitoses, and hyper-chromatic nuclei. Figure 1.8 illustrates an H+E stained SCC of the oral cavity.

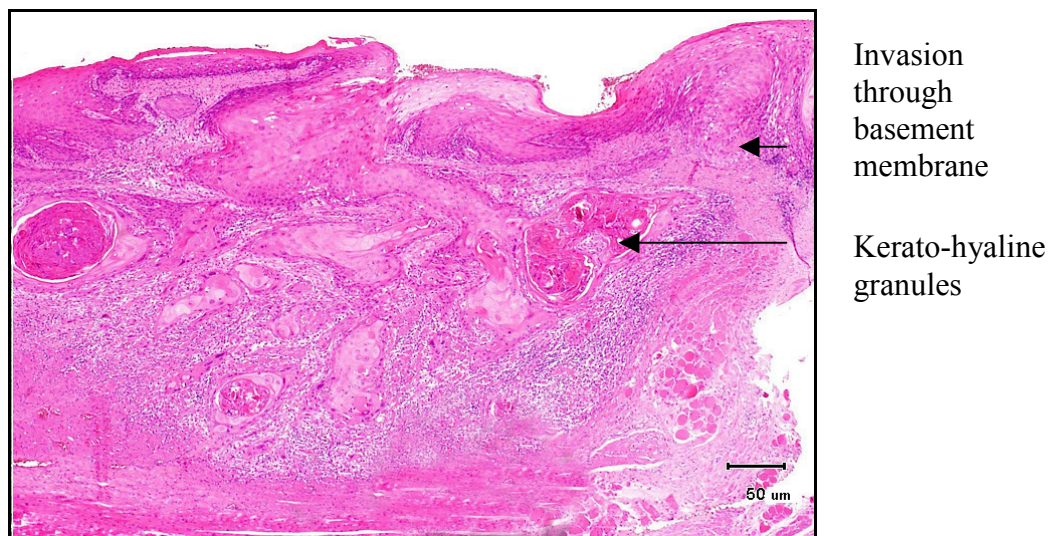


Figure 1.8: Squamous cell carcinoma of the oral cavity

H+E histological specimens are graded into well, moderately and poorly differentiated cancers. Well-differentiated SCCs closely resemble normal keratinising squamous cells. Moderately differentiated SCCs, have a reduced amount of keratin present, increased nuclear pleomorphism, mitosis and cellular atypia. Poorly differentiated cancers have non-cohesive inter-cellular bridges, and either no or small amounts of keratin within the specimen [43].

1.8 Presentation

Patients may present in a number of different ways. Asymptomatic patients are rare and often diagnosed incidentally either following a dental consultation, or the discovery of a painless neck mass.

Symptoms depend on the primary site and stage of disease. The commonest symptoms include: change in voice quality for more than 6 weeks, oral pain or ulceration for more than 3 weeks, neck mass, mass within the oral cavity, and dysphagia or pain on swallowing for more than 3 weeks. Others symptoms include: new or persistent pain within the extra-cranial HN, unilateral nasal

obstruction with nasal discharge, and mobile teeth without co-existent peri-dontal disease.

Patients with locally advanced or metastatic disease may experience lethargy, weight loss, shortness of breath and stridor, cough, or symptoms associated with tumour fungation and secondary infection.

1.9 Clinical Examination and Investigations

Following a full patient history to elicit the presenting symptoms and associated aetiological risk factors, a full HN examination is undertaken. The aim is to assess each anatomical site, and determine the extent of any visible or palpable disease, and associated metastases to regional LNs. This includes a fibre-optic nasendoscopy to allow direct visualisation of the post-nasal space, pharynx and larynx, examination of the oral cavity and oropharynx, and palpation of all cervical and supra-clavicular LN groups.

Initial investigations include baseline haematological (full blood count) and biochemical (renal and liver function, and bone profile) blood tests. Examination under anaesthesia is usually undertaken, allowing visualisation and bi-manual palpation of all possible disease sites. Histological confirmation through USS guided FNA or biopsy will increase the likelihood of obtaining positive histology and corroborate the clinical signs.

1.10 Imaging

Imaging provides anatomical delineation of disease sites and associated invasion into surrounding structures. USS, contrast enhanced CT, and MRI of the HN allows the patient to be effectively staged for loco-regional disease. A CT chest will detect metastatic disease outside the extra-cranial HN. This information guides prognosis and treatment decisions. Functional imaging using combined Computed Tomography-Positron Emission Tomography (CT-PET) is increasingly used to stage patients.

1.10.1 Ultrasound Imaging

USS is a simple, highly operator dependent procedure. High frequency (7 to 15MHz) sound waves are emitted in a pulse, generated from a transducer through the application of an alternating current across piezoelectric crystals. The wave attenuation is detected by the transducer, and characterises the tissue. Doppler studies allow the assessment of vascularity within the region.

1.10.1.2 Indications for Ultrasound use in Head and Neck Cancer

USS may characterise benign or malignant tissue in combination with FNA, either at the time of diagnosis, during the follow up for recurrence, or less commonly in combination with endoscopy for endo-luminal assessment.

1.10.2 Computed Tomography

CT was first reported by Hounsfield in 1973 [45]. This uses x-ray beam transmission, and the subsequent attenuation of that beam as it passes through the patient to provide anatomical information. Multi-slice CT imagers are currently used in clinical practice.

The x-ray beam is generated from x-ray tubes rotated across the field of view. X-ray attenuation can then be measured at any distance from the centre of rotation. Multi-slice CT utilises multiple banks of detectors (8 to 64 rows). Within a single 360 degree rotation as the patient moves on the couch through the gantry, multiple image sets are acquired for example 4, 16, 32, and 64 slices. An x-ray cone beam is used in multi-slice CT imagers, and the attenuation data corresponds to the detection of x-rays between the volumes of two adjacent cones.

Helical CT imagers use fan beam x-rays, and data is acquired as the couch moves at a steady speed through the gantry as the x-ray tube and detectors rotate around the patient. The images obtained are in the form of a continuous ribbon of contiguous slices angulated through the path of the spiral or helix [46].

The transmitted attenuated x-ray beam is converted into a current signal and reconstructed into an image. The CT slice is divided into a matrix containing 3D

3 dimensional) voxels (in the x, y, and z directions) or 2D (two dimensional) pixels (x and y directions). The matrix has 512 x 512 voxels per slice, each voxel measuring 0.5mm x 0.5mm. The attenuation within each voxel is reconstructed by filtered back projection to the point of origin. The attenuation values are represented as grayscale on the 2D image, and these are then converted to Hounsfield units (HU). This incorporates a linear attenuation co-efficient of tissue and water. For example, the HU for water is 0, soft tissues 0 to 100 (depending on the water content), fat 100, and bone 1000. The operator is able to alter the window level and window width, to adjust the brightness and contrast and view structures accordingly for example, bone, soft tissue, and lung [47].

1.10.2.1 Indications for Computed Tomography in Head and Neck Cancer

CT allows the accurate diagnosis and staging (bone/cartilage invasion and soft tissue extension, and detection of lung parenchymal metastases), post-treatment follow-up, and detection of suspected recurrence of SCCHN.

1.10.2.2 Computed Tomography and Radiotherapy Planning

CT data and images guide RT (IGRT) planning, and are required for treatment planning systems (TPS). This allows target volume (TV) delineation without distortion from surrounding structures, and provides information on electron density for the TPS algorithms to calculate the radiation dose. In oropharyngeal and oral cavity cancers, the presence of dental amalgam, or metal prostheses is associated with artefacts affecting the image quality, and ability to delineate the TV from normal tissue.

1.10.3 MRI

MRI is based on the application of an external magnetic field and pulsed radio-waves. Free and attached protons in water and fat re-align either parallel or anti-parallel to the field and precess at the same frequency as the magnetic field. A radio-frequency pulse (less than 1millisecond) is applied at 90 degrees to the magnetic field, and alternates with it. This causes the protons to precess in phase with each other rather than independently. This proton deflection signal is proportional to the strength of the radio-frequency pulse. Once the pulse is

removed the protons re-align in the direction of the external magnetic field (T1 recovery) and precession continues un-synchronised (T2 decay).

The signal alternation is detected by the receiving coils within the MRI unit, and processed to produce a pixel intensity map and the grayscale image. The signal intensity depends on the number of protons within each voxel, the strength of the applied magnetic field, and the direction of alignment of the protons around the axis following application of the magnetic field.

1.10.3.1 Indications for MRI of the Head and Neck

MRI is principally used to assess soft tissue and bony extension of SCCHN at diagnosis, and the extent of local recurrence. MRI has the advantage of improved diagnostic accuracy compared to CT imaging, especially for nasopharyngeal and oropharyngeal carcinomas. Improved detection of: extension of carcinomas into the musculature of the tongue base, cranial nerves, peri-neural invasion and spread, and the detection of either early bone marrow involvement or focal bone erosions is possible [48].

1.10.4 Computed Tomography-Positron Emission Tomography

The use of CT-PET is increasingly common in the investigative process for SCCHN. The commonest radio-nuclide used in clinical practice is ^{18}F Fluoro-2-deoxyglucose (^{18}F FDG). Chapter 2 describes the principles of PET imaging and ^{18}F FDG in detail.

1.10.5.1 Carcinoma of Unknown Primary

The incidence of carcinoma of unknown primary in cervical LN metastases is between 1 to 2% of all HN cancer diagnoses [49]. ^{18}F FDG CT-PET is indicated when no primary site is detected after MRI or CT imaging, but before pan-endoscopy and biopsy. Functional imaging up to 6 weeks after biopsy may lead to a false positive result. ^{18}F FDG CT-PET can detect the primary site in up to 25% of patients, as well as distant metastases in a further 11%, and loco-regional metastases in 16% [50]. When undertaken prior to pan-endoscopy, the detection rate was further increased to 45.2% [51].

In up to 16% of patients with a negative CT-PET, panendoscopy and biopsy of the post-nasal space, base of tongue, bilateral tonsils, and pyriform fossae, will histologically confirm the primary site [49]. Detection of primary cancers within the supraglottis and Waldeyer's ring can be difficult, because the primary may be small or superficial, normal lymphoid tissue may be adjacent to the primary site, and ^{18}F FDG is secreted in saliva accumulating in the valleculae and pyriform fossa [52].

1.10.5.2 Lymph Node Metastases

The detection of metastatic disease within LNs can be difficult because the primary tumour may be adjacent to a LN producing an overlap of ^{18}F FDG avidity, or the node is small. Correlation with pathology may improve this [53].

1.10.5.3 Extra-Cranial Metastases and Pulmonary Nodules of Unknown Significance

The incidence of second primaries and extra-cranial HN metastases detected by CT-PET imaging is up to 20% [49].

1.10.5.4 Recurrent Disease

Following treatment, recurrent disease can be difficult to detect by conventional imaging because of resolving tissue inflammation, anatomical changes, and scar formation, producing soft tissue distortion.

The optimal time to assess residual disease after RT or CRT is 3 to 4 months. From 3 months post treatment, the accuracy of recurrence detection increases up to 94% [54,55]. One month after treatment up to 28% of patients with negative scans have persistent or recurrent disease. Eighty-six percent of patients with positive PET scans have histological confirmation of recurrence [56].

1.10.5.5 The Use of ^{18}F FDG PET to Aid Radiotherapy Planning of the Head and Neck

CT data sets are used to delineate TVs in patients with SCCHN. The use of PET information in this process is becoming increasingly important but not common. The use of ^{18}F FDG CT-PET data is well established in planning radical RT for

non-small cell lung cancer (NSCLC), and has been associated with a smaller delineated gross tumour volume (GTV), and reduced volumes of normal irradiated lung.

Optimisation of TV delineation is vital for intensity modulated RT (IMRT) planning and delivery, because steep dose gradients at the volume edge, lead to rapid dose fall-off. Inaccurate TV delineation due to imaging, or observer variation, may reduce the dose to the high risk TV. This translates into reduced local control and overall survival and may increase late morbidity to organs at risk. Information from PET can alter either the planned treatment by 29% [57], radiation field arrangement by 14 to 53%, or prescribed dose by 11% [58,59] in patients with SCCHN.

1.11 Guidance to Improve Outcomes in Head and Neck Cancer

The National Institute of Clinical Excellence (NICE) [60] has issued guidelines aimed at improving the diagnosis, treatment and outcome of patients with HN cancer. A number of core standards have been recommended within England to achieve these improvements. They include for example: urgent referral, and suggestions of investigative pathways and service provision (including multi-disciplinary approaches).

1.12 Management Options

Curative treatment in all cases depends on RT, CRT, or surgery. These are often combined to improve outcome. Such aggressive treatment can be at the cost of long-term morbidity affecting the patient's quality of life. Speech and swallowing difficulties are significant with any treatment option.

1.12.1 Surgery

Surgical excision of the primary tumour and any suspected or actual LN metastatic disease depends on a number of factors including: site, staging, and

long-term morbidity (verbalisation, and swallowing), with the aim of disease control and functional preservation.

Surgery has advantages such as reduced treatment time and avoidance of the short and long term side effects of RT. The loco-regional control is improved with the addition of adjuvant RT or CRT.

Surgical resection options of the primary cancer range from: trans-oral laser, wide local excision, and excision en-bloc with adjacent structures. Reconstruction will be required if a significant defect has been created by the surgical procedure. Reconstruction methods include for example an arterio-venous anastomosis of a latissimus dorsi, or a radial forearm free flap. Reconstruction may be immediate at the time of surgery or delayed to allow for tissue recovery.

Neck dissections (ND) are undertaken either as primary treatment with or without resection of the primary cancer, alone if no known primary is found, as a staged procedure following CRT or radical RT, or as salvage at the time of loco-regional recurrence. The ND procedures may be extended radical, radical, modified, or selective (postero-lateral, lateral, anterior, supra-omohyoid). The recurrence rates are similar for radical, modified and selective NDs [61-63], and depend on the pathological presence of extra-capsular spread, the number of positive LNs, and the addition of adjuvant RT/CRT.

1.12.2 External Beam Radiotherapy

RT is the curative treatment modality in SCCHN, and this is dependent on the total dose and the overall treatment time. Treatment is delivered to encompass the macroscopic primary and LN disease, along with adjacent areas at highest risk of recurrence. The regional ipsi-lateral or bilateral LNs may be prophylactically treated depending on the risk of metastases associated with the primary cancer.

RT is delivered commonly as 3D conformal RT (3DCRT) via a linear accelerator (LINAC) at mega-voltage (MV) energies as photons and electrons.

Prior to treatment, dental assessment and percutaneous gastrostomy placement may be undertaken to optimise nutrition and hydration. Following this, speech, language and dietetic assessment continue to promote the normal laryngeal and pharyngeal function.

The acute side effects of RT include: skin erythema, dry and moist desquamation, increased oral secretions (due to radiation induced mucositis), dry mouth (reduced salivary gland secretions), pain, and rarely secondary bacterial infection (due to poor oral hygiene and compliance with treatment advice during RT). Late effects (from 6 months post completion of treatment) include: skin fibrosis, telangiectasia, and oedema, dry mouth, accelerated dental caries can significantly add to the morbidity experienced and so reduce the quality of life experienced.

Treatment volumes (GTV, clinical TV [CTV], and planning TV [PTV]) have been described by the International Commission of Radiation Units (ICRU) [64].

GTV:

Visible or palpable macroscopic disease on clinical examination, and imaging.

CTV:

Encompasses the microscopic spread not visible on imaging or clinical examination.

PTV:

This takes into account daily geographical variation caused by internal organ motion or inaccuracies in the treatment field position (systematic and random errors), to ensure the PTV has received 95 to 107% of the prescribed dose.

Each of these volumes creates a margin (which may be limited by barriers of spread or around organs at risk) to ensure both macro and microscopic disease is within the radiation field. Irradiation of microscopic disease reduces the risk of loco-regional recurrence. These LN CTVs are delineated according to the Radiation Therapy Oncology Group (RTOG) Collaboration guidelines [65].

The treatment technique and delivered dose minimise toxicity to organs at risk and ensure that the tolerance doses for individual organs are not exceeded. Radiation dose is delivered per fraction in Gray (Gy). The size of each fraction depends on the treatment schedule for example: conventional fractionation 2Gy per fraction Monday to Friday, one fraction per day. Typically a two-phased technique is employed (Phase 1 macroscopic and microscopic sites [primary and nodal], and Phase 2 macroscopic disease only) to a total dose of 66 to 70Gy, Monday to Friday over 6.5 to 7 weeks with MV photons.

1.12.2.1 Prophylactic Lymph Node Irradiation in Node Negative Neck

Irradiation is usually undertaken when the risk of occult LN disease is more than 20% [39,63,66]. In conventionally fractionated RT, doses are between 44 to 50Gy.

1.12.2.2 Node Positive Neck

The risk of loco-regional recurrence is directly related to the development of extra-capsular LN extension, in patients with clinical or radiological evidence of LN disease. This risk is positively correlated to the size of the LN [67]. For example in LNs less than 1cm the risk of extra-capsular spread is 17 to 43%, 1 to 3cm the risk is 53 to 83%, and greater than 3cm the risk of extra-capsular spread is 74 to 95% [68-70].

The treatment options include: RT alone, CRT, or a ND followed by adjuvant treatment, or a planned ND 6 weeks following the completion of primary RT or CRT. The decision is dependent on the size of the involved LNs and the relationship to surrounding structures.

1.12.3 Brachytherapy

Brachytherapy is the use of a radioactive source (¹⁹²Iridium) directly placed into the cancer either manually (low dose rate), or via a remote after-loading system (high dose rate, fractionated regime). It may be a sole modality of treatment for T1 to T2 lateral tongue and floor of mouth carcinomas, or as a boost to these sites following RT. The Head and Neck European Group of Curietherapy linked to the European Society of Therapeutic Radiology and Oncology has published

recommendations for brachytherapy use is SCCHN [71]. The delivered dose is 60 to 66Gy.

1.12.4 Neo-Adjuvant Chemo-Radiotherapy

The initial outcomes for oral cavity, laryngeal, oropharyngeal and hypopharyngeal SCC treatments reported an 8% 5-year overall survival advantage when concomitant platinum based CRT was used to treat locally advanced disease. The absolute survival benefit was 4.4% at 5 years with the addition of chemotherapy, taking the 5-year overall survival from 31.6% to 36.0%. The benefit of both concomitant chemotherapy and altered fractionation RT reduced with increasing age, and was no longer of benefit over the age of 71 [72,73].

1.12.5 Neoadjuvant/Induction Chemotherapy

The use of neoadjuvant chemotherapy has previously been restricted to patients with nasopharyngeal carcinoma [74], or when there was a significant delay in starting RT treatment which may potentially allow the disease to progress.

Platinum based neoadjuvant chemotherapy in the treatment of SCCHN either alone or in combination with 5-fluorouracil has not shown a significant benefit compared to local treatment alone [72,73].

Docetaxel (75mg/m^2) has been added to cisplatin and 5-fluorouracil schedules, and shown to significantly improve the median progression-free survival, reduce the risk of disease related death, and improve the 3-year overall survival by 10 to 14%. However the loco-regional failure rate was still 57 to 65%, and the toxicity related death doubled to 5.5% [75,76].

1.12.6 Post-Operative Radiotherapy

Indications for PORT depend on factors that predict the risk of local recurrence. The most important are positive resection margins, and extra-capsular LN extension. Either of these are an indication for adjuvant RT. PORT is also recommended when two or more of the following factors are present: close margins of less than 5mm, soft tissue invasion, two or more positive LNs, more

than 1 LN group involved, any LN more than 3cm, multi-centric primary cancer, peri-neural invasion, lympho-vascular invasion, poorly differentiated histology, T3 or 4 disease, oral cavity primary site, carcinoma in-situ or dysplasia at the edge of the resection margin, and uncertain surgical or pathological findings.

RT according to the ICRU guidelines [64,77] is delivered to encompass the surgical bed (CTV), to include any possible microscopic contamination within the surgical field. Accordingly, the ipsi-lateral (IL), or contra-lateral (CL) naïve or operated neck may be included in the treatment volume depending on risk. LN delineation of the CTV in the post-operative, and node positive neck has been described [78]. The RT dose delivered is 60Gy in 30 fractions (2Gy per fraction). High-risk disease (positive margins, extra-capsular nodal spread) will receive a total dose of 64Gy in 32 fractions.

1.12.7 Post Operative Chemo-Radiotherapy

Higher rates of local recurrence (27 to 61%) are associated with certain pathological features including: extra-capsular spread, positive mucosal resection margins, and two or more LNs. The presence of any of these features will reduce the 5-year overall survival to 27 to 34% [79].

Initial studies compared PORT alone, or in combination with 3 cycles of cisplatin and 5-fluorouracil following surgery [80]. The rate of local recurrence was 30%, distant relapse rate 23%, and the over all survival was 40% at 5 years in those treated with PORT alone.

Combined modality treatment for SCCHN in the post-operative setting has proved to be beneficial in high-risk individuals (pT3 to 4, two or more regional LNs, extra-capsular extension of LN disease, positive resection margins, or two or more indications of PORT). Cisplatin-based post-operative CRT (cisplatin at 100 milligram per meter squared [mg/m^2], 60 to 66Gy of RT) is associated with a 2-year loco-regional control rate of 82% in those who received post-operative CRT, compared with 72% in the PORT alone group. The 5-year loco-regional relapse was 42% greater for PORT alone. The 5-year overall survival was up to

13% greater in those who received chemotherapy. There was no difference in the late toxicity with the addition of chemotherapy [81,82].

1.12.8 IMRT

IMRT is the delivery of radiation via a number of small beamlets through the use of multi-leaf collimators, either as a dynamic or step and shoot LINAC based treatment, or helical tomotherapy. This allows the radiation beam to be shaped, improving conformity, and allows for dose escalation by sparing organs at risk. This technique may be administered in the primary or adjuvant setting.

1.12.9 Biological Agents

The epidermal growth factor receptors (EGFR) are linked to a tyrosine kinase (TK) residue, and expressed at increased levels of 90 to 100% in SCCHN [83]. Ligand binding to the receptor activates TK, and down stream signal transduction.

Cetuximab is a humanised murine monoclonal antibody (MAB) to the receptor extra-cellular domain, inhibiting the activation of the TK. In patients with locally advanced SCC of the oropharynx, larynx, and hypopharynx, cetuximab (400mg/m² 1 week prior to the start of RT, followed by 250mg/m² weekly during RT) significantly improved the 3-year overall survival by 10% compared to RT alone, and loco-regional control by 32% [84]. Cetuximab is indicated for patients with stage III or IV SCCHN who would have been treated with platinum based CRT, but are unable to receive the chemotherapy due to other medical problems [85].

The acneiform rash side effect following EGFR inhibition positively correlates with clinical outcome, and is evident within three weeks of starting therapy. The overall survival is improved in those who experience increased severity of this cutaneous side effect.

1.13 Metastatic Disease

The management of advanced SCCHN is focused on symptom control and the maintenance of quality of life. Palliative chemotherapy and RT, analgesia, nutritional and psychological support are components of this supportive care. Outcome is poor, with a median survival of 6 to 9 months. The 1-year survival is between 20 to 40% if patients receive palliative chemotherapy [86].

In the UK, the commonest first line agents are combination cisplatin (75mg/m², day 1) and infusional 5-fluorouracil (750 to 1000mg/m² days 1 to 4). Single agent taxanes are used second line. Palliative RT may be a single fraction (8Gy) or hypo-fractionated (27Gy in 6 fractions, 39Gy in 13 fractions).

1.14 Survival and Outcome

The 5-year survival of patients with SCCHN is dependent on early diagnosis, stage and primary site, and remains at 35%. In the UK, 2,496 deaths (35.84%) from HN cancer were recorded in 2006 [87]. The number of deaths increased sharply after the age of 60. Over the past 30 to 40 years there has been minimal change in the European age-standardised mortality rate [88], which is illustrated in figure 1.9.

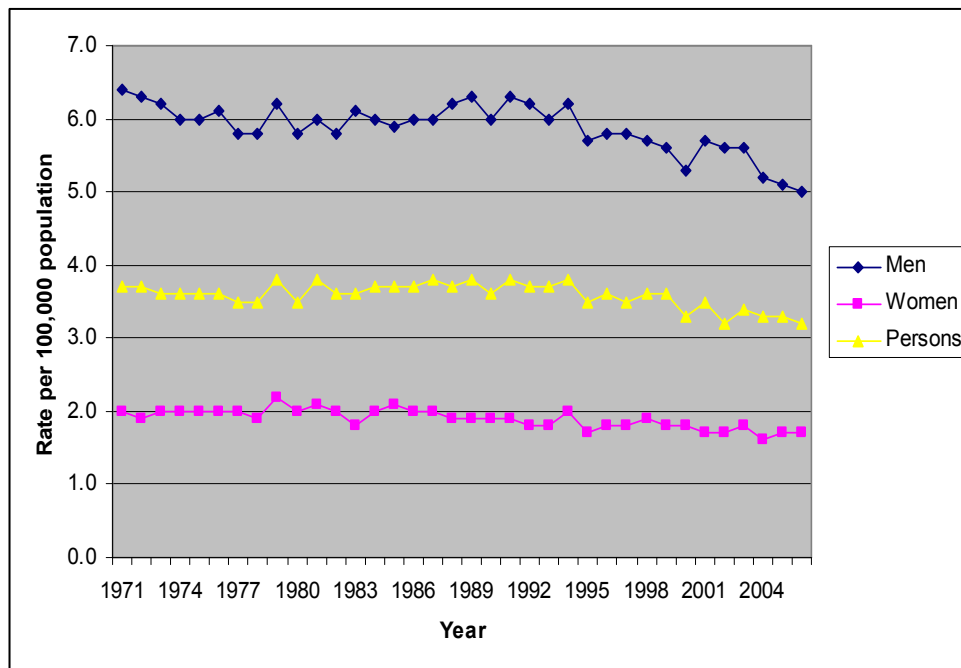


Figure 1.9: European age standardised mortality rates in men and women with Head and Neck cancer between 1971 and 2006

1.15 Thesis Aims

Treatment failure in patients with SCCHN is principally due to poor local control. Fifty percent fail in this region, and only 20% will go on to develop metastases outside the HN.

Local failure is due to the extent of disease at presentation and tumour biology (hypoxic radio-resistance, and increased metabolism). Failure after treatment results in disease that is difficult to treat and is a major cause of death despite changes in surgical, chemotherapeutic, and radiation treatment.

RT dose escalation to regions at risk of local failure has the potential to improve control and so outcome.

CT-PET imaging can identify TVs that reflect the underlying tumour biology. A number of radio-nuclides have been used for example ^{18}F FDG (glucose metabolism), ^{64}Cu -ATSM (^{64}Cu (II) diacetyl-bis(N^4 methylthiosemicarbazone))

and ^{18}F -misonidazole (hypoxia), 3'-deoxy-3'- ^{18}F -fluorothymidine (proliferation/DNA synthesis). The incorporation of biological imaging in the patient's investigative and treatment pathway can depend on the physical isotope properties and radio-chemistry for production, and most importantly the ability to define and treat the representative biological volumes.

This thesis is focused on the application of two radio-nuclides in CT-PET imaging of SCCHN to delineate intra-tumoural metabolic and hypoxic TVs that may be dose escalated with RT, to reduce the rate of local failure.

Firstly, ^{18}F FDG has the potential to make the greatest clinical impact, and be the most widely applicable to IGRT because it images metabolically active tumour, which may result in failure to cure with RT. There is no agreed method of TV delineation. Three separate methods (two fixed and one adaptive) have been directly compared before and during RT in patients undergoing RT or CRT for locally advanced SCCHN. This evaluated differences in the defined TV, factors that may influence any volume change, and gave guidance as to the most appropriate method for RT planning. PETVCAR software was used to automatically delineate volumes at each imaging point by 4 SUV cut off thresholds, 5 thresholds of the percentage of the SUVmax, and an individualised adaptive threshold. The volumes defined during RT were directly compared with those before the start of treatment. The SUVmax was assessed within these volumes, as well as the background uptake of ^{18}F FDG.

Secondly ^{64}Cu -ATSM has been suggested as a novel hypoxic radio-nuclide in SCCs. The retention pattern at 5 to 20, 40 to 60 minutes and 18 hours following injection has been investigated in patients with locally advanced disease who were due to be treated with primary surgery. The TVs were defined by tumour to muscle, blood and background ratios at these time points. The exogenous and endogenous hypoxic fraction was calculated by immuno-histochemical methods on the surgical specimen, and correlated with the intra-tumoural distribution of ^{64}Cu -ATSM. Perfusion parameters were evaluated to map blood flow with the retention of ^{64}Cu -ATSM.

1.16 References

1. Office for National Statistics. Cancer Statistics registrations: Registrations of cancer diagnosed in 2004, England. In: www.statistics.gov.uk ed, ; 2007
2. Northern Ireland Cancer Registry. Cancer Incidence and Mortality. In: www.qub.ac.uk/nicr/ ed; 2007
3. Welsh Cancer Intelligence and Surveillance Unit. Cancer Incidence in Wales. In: www.wales.nhs.uk ed; 2007
4. Office of National Statistics. Census 2001. In: www.statistics.gov.uk; 2004
5. Macfarlane GJ, Boyle P, Scully C. Oral cancer in Scotland: changing incidence and mortality. BMJ 1992;305:1121-1123
6. Macfarlane GJ, Boyle P, Evstifeeva TV, Robertson C, Scully C. Rising trends of oral cancer mortality among males worldwide: the return of an old public health problem. Cancer Causes Control 1994;5
7. Office for National Statistics. General Household Survey 2003/4. In: www.statistics.gov.uk ed; 2008
8. Blot WJ, McLaughlin JK, Winn DM, et al. Smoking and drinking in relation to oral and pharyngeal cancer. Cancer Research 1994;48:3282-3287
9. Balaram P, Sridhar H, Rajkumar T, et al. Oral cancer in southern India: the influence of smoking, drinking, paan-chewing and oral hygiene. Int J Cancer 2002;98:440-445
10. Samet J. Health benefits of smoking cessation. Clin Chest Med 1991;12:669-679

11. International Agency for Research on Cancer. IARC Monographs on the Evaluation of Carcinogenic Risks to Humans: Tobacco smoke and involuntary smoking. In: www.iarc.fr/ ed; 2004
12. Office of National Statistics. Living in Britain: Results from the 2002 General Household Survey. In: www.statistics.gov.uk ed; 2004
13. Hedges B, di Salvo P. Alcohol consumption and smoking. In, Health survey for England. London: Stationery Office; 1996
14. Currie C, Roberts C, Morgan A, et al. Young People's Health in Context: international report from the HBSC 2001/02 survey. WHO Policy Series: Health policy for children and adolescents. In: Europe WROf ed. Copenhagen; 2004
15. Rodriguez T, Altieri A, Chatenoud L, et al. Risk factors for oral and pharyngeal cancer in young adults. Oral Oncology 2004;40:207-213
16. Macfarlane GJ, Zheng T, Marshall JR, et al. Alcohol, tobacco, diet and the risk of oral cancer: a pooled analysis of three case-control studies. Eur J Cancer B Oral Oncol 1995;31B:181-187
17. Freedman ND, Park Y, Subar AF, et al. Fruit and vegetable intake and head and neck cancer risk in a large United States prospective cohort study. Int J Cancer 2008;122:2330-2336
18. Key TJ, Schatzkin A, Willett WC, et al. Diet, nutrition and the prevention of cancer. Public Health Nutr 2004;1A:187-200
19. Pelucchi C, Talamini R, Negri E, et al. Folate intake and risk of oral and pharyngeal cancer. Ann Oncol 2003;14:1677-1681
20. Garavello W, Randi G, Bosetti C, et al. Body size and laryngeal cancer risk. Ann Oncol 2006;17:1459-1463

21. Liu SA, Tsai WC, Wong YK, et al. Nutritional factors and survival of patients with oral cancer. *Head Neck* 2006;28:998-1007
22. Gillison ML, Koch WM, Capone RB, et al. Evidence for a causal association between human papillomavirus and a subset of head and neck cancers. *J Natl Cancer Inst* 2000;92:709-720
23. Ryerson AB, Peters ES, Coughlin SS, et al. Burden of potentially human papillomavirus-associated cancers of the oropharynx and oral cavity in the US, 1998-2003. *Cancer* 2008;113:2901-2909
24. Szeto CH, Shek TW, Lie AK, et al. Squamous cell carcinoma of the tongue complicating chronic oral mucosal graft-versus-host disease after allogeneic hematopoietic stem cell transplantation. *Am J Haematology* 2004;77:200-202
25. Butt FM, Chindia ML, Rana F, Machigo FG. Pattern of head and neck malignant neoplasms in HIV-infected patients in Kenya. *Int J Oral Maxillofac Surg* 2008;37:907-911
26. Frisch M, Biggar RJ, Engels EA, Goedert JJ. Association of cancer with AIDS-related immunosuppression in adults. *JAMA* 2001;285:1736-1745
27. Rodrigues VC, Moss SM, Tuomainen H. Oral cancer in the UK: to screen or not to screen. *Oral Oncology* 1998;34:454-465
28. van der Waal I, Schepman KP, van der Meij EH, Smeele LE. Oral leukoplakia: a clinicopathological review. *Oral Oncology* 1997;33:291-301
29. Scheifele C, Reichart PA. Is there a natural limit of the transformation rate of oral leukoplakia? *Oral Oncology* 2003;39:470-475
30. Shafer WG, Waldron CA. Erythroplakia of the oral cavity. *Cancer* 1975;36:1021-1028

31. Zhang ZF, Morgenstern H, Spitz MR, et al. Marijuana use and increased risk of squamous cell carcinoma of the head and neck. *Cancer Epidemiol Biomarkers Prev* 1999;8:1071-1078
32. Warnakulasuriya KA, Robinson D, Evans H. Multiple primary tumours following head and neck cancer in southern England during 1961-98. *J Oral Pathol Med* 2003;32:443-449
33. Cianfriglia F, Di Gregorio DA, Manieri A. Multiple primary tumours in patients with oral squamous cell carcinoma. *Oral Oncology* 1999;35:157-163
34. Sobin LH. *TNM Classification of Malignant Tumours*, 6th Edition: John Wiley & Sons; 2002
35. Gray H. *Anatomy of the Human Body*. 20th ed. Philadelphia: Lea & Febiger; 1918
36. Lindberg R. Distribution of cervical lymph node metastases from squamous cell carcinoma of the upper respiratory and digestive tracts. *Cancer* 1972;29:1446-1449
37. Som PM. Detection of metastasis in cervical lymph nodes: CT and MR criteria and differential diagnosis. *AJR Am J Roentgenol* 1992;158:961-969
38. Som PM, Curtin HD, Mancuso S. An imaging-based classification for the cervical nodes designed as an adjunct to recent clinically-based nodal classifications. *Arch Otolaryngol* 1999;125:388-396
39. Shah JP, Candela FC, Poddar AK. The patterns of cervical lymph node metastases from squamous carcinoma of the oral cavity. *Cancer* 1990;66:109-113

40. Woolgar J. Detailed topography of cervical lymph-node metastases from oral squamous cell carcinoma. *Oral and Maxillofacial Surgery* 1997;26:3-9
41. Woolgar JA, Rogers SN, Lowe D, Brown JS, Vaughan ED. Cervical Lymph node metastasis in oral cancer: the importance of even microscopic spread. *Oral Oncology* 2003;39:130-137
42. Woolgar JA. The topography of cervical lymph node metastases revisited: the histological findings of 526 slide of neck dissection from 439 previously untreated pateints. *Oral and Maxillofacial Surgery* 2007;36:219-225
43. Levison DA, Reid R, Burt AD, Harrison DJ, Fleming S. Muirs' Textbook of Pathology. London: Hodder Arnold; 2008
44. Daley T, Darling M. Nonsquamous cell malignant tumours of the oral cavity: an overview. *J Can Dent Assoc* 2003;69:577-582
45. Hounsfield GN. Computerized transverse axial scanning (tomography). 1. Description of system. *Br J Radiol* 1973;46:1016-1022
46. Kalender WA, Seissler W, Klotz E, Vock P. Spiral volumetric CT with single-breath-hold technique, continuous transport, and continuous scanner rotation. *Radiology* 1990;176:181-183
47. Goldman LW. Principles of CT and CT technology. *J Nucl Med Technol* 2007;35:115-128; quiz 129-130
48. Maroldi R, Battaglia G, Farina D, Maculotti P, Chiesa A. Tumours of the oropharynx and oral cavity: perineural spread and bone invasion. *JBR-BTR* 1999;82:294-300
49. Wong RJ. Current status of FDG-PET for head and neck cancer. *J Surg Oncol* 2008;97:649-652

50. Rusthoven KE, Koshy M, Paulino AC. The role of fluorodeoxyglucose positron emission tomography in cervical lymph node metastases from an unknown primary tumor. *Cancer* 2004;101:2641-2649
51. Miller FR, Karnad AB, Eng T, et al. Management of the unknown primary carcinoma: long-term follow-up on a negative PET scan and negative panendoscopy. *Head Neck* 2008;30:28-34
52. Schechter NR, Gillenwater AM, Byers RM, et al. Can positron emission tomography improve the quality of care for head-and-neck cancer patients? *Int J Radiat Oncol Biol Phys* 2001;51:4-9
53. Adams S, Baum RP, Stuckensen T, Bitter K, Hor G. Prospective comparison of 18F-FDG PET with conventional imaging modalities (CT, MRI, US) in lymph node staging of head and neck cancer. *Eur J Nucl Med* 1998;25:1255-1260
54. Lonneux M, Lawson G, Ide C, et al. Positron emission tomography with fluorodeoxyglucose for suspected head and neck tumor recurrence in the symptomatic patient. *Laryngoscope* 2000;110:1493-1497
55. Lowe VJ, Boyd JH, Dunphy FR, et al. Surveillance for recurrent head and neck cancer using positron emission tomography. *J Clin Oncol* 2000;18:651-658
56. Greven KM, Williams DW, 3rd, McGuirt WF, Sr., et al. Serial positron emission tomography scans following radiation therapy of patients with head and neck cancer. *Head Neck* 2001;23:942-946
57. Wong RJ, Lin DT, Schoder H, et al. Diagnostic and prognostic value of [(18)F]fluorodeoxyglucose positron emission tomography for recurrent head and neck squamous cell carcinoma. *J Clin Oncol* 2002;20:4199-4208

58. Koshy M, Paulino AC, Howell R, et al. F-18 FDG PET-CT fusion in radiotherapy treatment planning for head and neck cancer. *Head Neck* 2005;27:494-502
59. Wong WL, Saunders M. The impact of FDG PET on the management of occult primary head and neck tumours. *Clin Oncol (R Coll Radiol)* 2003;15:461-466
60. Cancer Research UK Information Divison (Online). www.cancerresearchuk.org. In; 2005
61. Spiro RH, Morgan GJ, Strong EW, Shah JP. Supraomohyoid neck dissection. *Am J Surg* 1996;172:650-653
62. Byers RM, Clayman GL, McGill D, et al. Selective neck dissections for squamous carcinoma of the upper aerodigestive tract: patterns of regional failure. *Head Neck* 1999;21:499-505
63. Byers RM, Wolf PF, Ballantyne AJ. Rationale for elective modified neck dissection. *Head Neck Surg* 1988;10:160-167
64. ICRU. ICRU Report 50. Prescribing, recording, and reporting photon beam therapy. In: International Commission on Radiation Units and Measurements, Bethesda, MD; 1993
65. Gre'goire V, Levendag P, Ang KK, et al. CT-based delineation of lymph node levels and related CTVs in the node-negative neck: DAHANCA, EORTC, GORTEC, NCIC, RTOG consensus guidelines. *Radiotherapy and Oncology* 2003;69:227-236
66. Bataini JP, Bernier J, Brugere J, et al. Natural history of neck disease in patients with squamous cell carcinoma of oropharynx and pharyngolarynx. *Radiother Oncol* 1985;3:245-255

67. Huang DT, Johnson CR, Schmidt-Ullrich R, Grimes M. Postoperative radiotherapy in head and neck carcinoma with extracapsular lymph node extension and/or positive resection margins: a comparative study. *Int J Radiat Oncol Biol Phys* 1992;23:737-742
68. Snow GB, Annyas AA, van Slooten EA, Bartelink H, Hart AA. Prognostic factors of neck node metastasis. *Clin Otolaryngol Allied Sci* 1982;7:185-192
69. Johnson JT, Barnes EL, Myers EN, et al. The extracapsular spread of tumors in cervical node metastasis. *Arch Otolaryngol* 1981;107:725-729
70. Hirabayashi H, Koshii K, Uno K, et al. Extracapsular spread of squamous cell carcinoma in neck lymph nodes: prognostic factor of laryngeal cancer. *Laryngoscope* 1991;101:52-506
71. Mazon JJ, Ardiet JM, Haie-Meder C, et al. GEC-ESTRO recommendations for brachytherapy for head and neck squamous cell carcinomas. *Radiother Oncol* 2009;91:150-156
72. Pignon JP, Bourhis J, Domenge C, Designe L. Chemotherapy added to locoregional treatment for head and neck squamous-cell carcinoma: three meta-analyses of updated individual data. MACH-NC Collaborative Group. Meta-Analysis of Chemotherapy on Head and Neck Cancer. *Lancet* 2000;355:949-955
73. Pignon JP, le Maitre A, Bourhis J. Meta-Analyses of Chemotherapy in Head and Neck Cancer (MACH-NC): an update. *Int J Radiat Oncol Biol Phys* 2007;69:S112-114
74. Al-Sarraf M, LeBlanc M, Giri PG, et al. Chemoradiotherapy versus radiotherapy in patients with advanced nasopharyngeal cancer: phase III randomized Intergroup study 0099. *J Clin Oncol* 1998;16:1310-1317

75. Vermorken JB, Mesia R, Rivera F, et al. Platinum-based chemotherapy plus cetuximab in head and neck cancer. *N Engl J Med* 2008;359:1116-1127
76. Posner MR, Hershock DM, Blajman CR, et al. Cisplatin and fluorouracil alone or with docetaxel in head and neck cancer. *N Engl J Med* 2007;357:1705-1715
77. ICRU. ICRU Report 62. Prescribing, recording, and reporting photon beam therapy (Supplement to ICRU Report 50). In, International Commission on Radiation Units and Measurements Bethesda, MD; 1999
78. Gregoire V EA, Hamoir M, Levendag P. Proposal for the delineation of the nodal CTV in the node-positive and the post-operative neck. *Radiotherapy and Oncology* 2006;79:15-20
79. Cooper JS, Pajak TF, Forastiere AA, et al. Precisely defining high-risk operable head and neck tumors based on RTOG #85-03 and #88-24: targets for postoperative radiochemotherapy? *Head Neck* 1998;20:588-594
80. Laramore GE, Scott CB, al-Sarraf M, et al. Adjuvant chemotherapy for resectable squamous cell carcinomas of the head and neck: report on Intergroup Study 0034. *Int J Radiat Oncol Biol Phys* 1992;23:705-713
81. Cooper JS, Pajak TF, Forastiere AA, et al. Postoperative concurrent radiotherapy and chemotherapy for high-risk squamous-cell carcinoma of the head and neck. *N Engl J Med* 2004;350:1937-1944
82. Bernier J, Dometge C, Ozsahin M, et al. Postoperative irradiation with or without concomitant chemotherapy for locally advanced head and neck cancer. *N Engl J Med* 2004;350:1945-1952
83. Dassonville O, Formento, JL, Francoual, M, Ramaioli, A, Santini, J, Schneider, M, Demard, F, Milano, G. Expression of epidermal growth

factor receptor and survival in upper aerodigestive tract cancer. J Clin Oncol 1993;11:1873-1878

84. Bonner JA, Harari PM, Giralt J, et al. Radiotherapy plus cetuximab for squamous-cell carcinoma of the head and neck. N Engl J Med 2006;354
85. NICE. Cetuximab for the treatment of locally advanced squamous cell cancer of the head and neck. In; 2008
86. Colevas A. Chemotherapy Options for Patients With Metastatic or Recurrent Squamous Cell Carcinoma of the Head and Neck. JCO 2006;24:2644-2652
87. Office for National Statistics. Mortality Statistics: Cause, 2005. In: www.statistics.gov.uk ed; 2007
88. Information Services Division Scotland. Cancer Incidence and mortality data 2005. www.widscotland.org 2007

Chapter 2

¹⁸Fluoro-2-deoxyglucose CT-PET Functional Imaging and Target Volume Delineation in Squamous Cell Cancer of the Head and Neck

MRI and CT-PET are the two main functional imaging modalities. Intra-tumoural homeostatic pathways may be assessed such as: glucose metabolism, and hypoxia (Chapter 3), as well as perfusion parameters. Perfusion imaging will be discussed in Chapter 3 section 3.7.

2.1 Positron Emission Tomography

Emitted neutron radiation from ¹⁰Boron was first imaged by Javid et al in 1952 [1] and then in 1956 with positrons in the assessment of intra-cranial lesions [2]. CT and MRI localise and visualise abnormal tissue in relation to normal anatomical structures. The combination of CT and PET provides additional information of physiological processes related to the anatomical region. For example: glucose metabolism, hypoxia, and deoxyribonucleic acid (DNA) synthesis. The automatic co-registration of these data sets through hybrid combination CT-PET machines has improved the interpretation of PET images compared to PET alone.

2.1.1 Emission and Detection of Positrons

Unstable radio-active isotopes return to the stable state by positron (positively charged electrons/anti-matter) emission, or capture of an orbiting electron.

These radio-nuclides may be produced by the addition of a proton to the parent nucleus, or neutron ejection from the nucleus in a nuclear reactor. An example of these reactions is shown.

Proton Addition $^{18}\text{O} + \text{Proton} \rightarrow ^{18}\text{F}$

Neutron Ejection $^{62}\text{Zn} \rightarrow ^{62}\text{Cu} + \text{Neutron}$

The energy emitted by the positrons is proportional to the number of protons within the nucleus. These positrons interact with electrons in the surrounding environment over a short distance. The final interaction is an annihilation reaction (converting mass to energy), to generate two co-incident photons, each with an emitted energy of 511KeV (Kilo electron Volt). The photons travel in opposite directions to each other at 180 degrees. Residual kinetic energy from the annihilation reaction may deflect the positrons by up to 0.5 degrees from this path [3].

Annihilation co-incidence photons are detected by multiple 3D rings of crystals (photo-diodes) in blocks, which rotate around the couch within the positron emission tomography (PET) scanner. The photons are converted to light, and software algorithms are used to reconstruct the image.

These photons are detected as random or true events following the annihilation reaction. The true events occur when the co-incidence photons travel along their projected path when the two photons reach the detectors within 20 nano seconds, at 180 degrees to each other. Random co-incidence events occur when a single photon is detected, or when two random photons are detected at the same time. Random events increase the background activity and reduce the image quality.

The sensitivity of the scanner is dependent on: the thickness of the detector crystal (50% reduction in the thickness will reduce the sensitivity by a factor of four), the number of detectors, their size and position from the region of interest (ROI), and the photo-diode material.

2.1.2 Detector Crystals

The commonest detector crystals are lutetium oxyorthosilicate, and bismuth germanium oxide [4]. The properties of the crystal include: density, generated light pulse width, light output, and the scintillator light wavelength. Lutetium

oxyorthosilicate is the most efficient at photon detection because it produces a lower number of scattered and random co-incidence events. Table 2.1 shows the attributes of each of the commonest detector crystals.

Table 2.1: The physical properties of Lutetium Oxyorthosilicate and Bismuth Germanium Oxide

	Density (g/cm³)	Maximum Wavelength (nm)	Photon (MeV)	Decay Time (ns)
Lutetium Oxyorthosilicate	7.4	420	30,000	40
Bismuth Germanium Oxide	7.13	480	8,200	60,300

2.1.3 Spatial Resolution

The camera resolution is defined as the full width half maximum. This is the minimum distance that the detectors are able to register the emitted annihilation photons as two separate events. The resolution depends most importantly on the crystal width, range and non-linear deflection of the photons, along with the software used to reconstruct the images. The resolution of combined scanners is between 4 to 6mm.

2.1.4 Scatter

Scatter occurs when the annihilation photons are deviated from their true path. The scatter increases the signal to background ratio of the scanner, affecting the image quality, blurring the ROI on the reconstructed image. The Monte Carlo calculation is the optimal method to reduce scatter, based on the Klein Nishina formula [3]. This utilises the attenuation map from the CT data, and the first image reconstruction to calculate the expected background scatter. Other methods include: shielding in the form of projections between the photo-diode blocks (small septa improve photon detection from adjacent planes, but increase scatter), time of flight projections to enhance image reconstruction [5],

deconvolution of the scatter projections, and review of the PET matrix depending on the detected activity outside the ROI.

2.1.5 Attenuation and Dead Time

Annihilation photons may be attenuated along their projected path by surrounding tissue. This attenuation can be corrected using the HU from the CT data set.

The detector system may not register each individual detection event (dead time) if it occurs within a short time period from another event. This occurs when the radio-nuclide emits high annihilation photon counts per second, for example ^{15}O and ^{13}N . A time elapse is required to allow the detection of each photon event (2 μs). The dead time is dependent on the rate of decay of light within the photo-diode block, and the photo-multiplier tube.

2.1.6 CT Contrast Agents in Combination with CT-PET

The administration of intra-venous iodinated contrast during CT-PET imaging allows improved detection and characterisation of pathological lesions, and surrounding anatomical structures. The evaluation and detection of regional LN groups is an example of this. Contrast is contra-indicated in patients with iodine allergies, significant renal impairment, and hyperthyroidism [6]. It also allows a dynamic contrast enhanced CT (DCE-CT) to be undertaken with the patient in the same position as the CT-PET scan.

Oral contrast agents define the intestinal tract with either positive or negative attenuation.

Artefacts may occur during the co-registration of the CT and PET image sets in high contrast attenuation regions or near dental amalgam. Artefacts appear as regions of high ^{18}F FDG uptake [7], and are usually only present in the attenuation corrected (AC) PET images.

2.1.7 Patient Position

Imaging takes between 20 to 60 minutes depending on the extent of the anatomical region to be visualised. Arm position is dependent on site of imaging, beam hardening and streak artefacts can occur on the CT data set [8] depending on position.

When CT-PET images are used to plan RT in SCCHN, arms flexed above the head will produce beam hardening, and potentially attenuate the radiation beam during dosimetry calculations. Patients are therefore imaged with their arms by their sides, both for treatment planning scans, and ideally for diagnostic imaging as well. Conversely, the arms are raised, and elbows flexed when the abdomen is imaged.

2.1.8 Image Reconstruction and Algorithms for the Fusion of CT and PET

Image reconstruction defines the spatial distribution of the radio-nuclide within the body, accounts for random scatter, and the photon emission rate.

The lines of projection of the annihilation photons are grouped and ordered into a sinogram, to identify the spatial distribution of the radio-nuclide within each individual PET image. This data is then smoothed and filtered to reduce the noise and deblur the image, inversely transformed, and filter back projected (along the line of projection of the emitted photon) to the point of annihilation.

The PET and CT images generated can then be fused automatically using integrated software or manually to achieve the final image. The CT data is acquired first in full expiration, followed by the PET during shallow tidal breathing from combined CT-PET machines. Movement artefact can lead to mis-registration of the image sets. This is less within the HN region compared to thorax but may be improved by the use of immobilisation devices such as the thermoplastic HN shell for RT planning scans.

2.2 Radio-Pharmaceutical Properties of ^{18}F Fluorine

^{18}F FDG is the commonest radio-nuclide in clinical use, and its structure is shown in figure 2.1 with the ^{18}F Fluorine linked to the carbon atom at position two of the ring structure.

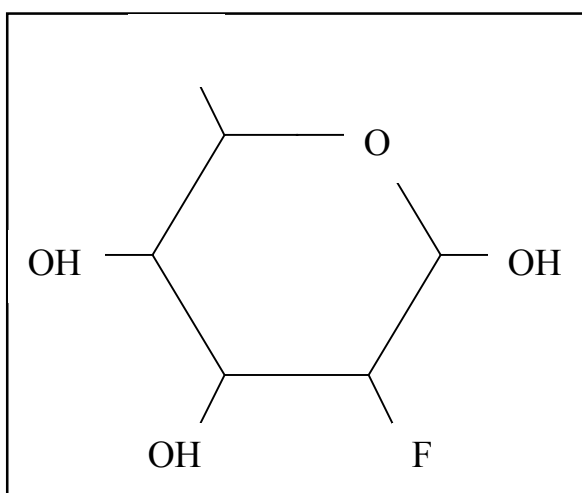


Figure 2.1: The structure of ^{18}F Fluoro-2-deoxyglucose

^{18}F FDG can be produced by two methods: either by the addition of elemental fluorine (directly or indirectly) to deoxyglucose, or most commonly by a nucleophilic substitution reaction in a cyclotron. In this reaction, ^{18}O Oxygen incorporated into water, is bombarded with high energy (less than 15MeV) protons within the target of the cyclotron [9]. ^{18}F FDG is produced through robotic automated methods to improve purity, sterility, and reduce the radiation exposure to production staff.

The imaging properties of ^{18}F Fluorine correspond to the emitted photon energies. More than 96% of positrons are emitted by $^+\beta$ decay, and the energy of these is 635KeV. The average tissue range is 0.64 millimeters (mm) with a maximum path length of 2.4mm, and this improves the image resolution [10]. The half-life ($t_{1/2}$) of ^{18}F Fluorine is 110 minutes. This facilitates the incorporation of ^{18}F FDG into the intra-cellular glucose metabolic pathway.

2.3 ¹⁸Fluoro-2-deoxyglucose

2.3.1 Glucose Metabolism and Transport

Glucose is transported by facilitated diffusion via GLUT (Glucose Transporter) trans-membrane channels from the extra-cellular space to the intra-cellular cytoplasm regulated by insulin secretion.

Initially, intra-cellular glucose is converted to glucose-6-phosphate by hexokinase (rate limiting), and then by a multi-enzyme step into pyruvate with the production of NADH (nicotine adenine dinucleotide – reduced form) and adenosine tri-phosphate (ATP) illustrated in figure 2.2. Hexokinase is inhibited by increased concentrations of glucose-6-phosphate (negative feedback).

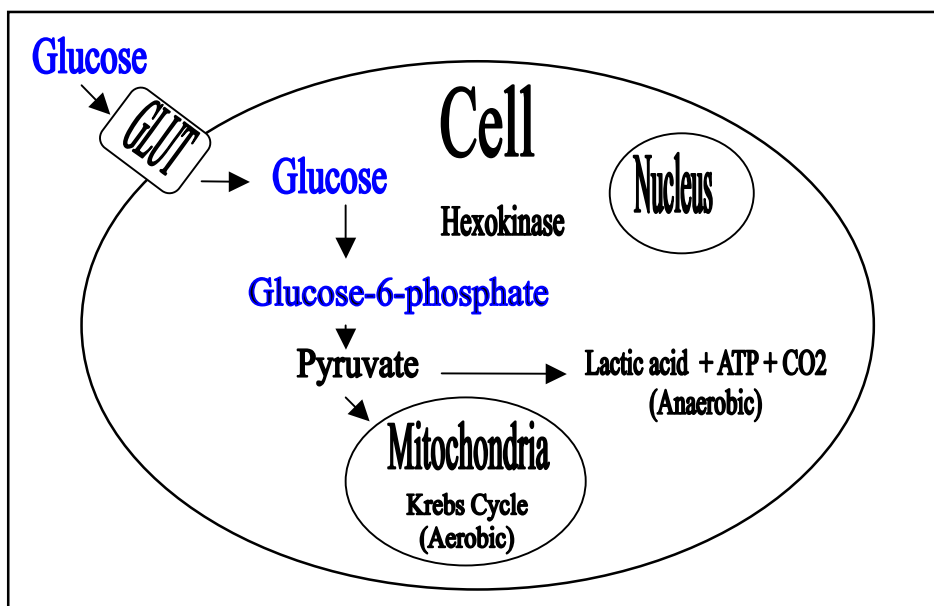


Figure 2.2: The transport of glucose from the extra-cellular to intra-cellular environment, and its intra-cellular metabolic pathway

Under aerobic conditions, pyruvate is transported from the cytoplasm to the mitochondria, and converted to acetylCoA. This is incorporated into the Krebs cycle by conversion to citric acid and oxaloacetate. Electrons are transported along the electron transport chain within the mitochondrial membrane through the reduction of NAD (nicotine adenine dinucleotide) to NADH. Oxygen is the final electron acceptor, leading to the production of carbon dioxide and water.

ATP is generated during this oxidative phosphorylation. Pyruvate is retained in the cytoplasm in anaerobic conditions, and converted to lactic acid, generating ATP. Electron transport occurs with the final electron acceptance by carbon dioxide.

The hallmarks of cancer include self sustaining growth, lack of effect of growth inhibitory factors/cytokines, evasion of apoptosis, unlimited replication, angiogenesis, cell migration, invasion, and metastasis formation [11]. The up-regulation of glucose metabolism in cancer cells is due to this increased metabolic demand. These all require ATP from glucose metabolism, and contribute to the generation of ^{18}F FDG CT-PET images.

2.3.2 GLUT Trans-Membrane Transporters

The GLUT family consists of 7 glycosylated trans-membrane transporter proteins. Glucose transportation is facilitated by a conformational change following glucose binding to their extra-cellular domain. GLUT1 is located on red blood cells for example.

The up-regulation of glucose metabolism in cancer cells was initially reported by Warburg [12]. Glycolysis and the production of lactic acid are greatest in cancer cells compared to normal cells under aerobic conditions. The rate of metabolism is dependent on up-regulated glucose transport [13], hexokinase and glucose-6-phosphate concentration. There is increased expression of the genes encoding hexokinase (bound to the mitochondrial membrane in cancer cells), GLUT1 and 3, and mRNA (messenger ribo-nucleic acid) transcription [14] in cancer cells. These up-regulated events are all absent from physiologically normal cells [15].

2.3.3 Intra-cellular trapping of ^{18}F Fluoro-2-deoxyglucose

The ^{18}F FDG enters the cells via GLUT and is phosphorylated by hexokinase to ^{18}F Fluoro-2-deoxyglucose-6-phosphate. This is metabolically inactive, and trapped within the cell by the fluorine ion at the second carbon position, preventing its conversion to pyruvate. Within the cell, low levels of glucose-6-phosphatase prevent dephosphorylation, further increasing the concentration of

^{18}F FDG. The accumulation of ^{18}F FDG is proportional to the rate of intra-cellular glucose metabolism [10].

Increased transcription of GLUT1 and 3 in cancer cells leads to faster uptake of ^{18}F FDG compared to normal cells [16]. Figure 2.3 illustrates the transport and metabolism of ^{18}F FDG.

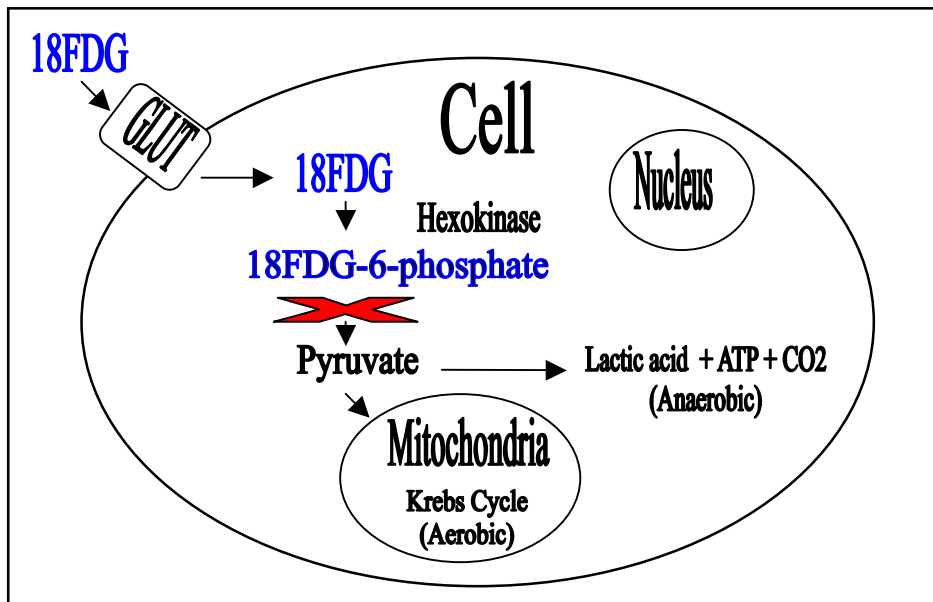


Figure 2.3: The transport of ^{18}F FDG from the extra-cellular to the intra cellular environment, and its intra-cellular metabolic pathway

^{18}F FDG is therefore a surrogate marker of glucose metabolism, and is rapidly distributed in plasma, extra-cellular and intra-cellular compartments.

2.4 Radio-nuclide Quantification

The uptake of ^{18}F FDG is quantified by: visual interpretation, the standardised uptake value (SUV), and kinetic modelling. Each method was reviewed by the National Institute of Health in 2006, and Consensus Recommendations [17] published. Other methods include the Patlak-Gjedde analysis, and total lesion glycolysis (TLG).

2.4.1 Visual Interpretation

Visual interpretation is the simplest method to assess ^{18}F FDG uptake, and can be used regardless of blood samples, the length of image acquisition, and the type of imaging. However this method is subjective, dependent on the interpretation of background uptake, and static imaging does not account for changes in uptake with time. This method is dependent on the time period from injection to imaging, the blood glucose concentration, and effects from partial voluming [17].

2.4.2 Standard Uptake Value

The SUV is the most commonly used semi-quantitative tool to quantify ^{18}F FDG uptake at a specific time point. The concentration of radio-nuclide is normalised to the injected dose, and the patient's body weight (bw) [18]. This has previously been reported as the Dose Uptake Ratio [19], Differential Absorption Ratio [20], or Differential Uptake Ratio [21]. The term SUV has now replaced these. The equation for the calculation of the SUV is shown below.

$$\text{SUV (MBq/g/ml)} = \frac{\text{Tissue Uptake of Radio-nuclide (MBq/ml)}}{\text{Injected Radio-nuclide Dose (MBq) / (body weight (kg) x 1000)}}$$

(MBq/g/ml – MegaBequerel per gram per millilitre)

The SUV_{max} indicates the maximum SUV detected within the ROI, whereas the SUV_{mean} is the mean or average SUV within the ROI.

The uptake and concentration of ^{18}F FDG and other radio-nuclides is dependent on a number of factors [22], which are shown in table 2.2.

Table 2.2: The parameters affecting radio-nuclide uptake

Parameters Affecting Radio-nuclide Uptake
Quantity of radio-nuclide administered
Route of administration
Pharmaco-kinetics and pharmaco-dynamics of radio-nuclide
Competition by endogenous substrate for target site
Non-specific interactions within the surrounding environment
Biochemistry of ligand
Vascular volume of the tissue
Time of uptake after administration

The SUV method can be used with static and whole body imaging, provides semi-quantitative interpretation, and no requirement for blood samples. Small changes in the SUV are more difficult to detect if the calculation is not normalised [17].

The calculation of the SUV can be influenced by a number of factors [23,24], shown in table 2.3.

Table 2.3: Factors affecting the SUV calculation

Factor	Affect on SUV
Time Period from Injection to Imaging	Final SUV (often use injection to mid-image acquisition time point [19])
Attenuation Correction	Always required, accounts for noise, counts obtained, gamma energy of radio-nuclide, the use of intra-venous contrast agent
Region of Interest Shape	Averaged volume of pixels or voxels within defined boundary
Partial Volume	Dependent on reconstruction algorithm and average pixel/voxel intensity

Hardware	Calibration, recovery co-efficients effect noise and image resolution
Software	Reconstruction algorithm influences noise and image resolution
Co-registration	Depends on accuracy of registration and correlation of ROI in time and final SUV
Body Size/Weight	Whole body imaging does not take into account uptake in fatty tissue.
Lean Body Mass/Body Surface Area	Account for changes in weight in whole body imaging, and correct for sex

These factors can often be corrected by normalisation and calibration calculations.

The SUV will peak and then plateau in malignant lesions up to 90 minutes after injection [25,26], or later in some cases. Imaging usually commences 90 minutes after ^{18}F FDG injection to aid the differentiation of benign and malignant lesions. The time point of imaging is especially important when comparing ROI within serial CT-PET images. The peak and plateau of ^{18}F FDG concentration within the ROI is dynamic, and unless serial scans are imaged at the same time point after injection, then time differences will lead to variations in the calculated SUV. In practise this can be difficult because the number of patients to be imaged and the time of injection of ^{18}F FDG relative to the time of imaging.

2.4.2.1 Normalisation to Body Weight, Lean Body Mass, and Body Surface Area

Currently, the most widely accepted normalisation is to the patient's body weight.

Other SUV normalisation methods include: lean body mass (lbm) [27], or body surface area (BSA) [28]. These values account for weight loss. All the normalised SUVs (body weight, lbm, and BSA) positively correlate with the absolute metabolic rate [17]. The equations below illustrate the SUV normalised to the lbm and BSA.

$$\text{SUV}_{\text{lbm or BSA}} = \frac{\text{Tissue Uptake of Radio-nuclide (MBq/ml)}}{\text{Injected Dose of Radio-nuclide (MBq) x lbm (kg) or BSA (m}^2\text{)}}$$

$$\text{Female lbm} = (1.07 \times \text{body weight (kg)} - 148 [\text{body weight (kg)} / \text{height (cm)}])^2$$

$$\text{Male lbm} = (1.1 \times \text{body weight (kg)} - 120 [\text{body weight (kg)} / \text{height (cm)}])^2$$

$$\text{BSA} = 0.007184 \times \text{body weight (kg)}^{0.425} \times \text{height (cm)}^{0.725}$$

2.4.2.2 Normalisation to Blood Glucose

The SUV can also be normalised to the patient's blood glucose (SUV_{gluc}) as shown.

$$\text{SUV}_{\text{gluc}} = \frac{\text{SUV x Glucose value (mmol/l)}}{5.5\text{mmol/l}}$$

Glucose normalised SUVs in patients with SCCHN were used to assess local recurrence after radical RT. The mean SUV_{gluc} pre-treatment was 2.25 to 28.5g/ml compared to 7.2g/ml in those patients without local recurrence. While at 1 month post RT on ^{18}F FDG PET imaging, the mean SUV_{gluc} was 1.8 to 9.97g/ml in those with local recurrence and 3.74g/ml in those patients without local recurrence [29]. When patients were imaged after fasting, and then following an oral glucose tolerance test (250ml water and 50g oral glucose), the fasting SUVs ranged from 4.1 to 10.9g/ml, and SUV reduced significantly by 2.2 to 5.9g/ml after the oral glucose tolerance test. This may suggest the sensitivity of ^{18}F FDG blood glucose concentration. However, these results should be interpreted with caution as patients were imaged 1 month after RT, which may

elevate the values, and image quality can be impaired after a glucose load because of increased muscle uptake of ^{18}F FDG [30].

2.4.3 Kinetic Modelling

Data is acquired dynamically in kinetic modelling. Arterial blood samples are used to calculate the rate constants and compartmental model under investigation. The derivation of these constants is complex as they reflect the differences in radio-nuclide transport, and metabolism. For example, the lump constant reflects differences in transport between ^{18}F FDG and glucose, phosphorylation by hexokinase and dephosphorylation [22,31].

This method is a research tool, and has limited use in everyday clinical imaging due to patient compliance with arterial blood samples, and complexity of the procedure. The model is highly dependent on the quality of data and samples collected as well as partial volume effects [17].

2.4.4 Patlak-Gjedde Analysis

The Patlak-Gjedde analysis quantifies radio-nuclides that are irreversibly trapped within cells, such as ^{18}F FDG. The influx rate constant can be determined. The data is acquired dynamically, and time-activity curves calculated [32]. This method accounts for the distribution of the radio-nuclide within the whole body, although patient movement can produce errors in the curve [25].

2.4.5 Total Lesion Glycolysis

The TLG is a non-invasive estimate of the glycolytic rate within the ROI. The change in the TLG can be calculated either directly or as the Larson-Ginsberg Index [33] which is shown in the equation below.

$$\text{TLG} = \text{Delineated Volume of ROI} \times \text{SUV}_{\text{mean}}$$

Larson-Ginsberg Index =

$$\frac{[\text{SUV}_{\text{mean pre-treatment}} \times (\text{pre-treatment volume} - \text{SUV}_{\text{mean post treatment}} \times \text{volume post-treatment})]}{[(\text{SUV}_{\text{mean pre-treatment}} \times \text{pre-treatment volume})]}$$

The calculation of absolute glucose utilisation rates requires complex kinetic modelling and rate constant determination [22].

2.5 Physiological Uptake of ^{18}F Fluoro-2-deoxyglucose

Physiological uptake of ^{18}F FDG can influence the interpretation of CT-PET images. Uptake can be increased within the myocardium, skeletal muscle, brown fat, gastro-intestinal tract, lymphatic tissue (tonsil, adenoids, thymus, and bone marrow), urinary tract, and low-grade uptake within the breast, ovaries and uterus. Fasting prior to imaging reduces the circulating insulin levels, and so the uptake of ^{18}F FDG uptake into muscle and fat. Ensuring that patients are kept warm prior to and during their scan has a similar effect.

Increased bone marrow uptake is particularly prominent following chemotherapy, and in those patients who require granulocyte colony stimulating factor injections for the treatment of chemotherapy induced neutropenia. These all potentially reduce the scan sensitivity.

False positive interpretations of ^{18}F FDG CT-PET may be secondary to: prolonged wound healing (especially in the presence of activated macrophages), infection, seromas, RT induced inflammation, granulomatous diseases (tuberculosis, sarcoidosis and histoplasmosis), and endocrine disorders (Paget's and Grave's disease). Conversely, reduced uptake (false negative) may occur in areas of necrosis.

2.5.1 Physiological Uptake within the Head and Neck

^{18}F FDG avidity may occur in dental implants, periodontal infections, normal musculature of the HN, and the Waldeyer's ring.

Dental implants produce stripe artefacts that appear as areas of increased ^{18}F FDG uptake on AC images. Reduced uptake is due to increased absorption of emitted photons by the metallic implant. Periodontal and dental space disease associated with an inflammatory reaction will locally increase the uptake of ^{18}F FDG.

Anterior floor of mouth, masticator muscles, anterior tip of the tongue, muscles of the face, neck, and larynx [34] all physiologically take up ^{18}F FDG. These are more prominent in nervous patients or those who talk after ^{18}F FDG administration.

Lymphoid tissue within the Waldeyer's ring also produces low-grade uptake (tonsil and posterior third of tongue).

Small amounts of glucose are present in the saliva and correspond to low-grade uptake within the salivary glands. Post-operatively, uptake within granulation tissue around the tracheal stoma may be present in patients who have undergone a laryngectomy.

2.6 Methods to Delineate ^{18}F Fluoro-2-deoxyglucose CT-PET Guided Target Volumes for Radiotherapy Planning

The method of delineation of metabolically active TVs is vitally important, as this will impact RT planning, dosimetry, and the final dose deliverable in dose escalation strategies aimed at improving local control. Threshold methods for TV delineation in SCCHN have been extrapolated from those used in NSCLC, and may be fixed or adaptive. The majority of published studies have not used combined CT-PET machines, and the CT and PET datasets were acquired separately and often at different time points.

Software available for delineation can be commercial or generated by a computer team within an institution limiting the reproducibility of data. Automatic segmentation allows the software user to define either a fixed or adaptive threshold. The edge of the volume is then automatically defined. Clinician choice therefore depends on resource availability.

2.6.1 Visual Interpretation

The individual clinician can adjust the threshold depending on contouring preference, without taking into account information from the CT data set, to define the ^{18}F FDG TV.

There is considerable inter-observer variation in ^{18}F FDG PET TV delineation by this method. This is reduced when protocols incorporate settings for window width and level, and inclusion of CT criteria to define disease [35]. In NSCLC, the information from PET defined TVs changed the RT field size by 25 to 34% [36,37]. This was also true for the two studies reported in SCCHN. The TVs corresponded in 90% of cases on CT, MRI and ^{18}F FDG PET imaging [38]. The TV delineation and normal tissue sparing were improved when CT and PET images were fused. The GTV reduced by at least 25% in 33% of patients, and in 46% the PTV was increased or decreased by 20% [39].

Figure 2.4 a, b, and c illustrates this in SCCHN. The higher the threshold, the more ^{18}F FDG background uptake is excluded, and the smaller the volume as in figure 2.4 c.

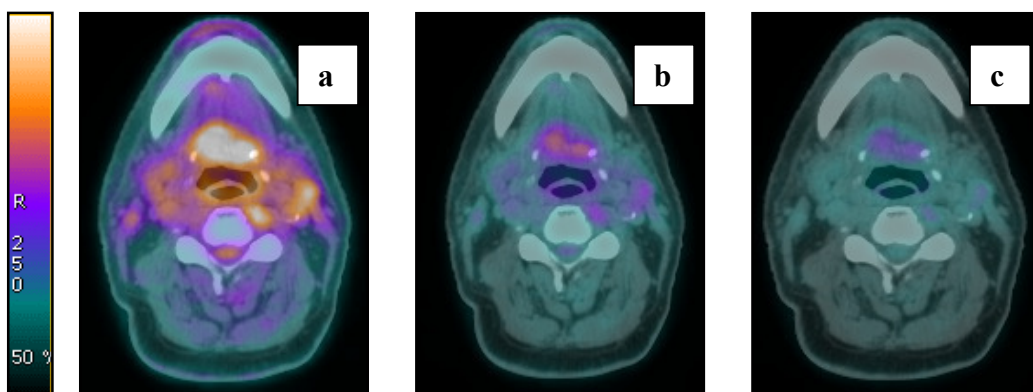


Figure 2.4: Clinician thresholded CT-PET images by visual interpretation

The use of visual interpretation within centres should be clearly defined, and will be improved when used with criteria for inclusion of disease extension (CT criteria for soft tissue enhancement) into the functional volume (FV).

2.6.2 Fixed Thresholds

The SUV Cut Off (SUVCO) is an absolute fixed threshold. The threshold excludes any ^{18}F FDG positive regions that are below the pre-determined level, and includes regions that are equal to or greater than it.

The percentage threshold of the SUVmax (PTSUVmax) defines the delineating edge according to a pre-determined percentage of the SUVmax. For example a 40% threshold to define a ROI with a SUVmax of 10g/ml will use a 4.0g/ml SUV threshold.

The main disadvantage of both methods is neither the background uptake nor the individual SUV within the ROI are taken into consideration. Both methods do not require information from the CT data set.

2.6.2.1 SUV Cut Off

The use of an SUVCO threshold of 2.5g/ml has been reported to differentiate normal and tumour tissue [40] in NSCLC. When compared to the CT defined volume, the ¹⁸FDG avid TV was on average 12.64% smaller for the SUVCO threshold of 2.5g/ml, and 61.66% smaller when contoured by the 40% of the SUVmax threshold. When the SUV was assessed according to the delineated volume, there was improved correlation at higher absolute thresholds greater than 6 and 7g/ml compared to the percentage threshold method. Smaller fixed absolute SUVCO thresholds of 4 to 6g/ml corresponded to tumour volumes less than 10.0 centimetres cubed (cm³) when compared to the CT volume [41]. This threshold was recommended for tumour delineation in NSCLC.

Other studies have used this 2.5g/ml cut off to differentiate tumour from normal tissue, and then applied a percentage SUVmax threshold to define the TV [42]. PET aided tumour delineation from surrounding atelectasis in NSCLC. The surrounding low-grade ¹⁸FDG uptake in areas of atelectasis significantly influenced the PET defined volume in more than 50% of patients [43] resulting in treatment modification.

Similarly, an SUVCO threshold of 3 to 4g/ml used to manually delineate the PET based TV was evaluated in patients undergoing radical RT for SCCHN [44]. Unlike other studies this reported increased observer variation when PET imaging was used to plan RT. However this study was biased as clinicians were not blinded, and each clinician arbitrarily set the SUV threshold to contour the volumes in line with visual interpretation.

2.6.2.2 Percentage threshold of the SUVmax

The 36 to 50% threshold of the SUVmax has been used to define the ^{18}F FDG PET TV in patients with SCCHN and NSCLC.

The 40% of the SUVmax reduced the volume of irradiated lung by 22.8% in 12 NSCLC patients who underwent curative RT [45]. However, the tumour SUVmax was defined as the largest region of highest uniform ^{18}F FDG uptake rather than the maximum SUV within an individual PET voxel. Similar differences in PET guided TV delineation and irradiated lung volumes have also been reported by this method [46,47].

In 75% of patients with SCCHN, PET TVs delineated by the 50% of the SUVmax threshold were smaller than those derived from CT data alone [48]. However 25% of this group had the high-risk macroscopic disease under treated when IMRT was planned on the CT data set only.

Following this, Daisne initially reported automatic segmentation of PET volumes using signal to background information calculated from a lucite phantom [49]. Further studies by this group validated CT, MRI and PET imaging with macroscopic pathological specimens from patients who underwent laryngectomies. The gold standard laryngeal GTV was the pathological volume in 2mm laryngeal axial sections delineated by an experienced Pathologist. There was no significant difference in the TVs delineated by CT and MRI. The PET volume was 28 to 37% smaller than those delineated by CT and MRI, and the pathological volume was a further 46% smaller than the PET volume [50]. Some of the pathological volumes were up to 107% larger than the PET defined volumes due to partial volume effects, and the inability of PET to adequately detect extra-laryngeal extension. CT over estimated the pathological volume in 65% and MRI in 89% of cases.

2.6.3 Adaptive Thresholds

Adaptive thresholds use information from parameters within the ROI such as the SUVmax to calculate an individual threshold to define the edge for each TV. The background uptake is taken into account during this process to aid the distinction

of pathological and normal tissue uptake. The threshold is usually then generated by an algorithm written into the software

Phantom studies using glass spheres filled with various amounts of ^{18}F FDG have been used to create such an algorithm in patients with NSCLC. The results were then applied to RT planning. This suggested that the SUVCO threshold of 2.5g/ml reflected TVs that were up to 23% smaller compared to the true phantom volume. The SUV was linearly related to the defined volume. Similar volumes at 42% of the SUVmax were defined with a difference of 67% between the true phantom volume and the SUVCO volume [51]. These differences were due to tumour heterogeneity, as they were not present within the phantom model. A signal to background algorithm was then proposed from this linear relationship to define the TV ($[0.307 \times \text{mean target SUV}] + 0.588$). This provided the adaptive threshold for each individual ROI/FV. The inherent difficulty with this method is the SUVmean within the ROI is dependent on the volume size.

In SCCHN, Geets et al confirmed that PET TVs were smaller than anatomically delineated volumes [52]. This group reported 18 patients with SCCHN (stage II to IV) who were due to receive 70Gy in 7 weeks of radical CRT, or accelerated RT (70Gy in 6 weeks). All patients underwent CT, MRI and ^{18}F FDG PET imaging prior to treatment and after a mean dose of 46Gy. The PET guided TVs were automatically delineated by software developed within the institution, and were up to 38% smaller than those based on CT and MRI. There was no difference between CT and MRI delineated volumes.

The volume change significantly corresponded to an 8% reduction in the mean IL parotid dose and 3% reduction in the mean CL parotid dose. The volume reduction corresponded to a smaller PTV, improving the dose distribution. Imaging during treatment resulted in significantly smaller delineated TVs by 57% for MRI and 42% for CT when compared to the pre-treatment planning CT.

Gradient-based threshold methods have also been developed to improve ^{18}F FDG PET guided TV delineation. This process involves denoising (attenuates statistical noise), deblurring and then deconvoluting (compensates for the effects

of scatter point spread function, and ensures the image is independent from the PET camera) the image. Finally vector gradients are estimated across each voxel. In phantom studies, the gradient-based method under-estimated the volume of each sphere by 10 to 20% [53]. On review of the work by Daisne et al [50] neither the threshold, nor gradient-based methods of ^{18}F FDG PET TV delineation completely encompassed the macroscopic pathological volume.

The threshold methods reported all have the disadvantage of not being transferable between institutions, and over-estimate the true volume by up to 68% [50]. The relation of the threshold to the signal to background ratio is dependant on the cameras calibration curve and acquisition parameters. The parameters involved include the radio-nuclide administered, emitted gamma count rate, camera resolution, image reconstruction algorithms, and the use of smoothing kernels. These require a different calibration in individual cameras. The phantom used to gain this information during calibration (size, shape) will affect the parameter obtained.

2.6.4 Halo Edge Detection

This was initially used in NSCLC [54], and then applied to SCCHN [55]. The halo is defined by its specific colour, thin wall, low SUV, and location around maximal metabolic activity within the TV. An SUV Cut Off of 2.5g/ml was used to define pathological uptake within the nodal and primary sites from normal background activity. The halo had an SUV of 2.19g/ml, and in 68% of cases this resulted in modification of the final TV.

2.6.5 Comparison of Delineation Methods

Four different segmentation methods in NSCLC have been directly compared (visual interpretation, SUVCO threshold of 2.5g/ml, 40% of the SUVmax, and a signal to background ratio based adaptive algorithm). The volume defined by the percentage maximum did not encompass all the disease outlined on CT. There was a positive correlation between the PET guided TV defined by the SUVCO threshold, signal to background ratio, and visual interpretation methods ($p < 0.02$, correlation co-efficient 0.96 to 0.98). The SUVmax, and tumour volume positively correlated ($p < 0.01$) when the ^{18}F FDG PET TV was defined by

the SUVCO threshold method [56]. The SUVCO threshold needed to be increased in patients with a higher background uptake of ^{18}F FDG to ensure clear delineation, because the background uptake varied due to inflammation [57].

Two studies in SCCHN have compared TV delineation by SUVCO threshold of 2.5g/ml, PTSUVmax 50%, and an adaptive threshold [58,59] prior to the start of RT, and are discussed in section 4.4 of chapter 4.

2.7 Aims of ^{18}F Fluoro-2-deoxyglucose CT-PET Guided Target Volume Delineation Study

The method of ^{18}F FDG CT-PET guided volume delineation is intricately related to the ability to dose escalate and reduce local failure. With no consensus, published studies are small and often difficult to replicate due to differences in software. The availability of commercial software to automatically delineate volumes will increase the need for consensus on volume definition especially if collaborative dose escalation studies are to be developed.

Three methods of ^{18}F FDG CT-PET guided TV delineation have been directly compared to assess the impact on the delineated volume using an automatic delineation software package by GE Healthcare before and at three time points during curative RT or CRT in patients with SCCHN.

These methods were: SUVCO, PTSUVmax, and an individualised adaptive threshold (IAT). Within each method different thresholds were used (4 thresholds for the SUVCO, 5 thresholds for the PTSUVmax, and 1 IAT) to further evaluate the effect of the threshold on volume change. The relationship between dose and volume, and dose and SUVmax was assessed by the co-registration of the individual CT-PET data sets at 8 to 18Gy, 36 to 50Gy, and 66Gy with the pre-treatment CT-PET. The influence of the SUVmax on the volume was also evaluated, as well as the background uptake of ^{18}F FDG within the CL SCM. Other parameters were analysed included the SUV mean, TLG,

and glucose normalised values but these have not been reported in this thesis due to space constraints.

2.8 References

1. Javid M, Brownell GL, Sweet WH. The possible use of neutron-capturing isotopes such as boron 10 in the treatment of neoplasms. II. Computation of the radiation energies and estimates of effects in normal and neoplastic brain. *J Clin Invest* 1952;31:604-610
2. Brownell GL, Sweet WH. Scanning of positron-emitting isotopes in diagnosis of intracranial and other lesions. *Acta radiol* 1956;46:425-434
3. Budinger TF. PET instrumentation: what are the limits? *Semin Nucl Med* 1998;28:247-267
4. Blodgett TM, Meltzer CC, Townsend DW. PET/CT: form and function. *Radiology* 2007;242:360-385
5. Karp JS, Surti S, Daube-Witherspoon ME, Muehllehner G. Benefit of time-of-flight in PET: experimental and clinical results. *J Nucl Med* 2008;49:462-470
6. Antoch G, Freudenberg LS, Beyer T, Bockisch A, Debatin JF. To enhance or not to enhance? 18F-FDG and CT contrast agents in dual-modality 18F-FDG PET/CT. *J Nucl Med* 2004;45 Suppl 1:56S-65S
7. Antoch G, Freudenberg LS, Egelhof T, et al. Focal tracer uptake: a potential artifact in contrast-enhanced dual-modality PET/CT scans. *J Nucl Med* 2002;43:1339-1342
8. Blodgett TM, McCook BM, Federle MP. Positron emission tomography/computed tomography: protocol issues and options. *Semin Nucl Med* 2006;36:157-168
9. Beuthien-Baumann B, Hamacher K, Oberdorfer F, Steinbach J. Preparation of fluorine-18 labelled sugars and derivatives and their

application as tracer for positron-emission-tomography. Carbohydrate Research 2000;327:107-118

10. Vallabhajosula S. (18)F-labeled positron emission tomographic radiopharmaceuticals in oncology: an overview of radiochemistry and mechanisms of tumor localization. Semin Nucl Med 2007;37:400-419
11. Hanahan D, Weinberg RA. The hallmarks of cancer. Cell 2000;100:57-70
12. Warburgh O. On the origin of cancers cells. Science 1956;123:309-314
13. Hatanaka M. Transport of sugars in tumor cell membranes. Biochim Biophys Acta 1974;355:77-104
14. Bell GI, Burant CF, Takeda J, Gould GW. Structure and function of mammalian facilitative sugar transporters. J Biol Chem 1993;268:19161-19164
15. Arora KK, Fanciulli M, Pedersen PL. Glucose phosphorylation in tumor cells. Cloning, sequencing, and overexpression in active form of a full-length cDNA encoding a mitochondrial bindable form of hexokinase. J Biol Chem 1990;265:6481-6488
16. Pauwels EK, Ribeiro MJ, Stoot JH, et al. FDG accumulation and tumor biology. Nucl Med Biol 1998;25:317-322
17. Shankar LK, Hoffman JM, Bacharach S, et al. Consensus recommendations for the use of 18F-FDG PET as an indicator of therapeutic response in patients in National Cancer Institute Trials. J Nucl Med 2006;47:1059-1066
18. Strauss LG, Conti PS. The applications of PET in clinical oncology. J Nucl Med 1991;32:623-648; discussion 649-650

19. Hamberg LM, Hunter GJ, Alpert NM, et al. The dose uptake ratio as an index of glucose metabolism: useful parameter or oversimplification? *J Nucl Med* 1994;35:1308-1312
20. Strauss LG, Clorius JH, Schlag P, et al. Recurrence of colorectal tumors: PET evaluation. *Radiology* 1989;170:329-332
21. Minn H, Joensuu H, Ahonen A, Klemi P. Fluorodeoxyglucose imaging: a method to assess the proliferative activity of human cancer in vivo. Comparison with DNA flow cytometry in head and neck tumors. *Cancer* 1988;61:1776-1781
22. Huang SC. Anatomy of SUV. Standardized uptake value. *Nucl Med Biol* 2000;27:643-646
23. Thie JA. Understanding the standardized uptake value, its methods, and implications for usage. *J Nucl Med* 2004;45:1431-1434
24. Keyes JW, Jr. SUV: standard uptake or silly useless value? *J Nucl Med* 1995;36:1836-1839
25. Weber WA, Ziegler SI, Thodtmann R, Hanauske AR, Schwaiger M. Reproducibility of metabolic measurements in malignant tumors using FDG PET. *J Nucl Med* 1999;40:1771-1777
26. Thie JA, Hubner KF, Smith GT. Optimizing imaging time for improved performance in oncology PET studies. *Mol Imaging Biol* 2002;4:238-244
27. Zasadny KR, Wahl RL. Standardized uptake values of normal tissues at PET with 2-[fluorine-18]-fluoro-2-deoxy-D-glucose: variations with body weight and a method for correction. *Radiology* 1993;189:847-850
28. Kim CK, Gupta NC, Chandramouli B, Alavi A. Standardized uptake values of FDG: body surface area correction is preferable to body weight correction. *J Nucl Med* 1994;35:164-167

29. Greven KM, Williams DW, 3rd, McGuirt WF, Sr., et al. Serial positron emission tomography scans following radiation therapy of patients with head and neck cancer. *Head Neck* 2001;23:942-946
30. Lindholm P, Minn H, Leskinen-Kallio S, et al. Influence of the blood glucose concentration on FDG uptake in cancer--a PET study. *J Nucl Med* 1993;34:1-6
31. Spence AM, Muzi M, Graham MM, et al. Glucose metabolism in human malignant gliomas measured quantitatively with PET, 1-[C-11]glucose and FDG: analysis of the FDG lumped constant. *J Nucl Med* 1998;39:440-448
32. Patlak CS, Blasberg RG, Fenstermacher JD. Graphical evaluation of blood-to-brain transfer constants from multiple-time uptake data. *J Cereb Blood Flow Metab* 1983;3:1-7
33. Larson SM, Erdi Y, Akhurst T, et al. Tumor Treatment Response Based on Visual and Quantitative Changes in Global Tumor Glycolysis Using PET-FDG Imaging. The Visual Response Score and the Change in Total Lesion Glycolysis. *Clin Positron Imaging* 1999;2:159-171
34. Goerres GW, von Schulthess GK, Hany TF. Positron Emission Tomography and PET CT of the Head and Neck: FDG Uptake in Normal Anatomy, in Benign Lesions, and in Changes Resulting from Treatment. *Am J Roentgenol* 2002;179:1337-1343
35. Macmanus MP, Bayne M, Fimmell N, et al. Reproducibility of "Intelligent" Contouring of Gross Tumor Volume in Non-Small Cell Lung Cancer on PET/CT Images Using a Standardized Visual Method. *Int J Radiat Biol* 2007;69 (Supplement 2):S154 to S155

36. Kiffer JD, Berlangieri SU, Scott AM, et al. The contribution of 18F-fluoro-2-deoxy-glucose positron emission tomographic imaging to radiotherapy planning in lung cancer. *Lung Cancer* 1998;19:167-177
37. Munley MT, Marks LB, Scarfone C, et al. Multimodality nuclear medicine imaging in three-dimensional radiation treatment planning for lung cancer: challenges and prospects. *Lung Cancer* 1999;23:105-114
38. Nishioka T, Shiga T, Shirato H, et al. Image fusion between 18FDG-PET and MRI/CT for radiotherapy planning of oropharyngeal and nasopharyngeal carcinomas. *International Journal of Radiation Oncology*Biology*Physics* 2002;53:1051-1057
39. Ciernik IF, Dizendorf E, Baumert BG, et al. Radiation treatment planning with an integrated positron emission and computer tomography (PET/CT): a feasibility study. *International Journal of Radiation Oncology*Biology*Physics* 2003;57:853-863
40. Paulino AC, Johnstone PA. FDG-PET in radiotherapy treatment planning: Pandora's box? *Int J Radiat Oncol Biol Phys* 2004;59:4-5
41. Hong R, Halama J, Bova D, Sethi A, Emami B. Correlation of PET standard uptake value and CT window-level thresholds for target delineation in CT-based radiation treatment planning. *Int J Radiat Oncol Biol Phys* 2007;67:720-726
42. Bradley J, Thorstad WL, Mutic S, et al. Impact of FDG-PET on radiation therapy volume delineation in non-small-cell lung cancer. *Int J Radiat Oncol Biol Phys* 2004;59:78-86
43. Nestle U, Walter K, Schmidt S, et al. 18F-deoxyglucose positron emission tomography (FDG-PET) for the planning of radiotherapy in lung cancer: high impact in patients with atelectasis. *Int J Radiat Oncol Biol Phys* 1999;44:593-597

44. Riegel AC, Berson AM, Destian S, et al. Variability of gross tumor volume delineation in head-and-neck cancer using CT and PET/CT fusion. *International Journal of Radiation Oncology*Biology*Physics* 2006;65:726-732
45. Giraud P, Grahek D, Montravers F, et al. CT and (18)F-deoxyglucose (FDG) image fusion for optimization of conformal radiotherapy of lung cancers. *Int J Radiat Oncol Biol Phys* 2001;49:1249-1257
46. Mah K, Caldwell CB, Ung YC, et al. The impact of (18)FDG-PET on target and critical organs in CT-based treatment planning of patients with poorly defined non-small-cell lung carcinoma: a prospective study. *Int J Radiat Oncol Biol Phys* 2002;52:339-350
47. Erdi YE, Mawlawi O, Larson SM, et al. Segmentation of lung lesion volume by adaptive positron emission tomography image thresholding. *Cancer* 1997;80:2505-2509
48. Paulino AC, Koshy M, Howell R, Schuster D, Davis LW. Comparison of CT- and FDG-PET-defined gross tumor volume in intensity-modulated radiotherapy for head-and-neck cancer. *International Journal of Radiation Oncology*Biology*Physics* 2005;61:1385-1392
49. Daisne J-F, Sibomana M, Bol A, et al. Tri-dimensional automatic segmentation of PET volumes based on measured source-to-background ratios: influence of reconstruction algorithms. *Radiotherapy and Oncology* 2003;69:247-250
50. Daisne JF, Duprez T, Weynand B, et al. Tumor volume in pharyngolaryngeal squamous cell carcinoma: comparison at CT, MR imaging, and FDG PET and validation with surgical specimen. *Radiology* 2004;233:93-100

51. Black QC, Grills IS, Kestin LL, et al. Defining a radiotherapy target with positron emission tomography. *Int J Radiat Oncol Biol Phys* 2004;60:1272-1282
52. Geets X, Daisne JF, Tomsej M, et al. Impact of the type of imaging modality on target volumes delineation and dose distribution in pharyngo-laryngeal squamous cell carcinoma: comparison between pre- and per-treatment studies. *Radiother Oncol* 2006;78:291-297
53. Geets X, Lee JA, Bol A, Lonneux M, Gregoire V. A gradient-based method for segmenting FDG-PET images: methodology and validation. *Eur J Nucl Med Mol Imaging* 2007;34:1427-1438
54. Ashamalla H, Rafla S, Parikh K, et al. The contribution of integrated PET/CT to the evolving definition of treatment volumes in radiation treatment planning in lung cancer. *Int J Radiat Oncol Biol Phys* 2005;63:1016-1023
55. Ashamalla H, Guirgius A, Bieniek E, et al. The Impact of Positron Emission Tomography/Computed Tomography in Edge Delineation of Gross Tumor Volume for Head and Neck Cancers. *International Journal of Radiation Oncology*Biological*Physics* 2007;68:388-395
56. Nestle U, Kremp S, Schaefer-Schuler A, et al. Comparison of different methods for delineation of 18F-FDG PET-positive tissue for target volume definition in radiotherapy of patients with non-Small cell lung cancer. *J Nucl Med* 2005;46:1342-1348
57. Gonzalez-Stawinski GV, Lemaire A, Merchant F, et al. A comparative analysis of positron emission tomography and mediastinoscopy in staging non-small cell lung cancer. *J Thorac Cardiovasc Surg* 2003;126:1900-1905

58. Greco C, Nehmeh SA, Schoder H, et al. Evaluation of different methods of 18F-FDG-PET target volume delineation in the radiotherapy of head and neck cancer. *Am J Clin Oncol* 2008;31:439-445
59. Schinagl DA, Vogel WV, Hoffmann AL, et al. Comparison of five segmentation tools for 18F-fluoro-deoxy-glucose-positron emission tomography-based target volume definition in head and neck cancer. *Int J Radiat Oncol Biol Phys* 2007;69:1282-1289

Chapter 3

Hypoxia and Hypoxic Functional Imaging using ^{64}Cu -ATSM in Squamous Cell Carcinoma of the Head and Neck

3.1 Radiation Induced Cell Death

3.1.1 Oxygen and Radiation-Induced Cell Death

Orbiting electrons within atoms are ionised by free electrons from radiation, producing a cascade of ionisations.

Ionised electrons interact with water to produce hydrated electrons, and ionised water molecules (radio-lysis). The positively charged, unstable, and highly reactive ionised water breaks down into a hydroxide free radical and hydrogen ion.

Single and double-stranded DNA breaks, base changes, protein cross-links with DNA and intra-cellular macromolecules are produced by radiation-induced free radical damage. Double-strand DNA breaks are lethal to the cell. Repair of the damage may produce chromosomal aberrations and altered gene expression resulting in apoptosis, or mutations that promote cell survival.

Oxygen (O_2) is critical to radiation-induced cell death, to fix free radical DNA damage, which generates further free radical products. O_2 modifies the radiation dose to achieve cell kill, quantified by the Oxygen Enhancement Ratio (OER). The OER exponentially increases from 1.0 when the oxygen tension is between 0 to 20 millimetres of mercury (mmHg), indicating hypoxic radio-resistance. Under hypoxic conditions three times the radiation dose is needed to achieve the same level of cell kill as in normoxia ($\text{OER} = 1.0$) [1].

3.2 Hypoxia

3.2.2 Types of Hypoxia

Hypoxia is dynamic within the tumour, and develops when oxygen demand exceeds supply. The partial pressure of O₂ (pO₂) of 0.5 to 20mmHg predicts the response to fractionated RT [2].

Acute hypoxia is perfusion related. For example: vessel occlusion or collapse due to trapping of red blood cells, high intra-tumoural tissue pressure, and disorganised neo-vasculature secondary to angiogenesis. Anaemia, and hypoxaemia contributes to this.

Chronic hypoxia occurs when cells are more than 70micrometers (µm), and typically 100 to 200µm from the afferent capillary, and in the presence of counter-current blood flow. As cancer cells proliferate, mature cells are displaced further away from the vessel, creating an oxygen diffusion gradient. Chronic hypoxia develops as the diffusion distance of oxygen increases, causing radio-resistance.

3.3 Intra-cellular Effects of Hypoxia

Acidosis develops due to the loss of ion gradients, membrane depolarisation, and influx of extra-cellular chloride and calcium. At pO₂ levels less than 10mmHg intra-cellular ATP levels reduce. Mitochondrial function fails as oxygen tensions fall below 1mmHg, uncoupling oxidative phosphorylation [3].

Post-transcriptional changes of hypoxia-regulated genes alter downstream signalling of hypoxia-inducible factors. This promotes cellular differentiation, cell cycle arrest, apoptosis and reduced growth or dormancy until improved intra-cellular conditions (re-oxygenation) develop, and accelerated growth begins. For example, the G1 to S phase transition requires retinoblastoma protein phosphorylation by specific cyclin-dependent kinase. In hypoxia, cyclin-

dependent kinase inhibitor (p27) is induced, preventing cell cycle progression into S phase by retinoblastoma protein hypophosphorylation [4].

Point mutations, gene amplifications, and chromosomal re-arrangements immortalise the cell, reducing apoptosis, and promoting angiogenesis. This increases the stem cell population, further increasing intra-cellular hypoxia. Post-transcriptional and translational modifications occur when the pO_2 is 1 to 2mmHg, and gene mutations less than 1mmHg [3].

3.3.1 Hypoxia and Chemo-Sensitivity

Disordered angiogenesis, and increasing cell distance from the vasculature reduce the access of chemotherapeutic drugs. Hypoxia induced cell cycle arrest reduces chemo-sensitivity, accumulating cells in the G2 phase, with a reduced S-phase fraction [4].

3.4 Detection and Quantification of Hypoxia

3.4.1 Polarographic Oxygen Electrodes

Polarographic electrodes are the gold standard method for hypoxia detection. A negative current applied between the anode and the cathode reduces tissue O_2 at the cathode tip. The measured pO_2 is proportional to the current. Real time in-vivo acute and chronic hypoxia can be measured.

Electrodes are invasive, and require an accessible superficial ROI. The electrode path distorts tissue architecture, reducing histological information. Abnormal readings can occur in regions of fibrosis and necrosis.

Normal tissue has a pO_2 of 40 to 60mmHg. Less than 10% of solid tumours are in this range, 60% have a pO_2 of less than 2.5mmHg, with the median less than 10mmHg [3].

The electrodes have been used to correlate prognosis and hypoxia in SCCHN. Hypoxia less than 2.5mmHg is the most significant factor to affect patient

survival. The 3-year overall survival was 28% when the tumour hypoxic fraction was less than 5mmHg, and 36% if greater than 5mmHg. The 5-year overall survival was 0 to 20% with a greater fraction less than 5mmHg [5].

Hypoxia within LN metastases from SCCHN significantly reduces local control. A LN pO_2 less than 2.5mmHg is an independent prognostic factor of local control and response to RT [6].

3.4.2 Optical Sensors

Sensors are based on pO_2 dependent changes in the excitation half-life of the luminophore within the tip of a fibre-optic probe. Compared to the polarographic electrode, pO_2 less than 2.5mmHg is difficult to detect, and the probe is static. Photo-luminescence has been correlated with pimonidazole (immuno-histochemistry) IHC in a xenograft SCC laryngeal model [7].

3.4.3 Immuno-Histochemistry

IHC detects exogenous or endogenous antigens of interest retrieved from fixed wax embedded tissue by a multi-step process.

Tissue is preserved prior to staining in neutral buffered formalin or other formaldehyde based fixative. Formalin produces hydroxymethylene cross-linked bridges with intra-cellular amino acids, proteins, or between proteins and nucleic acids. Fixation takes at least 24 to 48 hours. Distortion of tissue morphology, artefact formation, and masking of the antigen of interest are minimal. Deformation depends on how the tissue is placed in formalin. Large specimens require fixation in excess of 48 hours, altering the protein structure, and tissue architecture.

The formalin fixed tissue specimens are preserved by dehydration through graded alcohols, and then infiltrated with paraffin wax. The wax blocks can then be microtome sectioned, histo-pathologically reviewed after H+E staining or further investigated by IHC methods.

The embedded tissue is dewaxed and rehydrated to restore antigen immuno-reactivity. Antigen specific high-affinity antibody use ensures minimal non-specific background binding. The antibody is incubated at room temperature (time dependent on the antibody, antigen under investigation, and is usually between 10 to 60 minutes) with the rehydrated tissue.

The antibody may be detected by: direct, two step indirect, three step indirect, or soluble enzyme immune complex methods. Horseradish peroxidase (HRP) is a colourless substrate with an iron containing heme group at its active site. Exposure to hydrogen peroxide oxidises it to a brown pigment leading to visualisation of the antibody-bound antigen.

3.4.3.1 Pimonidazole

Pimonidazole is a 2-nitroimidazole. It can be administered intra-venously a minimum of 16 hours prior to tissue extraction (to allow for adduct fixation) and detected by IHC. It is irreversibly reduced by a 2 step electron reduction when the pO_2 is less than or equal to 10mmHg, and covalently bound to tissue. Initial studies in dogs reported a mean labelled fraction of 72% 24 hours after injection. The $t_{1/2}$ in solid tumours was greater than 3 days [8].

Pimonidazole is reduced through a nitro-radical anion intermediate to pimonidazole adducts that bind to intra-cellular sulphhydryl containing molecules such as glutathione. NADH and NADPH donate electrons in the first step of reductive activation to form the nitro-radical anion. The rate of pimonidazole oxidative metabolism is controlled by the redox state of NADPH. Anoxia associated with mitochondrial inhibition, and the uncoupling of oxidative phosphorylation will block NADPH and inhibit pimonidazole adduct formation [9].

Figure 3.1 illustrates the reduction of pimonidazole in the intra-cellular environment.

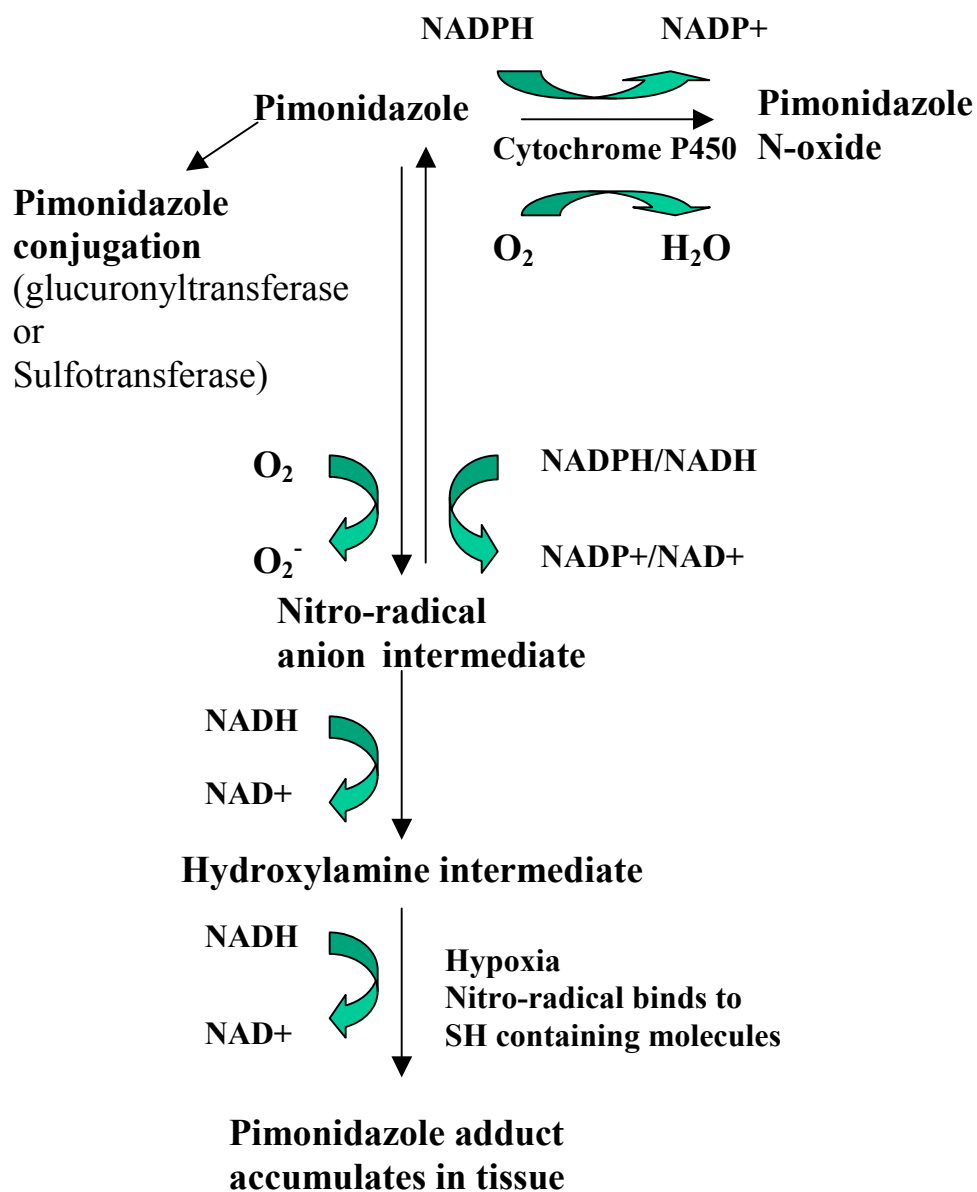


Figure 3.1: The reduction of pimonidazole in the intra-cellular environment

Normal tissue including: liver, oesophagus, kidney, skin, salivary glands (intra-lobular ducts), bone marrow and thymus positively stain for pimonidazole [10].

The kidneys excrete 69% of pimonidazole within 72 hours of injection. The central nervous system toxicity is dose-limiting. The commonest side effects are lethargy, flushing, and disorientation. These were reported when pimonidazole was used as a radio-sensitiser, and 500mg/m² was the highest tolerated dose without toxicity [11].

Pre-clinical and clinical studies have validated pimonidazole as a gold standard IHC surrogate marker of hypoxia.

Pimonidazole adduct detection in murine xenograft models, correlated with pO₂ polarographic oxygen electrode measurements [12], and areas of poorly perfused but viable tumour, which predicted radio-sensitivity [13]. There was no pimonidazole staining in areas of necrosis.

Clinical studies in patients with SCCHN have used 0.5g/m² of pimonidazole. Cytoplasmic adduct formation increased with increasing distance from blood vessels and increasing hypoxia [14]. Keratinisation in SCCs can over-estimate binding by up to 30% when co-localised [15]. Studies in SCC cervix [16,17], and SCCHN [18,19] have found pimonidazole positive hypoxic fractions of 0 to 79%. The 2-year local control was 48% for hypoxic tumours defined by pimonidazole adducts, and 87% for oxidic ones. This hypoxic fraction positively correlated with polarographic electrode measurements. The pimonidazole hypoxic fraction was 0.3 to 17.2% [20]. Loco-regional recurrence was associated with an average pO₂ of 4.1mmHg. Hypoxia reduced the disease-free survival by 50% [21].

3.4.3.2 GLUT1

GLUT1 expression is mediated by hypoxia inducible factor 1 alpha (HIF1a), and reduced oxidative phosphorylation. GLUT1 and GLUT3 are up-regulated in cancers, especially SCCHN.

GLUT1 is detected within the cell membrane and cytoplasm, with increased intensity surrounding necrotic regions. Staining is absent in connective tissue and necrosis. GLUT1 expression is an independent predictor of metastasis-free survival. There is a weak correlation between GLUT1 staining and pO₂ measurements by polarographic electrodes especially at O₂ concentrations less than 2.5mmHg [22]. GLUT1 positively correlated with pimonidazole and carbonic anhydrase IX (CAIX) [23].

In SCCHN, the pattern of GLUT1 staining was dependent on the degree of differentiation. In poorly-differentiated tumour regions, central, peri-necrotic staining was present, in a hypoxia-inducible pattern. Positive staining was within the periphery of the tumour in well-differentiated areas. The pattern of GLUT1 staining was distinguishable from normal epithelium [24]. GLUT1 staining is diffuse over the entire tumour in almost all tumours, and this is correlated with an increased risk of distant metastases, and a poor 5-year overall survival [25,26].

3.4.3.3 Carbonic Anhydrase IX

Carbonic anhydrase maintains intra-cellular pH by catalysing the conversion of carbon dioxide to carbonic acid, and is up-regulated in hypoxic conditions.

CAIX is a alpha isoenzyme of this 3 gene family, a transmembrane glycoprotein, normally expressed in gastro-intestinal mucosa, and the hepato-biliary system. Over expression occurs in SCCHN, SCC cervix, colo-rectal cancer, bladder cancer and NSCLC, in peri-necrotic regions, within the cell membrane [27].

In biopsies from patients with SCCHN, the CAIX positive hypoxic fraction was between 0 to 39%, and was at smaller distances from the blood vessel at 80µm compared to pimonidazole (greater than 120µm) [28]. High expression was associated with a significantly reduced complete response rate of 40% compared to 70.9% in patients who underwent CRT. Expression was not related to the primary site or stage. Positive staining occurred in areas of low micro-vessel density, and was absent within normal HN mucosa [29].

3.4.3.4 Hypoxia Inducible Factor 1a

HIF is an endogenous transcription factor. It translocates to the nucleus in hypoxic conditions, and binds to the hypoxia response element. For example: GLUT1, CAIX, erythropoietin, and vascular endothelial growth factor to form a heterodimer. The beta subunit is constitutively expressed.

In hypoxic conditions there is no post-translational ubiquitination of the alpha subunit, regulated by prolyl hydroxylase. This activates the hypoxia response elements on genes. In normoxia, HIF1a is bound to Von Hippel Lindau (VHL) protein, and endonuclease 1 maintains the subunit in a reduced state. Up-regulation of HIF1a mediates adaptive downstream signalling on target genes modulating angiogenesis, glycolysis, invasion and metastasis formation. HIF1a and CAIX expression are positively correlated because the CAIX promoter region is adjacent to the hypoxia response element [30].

In patients with SCCHN treated with RT, HIF1a was over expressed in 94%. Expression was focal in 65%, diffuse in 35%, weak in 57%, and negative in 6%. HIF1a expression inversely correlated with a complete response to treatment, and the local failure-free survival [31]. Both HIF1a and CAIX are independent prognostic factors for loco-regional control and survival, with an additive effect when co-localised [32].

3.4.4 Single Gel Electrophoresis

The COMET assay detects hypoxia within single cells. The single strand DNA breaks produced by radiation are detected within the tail of the comet. The length of the tail correlates with the single strand DNA breakage and so hypoxia. The assay has been correlated with pimonidazole staining [33].

3.4.5 Osteopontin

Osteopontin is secreted by a calcium binding glycoprophosphoprotein, and inversely associated with VHL activity. Levels greater than 450ng/ml in patients with SCCHN were associated with a 50% reduction in loco-regional control, and a 75% reduction in the 2.5-year overall survival [34].

3.4.6 Gene Analysis

DNA micro-arrays utilise DNA oligo-nucleotides, containing specific sequences detected by hybridised clonal DNA. The micro-array signal is quantified by fluorophore luminescence. In patients with SCCHN, hypoxia meta-gene sequences clustered around hypoxia regulating gene elements had increased

expression of CAIX and HIF1a genes. The median gene expression was an independent predictor of recurrence-free survival [35].

3.4.7 Hypoxia Functional Imaging

This is discussed in detail in section 3.8.

3.5 Hypoxia and Outcome in Squamous Cell Carcinoma of the Head and Neck

Hypoxia is present in 50% of solid tumours negatively impacting clinical outcome irrespective of tumour size or histology. The pre-treatment pO₂ is lower in the tumour than normal tissue regardless of stage and patient demographics, with significant variability between, compared to within tumours. Regions of local recurrences have a greater hypoxic fraction. Hypoxia is an independent prognostic factor for local control and overall survival in patients with SCCHN [3].

3.6 Methods to Overcome the Effects of Hypoxia

3.6.1 Hyper-Baric Oxygen

The O₂ at 100% concentration, pressurised to 101.3kPa is delivered via a compression chamber. Patients are pre-treated for 30 minutes prior to RT.

The Cochrane Collaboration reported an absolute reduction in the 5-year mortality from SCCHN by 9.2%, and improved local control. However the treatment sensitises both tumour and normal tissue and increased the risk of severe radiation necrosis 2.3 fold. This and the increased rate of fits during compression and patient compliance reduced the use of hyperbaric O₂ [36].

3.6.2 Radiotherapy with Hypoxic Modifiers

3.6.2.3 Radio-Sensitisers

Nitro-imidazoles have been extensively investigated as hypoxic radio-sensitisers. Like pimonidazole they undergo single or multi-step electron reductive bio-activation in hypoxic conditions. Radio-sensitisation is by electron migration along the DNA producing breaks, or by direct interaction between the 2-nitroimidazole and free radicals in DNA. Significant gastro-intestinal, irreversible peripheral neuropathy, and encephalopathy toxicity occurred initially with metronidazole and misonidazole. The benefit from these was minimal during RT in SCCHN [37].

Loco-regional control and overall survival significantly improved in SCCHN when new generation nitro-imidazoles were added to the RT schedule [38].

Nimorazole has the advantage of reversible peripheral neuropathy. The 1.2g/m² of nimorazole daily in combination with 62 to 68Gy of radical RT had a significant improvement in the 5-year local control rate, which was dependent on T and N stage, and the pre-treatment haemoglobin level [39] in patients with SCCHN. Late neuro-toxicity was not increased by the addition nimorazole.

3.6.2.1 Carbogen

Carbogen is a combination of 95% O₂ and 5% carbon dioxide, and correlated with higher pO₂ measurements by polarographic electrodes [40]. The impact of chronic hypoxia was reduced by a five fold increase in the pO₂ causing a shift to the right in the oxygen dissociation curve [41].

Nicotinamide (amide derivative of Vitamin B3) reduces the transient vessel occlusion, and improves perfusional related hypoxia [42].

These have been combined with accelerated RT to counteract the effects of acute and chronic hypoxia, and repopulation by tumour stem cells. Accelerated RT to 68Gy in 34 fractions was given to patients with SCCHN in conjunction with carbogen breathing prior to RT, and oral nicotinamide once a day, 90 minutes

prior to RT. Nausea and vomiting were the major toxicities in 68%, and nicotinamide was reduced from 80 to 60mg/Kg in all patients. The 3-year local control rate was 69% [43].

Continuous hyper-fractionated accelerated RT has been combined with carbogen and nicotinamide. Disease-free survival in patients with SCCHN improved, but gastro-intestinal toxicity was the limiting factor [44].

3.6.2.2 Tirapazamine

Tirapazamine is a benzotriazine that undergoes 1 step electron bio-activated reduction in hypoxia. Cell kill is additive when combined with RT, and synergistic with cisplatin [45].

Patients with SCCHN were treated with cisplatin based CRT and tirapazamine (290mg/m² 1 hour prior to cisplatin weeks 1, 4 and 7, and then weeks 2, 3, 5 and 6 as a single agent at 160mg/m² during RT). Acute radiation toxicity was not enhanced. The dose-limiting toxicity was grade 3 and 4 febrile neutropaenia. The median 3-year overall survival was 69% [46]. Hypoxia was improved when PET imaged with ¹⁸Fluoro-misonidazole (¹⁸FMISO) pre-treatment, and 5 weeks after CRT with tirapazamine [47].

3.6.5 Bio-Reductive Drugs

Quinone derivatives such as mitomycin C are selectively bio-activated in hypoxic conditions. Such combinations with RT have been largely replaced by cisplatin. The use of mitomycin C continues in CRT for the treatment of SCC of the oesophagus and anus.

3.6.1 Altered Fractionation Radiotherapy

Altered fractionation RT may either be accelerated, hyper-fractionated, or both. Altered fractionation in SCCHN had a 3.4% survival benefit at 5 years, which reduced to 2% if the total RT dose was not reduced, and 1.7% if the dose was reduced. Local control improved by 6.4%, especially within the primary site, but reduced over the age of 50. The survival benefit was 8% at 5 years for hyper-fractionated regimes [48].

3.6.3 Haemoglobin Modification

The haemoglobin concentration is an independent prognostic factor for treatment outcome, along with T and N stage, performance status, age, and total radiation dose to the primary site. The estimated 5-year survival in patients with a haemoglobin less than 14.5g/dl in men, and 13g/dl in women with SCCHN undergoing curative RT was 21.7% compared to 35.7%. However, loco-regional failure increased by 16.2%, and the late grade 3 radiation-induced toxicity by 19.8% compared to 7.1% at 5 years in anaemic patients [49].

Blood transfusion and recombinant human erythropoietin use to improve anaemia in patients undergoing radical RT or CRT has been controversial. Recombinant erythropoietin has been associated with poorer loco-regional control and overall survival in anaemic patients with SCCHN [50]. Blood transfusions may reduce outcome in patients undergoing radical RT due to the presence of interleukins that act as pro-angiogenic tumour growth factors [51].

3.6.7 Vascular Disrupting Agents

Vascular disrupting agents such as combretastatin disorganise microtubule function and impair endothelial cell adhesion. Haemorrhagic tumour necrosis occurs, and response rates to combined treatment with chemotherapy such as paclitaxel and RT [52] are increased. Cardiac ischaemia and hypertension are significant toxicities. Their use may be limited in patients with SCCHN who have co-existent smoking related vascular disease.

3.6.8 Hyperthermia

Hyperthermia may be local to the tumour, or generalised to the whole body. Increasing the temperature when radiation is given simultaneously produces a thermal enhancement ratio, increasing tumour cell kill for the same radiation dose. Hypoxic cells are more sensitive to heat damage because of low intracellular pH, and reduced blood flow to the tumour. Five studies have been published in patients with HN cancer, and on meta-analysis the combined treatment compared to RT alone improved loco-regional control by 18% [53].

3.6.9 Dose Escalation

Detection of hypoxia by CT-PET has increased interest in dose-escalation to overcome hypoxic radio-resistance. Such strategies are possible using IMRT for example to spare normal tissue and target dose on the CT-PET defined area. This is further discussed in section 3.8.2.

3.7 Perfusion Imaging

Perfusion and hypoxia imaging are intricately linked because well-perfused areas may be hypoxic or oxic, and the delivery of the radio-nuclide to the ROI is perfusion dependent.

3.7.1 MRI

Hypoxia detection by MRI exploits the magnetic properties of haemoglobin, the use of intra-venous contrast, and nuclear proton concentrations [54].

For example, Blood Oxygen Level Dependent MRI utilises paramagnetic deoxyhaemoglobin in red blood cells to detect acute hypoxia, because the haemoglobin concentration within the vessel, and the delivery of red blood cells to the ROI are assumed to be proportional to the pO_2 . Whereas, intra-tumoural blood volume (BV), capillary permeability (CP), and tumour oxygenation are assessed by dynamic contrast enhanced MRI (DCE-MRI) by the intra-vascular retention pattern of micro and macro molecular intra-venous contrast agents.

3.7.2 Dynamic Contrast Enhanced CT

DCE-CT is used to quantify BV, blood flow (BF), CP, and mean transit time (MTT) of the blood within a defined ROI, and has mainly been studied in patients with intra-cerebral vascular events or space occupying lesions.

Perfusion is the BF through a tissue of interest per unit volume. The ROI is selected prior to contrast injection and imaging. An intra-venous iodinated contrast agent is dynamically tracked during its first circulation through the capillary bed (dynamic first-pass approach). BF is calculated in HU 20 to 40

seconds after injection when a plateau is reached. The method assumes the contrast agent is completely retained in the intra-vascular compartment, and not metabolised or absorbed.

The BV can be calculated from the equation below.

$$\text{BV (ml/100g)} = \frac{\text{Concentration of contrast in the tissue of interest}}{\text{Concentration of contrast in the artery}}$$

Attenuation on CT images is directly related to the amount of contrast injected. The BV can then be calculated directly from the equation below.

$$\text{BV (ml/100g)} = \frac{\text{Hounsfield Units in tissue}}{\text{Hounsfield Units in the artery}}$$

Imaging of BF is better with DCE-CT compared to DCE-MRI because of the linear relationship between the BF and contrast within the ROI.

Complex mathematical models have been developed (deconvolution and non-deconvolution) to calculate BV, BF and MTT from DCE-CT data. Over-estimation can occur without this because contrast leaks from the intra-vascular into the extra-cellular space due to the vascular endothelium in tumours and inflammation [55].

3.7.2.1 Deconvolution Methods

Parametric or non-parametric deconvolution is used to calculate BF. The concentration of contrast after injection in each CT voxel is dependent on the impulse residual function and the arterial input function.

The impulse residual function is the concentration of the contrast agent within the voxel of interest, at time (t) following the ideal immediate administration of the agent. The arterial input function is measured from one of the major arterial vessels, for example within the HN: common, internal or external carotid

arteries. The concentration of the contrast within that vessel which supplies the voxel of interest at time (t) can then be estimated [56].

Deconvolution removes the effect of the arterial input function on the tissue concentration curve. The impulse residual function is then only dependent on the haemo-dynamics within the voxel of interest.

The MTT is the plateau of the impulse residual function after the increase in the concentration of the contrast within the voxel, and before the concentration reduces within the vessels. This is a measure of the time the contrast remains in the intra-vascular space within the ROI [55].

The calculation of BF from the parameters of BV and MTT has been described as the Central Volume Principle in the equation below [57].

$$\text{BF (ml/100g/min)} = \frac{\text{BV (ml/100g)}}{\text{MTT (sec)}}$$

The permeability surface area (PS) is a measure of the fractional vascular volume and outflux constant divided by the tissue density within the ROI. This may be calculated by two methods.

$$\text{PS (ml/100g/min)} = \frac{\text{Outflux constant} \times \text{fractional vascular volume}}{\text{Tissue density}}$$

or

$$\text{Fraction of extracted tracer} = 1 - \exp (-\text{PS} / \text{Fractional vascular volume})$$

3.7.2.2 Non-Deconvolution Methods

The calculation of BF by this method requires high contrast velocity (10ml/s) within the regional vascular bed. BF is often only 7ml/sec, and so rarely used in clinical imaging [56].

3.7.2.3 Treatment Response

The ROI must be defined prior to contrast injection and imaging. This is usually 2 to 4cm, and is assumed to be representative of the entire tumour. In large necrotic SCCs under or over-estimation may occur.

DCE-CT imaging was performed in patients with SCCHN before and 30 days after completion of 1 cycle of neoadjuvant cisplatin and 5-fluorouracil chemotherapy. The mean BV, BF and CP reduced by 20%, and the MTT increased in patients with a clinical response to neoadjuvant chemotherapy [58]. Higher pre-treatment parameters were correlated with a greater response to treatment. The degree of contrast enhancement within the tumour was proportional to the level of neo-vascularisation. Local control reduced by 50% 2 years after radical RT when the BF was less than the median [59].

3.8 Hypoxia Imaging with CT-PET

A number of radio-nuclides have been reported as hypoxia imaging agents in CT-PET. The most widely studied is ^{18}F MISO, but copper bithiosemicarbazone complexes (Cu-ATSM) are increasing in popularity. Others include: ^{18}F Fluoro-azomycin arabinoside (^{18}F FAZA), ^{18}F Fluoro-erythronitroimidazole (^{18}F FETNIM), ^{18}F Fluoro-etanidazole (^{18}F FETA), a tri-fluorinated etanidazole derivative (^{18}F -EF3), and a penta-fluorinated derivative (^{18}F -EF5).

3.8.1 ^{18}F Fluoro-2-deoxyglucose

^{18}F FDG as a hypoxic radio-nuclide is much debated with no clear consensus.

In human SCCHN cell lines, tritiated fluoro-2-deoxyglucose uptake was increased by 46% to 120% after hypoxic incubation for 6 hours [60] from a basal uptake of 20%, which correlated with increased immuno-cytochemical GLUT1 expression. In hepatoma xenograft models, the auto-radiographic distribution of ^{18}F FDG positively correlated with the IHC distribution of GLUT1, 3 and hexokinase 2 expression [61].

Correlation of ^{18}F FDG uptake on microPET and auto-radiography with pimonidazole IHC staining has been inconclusive with reduced differentiation of uptake between hypoxic and oxic regions. The ^{18}F FDG uptake in a hypoxic SCCVII model was not correlated with the tumour pO_2 measured by polarographic electrodes [62]. The distribution of ^{18}F FDG was central and homogeneous, compared to the peripheral and heterogeneous uptake of ^{18}F MISO [63] in dual tracer studies.

The majority of studies in patients with SCCHN have also reported no correlation of ^{18}F FDG uptake with pO_2 polarographic electrode measurements [64], or ^{18}F MISO uptake [65,66]. Correlation between ^{18}F MISO and ^{18}F FDG in patients with SCCHN may indicate an aggressive malignant phenotype with greater radio-resistance due to chronic hypoxia and high glucose metabolism.

3.8.2 ^{18}F Fluoro-Misonidazole

^{18}F MISO has been used to image chronic hypoxia, but it has limited widespread use because uptake changes with time and oxygen tension, and spatial resolution is poor compared to imaging with ^{18}F FDG [54].

Similar to other 2-nitro-imidazoles, ^{18}F MISO in the presence of hypoxia undergoes a multi-step electron reduction by nitro-reductases in viable mitochondria to an amine radical. This is retained within the cell. In the presence of oxygen, this radical is oxidised back to ^{18}F MISO, and diffuses out of the cell. ^{18}F MISO is lipophilic, and excreted via the kidneys and hepato-biliary system.

Uptake correlates with hypoxia in SCCHN detected by polarographic electrodes [54]. In SCCHN, the ^{18}F MISO defined (tumour to blood ratio of greater than 1.2) hypoxic FV was an independent predictor of overall survival. Four hours after injection, the tumour to muscle ratio and accumulation of ^{18}F MISO positively correlated with local recurrence [65].

Hypoxic volumes were assessed with ^{18}F MISO and ^{18}F FDG PET imaging pre-treatment, and at week 4 and 8 of cisplatin based CRT with tirapazamine in SCCHN. No residual ^{18}F MISO uptake was seen at the site of ^{18}F FDG activity after

treatment, but increased uptake was noted in patients with advanced disease at presentation [67]. Studies reported 71% of primary and nodal sites had hypoxia defined by $^{18}\text{FMISO}$. Loco-regional failure increased in patients with hypoxic volumes, and in those who did not receive tirapazamine [68]. The reduced $^{18}\text{FMISO}$ uptake may have been due to radio-sensitisation by tirapazamine, and re-oxygenation during treatment reducing the hypoxic volume.

Serial $^{18}\text{FMISO}$ CT-PET hypoxic FVs imaged on day 1 and 4 of curative RT correlated in 71% of patients with SCCHN when voxels were compared. However if a tumour to blood ratio of greater than or equal to 1.2 was used to delineate the volume this reduced to 46% [69] indicating the dynamic nature of hypoxia.

Re-oxygenation during RT has been imaged in patients who underwent $^{18}\text{FMISO}$ and ^{18}FDG PET prior to IMRT with concurrent chemotherapy, and after 20Gy. The time-activity retention exhibited three distinct patterns within the hypoxic volume: high perfusion and good oxygenation, perfusion with hypoxia, and severe hypoxia with reduced perfusion. It was suggested that $^{18}\text{FMISO}$ imaged re-oxygenation in those with less aggressive tumours [70].

The retention pattern of $^{18}\text{FMISO}$ predicted outcome to RT in patients with SCCHN. Classic hypoxia was associated with a poor outcome, with high radio-nuclide retention and lower than average perfusion within the hypoxic volume, suggesting inadequate vasculature [71]. Conversely, no radio-nuclide retention and normal or greater than average perfusion suggested an efficient vasculature and no hypoxia, and so a good prognosis. The retention patterns during curative RT, suggested the pattern of $^{18}\text{FMISO}$ at 30Gy was predictive of recurrence [72].

Dose escalation to hypoxic volumes requires serial imaging with $^{18}\text{FMISO}$, as single pre-treatment imaging cannot adequately predict the time to re-oxygenation following the start of RT in SCCHN. Also $^{18}\text{FMISO}$ uptake within the voxel does not accurately predict the true tumour hypoxia. The $^{18}\text{FMISO}$ hypoxic FV (40% of the SUVmax) defined in patients with SCCHN has been dose escalated using IMRT to 110% of the GTV dose (70Gy in 35 fractions) by a

uniform escalation across the volume or voxel based dose painting to a maximum to 2.4Gy per fraction. The escalated dose was calculated using a tumour control probability algorithm [71]. Other methods have used a tumour to blood ratio of 1.2 to 1.4, and delivered a uniform dose escalation of 20% to a total dose 84Gy, but also delivered a 50% dose escalation to 105Gy in 1 patient [73].

Dose escalation of 20 to 50% of 70Gy in 35 fractions significantly improved the tumour control probability within hypoxic FVs [74]. No increased normal tissue toxicity was noted in these studies. Voxel-based dose painting requires kinetic information from dynamic CT-PET imaging to calculate the dose to an individual voxel depending on the retention of the radio-nuclide within it.

However, as hypoxia is dynamic, with changing oxygen tensions within the tumour micro-environment, sequential ^{18}F MISO imaging can lead not only to poor correlation of temporally distinct scans (due to mis-registration, patient position and differences in noise) but also to reduced dose optimisation with the dose escalation process, as the hypoxic volume changes [75].

3.8.3 ^{18}F Fluoro-azomycin arabinoside

^{18}F FAZA is a lipophilic nitro-imidazole with hypoxia selectivity. Uptake is positively correlated with the immuno-fluorescence of pimonidazole adducts [76]. ^{18}F FAZA hypoxic volumes have also been dose escalated to 80.5Gy in 35 fractions with IMRT in SCCHN patients [77].

3.8.4 ^{18}F Fluoro-erythronitroimidazole

^{18}F Fluoro-erythronitroimidazole (FETNIM) is a 2-nitroimidazole hypoxic radio-nuclide. Uptake is spatially distinct compared to ^{18}F FDG, and hypoxia selective. This radio-nuclide is more hydrophilic than ^{18}F MISO, with hypoxic tumour to blood ratios at 2 hours of 1.8 ± 0.64 . The delineated ^{18}F FETNIM hypoxic FV in patients with SCCHN negatively correlated with intra-tumoural pO_2 measurements [78].

3.8.5 ^{18}F -Fluoro-etanidazole

^{18}F -Fluoro-etanidazole is 2-nitroimidazole radio-nuclide. Hypoxia selectivity peaks 2 to 4 hours after injection [79]. Retention at 60 minutes was greater in tumours with a higher fraction of pO_2 values less than 1mmHg. Retention 60 minutes after injection positively correlated with a pO_2 less than 5mmHg [80]. Human studies are awaited.

3.8.6 ^{18}F -EF3

^{18}F -EF3 is tri-fluorinated etanidazole. A small study in 10 patients with SCCHN reported a homogeneous distribution on whole body static 2D imaging, 30 minutes after injection. The tumour to muscle ratio varied between of 1.42 to 1.87 from 40 to 409 minutes [81].

3.8.7 ^{18}F -EF5

^{18}F -EF5 is penta-fluorinated etanidazole. In dynamically acquired CT-PET imaging over 60 minutes, and late static imaging at 2, 3 and 4 hours in patients with SCCHN the median tumour to muscle ratio was 1.38 3 hours after injection, and did not correlate with ^{18}F FDG uptake [82].

3.9 Copper bis(thiosemicarbazone)

Copper (Cu) is a transitional metal. Bisthiosemicarbazones were first noted to have tumouricidal properties in Ehrlich ascites tumour cells. This cyto-toxicity was linked to the redox potential of Cu, and correlated with the inhibition of mitochondrial oxidative phosphorylation [83,84]. The potential for copper radio-isotopes to be used as PET imaging agents has been further studied.

3.9.1 Isotopes

The availability of copper radio-nuclides has increased for CT-PET imaging ($^{60,61,62,\text{and } 64}\text{Cu}$), and targeted radio-nuclide therapy ($^{64\text{ and } 67}\text{Cu}$) [85,86]. Table 3.1 shows the available copper isotopes, and their radio-active properties.

Table 3.1: The radio-active properties of copper isotopes

Isotope	Half Life	Emitted Radiation	γ Energy of Penetrating Radiation (KeV)	β^+/ β^- Non-Penetrating Radiation (KeV)	Average Range of Non-Penetrating Radiation in Tissue (mm)
^{60}Cu	20 minutes	β^+ (93%), Electron Capture (7%)	511	873	4.4
^{61}Cu	3.3 hours	β^+ (62%), Electron Capture (38%)	511	527	2.6
^{62}Cu	9.74 minutes	β^+ (98%), Electron Capture (2%)	511	1315	6.6
^{64}Cu	12.7 hours	β^+ (19%), Electron Capture (41%), β^- (40%)	511	278	1.4
^{66}Cu	5.1 minutes	β^- (100%)	-	1109	5.6
^{67}Cu	62 hours	β^- (100%)	93	121	0.61

60 , 61 and ^{62}Cu are suitable for PET imaging due to their positron emission rates.

^{64}Cu is used for imaging and therapy [87]. The improved spatial resolution occurs because of the low initial positron emission rate (19%), but higher doses

are therefore also required. The high rate of electron capture increases the radiation dose to the imaged patient, which has the potential to limit its use in clinical imaging. The long half-life allows off site production, without measurable loss of activity at the point of administration.

66 and 67 Cu can be used for targeted therapies when linked to MABs [88].

The appropriateness of these isotopes for imaging depends on the spatial resolution, scatter fraction, and noise equivalent count rate. 60 and 62 Cu have a higher sensitivity, noise equivalent count rate, and lower spatial resolution (6.3mm and 7.2mm respectively) and are used in studies with small molecules that have faster kinetics such as perfusion imaging. Conversely, 61 and 64 Cu have slower kinetics, associated with lower sensitivity but better spatial resolution of 5.1mm and 4.7mm respectively, which compensates for the loss of contrast within the image [89].

3.9.2 Copper Bisthiosemicarbazone

Copper bisthiosemicarbazone complexes were investigated initially as perfusion agents Cu(II)-pyruvaldehyde-bis(N^4 methylthiosemicarbazone (Cu-PTSM) [90]. Cu-PTSM is highly lipophilic with a low molecular weight, and rapidly diffuses into cells. The distribution is proportional to BF [91].

3.9.3 Structure

The lipophilicity and redox potential of 13 64 Cu labelled complexes has been investigated in EMT6 mammalian cancer cells at time points up to 1 hour in oxic and hypoxic conditions, including re-oxygenation. Figure 3.2 shows the structure of Cu-ATSM.

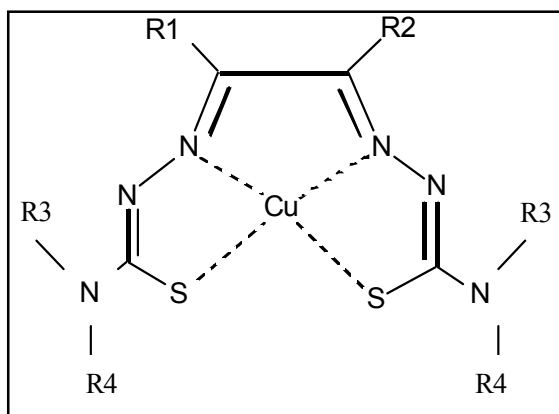


Figure 3.2: The chemical structure of copper bis(thiosemicarbazone)

Functional moieties attached to the R1 to 4 positions alter the structure-activity relationship, and lipophilicity. Alkylation at the terminal R3 and 4 amino position determines lipophilicity, but does not correlate with hypoxia selectivity [92].

The total number of alkyl groups along the diketone backbone at R1 and 2 positions determined the redox potential and hypoxia selectivity. The potential ranged from -0.42 to -0.59V [85,86].

^{64}Cu -ATSM was the most hypoxia selective, while other complexes depending on the di-amine backbone were selective in normoxia for example Cu-PTSM. Hypoxia selectivity of Cu-ATSM occurred with a reduction potential of less than -0.58V when compared to silver/silver chloride [86].

3.9.4 Hypoxia Selectivity and Intra-cellular Retention

Cu-ATSM was first documented in the Langendorff isolated perfused rat ischaemic heart model, after ^{62}Cu -ATSM was found to be selectively reduced by hypoxic rather than normoxic mitochondria [93]. This complex had a redox potential of -0.297V and was lower than Cu-PTSM, and similar to NADH (-0.315V). Cu(II) is reduced by complex I mitochondrial NADH-dependent reduction by NADPH cytochrome p450 reductase [94]. The reduction of ^{62}Cu -ATSM was increased four-fold by electron transport inhibition. Eighty percent of ^{62}Cu -ATSM was retained under hypoxic conditions due to the selectivity of mitochondrial complex I, and the rapidity of cell entry.

The cellular retention of Cu-ATSM has been debated, and three patterns proposed.

Firstly, the reduction of Cu(II) to Cu(I) was thought to promote irreversible cellular retention when the ATSM ligand dissociated from the unstable Cu(I) ion [93,95,96].

Secondly, in EMT6 cells, Cu-ATSM complexes are taken up and reduced regardless of cellular pO₂. Reduced Cu(I) was stable after dissociation from the ATSM ligand and retained within the cell. Oxygen has the potential to re-oxidise the Cu(I) back to Cu(II) which then diffuses out of the cell. Dissociation from the ligand aids cellular retention by preventing re-association with Cu(I). This hypoxia selectivity of Cu-ATSM [97] depends on the alkyl R1 and R2 position.

Thirdly, Cu metabolism is homeostatically maintained by import (Ctr 1) and export (Menkes and Wilsons protein) pumps. ⁶⁴Cu-ATSM uptake rapidly increased in anoxic and hypoxic FaDu cells during the first 30 to 60 minutes of incubation, and was 2 to 9 times greater in hypoxia compared to normoxia [98]. It was proposed that Cu-ATSM translocated across the cell membrane and was reduced to a charged Cu(I)-ATSM complex. This either dissociates to Cu(I) and ATSM, or is re-oxidised back to Cu(II)-ATSM in the presence of oxygen. The Cu(I) then becomes part of the intra-cellular pool of Cu, and is metabolised. The Cu pumps are up or down-regulated depending on the intra-cellular environment and cell line. Up-regulation increased the efflux of Cu(I) [99], reducing the intra-cellular Cu(I) pool. Cu(II)-ATSM could then be translocated into the cell, and the reduction cycle continued. Chaperone proteins prevent the re-oxidation of Cu(I) in the presence of oxygen [100].

Cu(II)-ATSM may be washed out of cells due to its membrane permeability. Cellular retention and washout are dependent on the reduction potential and degree of hypoxia. The ATSM ligand is linked to Cu(I) in high affinity and does not compete with the intra-cellular pool of Cu(I) binding proteins Atx1 and Ctr1c. In the presence of these proteins, the ligand will irreversibly transfer the

Cu(I) to the binding protein. This suggests the preferential reduction of Cu-ATSM in the presence of intra-cellular hypoxia and anoxia [101].

3.9.5 Bio-Distribution

^{64}Cu -ATSM and ^{64}Cu -PTSM in the EMT6 BALB/c mouse tumour model were rapidly cleared from the blood after 1 minute. A greater proportion of ^{64}Cu -ATSM was within the blood 40 minutes after injection compared to ^{64}Cu -PTSM. This then plateaued and remained up to imaging completion at 4 hours.

Intra-cerebral uptake occurred early and retention was greater for ^{64}Cu -PTSM. A similar pattern was seen in the heart and lung. Cu radio-nuclides are excreted by the renal and hepato-biliary systems.

Auto-radiography indicated ^{64}Cu -ATSM uptake was heterogeneous, and ^{64}Cu -PTSM homogenous [102]. At 1 minutes after injection, 20% of the activity was bound to plasma proteins and remained stable over the next 60 minutes [103].

This data has been computationally extrapolated in 5 patients with NSCLC injected with 480MBq of ^{60}Cu -ATSM. Uptake was noted in the liver, kidneys spleen, and intestine. It was suggested that ^{64}Cu -ATSM would remain in the blood pool for 1.25 hours (+/- 0.37hours) and the liver for 8.25 hours (+/- 0.17 hours) after injection [104].

3.9.6 Pre-Clinical Studies

^{18}F MISO uptake was 90% less than that of ^{64}Cu -ATSM in EMT6 cells at 1 hour in any hypoxic condition [102]. At 2 hours, ^{18}F MISO uptake was dependent on the oxygen concentration. Wash out studies suggested the initial oxygen concentration determined the amount of ^{64}Cu -ATSM washed out from the incubated cells.

Xenografted mice with SCCVII tumours injected with ^{64}Cu -ATSM and ^{18}F MISO were PET imaged for 90 minutes while breathing air, and then carbogen. The hypoxic fraction was compared to grayscale pimonidazole staining. The pimonidazole positive fraction was 36.0% in hypoxia, and 7.9% during carbogen

breathing. ^{18}F MISO uptake was modulated depending on the inspired conditions but ^{64}Cu -ATSM was not, suggesting irreversible binding [105]. This confirmed the suggestion that Cu(I) was retained within macromolecules of copper homeostatic mechanisms [98,106]

In a rat anaplastic prostate tumour model, imaging of ^{64}Cu -ATSM at 16 to 20 hours after injection corresponded to the distribution of ^{18}F MISO. The uptake of ^{64}Cu -ATSM positively correlated with pO_2 at 16 to 20 hours but not at 30 to 120 minutes after injection. Pimonidazole staining positively correlated with the late spatial distribution of ^{64}Cu -ATSM, but negatively correlated with the early distribution [107]. In FaDu tumour bearing rats there was no time dependent change in ^{64}Cu -ATSM distribution suggesting the uptake was dependent on differences in chaperone proteins, influx and efflux copper pumps between models.

A single study assessed the binding of ^{64}Cu -ATSM to serum albumin. In humans 95% of available ^{64}Cu -ATSM was bound to this protein. Increased binding improves the contrast between hypoxic and oxic tissue on imaging by reducing the cellular uptake of ^{64}Cu -ATSM in areas of high BF in normal tissue [108].

In a rat 9L gliosarcoma model pO_2 , ^{67}Cu -ATSM uptake on PET, and auto-radiography were compared. The pO_2 was 8mmHg lower in hypoxic conditions, which significantly increased the uptake of ^{67}Cu -ATSM by 37%. In 100% oxygen, uptake was reduced by 48%. The auto-radiographic distribution of ^{18}F FDG was compared to ^{67}Cu -ATSM and was distinctly different [106]. Cu-ATSM heterogeneously accumulated in the outer rim of hypoxic but viable tumour, and not in necrotic regions, and ^{18}F FDG was homogeneously distributed in the inner rim.

^{64}Cu -ATSM auto-radiography and IHC staining of EF5, pimonidazole, CAIX, and Hoescht 33342 (vascular marker) were correlated in various rat xenograft (mammary adenocarcinoma, fibrosarcoma, and 9L glioma) models. ^{64}Cu -ATSM uptake was tumour dependent. Correlation suggested the uptake of ^{64}Cu -ATSM was perfusion related in the fibrosarcoma model, and hypoxia related in the other

models. [109]. Myocardial ischaemia models indicated Cu-ATSM uptake was increased in hypoxic but not necrotic regions. When compared with the perfusion (^{11}C -acetate), the uptake was highest in areas of low perfusion [110,111].

3.9.7 Clinical Studies

3.9.7.1 Squamous Cell Cancer of the Cervix

^{60}Cu -ATSM has been investigated using 1-hour dynamic 3D PET imaging immediately after injection in 38 patients in conjunction with an ^{18}F FDG PET.

The mean tumour to muscle ratio was 3.8 ± 2.0 on the 30 to 60 minutes summed images. The ratio above 3.5 was randomly selected to define hypoxia. Progression-free survival was 71% with a tumour to muscle ratio of less than or equal to 3.5 compared to 28% for a ratio greater than this. The cause-specific survival was 74% and 49% respectively after completion of CRT. ^{18}F FDG uptake was not related to the ratio [112]. The expression of CAIX and EGFR was significantly increased in patients with a tumour to muscle ratio of greater than 3.5 [113].

3.9.7.2 Non-Small Cell Lung Cancer

Similarly, 481MBq of ^{60}Cu -ATSM was intra-venously administered followed by an immediate 1 hour 3D dynamic PET (frame length: 30 x 2 seconds, 12 x 10 seconds, 6 x 20 seconds, 5 x 60 seconds, and 10 x 300 seconds) in 19 patients with NSCLC. Tumour to muscle ratio of greater than 3.0 was used to define hypoxia on the summed 30 to 60 minute images. The mean ratio was 3.4, and was 1.5 times greater in patients who failed to respond to treatment [114].

^{62}Cu -ATSM and ^{62}Cu -PTSM were investigated in two patients with lung nodules of unknown significance. High uptake of both radio-nuclides and ^{18}F FDG occurred in regions of histologically confirmed SCC [115].

3.9.7.3 Squamous Cell Cancer of the Head and Neck

Chao et al in 2001 [116] reported a patient with SCC of the right tonsil who received dose-escalated IMRT to a ^{60}Cu -ATSM guided FV defined as a tumour to muscle ratio twice that of the CL SCM muscle.

The hypoxic FV received 80Gy in 35 fractions (2.3Gy per fraction), and the CT guided GTV received 70Gy in 35 fractions (2Gy per fraction) treated by a simultaneous integrated boost (SIB) technique.

3.9.7.4 Rectal Carcinoma

A single study has used ^{60}Cu -ATSM to predict response to neoadjuvant CRT. Seventeen patients with locally advanced rectal carcinoma underwent 3D dynamic PET imaging 2 weeks prior to 45Gy in 25 fractions of RT with concurrent 5-fluorouracil. Surgery was performed 6 weeks after the completion of treatment.

A tumour to muscle ratio greater than 2.6 was used to define the hypoxia. The overall and progression free survival was worse for those with hypoxic tumours. Those with a mean tumour to muscle ratio of 2.2 had their tumours down-staged on pathological review [117].

3.10 Aims of ^{64}Cu -ATSM CT-PET Imaging

^{18}F MISO has a number of limitations in hypoxic CT-PET imaging, and ^{64}Cu -ATSM has therefore been investigated as a potential hypoxic radio-nuclide.

^{64}Cu -ATSM uptake and retention was evaluated during CT-PET imaging in 4 patients who underwent primary surgery for the treatment of locally advanced SCCHN. A minimum of 48 hours prior to surgery, ^{64}Cu -ATSM was injected followed by an immediate 1 hour 3D dynamic CT-PET. Further late 3D static CT-PET imaging was undertaken 18 hours after injection. To assess the relationship of ^{64}Cu -ATSM with perfusion, a DCE-CT was performed after the 3D dynamic 1 hour CT-PET was completed.

The uptake and retention of ^{64}Cu -ATSM was assessed at 5 to 20 minutes, 40 to 60 minutes and 18 hours after injection to evaluate the change in uptake with time. The resulting tumour to muscle, background, and blood ratios were used to define the hypoxic FV with the PETVCAR software.

Eighteen hours prior to surgery, pimonidazole was administered. The patient then underwent their planned surgical procedure. Photographs were taken intra-operatively and margins were inked if required to aided orientation of the specimen. The surgical specimen was fixed in 10% neutral buffered formalin, diagnostically reviewed and macroscopically dissected by the reviewing Pathologist. The formalin fixed cut specimens were wax embedded, and microtomed sections IHC stained for pimonidazole, GLUT1, CAIX and HIF1 α . The stained IHC antigen fraction was calculated by a grid and total area method. These stained fractions were correlated for co-localisation.

The CT-PET images of ^{64}Cu -ATSM uptake were correlated at 5 to 20 minutes, 40 to 60 minutes, and 18 hours after injection with the exogenous, and endogenous IHC markers of hypoxia. The BF was correlated within a 4cm tumour region to the uptake of ^{64}Cu -ATSM at these time points

This potential validation of ^{64}Cu -ATSM as a surrogate marker of hypoxia and assessment of uptake in relation to BF allows future dose escalation studies to be conducted to attempt to overcome hypoxia associated radio-resistance and loco-regional failure in SCCHN.

3.11 References

1. Steel GG. Basic Clinical Radiobiology. 3rd ed: Hodder Headline Group; 2002
2. Vaupel P, Kallinowski F, Okunieff P. Blood flow, oxygen and nutrient supply, and metabolic microenvironment of human tumors: a review. *Cancer Res* 1989;49:6449-6465
3. Hockel M, Vaupel P. Tumor hypoxia: definitions and current clinical, biologic, and molecular aspects. *J Natl Cancer Inst* 2001;93:266-276
4. Gardner LB, Li Q, Park MS, et al. Hypoxia inhibits G1/S transition through regulation of p27 expression. *J Biol Chem* 2001;276:7919-7926
5. Nordsmark M, Bentzen SM, Rudat V, et al. Prognostic value of tumor oxygenation in 397 head and neck tumors after primary radiation therapy. An international multi-center study. *Radiother Oncol* 2005;77:18-24
6. Nordsmark M, Overgaard J. Tumor hypoxia is independent of hemoglobin and prognostic for loco-regional tumor control after primary radiotherapy in advanced head and neck cancer. *Acta Oncol* 2004;43:396-403
7. Bussink J, Kaanders JH, Strik AM, Vojnovic B, van Der Kogel AJ. Optical sensor-based oxygen tension measurements correspond with hypoxia marker binding in three human tumor xenograft lines. *Radiat Res* 2000;154:547-555
8. Azuma C, Raleigh JA, Thrall DE. Longevity of pimonidazole adducts in spontaneous canine tumors as an estimate of hypoxic cell lifetime. *Radiat Res* 1997;148:35-42

9. Arteel GE, Thurman RG, Raleigh JA. Reductive metabolism of the hypoxia marker pimonidazole is regulated by oxygen tension independent of the pyridine nucleotide redox state. *Eur J Biochem* 1998;253:743-750
10. Cobb LM, Nolan J, Butler SA. Distribution of pimonidazole and RSU 1069 in tumour and normal tissues. *Br J Cancer* 1990;62:915-918
11. Saunders MI, Anderson PJ, Bennett MH, et al. The clinical testing of Ro 03-8799--pharmacokinetics, toxicology, tissue and tumor concentrations. *Int J Radiat Oncol Biol Phys* 1984;10:1759-1763
12. Raleigh JA, Chou SC, Arteel GE, Horsman MR. Comparisons among pimonidazole binding, oxygen electrode measurements, and radiation response in C3H mouse tumors. *Radiat Res* 1999;151:580-589
13. Durand RE, Raleigh JA. Identification of nonproliferating but viable hypoxic tumor cells in vivo. *Cancer Res* 1998;58:3547-3550
14. Janssen HL, Hoebbers FJ, Sprong D, et al. Differentiation-associated staining with anti-pimonidazole antibodies in head and neck tumors. *Radiother Oncol* 2004;70:91-97
15. Raleigh JA, Chou SC, Calkins-Adams DP, et al. A clinical study of hypoxia and metallothionein protein expression in squamous cell carcinomas. *Clin Cancer Res* 2000;6:855-862
16. Varia MA, Calkins-Adams DP, Rinker LH, et al. Pimonidazole: a novel hypoxia marker for complementary study of tumor hypoxia and cell proliferation in cervical carcinoma. *Gynecol Oncol* 1998;71:270-277
17. Nordsmark M, Loncaster J, Aquino-Parsons C, et al. The prognostic value of pimonidazole and tumour pO₂ in human cervix carcinomas after radiation therapy: a prospective international multi-center study. *Radiother Oncol* 2006;80:123-131

18. Janssen HL, Haustermans KM, Sprong D, et al. HIF-1A, pimonidazole, and iododeoxyuridine to estimate hypoxia and perfusion in human head-and-neck tumors. *Int J Radiat Oncol Biol Phys* 2002;54:1537-1549
19. Raleigh JA, Calkins-Adams DP, Rinker LH, et al. Hypoxia and vascular endothelial growth factor expression in human squamous cell carcinomas using pimonidazole as a hypoxia marker. *Cancer Res* 1998;58:3765-3768
20. Kaanders JH, Wijffels KI, Marres HA, et al. Pimonidazole binding and tumor vascularity predict for treatment outcome in head and neck cancer. *Cancer Res* 2002;62:7066-7074
21. Brizel DM, Sibley GS, Prosnitz LR, Scher RL, Dewhirst MW. Tumor hypoxia adversely affects the prognosis of carcinoma of the head and neck. *Int J Radiat Oncol Biol Phys* 1997;38:285-289
22. Airley R, Loncaster J, Davidson S, et al. Glucose transporter glut-1 expression correlates with tumor hypoxia and predicts metastasis-free survival in advanced carcinoma of the cervix. *Clin Cancer Res* 2001;7:928-934
23. Airley RE, Loncaster J, Raleigh JA, et al. GLUT-1 and CAIX as intrinsic markers of hypoxia in carcinoma of the cervix: relationship to pimonidazole binding. *Int J Cancer* 2003;104:85-91
24. Burstein DE, Nagi C, Kohtz DS, Lee L, Wang B. Immunodetection of GLUT1, p63 and phospho-histone H1 in invasive head and neck squamous carcinoma: correlation of immunohistochemical staining patterns with keratinization. *Histopathology* 2006;48:717-722
25. Jonathan RA, Wijffels KI, Peeters W, et al. The prognostic value of endogenous hypoxia-related markers for head and neck squamous cell carcinomas treated with ARCON. *Radiother Oncol* 2006;79:288-297

26. Hoogsteen IJ, Marres HA, Bussink J, van der Kogel AJ, Kaanders JH. Tumor microenvironment in head and neck squamous cell carcinomas: predictive value and clinical relevance of hypoxic markers. A review. *Head Neck* 2007;29:591-604
27. Beasley NJ, Wykoff CC, Watson PH, et al. Carbonic anhydrase IX, an endogenous hypoxia marker, expression in head and neck squamous cell carcinoma and its relationship to hypoxia, necrosis, and microvessel density. *Cancer Res* 2001;61:5262-5267
28. Hoogsteen IJ, Marres HA, Wijffels KI, et al. Colocalization of carbonic anhydrase 9 expression and cell proliferation in human head and neck squamous cell carcinoma. *Clin Cancer Res* 2005;11:97-106
29. Koukourakis MI, Giatromanolaki A, Sivridis E, et al. Hypoxia-regulated carbonic anhydrase-9 (CA9) relates to poor vascularization and resistance of squamous cell head and neck cancer to chemoradiotherapy. *Clin Cancer Res* 2001;7:3399-3403
30. Harris AL. Hypoxia--a key regulatory factor in tumour growth. *Nat Rev Cancer* 2002;2:38-47
31. Aebersold DM, Burri P, Beer KT, et al. Expression of hypoxia-inducible factor-1alpha: a novel predictive and prognostic parameter in the radiotherapy of oropharyngeal cancer. *Cancer Res* 2001;61:2911-2916
32. Koukourakis MI, Bentzen SM, Giatromanolaki A, et al. Endogenous markers of two separate hypoxia response pathways (hypoxia inducible factor 2 alpha and carbonic anhydrase 9) are associated with radiotherapy failure in head and neck cancer patients recruited in the CHART randomized trial. *J Clin Oncol* 2006;24:727-735

33. Olive PL, Durand RE, Raleigh JA, Luo C, Aquino-Parsons C. Comparison between the comet assay and pimonidazole binding for measuring tumour hypoxia. *Br J Cancer* 2000;83:1525-1531
34. Le QT, Sutphin PD, Raychaudhuri S, et al. Identification of osteopontin as a prognostic plasma marker for head and neck squamous cell carcinomas. *Clin Cancer Res* 2003;9:59-67
35. Winter SC, Buffa FM, Silva P, et al. Relation of a hypoxia metagene derived from head and neck cancer to prognosis of multiple cancers. *Cancer Res* 2007;67:3441-3449
36. Bennett MH, Kertesz T, Yeung P. Hyperbaric oxygen for idiopathic sudden sensorineural hearing loss and tinnitus. *Cochrane Database Syst Rev* 2007:CD004739
37. Adams GE. Failla Memorial Lecture. Redox, radiation, and reductive bioactivation. *Radiat Res* 1992;132:129-139
38. Overgaard J. Clinical evaluation of nitroimidazoles as modifiers of hypoxia in solid tumors. *Oncol Res* 1994;6:509-518
39. Overgaard J, Hansen HS, Overgaard M, et al. A randomized double-blind phase III study of nimorazole as a hypoxic radiosensitizer of primary radiotherapy in supraglottic larynx and pharynx carcinoma. Results of the Danish Head and Neck Cancer Study (DAHANCA) Protocol 5-85. *Radiother Oncol* 1998;46:135-146
40. Martin L, Lartigau E, Weeger P, et al. Changes in the oxygenation of head and neck tumors during carbogen breathing. *Radiother Oncol* 1993;27:123-130
41. Kaanders JH, van der Maazen RW. A convenient and reliable method for carbogen breathing in man. *Radiother Oncol* 1993;29:341-343

42. Chaplin DJ, Horsman MR, Trotter MJ. Effect of nicotinamide on the microregional heterogeneity of oxygen delivery within a murine tumor. *J Natl Cancer Inst* 1990;82:672-676
43. Kaanders JH, Pop LA, Marres HA, et al. ARCON: experience in 215 patients with advanced head-and-neck cancer. *Int J Radiat Oncol Biol Phys* 2002;52:769-778
44. Bernier J, Denekamp J, Rojas A, et al. ARCON: accelerated radiotherapy with carbogen and nicotinamide in head and neck squamous cell carcinomas. The experience of the Co-operative group of radiotherapy of the european organization for research and treatment of cancer (EORTC). *Radiother Oncol* 2000;55:111-119
45. von Pawel J, von Roemeling R, Gatzemeier U, et al. Tirapazamine plus cisplatin versus cisplatin in advanced non-small-cell lung cancer: A report of the international CATAPULT I study group. *Cisplatin and Tirapazamine in Subjects with Advanced Previously Untreated Non-Small-Cell Lung Tumors. J Clin Oncol* 2000;18:1351-1359
46. Rischin D, Peters L, Hicks R, et al. Phase I trial of concurrent tirapazamine, cisplatin, and radiotherapy in patients with advanced head and neck cancer. *J Clin Oncol* 2001;19:535-542
47. Lee DJ, Trotti A, Spencer S, et al. Concurrent tirapazamine and radiotherapy for advanced head and neck carcinomas: a Phase II study. *Int J Radiat Oncol Biol Phys* 1998;42:811-815
48. Bourhis J, Overgaard J, Audry H, et al. Hyperfractionated or accelerated radiotherapy in head and neck cancer: a meta-analysis. *Lancet* 2006;368:843-854
49. Lee WR, Berkey B, Marcial V, et al. Anemia is associated with decreased survival and increased locoregional failure in patients with locally

advanced head and neck carcinoma: a secondary analysis of RTOG 85-27. *Int J Radiat Oncol Biol Phys* 1998;42:1069-1075

50. Henke M, Laszig R, Rube C, et al. Erythropoietin to treat head and neck cancer patients with anaemia undergoing radiotherapy: randomised, double-blind, placebo-controlled trial. *Lancet* 2003;362:1255-1260
51. Patel HB, Nasir FA, Nash GF, Scully MF, Kakkar AK. Enhanced angiogenesis following allogeneic blood transfusion. *Clin Lab Haematol* 2004;26:129-135
52. Siemann DW, Chaplin DJ, Walicke PA. A review and update of the current status of the vasculature-disabling agent combretastatin-A4 phosphate (CA4P). *Expert Opin Investig Drugs* 2009;18:189-197
53. Horsman MR, Overgaard J. Hyperthermia: a potent enhancer of radiotherapy. *Clin Oncol (R Coll Radiol)* 2007;19:418-426
54. Tatum JL, Kelloff GJ, Gillies RJ, et al. Hypoxia: importance in tumor biology, noninvasive measurement by imaging, and value of its measurement in the management of cancer therapy. *Int J Radiat Biol* 2006;82:699-757
55. Cenic A, Nabavi DG, Craen RA, Gelb AW, Lee TY. A CT method to measure hemodynamics in brain tumors: validation and application of cerebral blood flow maps. *AJNR Am J Neuroradiol* 2000;21:462-470
56. Konstas AA, Goldmakher GV, Lee TY, Lev MH. Theoretic basis and technical implementations of CT perfusion in acute ischemic stroke, part 1: Theoretic basis. *AJNR Am J Neuroradiol* 2009;30:662-668
57. Meier P, Zierler KL. On the theory of the indicator-dilution method for measurement of blood flow and volume. *J Appl Physiol* 1954;6:731-744

58. Gandhi D, Chepeha DB, Miller T, et al. Correlation between initial and early follow-up CT perfusion parameters with endoscopic tumor response in patients with advanced squamous cell carcinomas of the oropharynx treated with organ-preservation therapy. *AJNR Am J Neuroradiol* 2006;27:101-106
59. Hermans R, Meijerink M, Van den Bogaert W, et al. Tumor perfusion rate determined noninvasively by dynamic computed tomography predicts outcome in head-and-neck cancer after radiotherapy. *Int J Radiat Oncol Biol Phys* 2003;57:1351-1356
60. Minn H, Clavo AC, Wahl RL. Influence of hypoxia on tracer accumulation in squamous-cell carcinoma: in vitro evaluation for PET imaging. *Nucl Med Biol* 1996;23:941-946
61. Zhao S, Kuge Y, Mochizuki T, et al. Biologic correlates of intratumoral heterogeneity in ¹⁸F-FDG distribution with regional expression of glucose transporters and hexokinase-II in experimental tumor. *J Nucl Med* 2005;46:675-682
62. Sorensen M, Horsman MR, Cumming P, Munk OL, Keiding S. Effect of intratumoral heterogeneity in oxygenation status on FMISO PET, autoradiography, and electrode Po₂ measurements in murine tumors. *Int J Radiat Oncol Biol Phys* 2005;62:854-861
63. Kubota K, Tada M, Yamada S, et al. Comparison of the distribution of fluorine-18 fluoromisonidazole, deoxyglucose and methionine in tumour tissue. *Eur J Nucl Med* 1999;26:750-757
64. Zimny M, Gagel B, DiMartino E, et al. FDG--a marker of tumour hypoxia? A comparison with [¹⁸F]fluoromisonidazole and pO₂-polarography in metastatic head and neck cancer. *Eur J Nucl Med Mol Imaging* 2006;33:1426-1431

65. Rajendran JG, Schwartz DL, O'Sullivan J, et al. Tumor hypoxia imaging with [F-18] fluoromisonidazole positron emission tomography in head and neck cancer. *Clin Cancer Res* 2006;12:5435-5441
66. Thorwarth D, Eschmann SM, Holzner F, Paulsen F, Alber M. Combined uptake of [18F]FDG and [18F]FMISO correlates with radiation therapy outcome in head-and-neck cancer patients. *Radiother Oncol* 2006;80:151-156
67. Hicks RJ, Rischin D, Fisher R, et al. Utility of FMISO PET in advanced head and neck cancer treated with chemoradiation incorporating a hypoxia-targeting chemotherapy agent. *Eur J Nucl Med Mol Imaging* 2005;32:1384-1391
68. Rischin D, Hicks RJ, Fisher R, et al. Prognostic significance of [18F]-misonidazole positron emission tomography-detected tumor hypoxia in patients with advanced head and neck cancer randomly assigned to chemoradiation with or without tirapazamine: a substudy of Trans-Tasman Radiation Oncology Group Study 98.02. *J Clin Oncol* 2006;24:2098-2104
69. Nehmeh SA, Lee NY, Schroder H, et al. Reproducibility of intratumor distribution of (18)F-fluoromisonidazole in head and neck cancer. *Int J Radiat Oncol Biol Phys* 2008;70:235-242
70. Thorwarth D, Eschmann SM, Paulsen F, Alber M. A model of reoxygenation dynamics of head-and-neck tumors based on serial 18F-fluoromisonidazole positron emission tomography investigations. *Int J Radiat Oncol Biol Phys* 2007;68:515-521
71. Thorwarth D, Eschmann SM, Paulsen F, Alber M. Hypoxia dose painting by numbers: a planning study. *Int J Radiat Oncol Biol Phys* 2007;68:291-300

72. Eschmann SM, Paulsen F, Bedeshem C, et al. Hypoxia-imaging with (18)F-Misonidazole and PET: changes of kinetics during radiotherapy of head-and-neck cancer. *Radiother Oncol* 2007;83:406-410
73. Lee NY, Mechalakos JG, Nehmeh S, et al. Fluorine-18-labeled fluoromisonidazole positron emission and computed tomography-guided intensity-modulated radiotherapy for head and neck cancer: a feasibility study. *Int J Radiat Oncol Biol Phys* 2008;70:2-13
74. Popple RA, Ove R, Shen S. Tumor control probability for selective boosting of hypoxic subvolumes, including the effect of reoxygenation. *Int J Radiat Oncol Biol Phys* 2002;54:921-927
75. Lin Z, Mechalakos J, Nehmeh S, et al. The influence of changes in tumor hypoxia on dose-painting treatment plans based on 18F-FMISO positron emission tomography. *Int J Radiat Oncol Biol Phys* 2008;70:1219-1228
76. Busk M, Horsman MR, Jakobsen S, et al. Imaging hypoxia in xenografted and murine tumors with 18F-fluoroazomycin arabinoside: a comparative study involving microPET, autoradiography, PO₂-polarography, and fluorescence microscopy. *Int J Radiat Oncol Biol Phys* 2008;70:1202-1212
77. Grosu AL, Souvatzoglou M, Roper B, et al. Hypoxia imaging with FAZA-PET and theoretical considerations with regard to dose painting for individualization of radiotherapy in patients with head and neck cancer. *Int J Radiat Oncol Biol Phys* 2007;69:541-551
78. Lehtio K, Eskola O, Viljanen T, et al. Imaging perfusion and hypoxia with PET to predict radiotherapy response in head-and-neck cancer. *Int J Radiat Oncol Biol Phys* 2004;59:971-982

79. Rasey JS, Hofstrand PD, Chin LK, Tewson TJ. Characterization of [18F]fluoroetanidazole, a new radiopharmaceutical for detecting tumor hypoxia. *J Nucl Med* 1999;40:1072-1079
80. Barthel H, Wilson H, Collingridge DR, et al. In vivo evaluation of [18F]fluoroetanidazole as a new marker for imaging tumour hypoxia with positron emission tomography. *Br J Cancer* 2004;90:2232-2242
81. Mahy P, Geets X, Lonneux M, et al. Determination of tumour hypoxia with [18F]EF3 in patients with head and neck tumours: a phase I study to assess the tracer pharmacokinetics, biodistribution and metabolism. *Eur J Nucl Med Mol Imaging* 2008;35:1282-1289
82. Komar G, Seppanen M, Eskola O, et al. 18F-EF5: a new PET tracer for imaging hypoxia in head and neck cancer. *J Nucl Med* 2008;49:1944-1951
83. Chan-Stier CH, Minkel D, Petering DH. Reactions of bis(thiosemicarbazone) copper(II) complexes with tumor cells and mitochondria. *Bioinorg Chem* 1976;6:203-217
84. Petering HG, Buskirk HH, Underwood GE. The Anti-Tumor Activity of 2-Keto-3-ethoxybutyraldehyde Bis(thiosemicarbazone) and Related Compounds. *Cancer Research* 1964;24:367-372
85. Dearling JLJ, Lewis JS, McCarthy DW, Welch MJ, Blower PJ. Redox-active metal complexes for imaging hypoxic tissues: structure activity relationships in copper (II) bis(thiosemicarbazone) complexes. *Chem Commun* 1998:2531-2532
86. Dearling JLJ, Lewis JS, Mullen GED, et al. Design of hypoxia-targeting radiopharmaceuticals: selective uptake of copper-64 complexes in hypoxic cells. *European Journal of Nuclear Medicine* 1998;25:788-792

87. Blower PJ, Lewis JS, Zweit J. Copper radionuclides and radiopharmaceuticals in nuclear medicine. *Nuclear Medicine and Biology* 1996;23:957-980
88. Zweit J. Radionuclides and carrier molecules for therapy. *Phys Med Biol* 1996;41:1905-1914
89. Williams HA, Robinson S, Julyan P, Zweit J, Hastings D. A comparison of PET imaging characteristics of various copper radioisotopes. *Eur J Nucl Med Mol Imaging* 2005;32:1473-1480
90. Mathias CJ, Green MA, Morrison WB, Knapp DW. Evaluation of Cu-PTSM as a tracer of tumor perfusion: comparison with labeled microspheres in spontaneous canine neoplasms. *Nucl Med Biol* 1994;21:83-87
91. Rust TC, Kadrmas DJ. Rapid dual-tracer PTSM+ATSM PET imaging of tumour blood flow and hypoxia: a simulation study. *Phys Med Biol* 2006;51:61-75
92. John EK, Green MA. Structure-activity relationships for metal-labeled blood flow tracers: comparison of keto aldehyde bis(thiosemicarbazonato)copper(II) derivatives. *J Med Chem* 1990;33:1764-1770
93. Fujibayashi Y, Taniuchi H, Yonekura Y, et al. Copper-62-ATSM: a new hypoxia imaging agent with high membrane permeability and low redox potential. *J Nucl Med* 1997;38:1155-1160
94. Taniuchi H, Fujibayashi Y, Okazawa H, et al. Cu-pyruvaldehyde-bis(N4-methylthiosemicarbazone) (Cu-PTSM), a metal complex with selective NADH-dependent reduction by complex I in brain mitochondria: a potential radiopharmaceutical for mitochondria-functional imaging with

- positron emission tomography (PET). *Biol Pharm Bull* 1995;18:1126-1129
95. Fujibayashi Y, Wada K, Taniuchi H, et al. Mitochondria-selective reduction of ^{62}Cu -pyruvaldehyde bis(N4-methylthiosemicarbazone) (^{62}Cu -PTSM) in the murine brain; a novel radiopharmaceutical for brain positron emission tomography (PET) imaging. *Biol Pharm Bull* 1993;16:146-149
 96. Baerga ID, Maickel RP, Green MA. Subcellular distribution of tissue radiocopper following intravenous administration of ^{67}Cu -labeled Cu-PTSM. *Int J Rad Appl Instrum B* 1992;19:697-701
 97. Dearling JLJ, Lewis JS, Mullen GED, Welch MJ, Blower PJ. Copper bis(thiosemicarbazone) complexes as hypoxia imaging agents: structure-activity relationships. *J Biol Inorg Chem* 2002;7:249-259
 98. Burgman P, O'Donoghue JA, Lewis JS, et al. Cell line-dependent differences in uptake and retention of the hypoxia-selective nuclear imaging agent Cu-ATSM. *Nucl Med Biol* 2005;32:623-630
 99. Katano K, Safaei R, Samimi G, et al. The copper export pump ATP7B modulates the cellular pharmacology of carboplatin in ovarian carcinoma cells. *Mol Pharmacol* 2003;64:466-473
 100. Harris ED. Copper homeostasis: the role of cellular transporters. *Nutr Rev* 2001;59:281-285
 101. Xiao Z, Donnelly PS, Zimmermann M, Wedd AG. Transfer of copper between bis(thiosemicarbazone) ligands and intracellular copper-binding proteins. insights into mechanisms of copper uptake and hypoxia selectivity. *Inorg Chem* 2008;47:4338-4347

102. Lewis JS, McCarthy DW, McCarthy TJ, Fujibayashi Y, Welch MJ. Evaluation of ^{64}Cu -ATSM in vitro and in vivo in a hypoxic tumor model. *J Nucl Med* 1999;40:177-183
103. Bonnitcho PD, Vavere AL, Lewis JS, Dilworth JR. In vitro and in vivo evaluation of bifunctional bithiosemicarbazone ^{64}Cu -complexes for the positron emission tomography imaging of hypoxia. *J Med Chem* 2008;51:2985-2991
104. Laforest R, Dehdashti F, Lewis JS, Schwarz SW. Dosimetry of $^{60}/^{61}/^{62}/^{64}\text{Cu}$ -ATSM: a hypoxia imaging agent for PET. *Eur J Nucl Med Mol Imaging* 2005;32:764-770
105. Matsumoto K, Szajek L, Krishna MC, et al. The influence of tumor oxygenation on hypoxia imaging in murine squamous cell carcinoma using ^{64}Cu -ATSM or ^{18}F -Fluoromisonidazole positron emission tomography. *Int J Oncol* 2007;30:873-881
106. Lewis JS, Sharp TL, Laforest R, Fujibayashi Y, Welch MJ. Tumor uptake of copper-diacetyl-bis(N(4)-methylthiosemicarbazone): effect of changes in tissue oxygenation. *J Nucl Med* 2001;42:655-661
107. O'Donoghue JA, Zanzonico P, Pugachev A, et al. Assessment of regional tumor hypoxia using ^{18}F -fluoromisonidazole and $^{64}\text{Cu}(\text{II})$ -diacetyl-bis(N4-methylthiosemicarbazone) positron emission tomography: Comparative study featuring microPET imaging, Po_2 probe measurement, autoradiography, and fluorescent microscopy in the R3327-AT and FaDu rat tumor models. *Int J Radiat Oncol Biol Phys* 2005;61:1493-1502
108. Basken NE, Mathias CJ, Lipka AE, Green MA. Species dependence of ^{64}Cu -Bis(thiosemicarbazone) radiopharmaceutical binding to serum albumins. *Nucl Med Biol* 2008;35:281-286

109. Yuan H, Schroeder T, Bowsher JE, et al. Intertumoral differences in hypoxia selectivity of the PET imaging agent $^{64}\text{Cu}(\text{II})$ -diacetyl-bis(N4-methylthiosemicarbazone). *J Nucl Med* 2006;47:989-998
110. Fujibayashi Y, Cutler CS, Anderson CJ, et al. Comparative studies of Cu-64-ATSM and C-11-acetate in an acute myocardial infarction model: ex vivo imaging of hypoxia in rats. *Nucl Med Biol* 1999;26:117-121
111. Lewis JS, Herrero P, Sharp TL, et al. Delineation of hypoxia in canine myocardium using PET and copper(II)-diacetyl-bis(N(4)-methylthiosemicarbazone). *J Nucl Med* 2002;43:1557-1569
112. Dehdashti F, Grigsby PW, Lewis JS, et al. Assessing tumor hypoxia in cervical cancer by PET with ^{60}Cu -labeled diacetyl-bis(N4-methylthiosemicarbazone). *J Nucl Med* 2008;49:201-205
113. Grigsby PW, Malyapa RS, Higashikubo R, et al. Comparison of molecular markers of hypoxia and imaging with $(^{60})\text{Cu}$ -ATSM in cancer of the uterine cervix. *Mol Imaging Biol* 2007;9:278-283
114. Dehdashti F, Mintun MA, Lewis JS, et al. In vivo assessment of tumor hypoxia in lung cancer with ^{60}Cu -ATSM. *Eur J Nucl Med Mol Imaging* 2003;30:844-850
115. Wong TZ, Lacy JL, Petry NA, et al. PET of hypoxia and perfusion with ^{62}Cu -ATSM and ^{62}Cu -PTSM using a $^{62}\text{Zn}/^{62}\text{Cu}$ generator. *AJR Am J Roentgenol* 2008;190:427-432
116. Chao C, Bosch WR, Mutic S, et al. A novel approach to overcome hypoxic tumour resistance: Cu-ATSM-guided intensity modulated radiation therapy. *Int J Radiation Oncology Biol Phys* 2001;49:1171-1182
117. Dietz DW, Dehdashti F, Grigsby PW, et al. Tumor hypoxia detected by positron emission tomography with ^{60}Cu -ATSM as a predictor of

response and survival in patients undergoing Neoadjuvant
chemoradiotherapy for rectal carcinoma: a pilot study. Dis Colon Rectum
2008;51:1641-1648

Chapter 4

¹⁸Fluoro-2-deoxyglucose CT-PET Guided Target Volume Delineation Study

4.1 Materials and Methods

4.1.1 Trial Recruitment

Between March 2006 and May 2008, 12 patients were recruited at University College Hospitals NHS Foundation Trust, London (UCLH).

Fourteen patients were recruited at Mount Vernon Cancer Centre, Northwood, Middlesex during this time period. Unfortunately, because of software incompatibility issues for image analysis, only the UCLH patients were analysed and will be discussed.

Patients due to undergo radical RT (conventional fractionation of 66Gy, 2Gy per fraction treating daily Monday to Friday, over 6.5 weeks) or CRT with concurrent cisplatin were recruited according to the International Conference of Harmonisation Good Clinical Practice (GCP) guidelines. Patients were recruited after eligibility screening by Clinicians in the local multi-disciplinary team meeting.

The eligibility criteria included: age greater than or equal to 50, histological or cytological confirmation of SCCHN, locally advanced disease, Eastern Co-operative Oncology Group (ECOG) performance status 0 to 2, life expectancy greater than 12 weeks, and no major co-morbidities.

Patients were excluded from the study if they had a serious inter-current illness, diabetes mellitus, or psychiatric disorder.

Treatment was planned according to the departmental Head and Neck protocol. Patients received concurrent cisplatin chemotherapy (if eligible) either at a dose of 75 to 100mg/m² day 1, 22 and 43, or 50mg/m² per day on day 1 + 2, and day 29 + 30. The cisplatin dose was reduced if clinically required.

Once recruited, patients could be withdrawn from the study at any point if there was: failure of compliance, disease progression, or the development of severe inter-current illness. Similarly, patients were able to withdraw without reason or prejudice and continue their treatment. One patient died in the community from aspiration pneumonia prior to starting the protocol and another was withdrawn due to rapid disease progression, therefore ten patients underwent the imaging protocol.

4.1.2 Investigations Prior to Trial Enrolment

All patients underwent a full history and clinical examination, performance status assessment, height, weight, screening of peripheral blood samples (haematological and biochemical), and assessment of the glomerular filtration rate (if concurrent chemotherapy was administered).

4.1.3 Radiotherapy Planning Process

In line with current practice, an immobilisation shell was made for each patient prior to the start of RT and the first CT-PET scan. This ensured the accurate delivery of RT to the HN and image co-registration. All imaging was performed with the patient in the shell replicating the treatment position. A flat couch top was used on the CT-PET scanner and a Therapy Radiographer “Set Up” each patient at each scan time point.

RT was planned conventionally (virtual simulation or TV delineation for 3DCRT) with or without intra-venous contrast according to the diagnostic imaging, biopsy result, and overall staging information.

4.1.4 ^{18}F FDG CT-PET Examination

Prior to each CT-PET investigation, patients were fasted for 6 hours and their blood glucose noted prior to the intra-venous administration of ^{18}F FDG. Following injection, patients lay flat on a couch, in a warm darkened room for 1 hour, to ensure minimal ^{18}F FDG uptake in skeletal muscle.

4.1.5 Timing of Imaging

Image acquisition was undertaken on a GE Healthcare Discovery (DST-16) CT-PET scanner.

All patients underwent whole body 3D ^{18}F FDG CT-PET imaging 72 hours prior to the start of treatment (0Gy). Further CT-PET imaging of the HN only was planned at 10Gy, 44Gy and 66Gy (days 5, 32 and 47 of treatment). Following image acquisition the data was transferred to optical disk for storage within the Nuclear Medicine Department.

4.1.6 Patient Characteristics and Clinical Information

The patients' notes were reviewed and information collected included: age, gender, TNM staging, primary site, presenting symptoms, co-morbidities, prescribed medication, smoking and alcohol, concurrent chemotherapy (number of cycles prescribed and received), and radiation dose.

4.1.7 ^{18}F FDG Delineation of Metabolically Active Functional Volumes

In conjunction with Dr I Kayani, Nuclear Medicine Consultant at UCLH, the imaging was analysed between October 2008 and October 2009.

4.1.8 PET Volume Computerised Assisted Reading

The PETVCAR (PET Volume Computerised Assisted Reading) software (GE Healthcare Medical Systems, WI, USA) was used in conjunction with the GE Advantage Work Stations in the Nuclear Medicine Department at UCLH. The Advantage Work Stations are used to routinely report clinical CT-PET scans.

PETVCAR is based on the Volume Viewer 3.1 application of the reporting tool. It allows automatic image analysis of CT, PET and CT-PET images for use either

diagnostically to assess disease, or to aid contouring of the ROI that can be used in RT planning. The software also allows the analysis of the ROI in the baseline scan with the single visit application, and sequential scans can be compared to the baseline scan with the multi-visit application. Only one time point scan can be compared to another time point scan to allow response assessment.

The software automatically highlights and generates the defined ROI from the PET scan based on the threshold levels defined by the user. The ROI is automatically propagated when imaging sets are compared, allowing analysis of the selected FV. This software package can be used in conjunction with any PET radio-nuclide to measure the: FV, SUVmax and mean, TLG, and glucose normalised values within each ROI.

4.1.8.1 Retrieval of Patients Scans from Archive

CT-PET imaging was retrieved from the archived databases. Each central clinical and research database connected to the Advantage Workstation was selected and filtered. The patient was highlighted, along with all the image sets linked to that patient's identification number, and then copied from archive to the clinical workstation.

The height, weight and blood glucose (mmol/l) were corroborated with the written records to ensure the correct calculation of the SUV and associated parameters.

The AC CT HN, and PET AC data sets were selected for volume delineation with PETVCAR. CT and PET images were automatically co-registered.

Automatic co-registration was reviewed both in relation to soft tissue and bony (inner table of skull, and cervical spinous processes) anatomy in the axial, sagittal, and coronal planes and manually adjusted if required. The fused CT-PET images were represented as 50% CT and 50% PET content.

4.1.8.2 Definition of Primary and Lymph Node Regions of Interest on the Pre-Treatment Imaging

The pre-treatment image sets were loaded in to the single visit application. The ROI was defined on PET (grayscale), CT and fused CT-PET imaging. When the extent was unclear, for example low-grade uptake, imaging and histology reports were reviewed to corroborate the findings and adjust the ROI accordingly.

A bookmark was placed over the ROI and reviewed in all planes. The bookmark contained a cube shaped boundary box that surrounded the ROI. The size of the boundary box was adjusted to avoid overlap with other structures and exclude normal tissue from the ROI. The 3D cube contained only the auto-contoured and segmented ROI.

This process was repeated until all the ROI had been selected and optimised. Each ROI was annotated. The exact anatomical location of each ROI was noted for reference at a later date. For example 1 = right level II medial node at the angle of the mandible.

4.1.8.3 Background Uptake of ¹⁸Fluoro-2-deoxyglucose

A reference region was defined on each scan to calculate the background SUV. This was selected within SCM. A sphere was chosen, resized and moved depending on the changes that occurred between the scans if appropriate. The boundary of the sphere did not extend outside the boundary of the muscle.

4.1.8.4 Volume Definition on Multiple Image Sets

Similarly, the pre-treatment AC CT and PET data sets were selected, as well as the data sets at a single other study time point, and loaded into the multi-visit application.

The pre-treatment and comparison scans were automatically co-registered (rigid registration) by the software, based on the CT image set. The minimal CT resolution was 512 x 512 pixels. The computer mouse cursor was moved over the pedicles of the cervical vertebra to check the registration quality. The image sets were then adjusted in the x, y, and z directions and the co-registration was reset.

This process was continued until the registration was optimal (within a 1mm tolerance) especially within the ROI. Figure 4.1 illustrates an exaggerated mismatch in co-registration a) prior to manual adjustment, and b) after adjustment. The pre-treatment CT-PET was represented in grayscale, and the comparison CT-PET in blue.

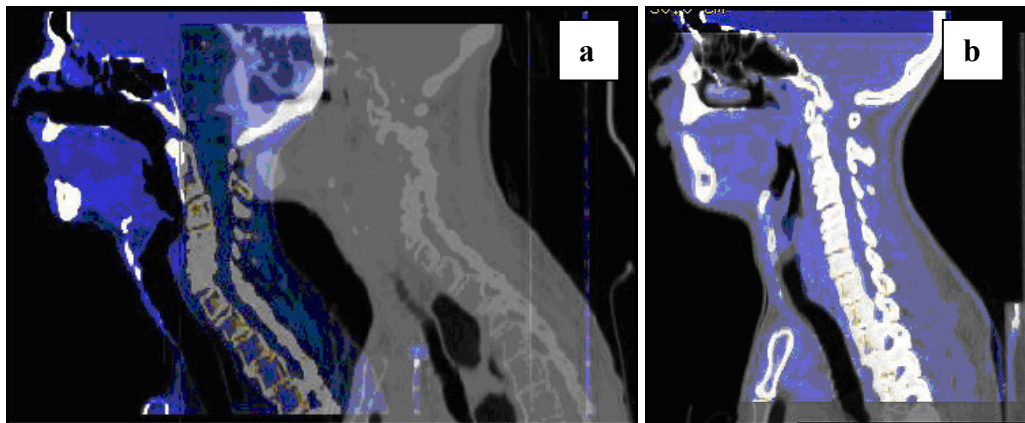


Figure 4.1: The co-registered CT-PET data sets, a) prior to correction, and b) after correction of co-registration

The bookmarks with their accompanying boundary boxes defined in the single visit application on the pre-treatment CT-PET were automatically propagated to the co-registered CT-PET either at the time point of 10Gy, 44Gy, or 66Gy. On completion, the comparison CT-PET data set had inherited the bookmarks including: boundary box size, identification of each ROI, and the segmented algorithm used to threshold the ROI. However, at the time of propagation, the software defaulted back to the original threshold factory settings, and therefore these required re-defining for each ROI on each image set.

This propagation application located the bookmark in the comparison scan to a position calculated during the co-registration process. Depending on the response during treatment, and on review with the Consultant Radiologist, the size of the boundary box, and the location was adjusted if required to optimise segmentation.

This process was repeated until each image set had been directly compared with the pre-treatment imaging.

4.1.8.5 Thresholds Used to Define the Functional Volume

Each ROI on the scan was defined according to the selected threshold, and delineation method on the single visit and multi-visit application. Table 4.1 indicates the thresholds used to define each ROI/FV. The SUV was automatically normalised to body weight in grams per millilitre (bwg/ml).

Table 4.1: The thresholds used to define each ¹⁸FDG functional volume

Threshold Method	Thresholds Investigated
SUV Cut-off	2.5, 3.0, 3.5, 4.0 (bwg/ml)
Percentage of the SUVmax	30, 35, 40, 45, 50
Individualised Adaptive Threshold	0.5 weighting factor

The software defaulted to an SUVCO threshold of 2.0bwg/ml, and a PTSUVmax of 50%. The thresholds were therefore individually set for each ROI, at each imaging point. The SUV used to contour the volume for the PTSUVmax method was individually calculated. The SUVmax was noted within each ROI at each imaging point. The percentage threshold was then calculated and the corresponding SUV manually entered into the software for each ROI on each scan in the single and multi-visit application.

4.1.8.6 Calculation of the Individualised Adaptive Threshold

The IAT was based on the individual SUV within each ROI and the background SUV.

An iterative algorithm was used to detect the threshold level that separated the ROI from the background tissue by weighting the SUVmax and SUVmean within the ROI with a weighting factor ($0 \leq \omega \leq 1$, where 0=background and 1=object of interest), represented as a Boolean variable. This weighting factor was automatically set at 0.5. Figure 4.2 graphically represents the process of FV delineation by this method as 4 steps.

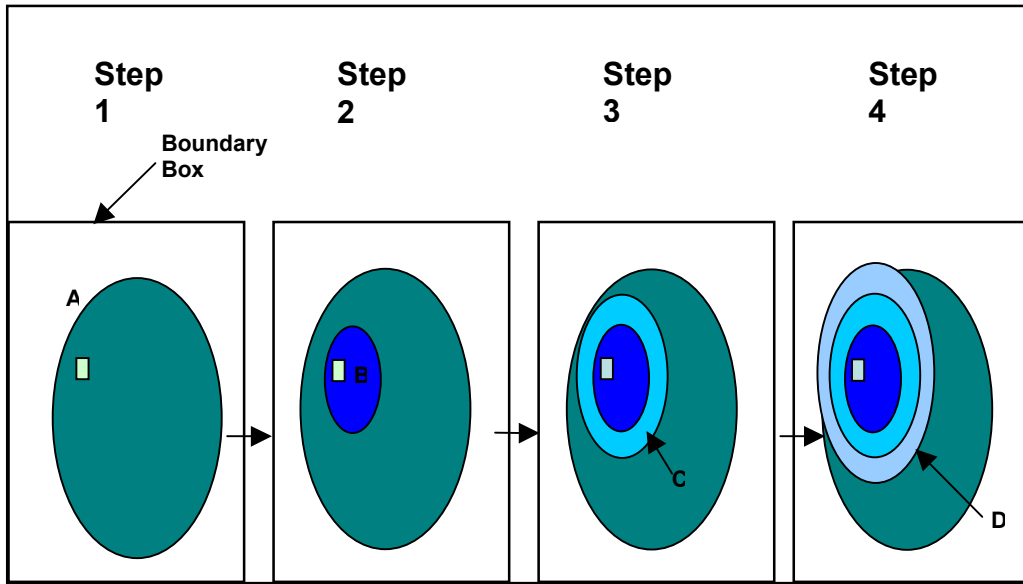


Figure 4.2: Graphical representation of the individualised adaptive threshold functional volume definition

Firstly, the intersection of the original PET volume, and the volume of the book-marked boundary box was defined as volume A. The SUV threshold (t) was calculated by multiplying the weighting factor (ω) by the SUVmax, which is represented as the turquoise square in volume A. Next the voxels with an SUV greater than or equal to the threshold were defined (volume B). This volume was then grown by a dilatation morphological operation (d) to represent a halo around volume B and is represented as volume C (volume $C = d[d(B)]/d(B)$) in step 3. Next a new threshold was calculated ($t_{\text{new}} = \text{SUVmean}[B] \times \omega + \text{SUVmean}[C] \times (1 - \omega)$), and the final volume B was the segmented ROI.

Up to 3 iterations of step three were completed if the new threshold did not equal the threshold (t) in step 1. Lastly in step 4, the volume was post-processed to achieve the final delineated volume (D). The resulting volume from the steps 1 to 3 was volume C, and volume D therefore is the halo around volume C generated by the dilatation morphological operation ($D = d[d(C)]/d(C)$).

4.1.9 Parameter Definition

Table 4.2 indicates the parameters recorded for each CT-PET scan.

Table 4.2: Definition of parameters used to assess the ^{18}F FDG functional volume prior to and during treatment

Parameter	Unit	Definition
Functional Volume	cm^3	Total volume of the ROI
SUVmax	bwg/ml	Maximum SUV detected within the ROI
SUVmean	bwg/ml	Mean SUV (SUV in each voxel summed within the ROI, and then divided by the number of voxels within the ROI)
Total Lesion Glycolysis	bwg	Volume x SUVmean

The parameters of SUVmax, SUVmean, and TLG were also normalised to the patient's blood glucose (mmol/l).

Only the functional volume, SUVmax, and SUV within the background region will be discussed in this chapter.

4.1.10 Radiotherapy Structure Sets

RT Structure Sets (RTSS) were created for each ROI at a SUVCO threshold of 3.0bwg/ml, and exported from the Advantage Work Station in the RT Planning Department at UCLH.

4.2 Statistical Analysis

Statistical advice was sought from the MRC Clinical Trials Centre, 5th Floor, 90 Tottenham Court Road, London. StatsDirect (StatsDirect Limited, Cheshire, WA14 4QA, UK) statistical software package was used to analyse the data. The data was first assessed for normality using the Shapiro Wilks Test.

The primary ^{18}F FDG FVs were normally distributed, and analysed by the paired t-test to compare the difference in the sample means either between thresholds, or imaging points, and the simple linear regression (SLR) model to assess the relationship of the outcome variable. For example: FV, SUVmax, to that of the

predictor variable for example: dose. The mean, and standard error of the mean (SEM) are stated.

The LN ¹⁸FDG FVs were not normally distributed, and were analysed by the Wilcoxon Summed Rank Test (WCSRT) to compare two sample populations. This was the non-parametric equivalent to the paired t-test. The SLR model was also used. The median and inter-quartile range (IQR) are stated.

The p-values quoted correspond to the 95% confidence interval (CI) for the sample, and one-way test results to assess for a reduction in values with an increase in the radiation dose.

The results are stated according to the imaging time interval for example 0Gy (pre-treatment imaging), 8 to 18Gy (imaging scheduled for 10Gy), 36 to 50Gy (imaging scheduled for 44Gy), and 66Gy, and the actual dose points were used for each imaging set for the SLR analysis.

The SLR modelling used the equation: $y = bx + a$

y= Outcome

b= Slope of the line of best fit

x= Predictor

a= Intercept of the line of best fit with the y axis

This was calculated by the least squares method (minimisation of the sum of the squares of deviation from a straight line), and allowed a theoretical outcome (y) to be calculated from the data. For example radiation dose (x) required to reduce the FV to zero. This was used to indicate a potential theoretical dose that would be required to eradicate the functional volume during dose escalation studies.

The values for the reference ROI were normally distributed and assessed by the parametric paired t-test.

4.3 Results

4.3.1 Patient Characteristics

Table 4.3 illustrates the patient characteristics from all ten patients recruited into the study who underwent imaging.

Table 4.3: The characteristics of study patients

Patient	Age	Gender	Primary Site	TNM Classification
1	58	Male	Larynx – Glottis	T3 N0 M0
2	55	Male	Nasal Cavity	T4 N0 M0
3	60	Male	Posterior 1/3 of the Tongue	T4 N2c M0
4	64	Male	Posterior Nasal Space	T3 N2a M0
5	71	Male	Posterior 1/3 of the Tongue	T4 N0 M0
6	75	Male	Larynx - Supraglottis	T2 N2c M0
7	65	Male	Pyriiform fossa	T3 N1 M0
8	56	Female	Tonsil	T3 N2c M0
9	54	Male	Larynx – Supraglottis	T2 N2b M0
10	61	Male	Posterior 1/3 of the Tongue	T2 N2c M0

Patients 4 and 8 could not be assessed because the CT-PET baseline images were not optically stored and have been highlighted in blue.

4.3.2 The Imaging Protocol

All eight patients analysed were imaged within 72 hours of the start of their planned radical treatment, and at 66Gy on treatment completion.

For the second imaging point, three patients were imaged at 10Gy according to the protocol, four patients were imaged 1 fraction earlier at 8Gy, and one patient was imaged 4 fractions later at 18Gy.

No patients were imaged at 44Gy according to the protocol. Five patients were imaged 2 fractions earlier at 40Gy, one patient was imaged 3 fractions earlier at

38Gy, one patient was imaged 4 fractions earlier at 36Gy, and one patient was imaged 3 fractions later at 50Gy.

4.3.3 ¹⁸Fluoro-2-deoxyglucose Delineated Functional Volume

Eight primary and twenty LN ¹⁸FDG positive regions were evaluated in these eight patients.

4.3.3.1 Primary Functional Volumes

4.3.3.1.1 SUV Cut Off

The mean FV and SEM is indicated in table 4.4 for each threshold and expressed as a histogram in figure 4.3 with the SEM represented as error bars.

Table 4.4: The mean and standard error of the mean for the delineated primary functional volumes by the SUV Cut Off method

SUV Cut Off Threshold (bwg/ml)		Functional Volume (cm ³)			
		0Gy	8 to 18Gy	36 to 50Gy	66Gy
2.5	Mean	34.95	30.93	25.98	18.77
	SEM	8.42	8.34	8.22	4.94
3.0	Mean	28.31	23.85	18.24	10.36
	SEM	7.26	6.70	5.94	2.61
3.5	Mean	23.9	20.09	13.25	6.01
	SEM	6.64	5.82	4.35	1.70
4.0	Mean	20.65	17.14	10.28	3.70
	SEM	6.16	5.06	3.38	1.30

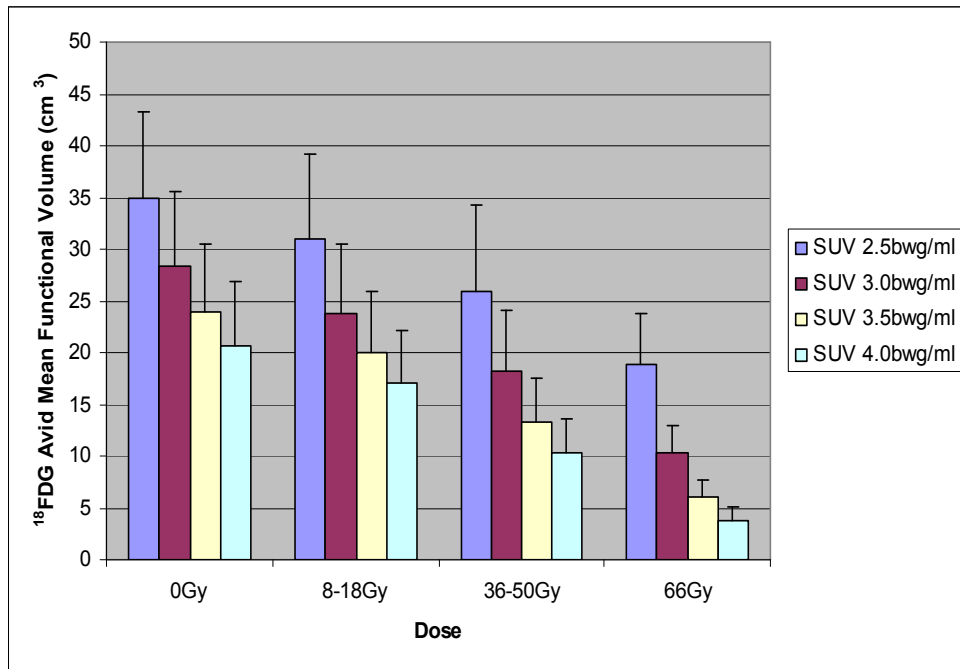


Figure 4.3: The mean ^{18}F FDG primary functional volume defined by the SUV Cut Off thresholds

There was a highly significant reduction in the FV at each imaging point between 2.5 to 3.0bwg/ml, 2.5 to 3.5bwg/ml, and 2.5 to 4.0bwg/ml indicated in table 4.5. This was most significant at 0Gy, and 8 to 18Gy. The percentage reduction between these thresholds is also shown, and was greatest between 2.5 and 4.0bwg/ml thresholds.

Table 4.5: The mean percentage, actual reduction, p-values, and 95% confidence intervals for the primary functional volume delineated by the SUV Cut Off method at each imaging point

SUV Cut Off Threshold (bwg/ml)	Imaging Point (Gy)	Mean Percentage Reduction	Mean Reduction (cm³)	p-value	95% CI (cm³)
2.5 to 3.0	<i>0</i>	18.98	6.64	0.004	2.42 - 10.84
	<i>8 to 18</i>	22.88	7.08	0.004	2.48 -11.67
	<i>36 to 50</i>	29.79	7.74	0.011	1.58 -13.81
	<i>66</i>	44.82	7.36	0.018	0.64 - 14.08
2.5 to 3.5	<i>0</i>	31.62	11.05	0.002	4.80 - 17.30
	<i>8 to 18</i>	35.05	10.84	0.004	3.94 - 17.73
	<i>36 to 50</i>	48.99	12.73	0.01	2.72 - 22.72
	<i>66</i>	67.96	11.16	0.015	1.15 - 20.90
2.5 to 4.0	<i>0</i>	40.92	14.30	0.002	6.10 - 22.50
	<i>8 to 18</i>	44.58	3.78	0.005	4.65 - 22.92
	<i>36 to 50</i>	60.44	15.70	0.01	3.30 - 28.10
	<i>66</i>	80.29	13.19	0.013	2.06 - 24.31

Table 4.6 indicates the percentage and actual reduction in primary volume at each delineation threshold when the pre-treatment volume was compared to: 8 to 18Gy, 36 to 50Gy, and 66Gy. There was no significant reduction in the FV at 8 to 18Gy compared to 0Gy at any SUVCO delineation threshold. However, there was a highly significant reduction at 66Gy and 36 to 50Gy compared to 0Gy at 3.0, 3.5, and 4.0bwg/ml thresholds only. This was greatest at 66Gy, and most significant when all imaging points were compared at the 3.0bwg/ml threshold.

Table 4.6: The mean percentage, actual reduction, p-values and 95% confidence intervals between the imaging points for the primary functional volume delineated at each SUV Cut Off threshold

SUV Cut Off Threshold (bwg/ml)	Compared Imaging Points (Gy)	Mean Percentage Reduction	Mean Reduction (cm³)	p-value	95% CI (cm³)
2.5	<i>0 to 8-18</i>	18.96	4.03	0.071	-0.46 to +8.51
	<i>0 to 36-50</i>	28.98	8.98	0.067	-18.78 to +0.83
	<i>0 to 66</i>	53.22	18.19	0.004	-30.11 to -6.26
3.0	<i>0 to 8-18</i>	25.54	4.47	0.072	-0.47 to +8.69
	<i>0 to 36-50</i>	38.29	10.08	0.013	-18.60 to -1.54
	<i>0 to 66</i>	63.68	18.98	0.007	-32.86 to -5.08
3.5	<i>0 to 8-18</i>	25.92	3.81	0.073	-0.48 to +8.1
	<i>0 to 36-50</i>	44.23	10.65	0.01	-19.07 to -2.22
	<i>0 to 66</i>	67.97	18.64	0.009	-32.86 to -4.41
4.0	<i>0 to 8-18</i>	26.39	3.51	0.101	-0.88 to +7.9
	<i>0 to 36-50</i>	46.23	10.38	0.011	-18.76 to -1.98
	<i>0 to 66</i>	67.05	17.41	0.01	-31.22 to -3.61

Figure 4.4a illustrates the pre-treatment volume delineated by the SUVCO threshold of 2.5bwg/ml for patient 6 in green (t1) using the PETVCAR software. This volume is located inside the green boundary box. Also, the LN regions (t2 to 4), and the reference region (Ref) for the background SUV are delineated in red. Figure 4.4b illustrates the corresponding coronal CT image.

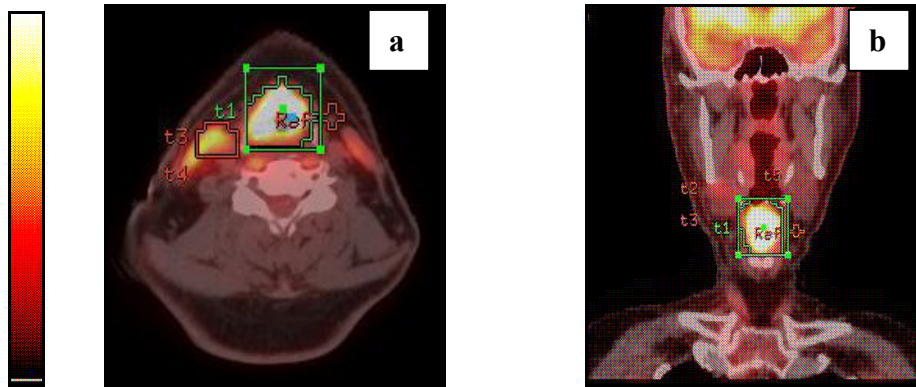


Figure 4.4a and b: The pre-treatment primary functional volume defined by the SUV Cut Off threshold of 2.5bwg/ml for patient 6. a) Axial fused CT-PET, and b) the coronal CT-PET image

The reduction in the primary FV during treatment is shown in figures 4.5a to d. Figure 4.5a illustrates the pre-treatment ^{18}F FDG primary FV delineated at 3.5bwg/ml on the CT-PET axial image (primary volume delineated in green (t1) surrounded by a green boundary box) in patient 6. Similarly, the LN regions (t3-4), and reference ROI (Ref) are delineated in red. Figure 4.5b, c, and d show this at 18Gy, 40Gy, and 66Gy respectively. There is also a reduction in the intensity of ^{18}F FDG uptake in the defined ROI during treatment compared to the pre-treatment level.

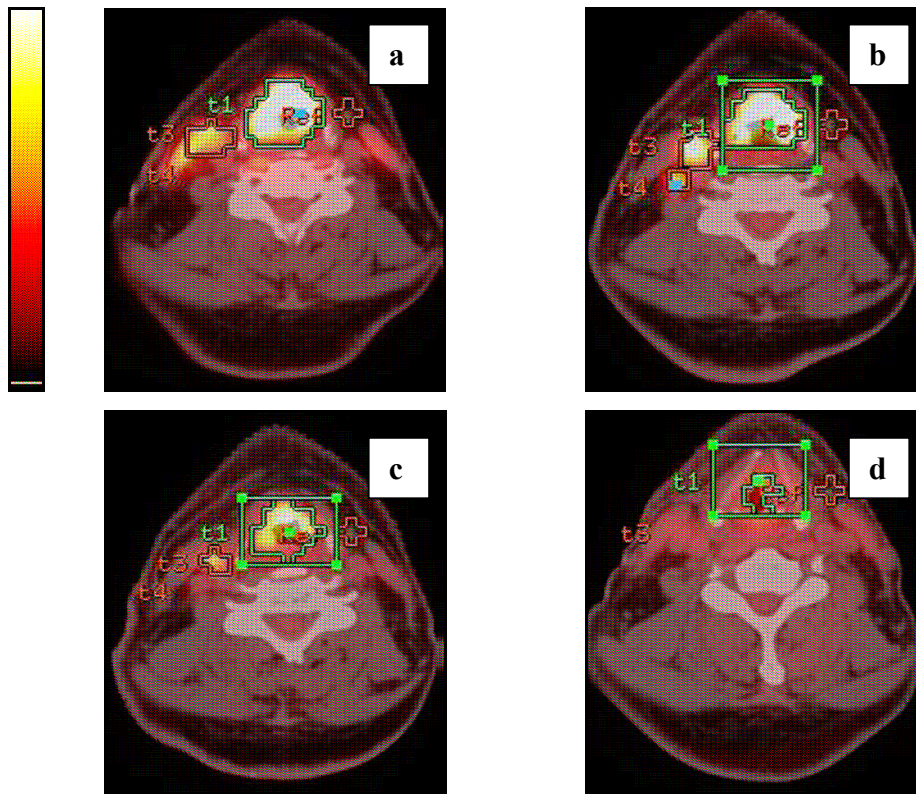


Figure 4.5a to d: The CT-PET primary functional volume for patient 6 defined by the 3.5bwg/ml SUV Cut Off threshold at 0Gy a), 18Gy b), 40Gy c), and 66Gy

This reduction in the primary FV was confirmed by a significant negative correlation with the radiation dose for the SUVCO thresholds of 3.0, 3.5, and 4.0bwg/ml. This negative correlation was greatest for the primary FV defined by the SUVCO threshold of 4.0bwg/ml (p-value 0.008, correlation co-efficient -0.468, 95% CI -0.71 to -0.14cm³), and this has been illustrated as an example in figure 4.6. The line of best fit is in green. Each circle on the graph represents a separate primary FV at each imaging point. The significance values for the other thresholds are indicated in table 1 Appendix 1, as well as the graphs in Appendix 2 (figure 1a to c).

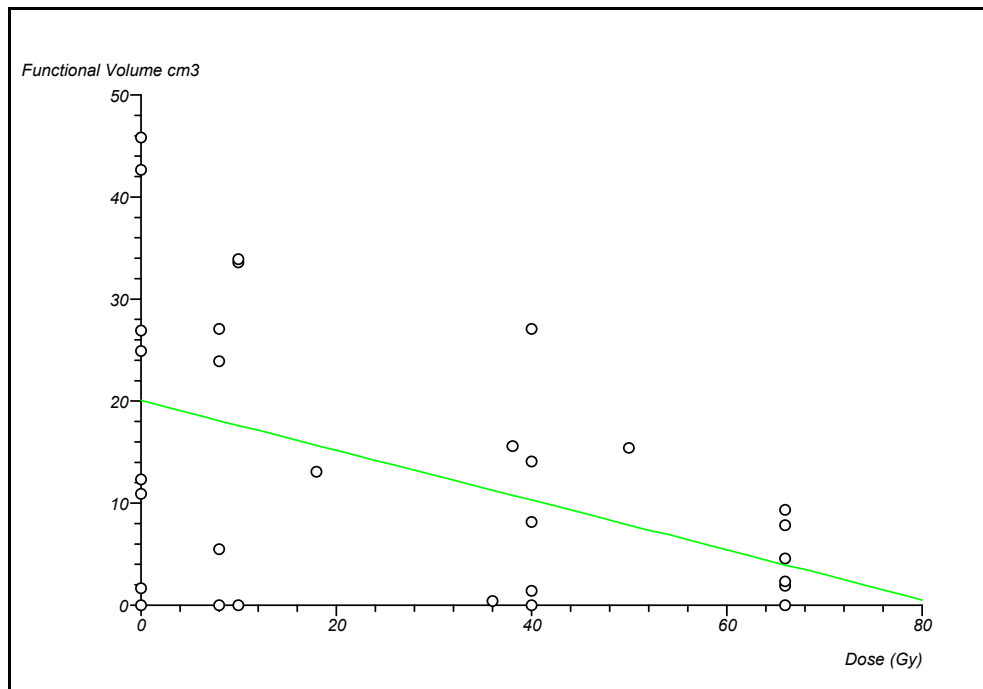


Figure 4.6: The negative correlation between the radiation dose and the primary functional volume delineated by the 4.0bwg/ml SUV Cut Off threshold

The theoretical radiation dose required to reduce the primary FV to zero was calculated from the slope of the line to potentially guide future dose escalation studies. The equation used for the primary FV defined by the SUVCO threshold of 4.0bwg/ml is indicated as an example. The equations for the other thresholds are documented in Appendix 3 (Equations 1 to 3).

SUV Cut Off 4.0bwg/ml: $FV (cm^3) = -0.244Dose(Gy) + 20.056$

The calculated doses required for possible dose escalation studies from these equations would be: 152Gy for the primary FV delineated by the 2.5bwg/ml threshold, 110Gy for the 3.0bwg/ml, 92Gy for the 3.5bwg/ml, and 84Gy for the 4.0bwg/ml thresholded primary FV.

4.3.3.1.2 Percentage of the SUVmax

The mean primary FV delineated by the PTSUVmax and the corresponding SEM is illustrated in table 4.7. Figure 4.7 illustrates these values as a histogram. Most strikingly, these delineated volumes increase, especially at 66Gy.

Table 4.7: The mean and standard error of the mean for the delineated primary functional volumes by the percentage threshold of the SUVmax method

Percentage Threshold of the SUVmax (%)		Functional Volume (cm ³)			
		0Gy	8 to 18Gy	36 to 50Gy	66Gy
30	Mean	23.55	24.13	27.64	55.51
	SEM	5.17	4.70	6.45	16.14
35	Mean	19.16	20.15	20.93	44.74
	SEM	4.26	4.07	4.95	13.07
40	Mean	16.18	16.76	15.16	35.04
	SEM	3.51	3.47	3.00	10.00
45	Mean	13.41	13.61	11.58	28.36
	SEM	2.85	2.75	2.07	8.32
50	Mean	10.95	10.94	8.44	21.44
	SEM	2.49	2.20	1.54	6.17

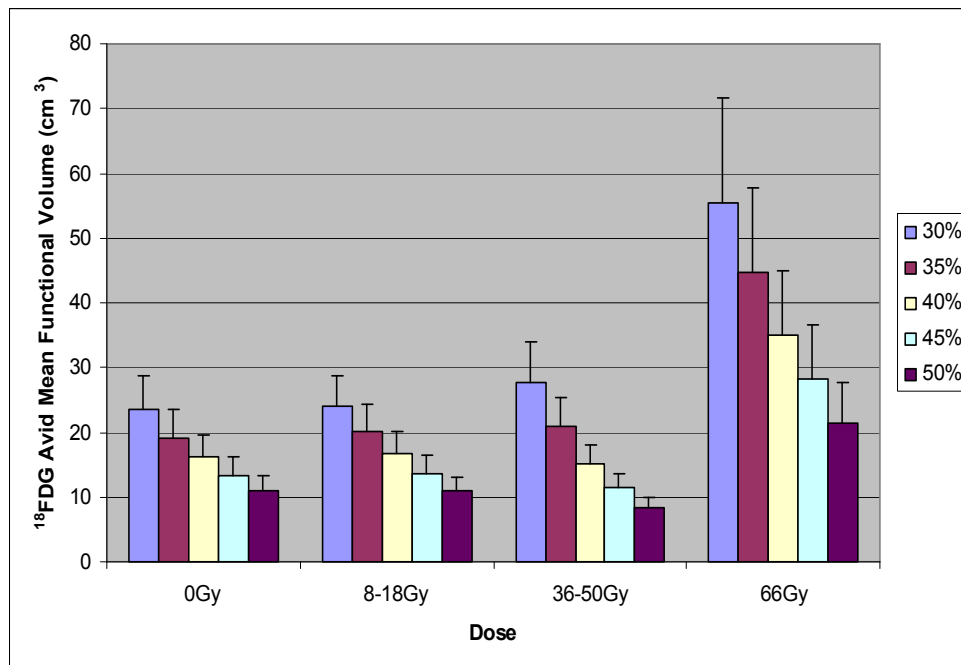


Figure 4.7: The mean ¹⁸F-FDG defined primary functional volume by the percentage of the SUVmax method

Table 4.8 indicates the highly significant reduction in the primary FV at each imaging point between 30 and 35%, 30 and 40%, 30 and 45%, and 30 and 50%. This was most significant at 0 and 36 to 50Gy.

Table 4.8: The mean percentage, actual reduction, p-values, and 95% confidence intervals for the primary functional volume delineated by the percentage of the SUVmax method at each imaging point

Percentage Threshold of the SUVmax (%)	Imaging Point (Gy)	Mean Percentage Reduction	Mean Reduction (cm³)	p-value	95% CI (cm³)
30 to 35	<i>0</i>	18.63	4.39	0.001	1.97 - 6.86
	<i>8 to 18</i>	6.48	3.98	0.001	1.83 - 6.12
	<i>36 to 50</i>	24.24	6.70	0.008	1.70 - 11.70
	<i>66</i>	9.89	9.50	0.029	0.45 - 19.45
30 to 40	<i>0</i>	25.52	7.36	0.003	2.86 - 11.86
	<i>8 to 18</i>	26.05	7.36	0.002	3.12 - 11.61
	<i>36 to 50</i>	25.39	12.48	0.007	3.25 - 21.69
	<i>66</i>	30.67	18.0	0.022	0.68 - 35.31
30 to 45	<i>0</i>	40.08	10.14	0.003	3.92 - 16.34
	<i>8 to 18</i>	36.20	10.51	0.001	5.00 - 16.03
	<i>36 to 50</i>	35.20	16.06	0.006	4.88 - 27.24
	<i>66</i>	39.75	23.87	0.017	2.27 - 45.48
30 to 50	<i>0</i>	51.38	12.60	0.002	5.48 - 19.72
	<i>8 to 18</i>	46.53	13.19	0.001	6.52 - 19.86
	<i>36 to 50</i>	43.81	19.15	0.005	6.24 - 32.06
	<i>66</i>	50.71	29.94	0.015	3.70 - 56.17

Unlike the primary FV delineated by the SUVCO thresholds, there was no significant reduction in volume at 8 to 18Gy, 36 to 50Gy and 60Gy when compared to the pre-treatment volume, which is indicated in table 4.9.

There was an increase in the mean primary FV delineated by the 30 to 45% of the SUVmax threshold between 0 to 18Gy, and in all thresholds between 36 to 50Gy and 66Gy when compared to the pre-treatment FV. However, this increase was not significant.

The largest increase was by 152.65% at the 50% of the SUVmax threshold. The increase between these two dose points was between 108.68% and 144.98% from 30% to 45% of the SUVmax threshold.

When the percentage change was reviewed throughout the entire radiation dose the volume increased between 35.73% and 133.49%. The increase was the greatest (133.49%) at the 35% of the SUVmax threshold.

Table 4.9: The mean percentage, actual change, p-values and 95% confidence intervals for the primary functional volumes delineated by the percentage of the SUVmax threshold between each imaging point

Percentage Threshold of the SUVmax (%)	Compared Imaging Points (Gy)	Mean Percentage Change	Mean Change (cm³)	p-value	95% CI (cm³)
30	<i>0 to 8-18</i>	+2.44	+0.58	0.414	-6.67 to +5.52
	<i>0 to 36-50</i>	+17.35	+4.09	0.211	-7.26 to +15.44
	<i>0 to 66</i>	+35.73	+25.53	0.065	-9.76 to +60.82
35	<i>0 to 8-18</i>	+5.16	+0.99	0.355	-7.06 to +5.08
	<i>0 to 36-50</i>	+9.26	+1.78	0.321	-6.88 to +10.43
	<i>0 to 66</i>	+133.49	+20.41	0.071	-8.79 to +49.61

40	<i>0 to 8-18</i>	+3.54	+0.58	0.401	-5.81 to +4.66
	<i>0 to 36-50</i>	-6.34	-1.03	0.334	-6.43 to +4.38
	<i>0 to 66</i>	+116.48	+14.89	0.078	-7.29 to +37.07
45	<i>0 to 8-18</i>	+1.49	+0.20	0.453	-4.05 to +3.65
	<i>0 to 36-50</i>	-13.70	-1.837	0.165	-6.00 to +2.33
	<i>0 to 66</i>	+111.43	+11.79	0.091	-7.01 to +30.58
50	<i>0 to 8-18</i>	-0.12	+0.01	0.496	-3.17 to +3.20
	<i>0 to 36-50</i>	-22.49	-2.462	0.075	-6.06 to +1.139
	<i>0 to 66</i>	+95.82	+8.19	0.101	-5.59 to 21.96

Figure 4.8 a to d illustrates the primary FV in patient 6 at the 30% of the SUVmax threshold on the axial CT-PET fused images. The FV is delineated in green (t1), and in figures b and c the green boundary box is visualised. The LN FVs (t3 and 4), and the reference region (Ref) are delineated in red. Figure 4.8a contours the primary FV at 0Gy, b) at 18Gy, c) at 40Gy, and d) at 66Gy.

With increasing radiation dose, the intensity of the ¹⁸FDG uptake within the primary region has reduced especially at 66Gy, but the defined volume is visibly larger and virtually encompasses the entire boundary box. This is especially evident when compared to the reduction in the primary FV delineated by the SUVCO method in figure 4.5a to d.

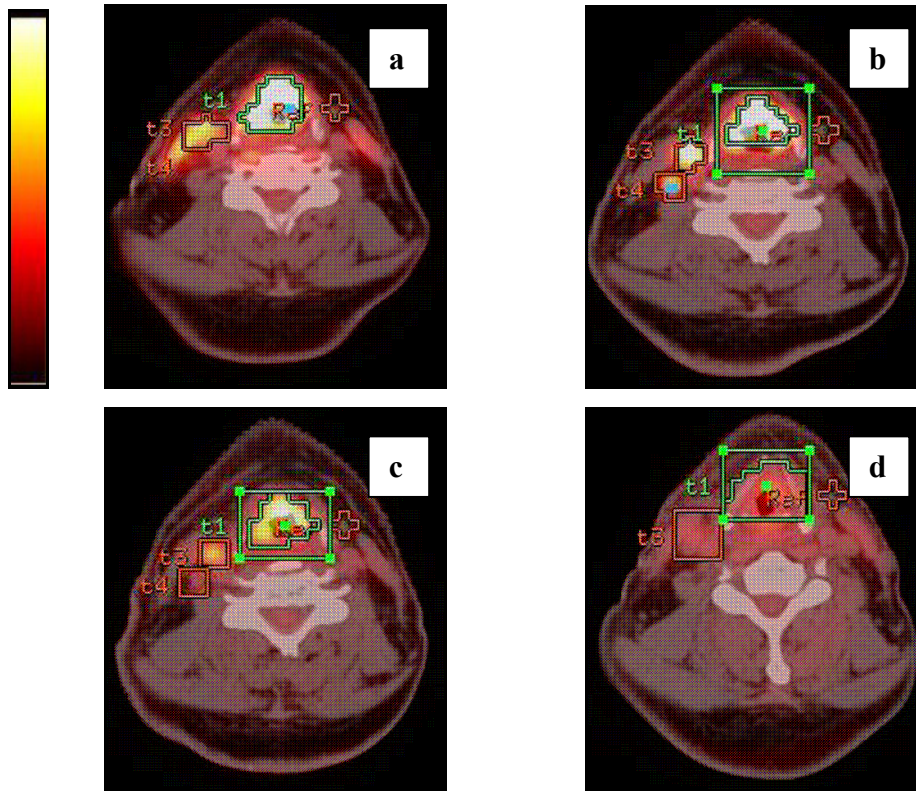


Figure 4.8a to d: The ^{18}F FDG primary functional volume delineated by the 30% of the SUVmax threshold in patient 6 at 0Gy a), 18Gy b), 40Gy c), and 66Gy d)

The SLR model confirmed there was no correlation between the primary FV delineated by the SUVmax threshold and the radiation dose. The line of best fit suggested a trend towards a positive correlation, and this is illustrated for the 30% threshold of the SUVmax in figure 4.9. Graphs for other thresholds are in figure 2a to d Appendix 2.

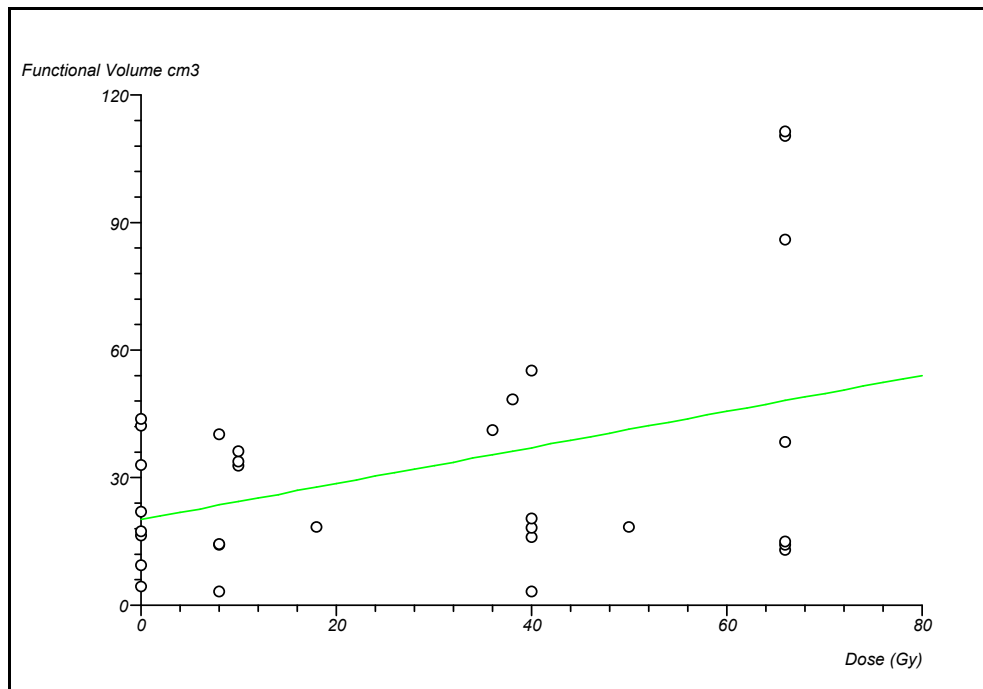


Figure 4.9: Simple linear regression between the radiation dose and the primary functional volume delineated by the 30% of the SUVmax threshold

The theoretical dose required to reduce the delineated primary FV by this method has been calculated for each percentage of the SUVmax threshold. The equation used for the 30% threshold is shown. This illustrates the increase in the FV with each increase in radiation dose. For example, at 66Gy the FV delineated at this 30% threshold of the SUVmax would be 44.01cm³, and at 80Gy this volume would theoretically increase to 48.91cm³, which equates to a 10.02% increase in volume.

30% of the SUVmax:
$$FV (cm^3) = 0.350Dose(Gy) + 20.913$$

However, at the 50% of the SUVmax threshold, this was less evident. For example this theoretical FV would be 16.09cm³ at 66Gy, and 17.50cm³, and equals an 8.06% increase in volume.

The equations for the other percentage of the SUVmax delineation thresholds are in Appendix 3 (Equations 4 to 7).

4.3.3.1.3 Individualised Adaptive Threshold

The mean pre-treatment FV was 23.82cm^3 (SE of mean 6.72cm^3). At 8 to 18Gy, this had reduced to 18.46cm^3 (SE of mean 5.73cm^3), and at 36 to 50Gy the volume had further reduced to 14.63cm^3 (SE of mean 6.41cm^3). However at 66Gy this volume had increased to 20.52cm^3 (SE of mean 15.92cm^3). This is illustrated in the histogram in figure 4.10.

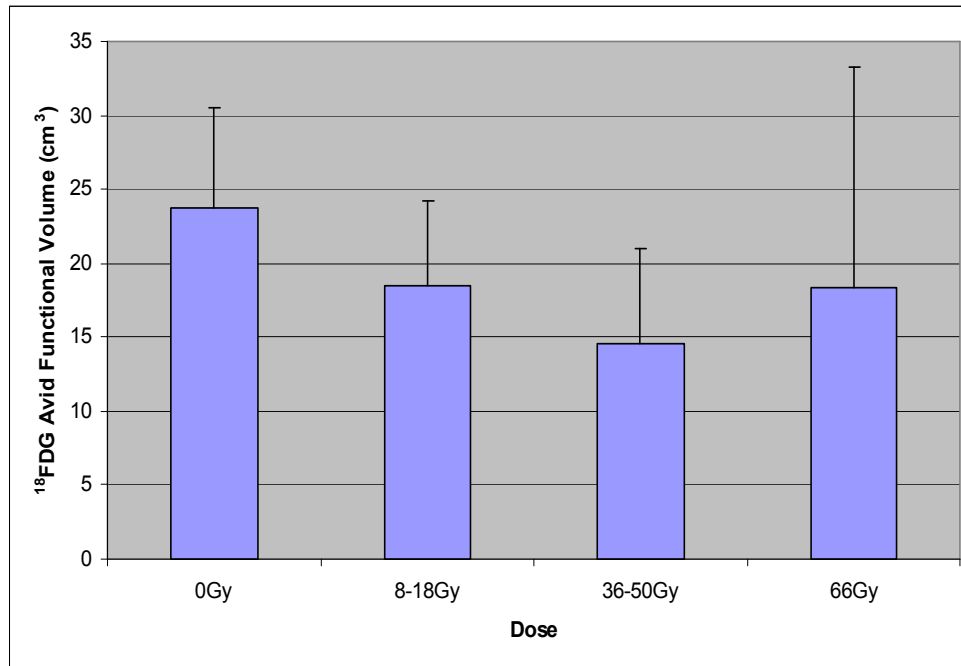


Figure 4.10: The mean ^{18}F FDG primary functional volume delineated by the individualised adaptive threshold

There was no significant difference in the primary FV delineated by the IAT method between 8 to 18Gy, 36 to 50Gy, and 66Gy when compared to the pre-treatment volume.

The mean absolute reduction was 5.35cm^3 at 8 to 18Gy, and the mean percentage reduction was 22.46% compared to the pre-treatment volume. At 36 to 50Gy, the absolute reduction was 9.19cm^3 , and the percentage reduction was 38.58%. However at 66Gy the mean reduction was 5.86cm^3 , and the mean percentage change was 22.83% when compared to the 0Gy volume, even though the data illustrates an increase in volume. This is due to the large volume changes across

data. The range of FVs at 0Gy was 4.4 to 60.2cm³, compared to 0 to 122.2cm³ at 66Gy.

This was confirmed by no significant correlation between the delineated FV and radiation dose (p-value 0.65, correlation co-efficient -0.083, 95% CI for the co-efficient -0.42 to 0.27cm³), which is illustrated in figure 3 of Appendix 2.

The theoretical dose required in escalation studies increased in a similar manner to that by the PTSUVmax.

Individualised Adaptive Threshold:

$$FV = 0.0786Dose(Gy) + 21.108$$

The theoretical FV at 66Gy was 26.29cm³, and at 80Gy was 27.39 cm³, and equalled a 4.01% increase between these dose points.

4.3.3.2 Lymph Node Functional Volumes

4.3.3.2.1 SUV Cut Off

The median LN FV and the corresponding SEM delineated by the SUVCO method are illustrated in table 4.10.

The box and whisker plot in figure 4.11 illustrates the median delineated LN FV by the 2.5bwg/ml SUVCO threshold. The box represents the 25th to the 75th centile. The colour change from teal to grey represents the median value of the data. The range of the data points is indicated by the error bars at either end of the box plot on the graph.

Table 4.10: The median and inter-quartile range for the lymph node functional volumes delineated by the SUV Cut Off thresholds

SUV Cut Off Threshold (bwg/ml)		Functional Volume (cm ³)			
		0Gy	8 to 18Gy	36 to 50Gy	66Gy
2.5	Median	2.65	1.15	0.40	0.00
	IQR	9.00	7.50	4.40	0.70
3.0	Median	1.70	0.40	0.05	0.00
	IQR	7.60	5.70	3.00	0.10
3.5	Median	1.20	0.10	0.00	0.00
	IQR	6.50	4.90	1.90	0.00
4.0	Median	0.80	0.05	0.00	0.00
	IQR	5.60	4.30	1.10	0.00

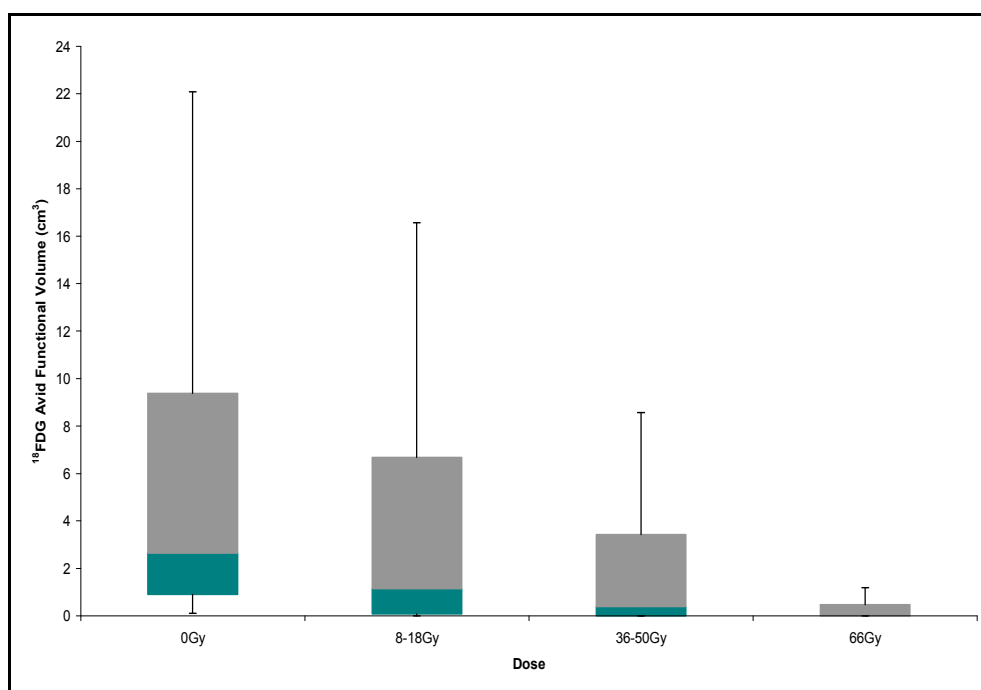


Figure 4.11: The median ¹⁸F-FDG lymph node functional volume delineated by the 2.5bwg/ml SUV Cut Off threshold

The box and whisker plots for the LN FV delineated by the 3.0, 3.5 and 4.0bwg/ml thresholds are illustrated in figures 4a to c of Appendix 2.

Similar to the primary FV delineated by this method, there was a significant reduction between thresholds at each imaging point when compared to the volume defined by the 2.5bwg/ml threshold, and at 36 to 50Gy, and 66Gy when compared to the FV defined at 0Gy by each threshold.

There was a highly significant reduction at each imaging point between the SUVCO thresholds of 2.5 to 3.0bwg/ml, 2.5 to 3.5bwg/ml, and 2.5 to 4.0bwg/ml ($p < 0.0001$ to 0.007 , median reduction 0.20 to 1.90cm^3 , 95% CI 0.00 to 3.90cm^3). At 66Gy, the percentage reduction could not be calculated between the thresholds because the median FV was zero when delineated by the 2.5bwg/ml threshold. Table 3 in Appendix 1 indicates these results in full.

There was no significant volume change between 0Gy and 8 to 18Gy for all the SUVCO thresholds investigated. However between 0Gy and 36 to 50Gy ($p < 0.0001$, median reduction 1.85 to 3.50cm^3 , 95% CI 0.25 to 5.90cm^3) and 0Gy and 66Gy ($p < 0.0002$, median reduction 2.00 to 3.53cm^3 , 95% CI 0.25 to 57.05cm^3) there was a highly significant reduction at each threshold. This was greatest at 66Gy for the 3.0bwg/ml SUVCO threshold. Table 4 in Appendix 1 indicates these results in full.

Figure 4.12a to d shows the fused CT-PET axial images of patient 6 at the SUVCO threshold of 3.5bwg/ml. The most representative slice of the second LN FV is delineated in green (t3). The reference region (Ref) and two other FVs present on these images (the primary (t1) and another LN (t4)) are delineated in red. The images represent the FVs at the doses of 0Gy a), 18Gy b), 40Gy c), and 66Gy d). The reduction in volume and ^{18}F FDG avidity with each increase in radiation dose is visualised and reflects that seen in the primary FV delineated by this method in figure 4.5 a to d.

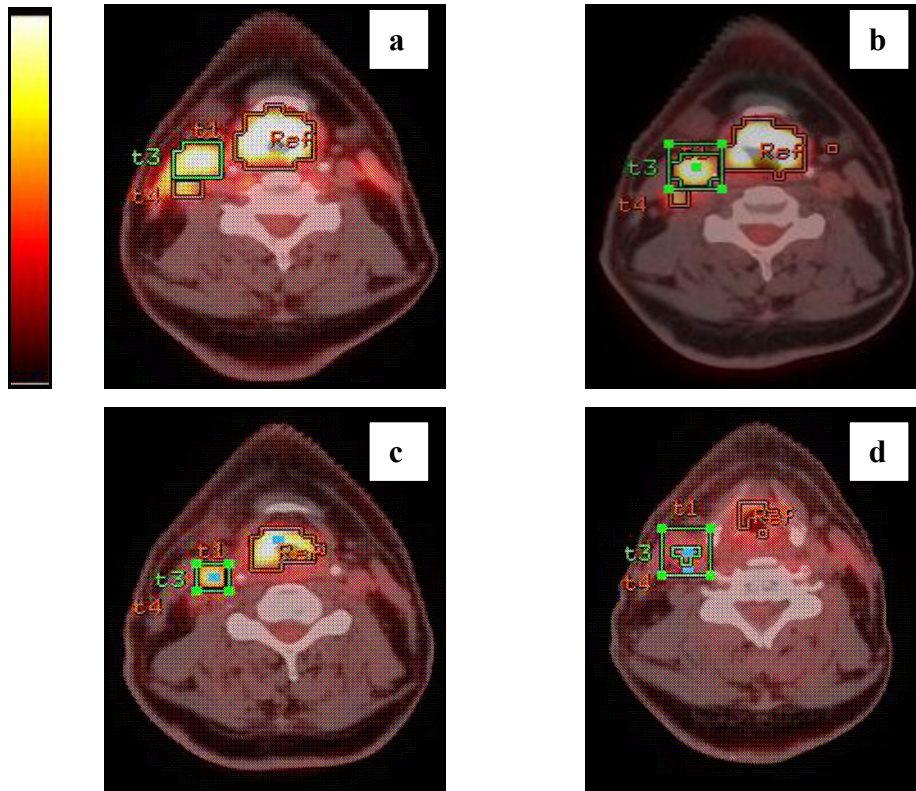


Figure 4.12a to d: The ^{18}F FDG lymph node functional volume delineated by the SUV Cut Off threshold of 3.5bwg/ml in patient 6 at 0Gy a), 10Gy b), 40Gy c), and 66Gy

The FV reduction was confirmed by a significant negative correlation between the radiation dose and delineated LN volume at each SUVCO threshold. This was most significant for the SUVCO threshold of 3.0bwg/ml (p-value 0.009, correlation co-efficient -0.291, 95% CI -0.48 to -0.08cm³). However the correlation co-efficients were less than those for the primary FV delineated by the same thresholds. The correlation co-efficient values for the other thresholds are in table 5 of Appendix 1, and graphs in figure 5a to d in Appendix 2.

An example of the equation used to calculate the theoretical dose required to eradicate the LN FV delineated by each SUVCO threshold is shown. Equations 8 to 10 in Appendix 3 illustrate the others.

SUV Cut Off 3.0bwg/ml: $\text{FV (cm}^3\text{)} = -0.089\text{Dose(Gy)} + 5.473$

The potential doses required for this are lower than those for the primary FV delineated by this method. These are 68Gy for the FV delineated by the SUVCO threshold of 2.5bwg/ml, 62Gy for 3.0bwg/ml, 60Gy for 3.5bwg/ml, and 58Gy for LN FVs delineated by the 4.0bwg/ml threshold.

There was a 55.26% reduction in dose required to reduce the LN FV to zero compared to the primary FV to zero at the SUVCO threshold of 2.5bwg/ml. This reduction was 43.64%, 34.78%, and 30.95%, at the respective thresholds of 3.0, 3.5, and 4.0bwg/ml.

4.3.3.2.2 Percentage of the SUVmax

The median LN FV delineated at each PTSUVmax, and the corresponding IQR are shown in table 4.11. These values increase for all delineation thresholds after 36Gy. This pattern was also exhibited by the primary FV delineated by this method.

Table 4.11: The median and inter-quartile range for the lymph node functional volumes delineated by the percentage thresholds of the SUVmax

Percentage Threshold of the SUVmax (%)		Functional Volume (cm ³)			
		0Gy	8 to 18Gy	36 to 50Gy	66Gy
30	Median	4.25	4.40	4.50	4.50
	IQR	5.90	4.80	6.40	4.30
35	Median	4.20	3.60	4.45	4.50
	IQR	4.70	4.30	4.10	4.30
40	Median	3.80	3.25	4.00	4.40
	IQR	5.00	3.50	3.70	2.60
45	Median	3.10	2.90	3.35	3.90
	IQR	4.70	2.90	2.90	2.20
50	Median	2.70	2.60	3.00	3.40
	IQR	4.10	2.30	1.80	2.30

Figure 4.13 illustrates an example of the box and whisker plot for the LN FV delineated by the 45% of the SUVmax threshold. Figure 6a to d in Appendix 2 illustrates these graphs for the remaining thresholds.

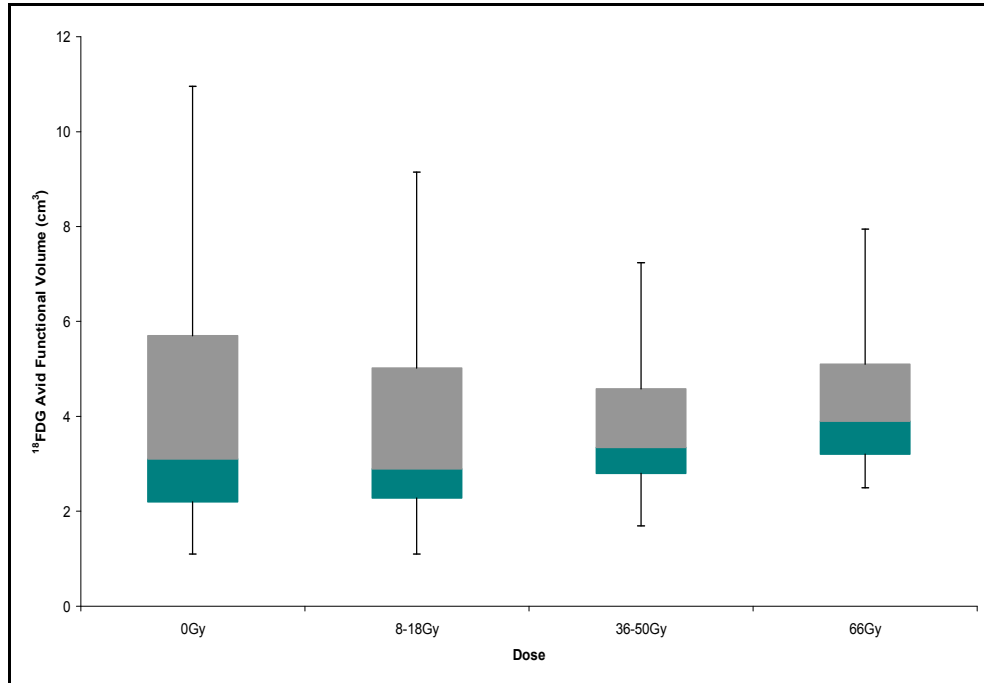


Figure 4.13: The median ^{18}F FDG lymph node functional volume delineated by the 45% threshold of the SUVmax

There was no significant reduction in the FV at each imaging point between the 30% and 35% threshold. However, there was a highly significant FV reduction at each imaging point between the 40%, 45%, and 50% when compared to the volume defined by the 30% of the SUVmax threshold ($p < 0.0001$, median reduction 0.40 to 2.63cm³, 95% CI 0.50 to 5.70cm³). Table 6 in Appendix 1 indicates these results in full.

There was no significant difference in the FV at 8 to 18Gy, 36 to 50Gy, and 66Gy compared to the pre-treatment volume at each threshold. Table 7 in Appendix 1 indicates these results in full.

Figure 4.14a to d illustrates the delineated LN at 30% of the SUVmax in green (t3). The primary site (t1) and the reference region (Ref) are delineated in red at 0Gy a), 10Gy b), 40Gy c), and 66Gy d) for patient 6. The FV reduced in size

between 0Gy and 40Gy (Figures 4.14a to c). At 66Gy, although the intensity of ^{18}F FDG uptake was reduced, the volume had increased compared to the 40Gy image. In this figure 4.14d this LN FV has been defined as the entire boundary box. This was similar to the change in the primary FV delineated by this method in figure 4.8 a to d, and different to the LN FV defined by the SUVCO threshold in figure 4.12 a to d.

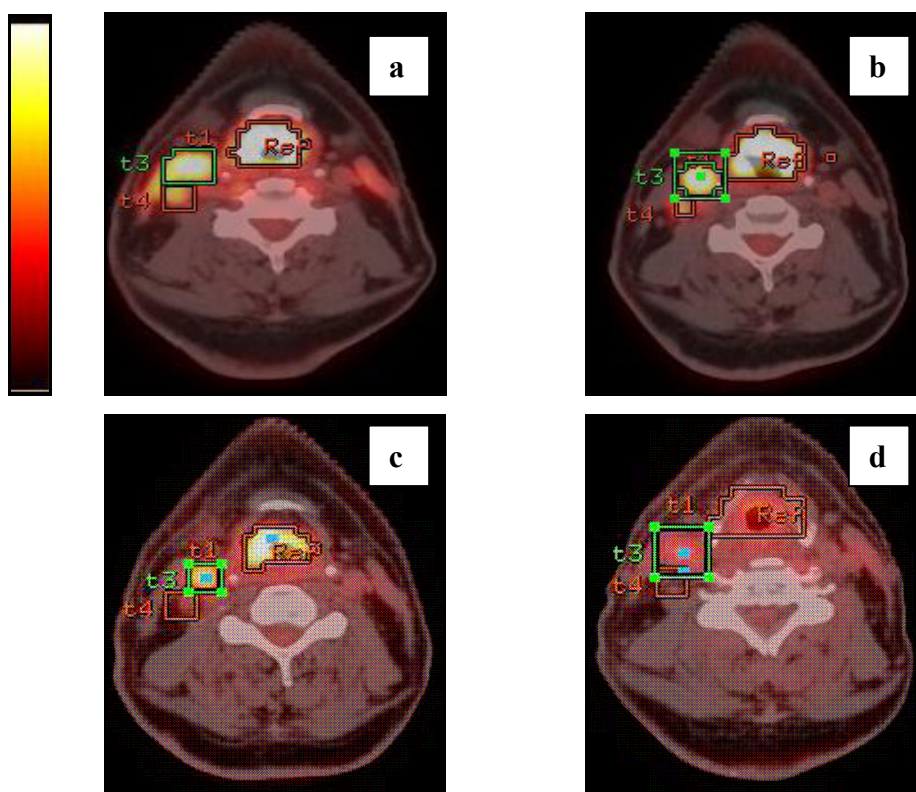


Figure 4.14a to d: The ^{18}F FDG lymph node functional volume delineated by the 30% of the SUVmax threshold in patient 6 at 0Gy a), 10Gy b), 40Gy c), and 66Gy d)

The lack of volume change with radiation dose was confirmed by no significant correlation on SLR modelling when the LN FV was defined by the PTSUVmax method. Table 8 in Appendix 1 documents the statistical results, with a trend towards a positive correlation co-efficient. Figure 7a to e in Appendix 2 illustrates this in graphical form.

The theoretical LN FV calculated from this model increased with radiation dose. An example of this increase is shown and the remaining equations are in Appendix 3 (Equations 11 to 14).

30% of the SUVmax:
$$FV (cm^3) = 0.034Dose(Gy) + 9.046$$

Similarly, the theoretical FV at 66Gy was $11.29cm^3$ and at 80Gy this was $11.76cm^3$. This equalled a 3.99% increase between these points. The theoretical LN FV delineated by the 50% threshold of the SUVmax at 66Gy was $6.05cm^3$, and at 80Gy this was $6.37cm^3$. This equalled a 5.01% increase between these points

4.3.3.2.3 Individualised Adaptive Threshold

Figure 4.15 illustrates the median LN FV delineated by the IAT method as a box and whisker plot graph. At 0Gy the median volume was $2.50cm^3$ (IQR $4.90cm^3$). This reduced to $2.15cm^3$ (IQR $3.20cm^3$) at 8 to 18Gy, $0.95cm^3$ (IQR $2.20cm^3$) at 36 to 50Gy, and $0.05cm^3$ (IQR $1.90cm^3$) at 66Gy.

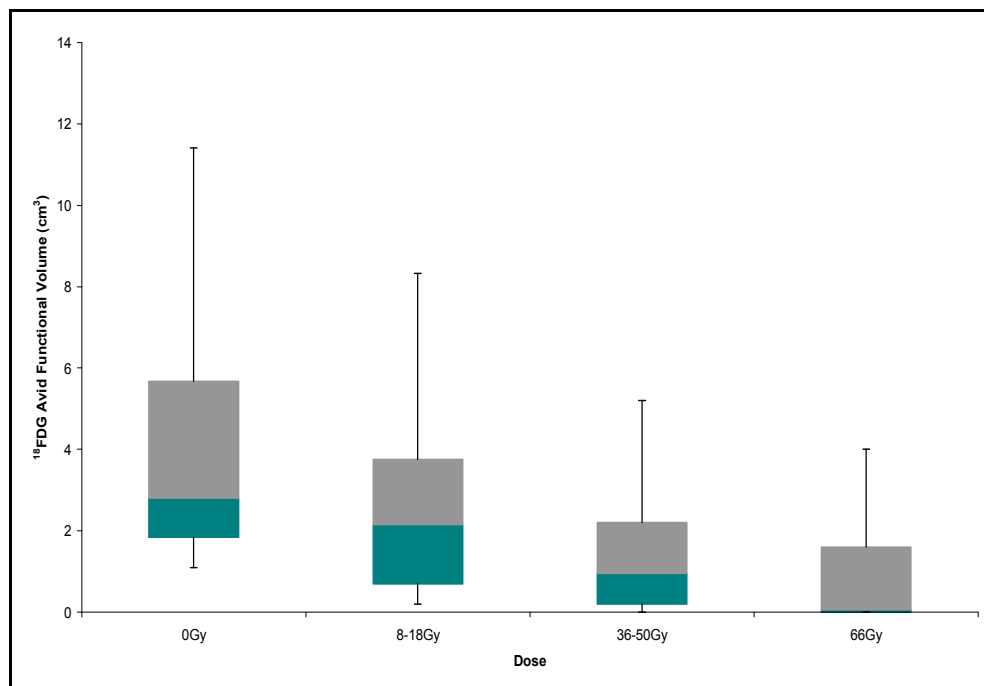


Figure 4.15: The median ^{18}F FDG lymph node functional volume delineated by the individualised adaptive threshold

The absolute median difference at 8 to 18Gy compared to 0Gy was $+1.23\text{cm}^3$ (p-value 0.996, 95% CI $+0.35$ to $+2.55\text{cm}^3$), and the percentage difference was 14%. At 36 to 50Gy the LN FV significantly reduced by -2.15cm^3 (p-value 0.0005, 95% CI -3.95 to -1.05cm^3), which equalled a 62% reduction. Finally between 66Gy and 0Gy there was a further significant reduction of -3.40cm^3 (p-value <0.0001 , 95% CI -6.6 to -1.55cm^3), which equated to a 98% reduction in volume.

Similar to the primary FV delineated by this method, there was no correlation between the defined LN FV and radiation dose (p-value 0.501, correlation coefficient -0.076 , 95% CI -0.291 to $+0.145\text{cm}^3$).

The theoretical dose required to reduce the LN FV to 0cm^3 from the line of the slope was 128Gy.

Individualised Adaptive Threshold: $\text{FV} = -0.179\text{Dose}(\text{Gy}) + 22.902$

4.3.4 The SUVmax within the Functional Volume

4.3.4.1 SUVmax within the Primary Functional Volume

4.3.4.1.1 SUV Cut Off

Table 4.12 indicates the mean SUVmax and the SEM within the primary FV delineated by the SUVCO method. This is further illustrated by the histogram in figure 4.16. The pre-treatment SUVmax was identical in the primary FV delineated by all the SUVCO thresholds.

Table 4.12: The mean and standard error of the mean for the SUVmax within the primary functional volume delineated by the SUV Cut Off thresholds

SUV Cut Off Threshold (bwg/ml)		SUVmax (bwg/ml)			
		0Gy	8 to 18Gy	36 to 50Gy	66Gy
2.5	Mean	12.38	10.57	7.71	5.75
	SEM	2.33	2.13	1.19	0.94
3.0	Mean	12.38	10.57	7.35	5.41
	SEM	2.33	1.14	0.76	0.60
3.5	Mean	12.38	10.18	7.35	5.41
	SEM	2.33	2.35	1.42	1.13
4.0	Mean	12.38	9.71	7.35	4.93
	SEM	2.33	2.57	1.42	1.31

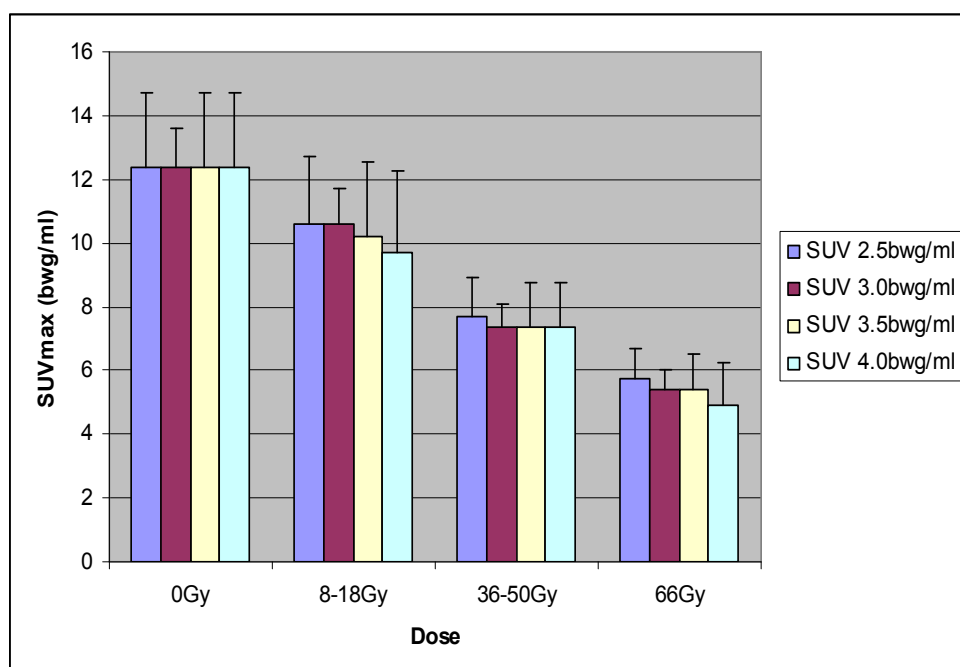


Figure 4.16: The SUVmax within the primary functional volume delineated by the SUV Cut Off thresholds

Table 4.13 shows the mean difference in the SUVmax within the primary FV delineated by the 3.0, 3.5, and 4.0bwg/ml compared to the 2.5bwg/ml threshold at each imaging point. The SUVmax reduced by 0.0 and 14.14% between the imaging points. The CI could not be calculated at 0Gy because there was no difference in the values and a star in the table indicates this.

Table 4.13: The mean percentage, actual reduction, p-values, and 95% confidence intervals for the SUVmax within the primary functional volume delineated by the SUV Cut Off thresholds at each imaging point

SUV Cut Off Threshold (bwg/ml)	Imaging Point (Gy)	Mean Percentage Reduction	Mean Reduction (bwg/ml)	p-value	95% CI (bwg/ml)
2.5 to 3.0	<i>0</i>	*	*	*	*
	<i>8 to 18</i>	0.00	+1.81	0.100	-1.19 to +4.81
	<i>36 to 50</i>	-4.37	+0.34	0.180	-0.46 to +1.14
	<i>66</i>	-5.89	+0.34	0.180	-0.46 to +1.14
2.5 to 3.5	<i>0</i>	*	*	*	*
	<i>8 to 18</i>	-3.67	-2.68	0.061	-1.19 to +4.81
	<i>36 to 50</i>	-4.37	-0.34	0.175	-1.14 to + 0.46
	<i>66</i>	-5.88	-0.34	0.175	-1.14 to + 0.46
2.5 to 4.0	<i>0</i>	*	*	*	*

	<i>8 to 18</i>	-8.13	-2.68	0.190	-9.43 to +4.08
	<i>36 to 50</i>	-4.37	-0.34	0.175	-1.14 to + 0.46
	<i>66</i>	-14.14	-0.34	0.175	-1.14 to + 0.46

Table 4.14 indicates the percentage and absolute mean difference in the SUVmax within the primary FV at each SUVCO threshold between the imaging points of 8 to 18Gy, 36 to 50Gy, and 66Gy compared to the pre-treatment value.

There was no significant reduction in the SUVmax at 8 to 18Gy compared to the pre-treatment value at any threshold investigated. However there was a significant reduction at 36 to 50Gy and 66Gy, compared to the pre-treatment values at all SUVCO thresholds investigated. This was most significant at 36 to 50Gy at the threshold of 3.0 and 3.5bwg/ml.

Table 4.14: The mean percentage, actual reduction, p-values and 95% confidence intervals for the SUVmax within the primary functional volume delineated by the SUV Cut Off thresholds between the imaging points

SUV Cut Off Threshold (bwg/ml)	Compared Imaging Points (Gy)	Mean Percentage Change	Mean change (bwg/ml)	p-value	95% CI (bwg/ml)
2.5	<i>0 to 8-18</i>	-11.97	+1.81	0.098	-1.19 to +4.81
	<i>0 to 36-50</i>	-31.24	-4.68	0.011	-8.42 to -0.93
	<i>0 to 66</i>	-38.31	-6.64	0.013	-12.23 to -1.05

3.0	<i>0 to 8-18</i>	-11.97	+1.81	0.098	-1.19 to +4.81
	<i>0 to 36-50</i>	-41.07	-5.01	0.006	-8.55 to -1.47
	<i>0 to 66</i>	-40.40	-6.98	0.014	-12.93 to -1.02
3.5	<i>0 to 8-18</i>	-18.66	+2.20	0.075	-1.02 to +5.42
	<i>0 to 36-50</i>	-41.07	-5.01	0.006	-8.55 to -1.47
	<i>0 to 66</i>	-40.40	-7.54	0.007	-13.03 to -2.05
4.0	<i>0 to 8-18</i>	-32.23	+2.24	0.071	-0.96 to +5.44
	<i>0 to 36-50</i>	-41.07	-4.58	0.013	-8.40 to -0.75
	<i>0 to 66</i>	-44.06	-7.58	0.011	-13.64 to -1.503

This was confirmed by a significant negative correlation between the radiation dose and the SUVmax within the primary FV. This was most significant at the SUVCO threshold of 3.0bwg/ml (p-value 0.006, correlation co-efficient -0.483, 95% CI -0.72 to -0.16bwg/ml), which is illustrated in figure 4.17. The graphs for the other thresholds are in figure 8a to c of Appendix 2, and the correlation co-efficients in table 9 of Appendix 1.

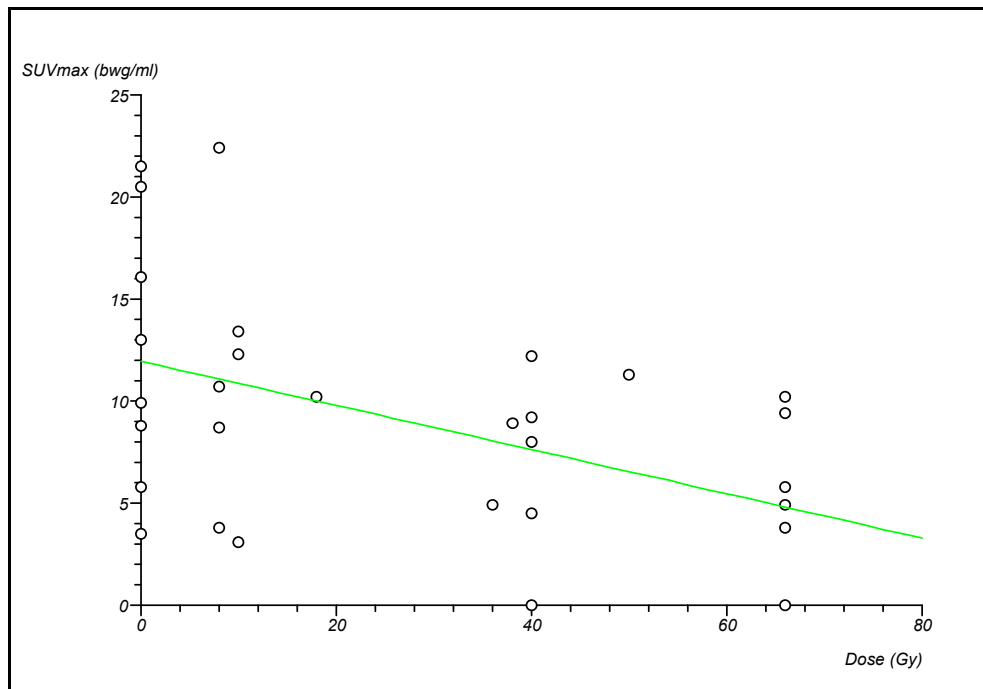


Figure 4.17: Simple linear regression relationship between the SUVmax within the primary functional volume delineated at SUV Cut Off threshold of 3.0bwg/ml and the radiation dose

The theoretical radiation dose required to reduce the SUVmax within the primary FV to zero was also calculated from the SLR model for each threshold. This is shown in the equation below for the SUVCO threshold of 3.0bwg/ml. The other equations are in Appendix 3 (Equations 15 to 17).

SUV Cut Off 3.0bwg/ml:

$$\text{SUVmax (bwg/ml)} = -0.108\text{Dose(Gy)} + 11.952$$

The radiation dose required was 128Gy at the 2.5bwg/ml threshold, and 112Gy, 122Gy, and 120Gy at the 3.0, 3.5, and 4.0bwg/ml thresholds respectively. The dose to reduce the SUVmax within the primary FV to zero when delineated by the SUVCO threshold of 3.0bwg/ml was only 2Gy more than the dose required to reduce the FV itself to zero.

4.3.4.1.2 Percentage Threshold of the SUVmax

The mean SUVmax within the primary FV at 0Gy was identical to that within the FV defined by the SUVCO method at 12.38bwg/ml (SEM 2.33bwg/ml). At 8 to 18Gy, this reduced to 10.57bwg/ml (SEM 2.13bwg/ml). There was a further

reduction at 36 to 50Gy to 7.71bwg/ml (SEM 1.19bwg/ml), and finally to 5.75bwg/ml (SEM 0.94bwg/ml) at 66Gy. A single SUVmax value only was gained for the primary site in each patient, and this was used to calculate the PTSUVmax.

The absolute mean SUVmax at 8 to 18Gy increased by +1.18bwg/ml (p-value 0.098, 95% CI -1.12 to +4.81). At 36 to 50Gy the SUVmax reduced by -5.68bwg/ml (p-value 0.014, 95% CI -10.56 to -0.78), and at 66Gy by -6.64bwg/ml (p-value 0.013, 95% CI -12.23 to -1.05) compared to the pre-treatment value. The reduction in the SUVmax was only significant between at 66Gy, and 36 to 50Gy when compared with the value at 0Gy. This equalled a mean increase of 9.54% at 8 to 18Gy, and a reduction of 45.88%, and 53.63% at 36 to 50Gy, and 66Gy respectively.

Similar to the SUVmax within the primary FV delineated by the SUVCO thresholds, there was a significant negative correlation between the SUVmax within the primary FV delineated by the PTSUVmax method and the radiation dose (p-value 0.007, correlation co-efficient -0.467, 95% CI -0.70 to -0.14bwg/ml).

The theoretical radiation dose required to reduce the SUVmax to zero within the primary FV delineated by the PTSUVMax thresholds was 128Gy.

Percentage of the SUVmax:

$$\text{SUVmax (bwg/ml)} = -0.094\text{Dose(Gy)} + 11.870$$

This is in comparison to the increasing primary FV with increasing radiation dose when defined by this method.

4.3.4.1.3 Individualised Adaptive Threshold

The mean SUVmax within the pre-treatment FV was the same as the other two methods at 12.38bwg/ml (SEM 2.33bwg/ml). This reduced to 10.64bwg/ml (SEM 2.14bwg/ml) at 8 to 18Gy, 7.71bwg/ml (SEM 1.20bwg/ml) at 36 to 50Gy, and 4.66bwg/ml (SEM 1.35bwg/ml) at 66Gy, and is shown in figure 4.18.

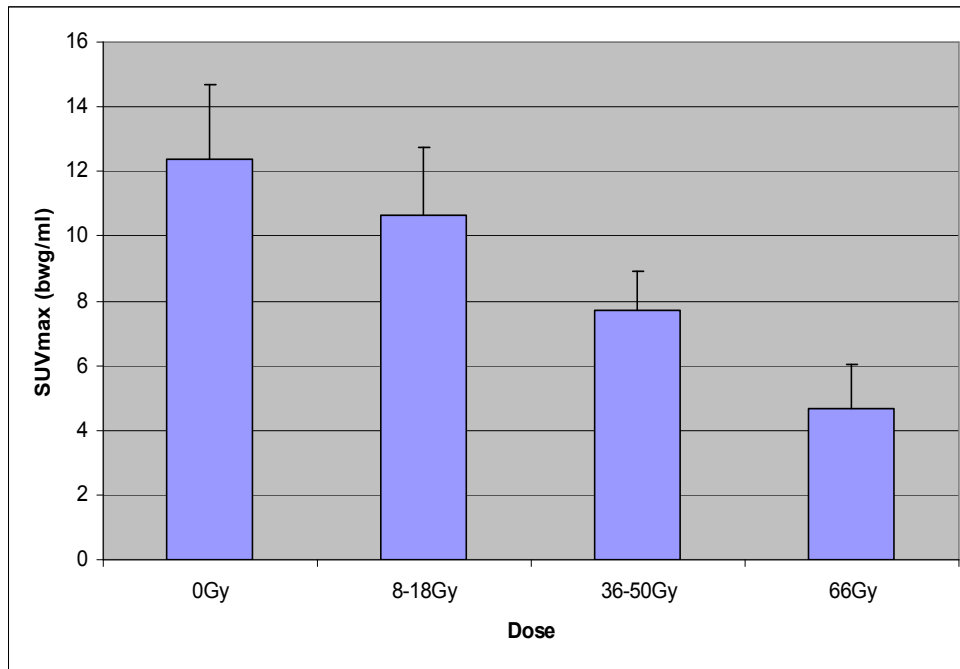


Figure 4.18: The SUVmax within the primary functional volume delineated by the individualised adaptive threshold

The absolute mean difference was -1.75bwg/ml (p-value 0.109, 95% CI -1.31 to +4.82bwg/ml) at 8 to 18Gy compared to the pre-treatment value.

Similar to the other delineation methods, the SUVmax significantly reduced at 36 to 50Gy by -4.66bwg/ml (p-value 0.011, 95% CI -8.42 to -0.94bwg/ml), and 66Gy by -7.73bwg/ml (p-value 0.015, 95% CI -14.49 to -0.96bwg/ml). This equated to a percentage reduction of 11.26% 8 to 18Gy, 31.43% 36 at 50Gy, and 44.81% at 66Gy. The SUVmax values calculated by this method were less than those by the other two methods.

A significant negative correlation was confirmed between the SUVmax within the primary FV and the radiation dose (p-value 0.003, correlation co-efficient -0.508, 95% CI -0.73 to -0.19bwg/ml) shown in figure 4.19. This correlation was greatest compared to the other two delineation methods.

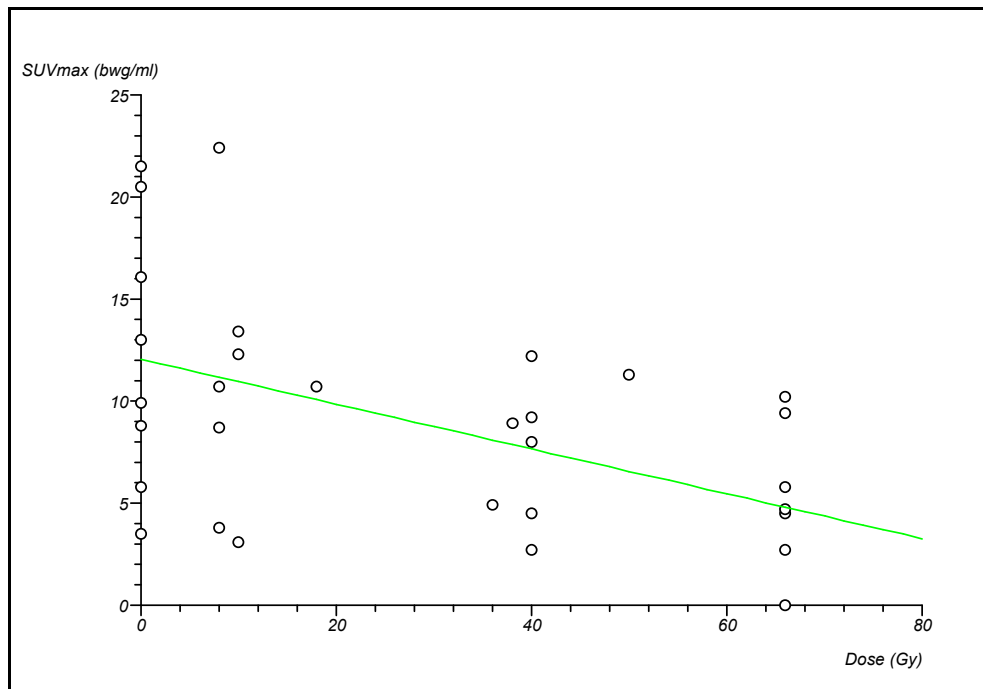


Figure 4.19: Simple linear regression relationship between the SUVmax within the primary functional volume delineated by the individualised adaptive threshold and the radiation dose

The theoretical radiation dose required to reduce the SUVmax within these primary FVs to zero was 112Gy.

Individualised Adaptive Threshold:

$$\text{SUVmax (bwg/ml)} = -0.109\text{Dose(Gy)} + 12.049$$

This is in comparison to the increasing primary FV with increasing radiation dose when defined by this method.

4.3.4.2.2 SUVmax within the Lymph Node Functional Volume

4.3.4.2.2.1 SUV Cut Off

The median pre-treatment SUVmax was identical within the LN FV delineated by all thresholds of the SUVCO method and is shown in table 4.15. Figure 4.20 illustrates this for the SUVmax within the LN FV delineated by the 3.0bwg/ml threshold as a box and whisker plot.

Table 4.15: The median and inter-quartile range for the SUVmax within the lymph node functional volume delineated by the SUV Cut Off thresholds

SUV Cut Off Threshold (bwg/ml)		SUVmax (bwg/ml)			
		0Gy	8 to 18Gy	36 to 50Gy	66Gy
2.5	Median	6.15	3.90	3.05	0.00
	IQR	7.80	8.40	5.50	3.10
3.0	Median	6.15	3.90	1.55	0.00
	IQR	7.80	8.40	5.50	3.10
3.5	Median	6.15	2.20	0.00	0.00
	IQR	11.11	8.40	5.50	3.10
4.0	Median	6.15	2.20	0.00	0.00
	IQR	11.11	8.40	5.50	0.00

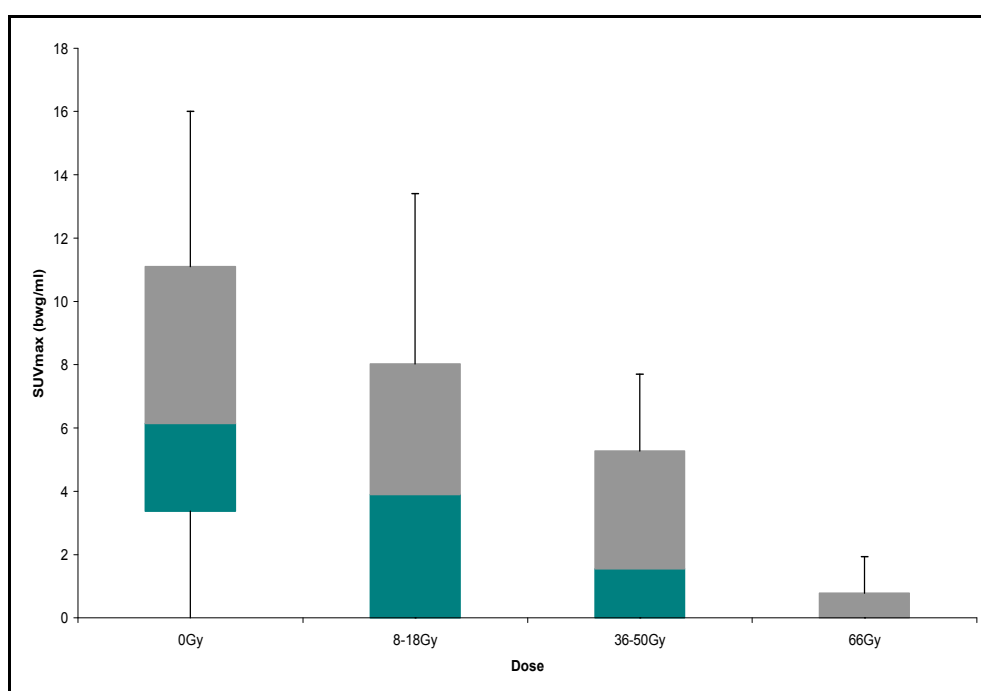


Figure 4.20: The SUVmax within the lymph node functional volume delineated by the 3.0bwg/ml SUV Cut Off threshold

Figures 9a to c of Appendix 2 illustrate the box and whisker plots for the other thresholds.

There was no significant reduction in the SUVmax within the LN FV between the SUVCO of 2.5bwg/ml and 3.0bwg/ml at any imaging point. Unlike the SUVmax within the primary FV, there was a significant reduction in the SUVmax within this LN FV at all imaging points between the SUVCO thresholds of 2.5 to 3.5bwg/ml and 2.5 to 4.0bwg/ml ($p < 0.0001$, median reduction 0.65 to 1.55bwg/ml 95% CI 0.0 to 1.75bwg/ml). Table 10 in Appendix 1 indicates these results in full.

The median difference increased initially at 8 to 18Gy. The SUVmax like that within the primary FV then significantly reduced at 36 to 50Gy ($p < 0.0001$, median reduction 3.60 to 4.05bwg/ml 95% CI 2.55 to 7.55bwg/ml), and 66Gy ($p < 0.0001$, median reduction 5.45 to 5.68bwg/ml 95% CI 3.40 to 8.20bwg/ml) compared to the pre-treatment value. Table 11 in Appendix 1 indicates these results in full.

This was confirmed by a significant negative correlation between the SUVmax within the delineated LN FV with the radiation dose at all SUV Cut Off thresholds. The correlation co-efficient was greatest at 2.5bwg/ml (p -value < 0.0001 , correlation co-efficient -0.537, 95% CI -0.64 to -0.36bwg/ml) and this is shown in figure 4.21. The results for the other thresholds are found in table 12 of Appendix 1 and figures 10a to c of Appendix 2.

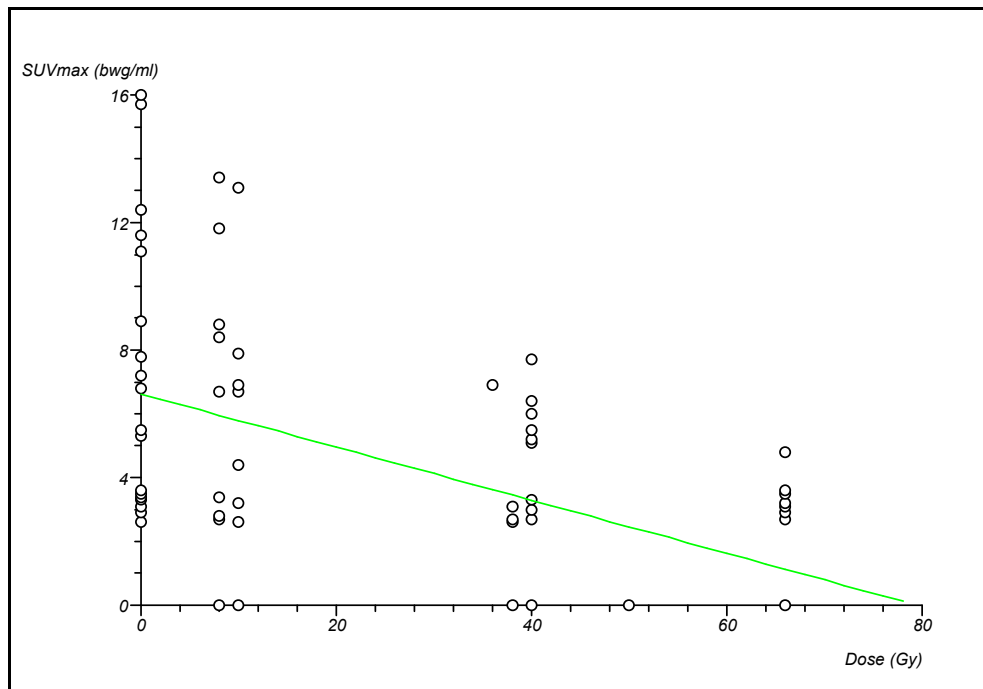


Figure 4.21: Simple linear regression relationship between the SUVmax within the lymph node functional volume delineated by the SUV Cut Off threshold of 2.5bwg/ml and the radiation dose

The theoretical radiation dose required to reduce the SUVmax within the LN FV to zero was 80Gy, 74Gy, 70Gy, and 68Gy for the value at 2.5, 3.0, 3.5, and 4.0bwg/ml respectively. The 2.5bwg/ml equation is indicated and the equations for the other thresholds are in Appendix 3 (Equations 18 to 20).

SUV Cut Off 2.5bwg/ml:

$$\text{SUVmax (bwg/ml)} = -0.083\text{Dose(Gy)} + 6.621$$

4.3.4.2.2 Percentage Threshold of the SUVmax

The median pre-treatment SUVmax within the LN FV delineated by the PTSUVmax method was also 6.15bwg/ml (IQR 7.80bwg/ml). This had reduced to 3.90bwg/ml (IQR 5.90bwg/ml) at 8 to 18Gy, 3.05bwg/ml (IQR 3.20bwg/ml) at 36 to 50Gy, and 2.30bwg/ml (IQR 1.20bwg/ml) at 66Gy. This is illustrated in figure 4.22.

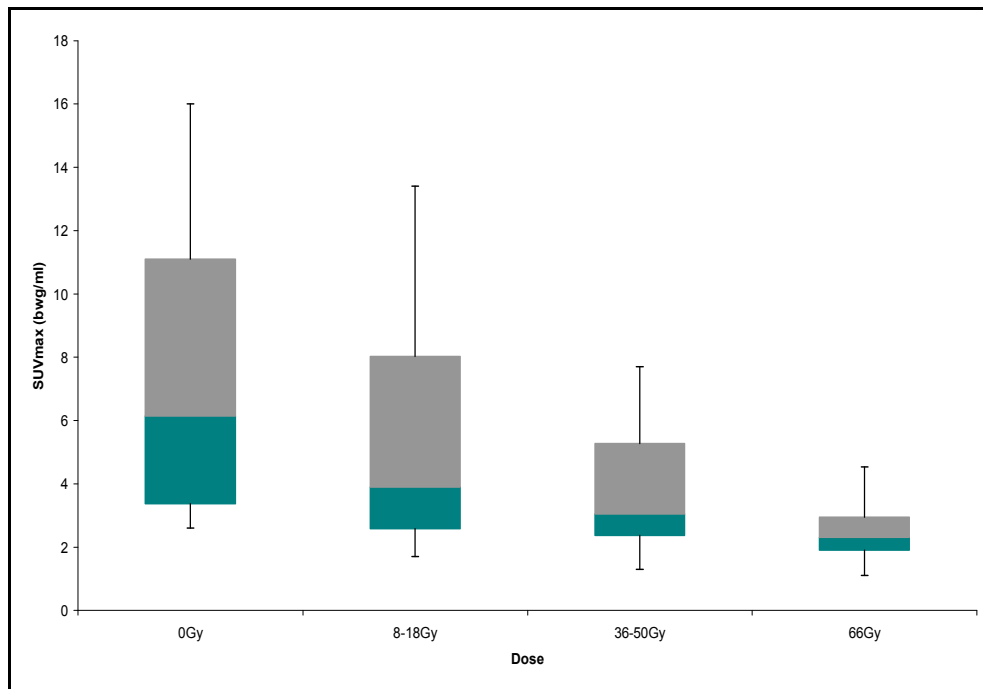


Figure 4.22: The SUVmax within the lymph node functional volume delineated by the percentage of the SUVmax method

There was a significant reduction in the SUVmax at 36 to 50Gy, and 66Gy when compared to 0Gy. The median difference initially increased at 8 to 18Gy by +1.45bwg/ml (p-value 0.999, 95% CI 0.70 to 2.35bwg/ml). This difference was then -3.15bwg/ml (p-value <0.0001, 95% CI -4.80 to -2.00bwg/ml) at 36 to 50Gy, and -4.43bwg/ml (p-value <0.0001, 95% CI -6.85 to -2.60bwg/ml) at 66Gy. This equated to a 23.55% increase at 8 to 18Gy, and then a reduction of 51.21% at 36 to 50Gy, and 72.03% at 66Gy compared to the 0Gy.

The SUVmax within the LN FV delineated by the PTSUVmax method was also negatively correlated with radiation dose (p-value <0.0001, correlation coefficient -0.508, 95% CI -0.65 to -0.32bwg/ml), and is shown in figure 11 of Appendix 2.

The theoretical radiation dose required to reduce the SUVmax within this delineated volume to zero was higher at 100Gy.

Percentage of the SUVmax:

$$\text{SUVmax (bwg/ml)} = -0.068\text{Dose(Gy)} + 6.765$$

4.3.4.2.2.3 Individualised Adaptive Threshold

The median pre-treatment SUVmax within the LN FV delineated by the IAT was the same as that in the FVs delineated by the other methods at 6.15bwg/ml (IQR 7.80bwg/ml). This reduced to 3.90bwg/ml (IQR 6.20bwg/ml) at 8 to 18Gy, 2.85bwg/ml (IQR 3.70bwg/ml) at 36 to 50Gy, and 0.80bwg/ml (IQR 2.30bwg/ml) at 66Gy. This is illustrated in figure 12 of appendix 2.

The median difference at 8 to 18Gy compared to 0Gy was +1.37bwg/ml (p-value 0.002, 95% CI -0.70 to 2.35bwg/ml). This difference was -3.63bwg/ml (p-value <0.0001, 95% CI -5.45 to -2.15bwg/ml) at 36 to 50Gy, and -6.20bwg/ml (p-value <0.0001, 95% CI -8.45 to -3.45bwg/ml) at 66Gy. This equated to a percentage change of +22.27% at 8 to 18Gy, 53.67% at 36 to 50Gy, and 86.99% at 66Gy.

This negative correlation between the SUVmax within the LN FV delineated by the IAT method and the radiation dose (p-value <0.0001, correlation co-efficient -0.589, 95% CI -0.72 to -0.43bwg/ml) was confirmed, and is shown in figure 12 of Appendix 2.

The theoretical radiation dose required to reduce the SUVmax within these volumes to zero was calculated as 80Gy.

Individualised Adaptive Threshold:

$$\text{SUVmax (bwg/ml)} = -0.0878\text{Dose(Gy)} + 6.889$$

4.3.5 The Background Uptake of ¹⁸Fluoro-2-deoxyglucose

4.3.5.1 SUV Cut Off and Percentage Threshold of the SUVmax

The mean background uptake of ¹⁸FDG was identical for the reference region defined by both the SUVCO and PTSUVmax, and is illustrated in figure 4.23.

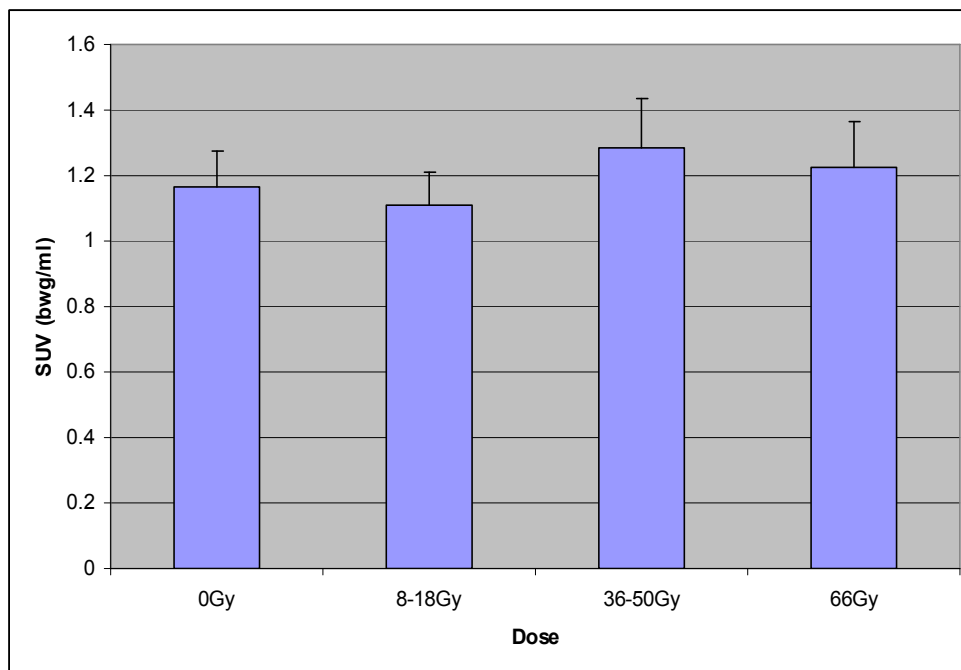


Figure 4.23: The mean background SUV within the reference region delineated by the SUV Cut Off and percentage of the SUVmax methods

The mean pre-treatment SUV was 1.16bwg/ml (SEM 0.11 bwg/ml, range 0.60-1.60bwg/ml). At 8 to 18Gy this was 1.11bwg/ml (SEM 0.10 bwg/ml, range 0.8-1.40bwg/ml). At 36 to 50Gy the mean SUV was 1.29bwg/ml (SEM 0.15bwg/ml, range 0.70-2.10bwg/ml), and at 66Gy the mean SUV was 1.23bwg/ml (SEM 0.14bwg/ml, range 0.60-1.70bwg/ml).

There was no significant difference and no correlation between in the SUV at imaging points during treatment compared to the pre-treatment value.

4.3.5.2 Individualised Adaptive Threshold

Figure 4.24 illustrates the mean background SUV when the reference ROI was delineated by the IAT method.

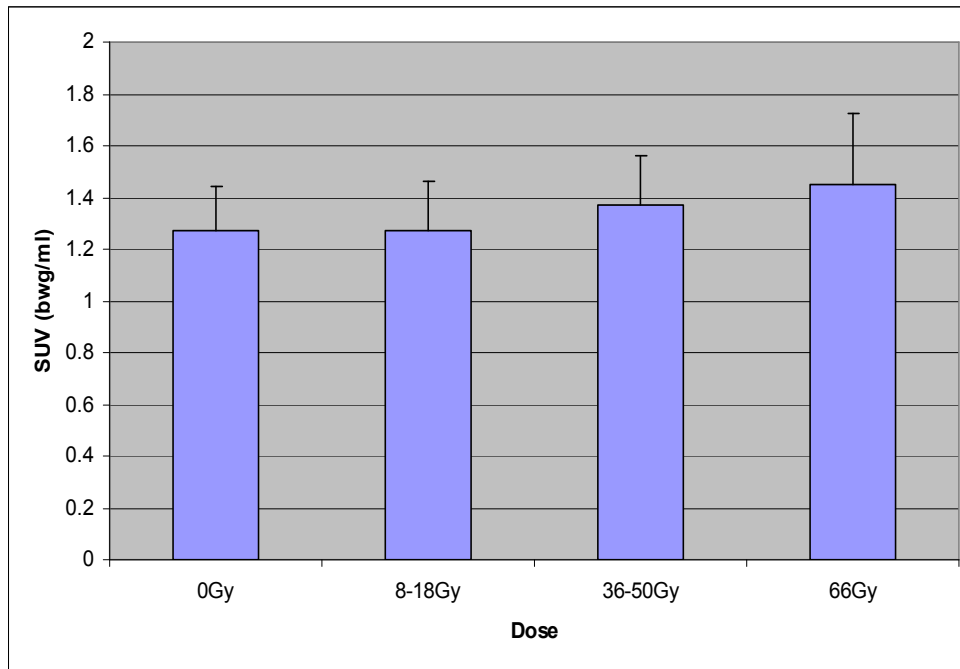


Figure 4.24: The mean background SUV within the reference region delineated by the individualised adaptive threshold

The mean background SUV within this reference ROI was 1.28bwg/ml (SEM 0.17bwg/ml, range 0.60-2.30bwg/ml) at 0Gy, 1.28bwg/ml (SEM 0.20bwg/ml, range 0.60-2.40bwg/ml) at 8 to 18Gy, 1.38bwg/ml (SEM 0.19bwg/ml, range 0.70-2.40bwg/ml) at 36 to 50Gy, and 1.45bwg/ml (SEM 0.27bwg/ml, range 0.60-2.90bwg/ml) at 66Gy. These values were higher than those delineated by the other methods.

There was no significant difference or correlation in the background SUV within the reference ROI delineated by the IAT with the radiation dose.

4.3.6 The Actual SUVmax Used to Define the Percentage Threshold of the SUVmax for the Functional Volume

4.3.6.1 Mean SUV to Define the Primary Functional Volume

The actual mean percentage values of the SUVmax used to define the edge of the primary FV at each percentage threshold of SUVmax are shown in figure 4.25.

At each imaging point there was a reduction in the SUV used to define the volume, in keeping with the reduction of the SUVmax within the FV.

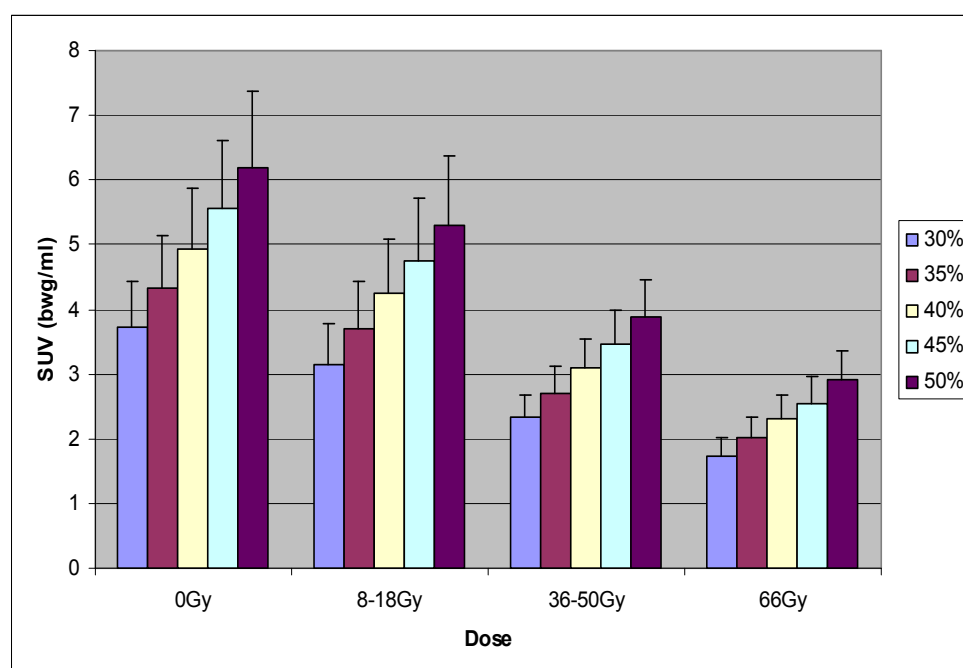


Figure 4.25: The actual SUV used to define the edge of the primary functional volume for each percentage of the SUVmax threshold

The values for the mean, and SEM at each imaging point are illustrated in table 13 of Appendix 1. Importantly, the mean SUV used to define the edge of the volume at 66Gy for the 30% threshold of the SUVmax was 1.73bwg/ml (SEM 0.28bwg/ml, range 0.80 to 3.10bwg/ml), and at 50% this was 2.90bwg/ml (SEM 0.46bwg/ml, range 1.90 to 5.1bwg/ml). This compared to the background uptake at this time point of 1.23bwg/ml (SEM 0.14bwg/ml, range 0.60-1.70bwg/ml). This indicates the background uptake was the same or equal to the SUV used to define the edge especially at the lower thresholds.

There was a significant increase in the SUV used to define the edge of each primary FV at the 35%, 40%, 45%, and 50% threshold compared to the 30% threshold. This was most significant at 40%, 45%, and 50% of the SUVmax (p-value 0.0002 to 0.001, mean increase in SUV 0.29 to 2.48bwg/ml 95% CI 0.29 to 2.48bwg/ml). This increase was greatest at 0Gy and 8 to 18Gy. This is illustrated in table 14 in Appendix 1.

The SUV used to delineate the edge of the primary FV at each of the PTSUVmax has been compared with the background SUV at each imaging point. The SUV used to define the edge was significantly greater than the background SUV for all thresholds at all imaging points. The exception to this was the SUV used to define the 30% threshold FV at 66Gy. At 66Gy, the difference was between 0.5 and 1.38bwg/ml depending on the threshold and is illustrated in table 4.16.

Table 4.16: The mean difference, p-values, and 95% confidence intervals for the SUV used to define the primary functional volume and the background SUV at each imaging time point by the percentage thresholds of the SUVmax

Percentage Threshold of the SUVmax (%)		Mean Difference (bwg/ml)	p-value	95% CI (bwg/ml)
30	<i>0</i>	2.56	0.004	0.95 to 4.16
	<i>8 to 18</i>	2.04	0.02	0.49 to 3.59
	<i>36 to 50</i>	1.04	0.017	0.25 to 1.83
	<i>66</i>	0.50	0.051	-0.13 to +1.13
35	<i>0</i>	3.18	0.003	1.31 to 5.05
	<i>8 to 18</i>	2.58	0.006	0.79 to 4.36
	<i>36 to 50</i>	1.40	0.005	0.46 to 2.34
	<i>66</i>	0.79	0.041	0.04 to 1.53
40	<i>0</i>	3.75	0.002	1.59 to 5.92
	<i>8 to 18</i>	3.13	0.004	1.07 to 5.18
	<i>36 to 50</i>	1.80	0.002	0.75 to 2.85
	<i>66</i>	1.08	0.02	0.22 to 1.92
45	<i>0</i>	4.39	0.002	1.95 to 6.82
	<i>8 to 18</i>	3.64	0.004	1.34 to 5.93
	<i>36 to 50</i>	2.16	0.002	0.97 to 3.36
	<i>66</i>	1.38	0.001	0.45 to 2.30
50	<i>0</i>	5.04	0.002	2.32 to 7.76
	<i>8 to 18</i>	4.91	0.003	1.65 to 6.74
	<i>36 to 50</i>	2.60	0.001	1.27 to 3.93

	66	1.66	0.003	0.62 to 2.70
--	----	------	-------	--------------

4.3.6.1 Median SUV used to Define the Lymph Node Functional Volume

The median SUV used to delineate the LN FV at each PTSUVmax is shown in table 4.17. These values reduced at each imaging point during treatment, and also increased depending on the threshold.

Table 4.17: The median and inter-quartile range for the SUV used to define the lymph node functional volume delineated by the percentage thresholds of the SUVmax

Percentage Threshold of the SUVmax (%)		SUV (bwg/ml)			
		0Gy	8 to 18Gy	36 to 50Gy	66Gy
30	Median	1.85	1.15	0.90	0.65
	IQR	1.50	0.10	0.10	0.10
35	Median	2.15	1.35	1.10	0.80
	IQR	1.70	1.30	0.10	0.10
40	Median	2.45	1.60	1.20	0.95
	IQR	1.90	1.40	0.10	0.10
45	Median	2.80	1.75	1.40	1.00
	IQR	1.90	1.60	0.10	0.10
50	Median	3.10	1.95	1.55	1.10
	IQR	2.40	1.70	0.10	0.10

Similar to the primary FV, the SUV used to define the LN FV significantly increased at each imaging point when the thresholds were compared to the SUV used at the 30% threshold ($p < 0.0001$, median increase in SUV 0.10 to 1.50bwg/ml 95% CI 0.10 to 1.55bwg/ml). Table 15 in Appendix 1 illustrates these values.

The SUV used to define the edge of the LN FV at each threshold and imaging point was compared to the background SUV within the reference ROI and is shown in table 4.18.

Table 4.18: The median difference, p-values, and 95% confidence intervals for the SUV used to define the lymph node functional volume and the background SUV at each imaging point by the percentage thresholds of the SUVmax

Percentage Threshold of the SUVmax (%)		Median Difference (bwg/ml)	p-value	95% CI (bwg/ml)
30	<i>0</i>	+1.00	0.001	+0.35 to +1.80
	<i>8 to 18</i>	+0.60	0.064	-0.05 to +1.35
	<i>36 to 50</i>	+0.13	0.297	-0.30 to +0.55
	<i>66</i>	-0.40	0.001	-0.60 to -0.20
35	<i>0</i>	+1.30	0.0002	+0.60 to +2.30
	<i>8 to 18</i>	+0.93	0.009	+0.15 to +1.75
	<i>36 to 50</i>	+0.05	0.391	-0.40 to +0.50
	<i>66</i>	-0.25	0.009	-0.45 to -0.05
40	<i>0</i>	+1.65	<0.0001	+0.80 to +2.75
	<i>8 to 18</i>	+1.15	0.0033	+0.35 to +2.10
	<i>36 to 50</i>	+0.20	0.226	-0.30 to +0.75
	<i>66</i>	-0.10	0.403	-0.37 to +0.10
45	<i>0</i>	+1.98	<0.0001	+1.05 to +3.20
	<i>8 to 18</i>	+1.43	0.0004	+0.45 to +2.55
	<i>36 to 50</i>	+0.40	0.1564	-0.15 to +0.95
	<i>66</i>	0.00	0.932	-0.25 to +0.20
50	<i>0</i>	+2.38	<0.0001	+1.30 to +3.70
	<i>8 to 18</i>	+1.68	<0.0001	+0.60 to +2.90
	<i>36 to 50</i>	+0.60	0.024	0.00 to +1.15
	<i>66</i>	+0.15	0.210	-0.10 to +0.35

The SUV used to define the edge of the FV was significantly greater at all thresholds than the background SUV at 0Gy, 8 to 18Gy, and 36 to 50Gy. However, at 66Gy this SUV was significantly smaller than that within the background for the 30%, and 35% thresholds, and there was no significant difference at the 40%, 45%, and 50% thresholds.

4.3.7 The Relationship between the SUVmax within the Functional Volume and the Delineated Functional Volume

4.3.7.1 Primary functional volume and the SUVmax

When the PTSUVmax defined the primary FV, there was a trend towards an increase in the delineated FV and a reduction in the SUVmax within that FV, but this was not significant. An example of this is shown in figure 4.26 for the 30% threshold. Similarly, there was no correlation with the FV defined by the IAT method.

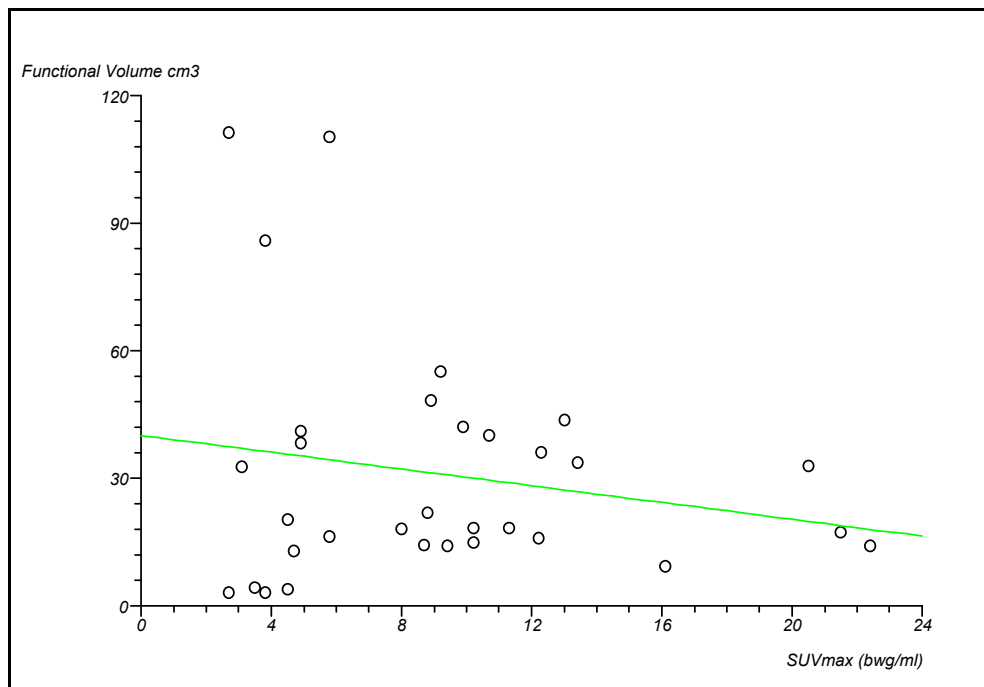


Figure 4.26: Simple linear regression relationship between the SUVmax and the primary functional volume delineated by the 30% threshold of the SUVmax

However, when the SUVmax was compared with the FV delineated by the SUVCO thresholds, there was a highly significant positive correlation. An example of this is shown in figure 4.27 for the SUVCO threshold of 3.0bwg/ml (p-value <0.0001, correlation co-efficient 0.718, 95% CI 0.49 to 0.86bwg/ml). The remaining graphs for the other thresholds are in Appendix 2 figure 14 a to c, and statistics in table 16 of Appendix 1.

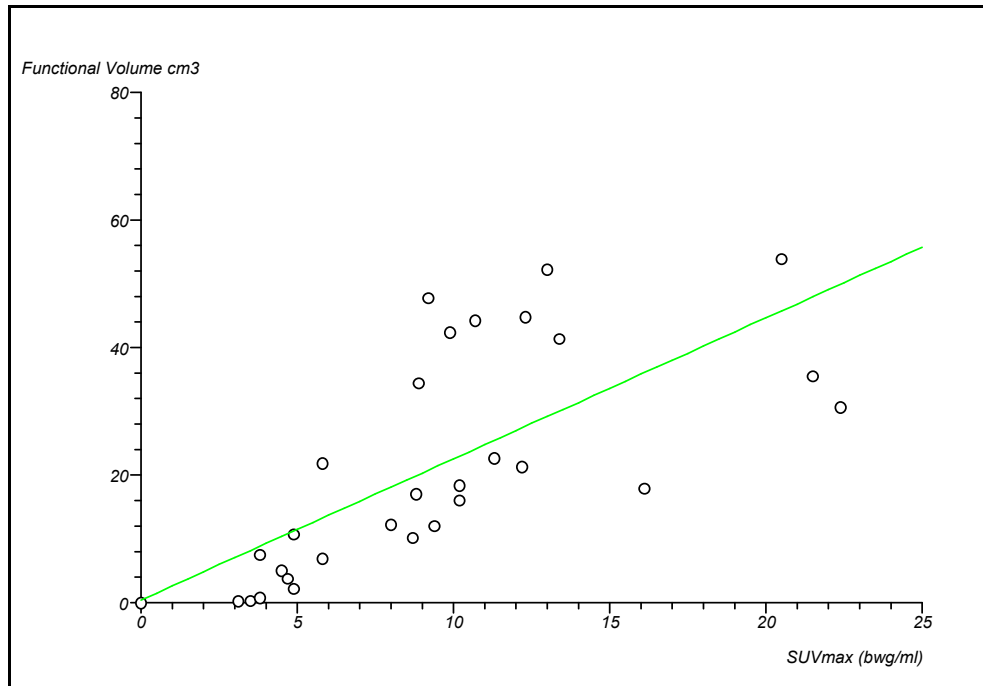


Figure 4.27: Simple linear regression relationship between the SUVmax and the primary functional volume delineated by the SUV Cut Off threshold of 3.0bwg/ml

From this relationship, the theoretical FV was calculated according to the SUVmax. An example of this equation is shown for the 3.0bwg/ml threshold. The other equations are in Appendix 3 (Equations 21 to 23).

SUV Cut Off threshold 3.0bwg/ml:

$$FV (cm^3) = 2.212SUVmax(bwg/ml) + 0.424$$

For example: a SUVmax of 11.0bwg/ml would calculate a theoretical FV of 24.76cm³.

4.3.7.2 Lymph Node Functional Volume and the SUVmax

There was no significant relationship between the delineated LN FV and the SUVmax within the volume when defined by the all the percentage thresholds of the SUVmax.

However, similarly there was a significant positive correlation between the LN FV delineated by the SUVCO thresholds and the SUVmax. This correlation was greatest at the SUVCO threshold of 3.0bwg/ml (p-value <0.0001, correlation co-efficient 0.631, 95% CI 0.49 to 0.75bwg/ml). Table 17 in Appendix 1, and figures 15 a to d in Appendix 2 illustrate the statistical and graphical values for the other thresholds.

There was also a weak positive correlation when the LN FV was defined by the IAT method (p-value 0.01, correlation co-efficient 0.276, 95% CI 0.06 to 0.47bwg/ml)

An example of the theoretical LN FV calculated from these SLR models is shown. The other equations are in Appendix 3 (Equations 24 to 26).

SUV Cut Off 3.0bwg/ml:
$$FV (cm^3) = 1.176SUVmax(bwg/ml) - 1.581$$

For example: a SUVmax of 11.0bwg/ml would calculate a theoretical FV of 11.35cm³.

4.4 Discussion

Three delineation methods were investigated: SUVCO, PTSUVmax, and IAT, with a combination of 10 thresholds. This study has shown that the defined FV before and during RT is intricately linked to the delineation method and threshold.

This volume change will impact on the potential dose that may be delivered through dose escalation strategies. Smaller FVs require a lower total dose to be reduced to zero. This volume reduction is also correlated with the SUVmax reflecting intra-tumoural glucose metabolism.

4.4.1 Statistical Methods

The difference in statistical normality of the volume distribution may have been due to the small number of patients because there were only eight primary, compared to 20 LN FVs.

Patients may have more than one LN positive depending on the primary site, and this has the potential to lead to heterogeneity of ^{18}F FDG uptake between LNs depending on the individual metastatic LN biology. Non-parametric tests could have been used if the primary and LN volumes were analysed together, but this would have over-represented the reduction in the primary volume and under-represented the reduction in the LN volume during radiation treatment. This also indicated the differences in the uptake of ^{18}F FDG in the LN and primary regions. Due to the small number of patients it was not possible to assess this change according to the individual LN levels within the neck.

4.4.2 SUVmax within the Region of Interest

The SUVmax most importantly defined the FV and therefore will be discussed first.

In both the primary and LN FVs, the SUVmax was significantly reduced only at 36 to 50Gy, and 66Gy compared to 0Gy at each SUVCO threshold. There was a

significant reduction in the SUVmax within the LN FV for the delineating threshold at 8 to 18Gy when the 3.5 and 3.0bwg/ml thresholds were compared with 2.5bwg/ml, and when the 4.0, 3.5, and 3.0bwg/ml thresholds were directly compared with that at 2.5bwg/ml at each imaging point.

The pattern of reduction of the SUVmax within the primary and LN FVs delineated by the PTSUVmax and IAT methods was also seen at 36 to 50Gy and 66Gy. There was a significant negative correlation for the SUVmax with radiation dose in volumes delineated by all methods.

A theoretical SUVmax calculated from these values would be reduced to zero after 112 to 128Gy of RT within the primary, and at 68 to 80Gy within the LN FV for the SUVCO thresholds. This reduction in the SUVmax within the primary FV would be at 128Gy, and 100Gy within the LN FV when defined by the PTSUVmax, and 122Gy within the primary, and 80Gy within the LN FV when delineated by the IAT. Since ^{18}F FDG is a surrogate marker of increased glucose metabolism, it would suggest that at these radiation doses intra-tumoural metabolism within the defined FV was reduced and cell growth prevented.

The pre-treatment SUVmax within the defined volumes was identical. This is an important point, as differences detected in the metabolic activity during RT are due to the delineation method and threshold used. This can be seen when the SUVmax at the other three imaging points are reviewed. For example, the differences ranged from: 0.062 and 0.92bwg/ml at 8 to 18Gy, 0.0 to 0.36bwg/ml at 36 to 50Gy, and 0.82 to 1.088bwg/ml at 66Gy for the primary FV between the thresholds and methods.

Increased ^{18}F FDG uptake has been noted 1 day after the administration of cisplatin in xenografted mice with SCC, and in a moderately differentiated human SCCHN cell line. This slowly reduced as the number of viable cells declined, suggesting ^{18}F FDG uptake can initially increase prior to a reduction in cell number. This may be cytokine mediated secondary to inflammation [1].

The SUVmax can change during a course of treatment reflecting the differences in metabolic activity within the tumour as RT progresses. The reduction in SUV acts as a surrogate marker for the decline in glucose metabolism as the viable cell population reduces.

This is not always the case, and the volume delineated (dependent on the delineation method) may or may not correlate with changes in the SUVmax. An increase in the SUV has been described at the beginning of RT in 6 patients with metastatic papillary carcinoma of the thyroid. The ^{18}F FDG avidity increased by 65 to 89% after 6Gy and did not start to decline until after 30Gy [2]. Four patients reported in the study from this chapter had the SUV increased by 4.02 to 13.73% in the primary, and by 5.93 to 7.46% in three LNs within the same patient (no increase in the SUVmax within the primary). This is the mostly likely reason why there was no significant reduction in the SUVmax within the primary volume at 8 to 18Gy.

A single study in 16 patients with SCCN assessed the change in the FV at 4 time points during CRT. These patients all received curative CRT to a total dose of 72Gy (30Gy in 15 fractions, once daily, 42Gy in 1.4Gy per fraction twice daily). They underwent an initial ^{18}F FDG PET pre-treatment followed by 3 further scans (end of the 1st/2nd (10 to 20Gy) week, 3rd/4th week (30 to 44Gy), and 5th/6th week (58 to 72Gy). The FV was delineated by a individual signal to background ratio algorithm with iterative background correction by automatic segmentation software (ROVER®, Fa. ABX, Radeberg, Germany). The SUVmax within the ROI continuously reduced during radiation treatment (15.2g/ml to 6.4g/ml), but this reduction was only significant after 30Gy. This finding is consistent with the results in this chapter, and this study also found the SUVmax increased in some patients prior to 30Gy. Using this automatic delineation algorithm, the mean FV increased during RT by 94.97% from 9.4cm³ to 17.9cm³ [3].

Only this iterative algorithm was reported, the nodal and primary FVs were combined rather than presented separately, and PET and CT modalities were acquired separately. Interestingly, this group concluded that SUVmax did not

affect the final delineated volume for this delineation method. Adaptive algorithms, which use the SUVmax to calculate the edge-defining threshold will automatically be influenced by the SUVmax within the FV under investigation.

The differences in the results from this chapter between the SUVmax within the primary and LN FVs are likely to reflect the differences in glucose metabolism due to tumour heterogeneity. For example small LNs with an organized surrounding vasculature are likely to have improved nutrient delivery, and so be in a faster phase of growth (increased glucose metabolism), and more susceptible to radiation-induced DNA damage and cell death. Similarly the calculated dose required to reduce the glucose metabolism (and therefore the ^{18}F FDG uptake) to zero was less for the LN than the primary FV. This may be because the primary FV was larger (for example: mean 23.55cm^3 at 30% of the SUVmax threshold, compared to a median LN volume of 4.25cm^3). The larger pre-treatment primary FV may have had a larger proportion of connective tissue, fibrosis, and necrosis, which would minimally influence the change in size, and the glucose metabolism compared to the fraction of viable cells.

4.4.3 Background Uptake of ^{18}F Fluoro-2-deoxyglucose

The background uptake of ^{18}F FDG did not significantly differ with increasing radiation dose when assessed by all methods. The background ^{18}F FDG uptake was slightly higher when the reference region was delineated by the IAT.

The most likely reason for this is the iterative algorithm used to assess the background SUV uptake. The ROI was in an identical position for the assessment at each threshold, and was not moved as the FVs were calculated. The threshold setting only was change and this was used to define the edge and calculate the parameters within the defined boundary box and segmented volume. This method may though be more representative of the background SUV over a larger area due to changes in the SUVmean and max within the volume.

The PETVCAR auto-segmentation IAT algorithm used to calculate the FV is based on a number of different mathematical operations. These operations subtract the ROI from the surrounding area. The segmentation and edge defining

techniques are based on a background symmetry algorithm in which the peak of intensity is detected within the pixel/voxel of the image, and this peak is assumed to be the dominant peak within the region as defined by the algorithm. The slope of the peak is then used to calculate the volume. This is dependent on the SUVmean, which in turn is dependent on the tumour volume.

In areas with generalised low-level background uptake of ^{18}F FDG, the edge definition is difficult because the peak of the slope is too small to define the edge of the volume, therefore the algorithm will grow the volume until the volume edge reaches the defining boundary box.

Figure 4.28a and b illustrate this phenomenon. Figure 4.28a indicates the peak of ^{18}F FDG uptake within the ROI (blue arrow), and the slope used to define the edge (red arrow). The red line at the base of the peak is the FV. The final delineated FV is oval in shape with a red edge. The higher ^{18}F FDG uptake is dark grey within this. This corresponds to the area within the peak, and is segmented from the black boundary box. The distance between the peak and the edge of the slope used to define the volume is indicated within the final delineated volume as a circle with a cross in the centre.

Figure 4.28b indicates the peak of the slope is smaller. The software algorithm cannot differentiate the numerous small peaks of uptake intensity from the slightly higher uptake of the dominant peak. For example smaller voxel peaks may have an SUV of 1.7bwg/ml, and the dominant peak 1.72bwg/ml. The auto-segmented defined volume is the entire boundary box in red, with the oval lower intensity pale grey uptake of ^{18}F FDG in the centre has not been successfully segmented from the background uptake.

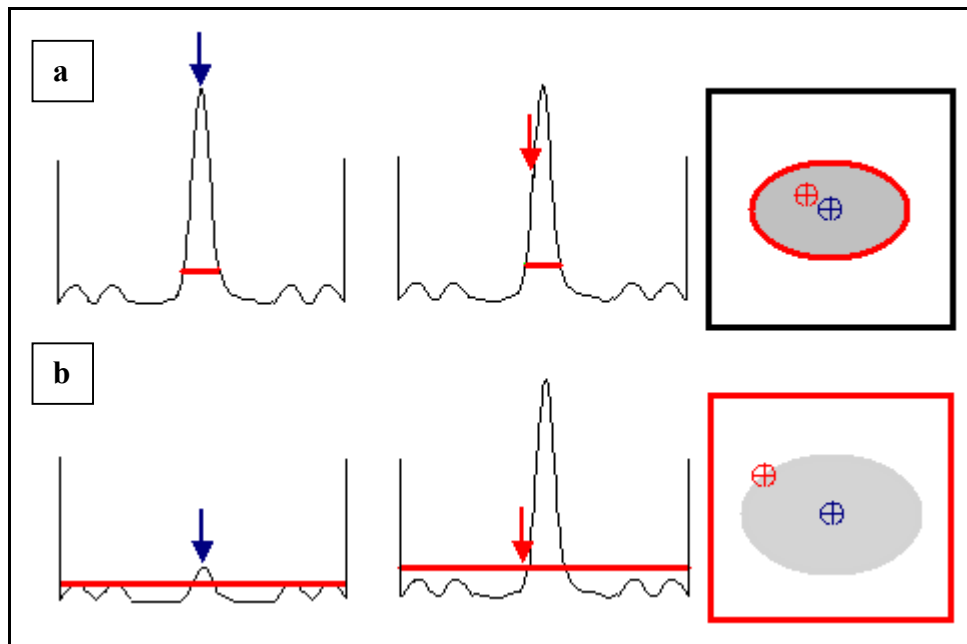


Figure 4.28a and b: The definition of the functional volume by the individualised adaptive threshold method. Well defined volume a), and poorly defined volume b)

Figure 4.29 illustrates the calculation of the edge of the FV defined by the IAT. The edge is defined when the gradient of the slope (red circle with red cross) changes. The vector (weighting) factor is automatically set to 0.5 for this point. This is between the peak ^{18}F FDG uptake (blue arrow and circle with blue cross) within the defined boundary box, and the point of the slope when the gradient is zero (indicated by the violet circle with a central violet cross). The change in gradient and slope steepness between the maximum and minimum voxels of SUV uptake is illustrated by the dotted arrows that extend from the peak to the base of the slope. The edge of the boundary box, and the background uptake of ^{18}F FDG are indicated by thick black arrows.

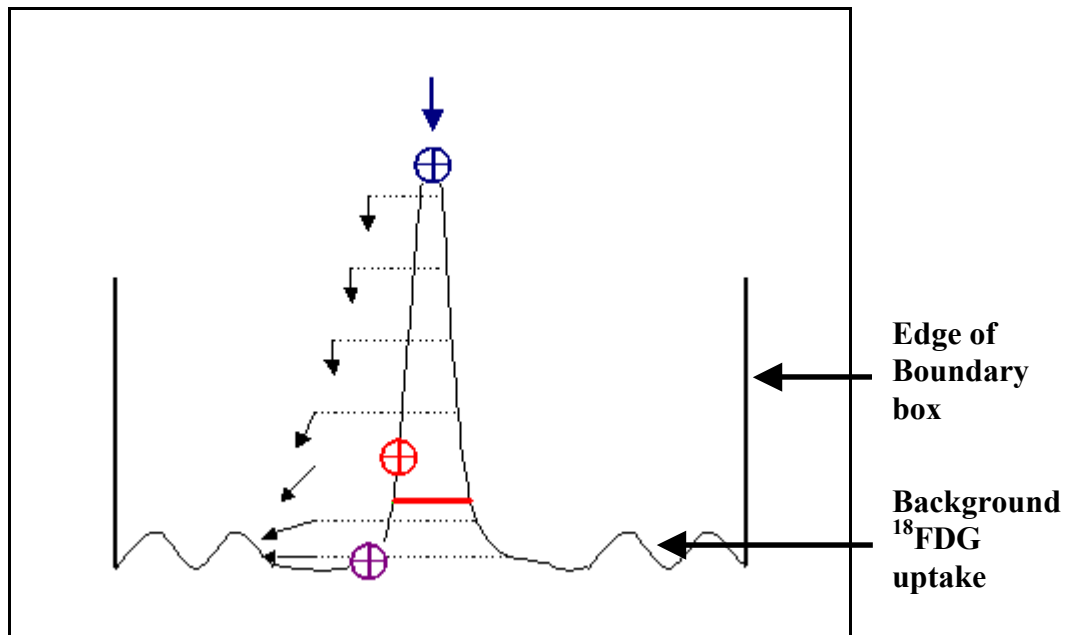


Figure 4.29: Edge definition by the individualised adaptive threshold according to the gradient of the slope

This is in contrast to the other two methods where the threshold is defined by the user of the software, and the contents of the defined volume are calculated. Therefore areas with a low SUVmax may be defined as falsely large because of the difficulty in edge definition by the software. This may account for the lack of correlation of the FV defined by the IAT with the radiation dose, despite a negative correlation of radiation dose with the SUVmax.

4.4.4 Inflammation and Background ^{18}F Fluoro-2-deoxyglucose Uptake

Low levels of ^{18}F FDG uptake occur in a number of situations including inflammation. During RT to the HN, inflammation develops within the tumour and the surrounding normal tissue.

In a human adenocarcinoma ovarian cancer cell line irradiated with a single 30Gy fraction, the basal uptake of ^{18}F FDG was 9.77 times greater in the irradiated than the non-irradiated group up to 12 days after irradiation. This occurred despite a reduction in the number of viable cells. When compared with the uptake of ^3H -thymidine (indicator of DNA synthesis), the basal uptake was up to 948% greater in cells with increased DNA synthesis after irradiation [1]. This suggests that the increased uptake of ^{18}F FDG is due to increased DNA repair,

synthesis, and cell re-population. Mononuclear white cells may infiltrate the area as part of an inflammatory reaction to degrade apoptotic cells.

The normal tissue reaction to RT depends on the tissue type and the rate of delivered radiation dose. Apoptotic cell death occurs at the time of mitosis when cells attempt to divide after radiation delivery. Epithelial cells may start to repopulate 8 days after radiation with a cell turnover time of 24 hours [4]. This early response to radiation is due to the stem cell turnover time in the tissue of interest. An inflammatory reaction and leukocyte infiltration of the irradiated tissue accompanies this due to a signalling cascade of cytokines. In patients with HN cancer after 30 to 60Gy of RT, the macrophage infiltration was found to be consistent with this inflammatory response [5].

The background uptake of ^{18}F FDG during RT was found to increase within macrophages associated with radiation-induced mucositis [6]. The risk of confluent mucositis of the oral mucosa after 65 to 70Gy is 50% [7]. In mice, ^{18}F FDG accumulated within granulation tissue and in macrophages at the necrotic tumour rim after irradiation. Dual tracer auto-radiography with ^3H -thymidine indicated DNA synthesis and cell re-population occurred in the same regions as increased glucose utilisation [8].

The SUV within the vertebra of 163 lymphoma patients with no known bone marrow infiltration was assessed on ^{18}F FDG PET after colony stimulating factor injections. The SUV increased by 2.37g/ml up to 90 days after the injections, and was greatest 0 to 7 days later [9]. This uptake was due to the mobilisation of marrow stem cells, and further suggests that activated leukocytes increase ^{18}F FDG uptake.

The increased uptake of ^{18}F FDG can continue after RT has completed making scan assessment difficult especially when salvage surgery for residual disease is to be considered. The SUVmax ranged from 2.5 to 7.0g/ml in patients with SCCHN who underwent salvage surgery after concurrent chemotherapy with IMRT, and had histologically proven residual disease. The SUV was 3.9g/ml in

those with no evidence of residual disease [10]. This SUV overlap between the two groups was due to post-treatment residual inflammation.

An SUV of 3.0g/ml is a common fixed criteria for residual disease after treatment in patients with SCCHN. Ong et al [10], after applying this threshold to areas of increased ^{18}F FDG uptake found the sensitivity was 66%, and specificity 81% for the detection of recurrent disease in the LN, and 57% and 84% respectively in the primary site. These values were greatest 12 weeks after the completion of treatment.

Similarly, Andrade et al [11] reported in 28 patients with SCCHN imaged 4 to 15.7 weeks after the completion of curative RT that the sensitivity was 76.9%, and specificity 93.3% for the detection of recurrent disease. The uptake of ^{18}F FDG within the previously irradiated field was low to moderate but not directly quantified. This suggested that the differentiation of normal tissue to residual tumour uptake continued to be difficult up to 12 weeks after the completion of curative RT/CRT.

The placement of the reference region to define the background ^{18}F FDG uptake is important. Physiological and patient related factors can influence this [12]. Anxious patients may tense their neck muscles, and this will increase the background SUV within the SCM muscle. Physiological uptake can also be noted in the larynx if the patient talks from injection to imaging, and would be especially problematic if the primary site was within the vocal cord.

All of the factors discussed have the potential of making the tumour edge definition difficult, but the method of delineation is vitally important. This is because ^{18}F FDG uptake in the normal tissue may be increased to the same level as that within the tumour, and result in the greatest difficulty in edge definition towards the end of RT treatment. The use of an SUVCO threshold set above the background uptake will exclude this from the calculated FV. The lowest SUVCO threshold was greater than the background uptake in the results from this chapter, and this method therefore was less susceptible to changes in background uptake of ^{18}F FDG.

Interestingly, the background ^{18}F FDG uptake during RT did not correlated with RT dose, but did increase during the study when calculated by the IAT method. This may be because of the small patient numbers (1 reference region to calculate the background SUV per patient), or the adaptive algorithm. The placement of multiple ROI within the muscle rather than 1 may have been appropriate, as well as the assessment of uptake within regions of pharyngeal mucositis. For this to be accurate the patient's imaging and clinical examination during RT treatment would need to have been assessed by the same person. This was not possible because the FVs were delineated after study completion. The mucositis is often at a peak after the completion of treatment, and in this study there was no imaging at this time point.

4.4.5 Delineated Functional Volume

The pre-treatment delineated FV varied between the thresholds and methods. The 40, 45, and 50% of SUVmax volumes were smaller than those delineated by other thresholds. The mean primary FV delineated by the 3.5bwg/ml SUVCO threshold was within 0.40cm^3 of the volume delineated by the 30% threshold of the SUVmax, and the IAT. This is shown in the histogram in figure 4.30.

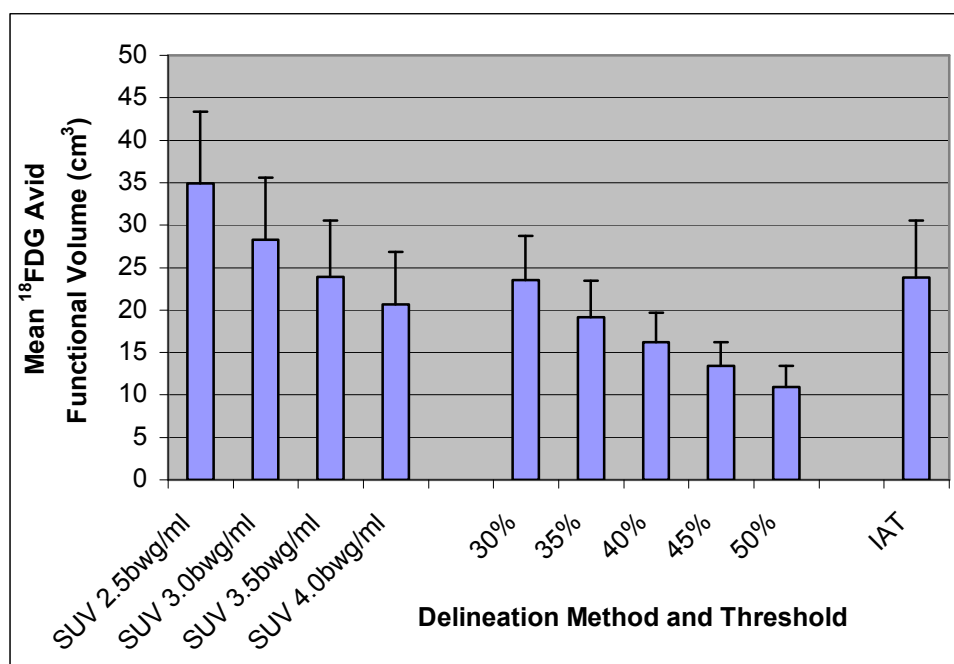


Figure 4.30: The mean pre-treatment primary functional volume delineated at each threshold for all the investigated methods

There was a 14.30cm³ (40.92%) reduction in volume between the 2.5 and 4.0bwg/ml SUVCO, and 12.60cm³ (36.47%) between the 30% and the 50% of the SUVmax thresholds.

The primary FV delineated at the 30% of the SUVmax, IAT, and 2.5bwg/ml SUVCO thresholds were within 0.15cm³ of each other at the start of treatment. The other LN volumes delineated by the 3.0 to 4.0bwg/ml SUVCO thresholds were all smaller than the volume delineated by the 50% of the SUVmax threshold.

The pre-treatment LN FVs delineated by all the thresholds of the SUVCO method were smaller than those delineated by any PTSUVmax, or IAT method. There was only a 0.15cm³ difference between the pre-treatment LN FV delineated by the 2.5bwg/ml (2.65cm³), 50% of the SUVmax (2.70cm³), and individualised adaptive (2.80cm³) thresholds.

Both the LN and the primary FV were significantly reduced between the delineating thresholds when compared to the minimum threshold of 2.5bwg/ml,

and 30% of the SUVmax. When the LN FV delineated by the 35% threshold of the SUVmax was compared with the 30% threshold this was not the case. This non-significant result was because the defining edge was similar. The median difference in the SUV used to define the edge was 0.05 to 0.30bwg/ml between 30 to 35% at each imaging point, compared to 0.60 to 1.15bwg/ml at 30 to 50% at each imaging point. There was minimal volume change between the thresholds. For example the median pre-treatment defined LN FV at the 30% of the SUVmax threshold was 4.25cm³ (IQR 5.90cm³), and at 35% this was 4.20cm³ (IQR 4.70cm³).

The LN and primary FV delineated by the SUVCO thresholds were significantly reduced at 36 to 50Gy, and 66Gy compared to 0Gy, which mirrored the reduction in the SUVmax. This was most significant at 3.0bwg/ml for both FVs. This was confirmed by a negative correlation of the defined volume with the increase in radiation dose. The volume change was dependent on the SUVmax within these volumes delineated by this method, and the SUVmax was positively correlated with the defined FV by this method.

The delineated FV was linked to the SUVmax within the volume and this was dependent on the method of delineation. There was a negative correlation between the radiation dose and the SUVmax in the FVs delineated by all methods. But the FV did not correlate with the SUVmax within the volume defined by the PTSUVmax. This was confirmed by the significant positive correlation between the FV delineated by the SUVCO thresholds and the SUVmax. One study found no association between these two variables in FVs delineated by an adaptive algorithm in patients with SCCHN [3]. The IAT defined primary FV used in this chapter did not correlate with the SUVmax, and only weakly with the LN FV.

The differences in FV between the thresholds will impact on dose escalation techniques. Higher thresholds that contour smaller volumes have the possibility of greater normal tissue sparing and increased escalated dose delivery. However, the SUV is not able to differentiate pathological SCCHN according to histological grade, and so a low SUV does not exclude SCC, it only indicates that

that particular area of tissue has a low rate of glucose metabolism. Therefore the main disadvantage of the SUVCO thresholds is the potential exclusion of cancerous tissue, as the SUV within the ROI is not taken into consideration in the threshold method.

The calculated theoretical dose required to reduce the primary FV to zero by the SUVCO method was 84 to 110Gy, and 58 to 68Gy for the LN volume. The greater the SUVmax, the larger the SUVCO defined FV will be. Larger volumes require larger doses of radiation to sterilise them, but interestingly the dose calculated here for the LN volume for the SUVCO thresholds of 2.5, 3.0, and 3.5bwg/ml is less than the standard macroscopic dose used in current RT regimes. This is purely due to the size of the defined volume because the theoretical dose required to reduce the LN FV to zero when defined by the IAT method was 80Gy.

The SLR model however cannot account for intra-tumoural biological changes and the development of resistant sub-populations of clonogenic cells during treatment. A lower SUV may also indicate cell cycle dormancy, which would need to be confirmed by proliferation markers, and mean that these volumes would be more likely to cause loco-regional failure.

The phenomenon of the increased primary and LN FV after 36Gy when defined by the thresholds of the percentage of the SUVmax despite a reduction in the SUVmax after these dose points is interesting. The primary and LN FV delineated by this method were susceptible to changes in background SUV uptake.

The LN FVs delineated by the IAT method were significantly reduced at 36 to 50Gy and 66Gy compared to the pre-treatment volume, but there was no significant correlation of dose and FV on regression modelling. There was also no significant reduction in the primary volume during treatment by this method. Neither volume correlated with radiation dose.

Unfortunately the PETVCAR software did not have the facility to overlay structure sets containing the FV defined either by different thresholds or by different methods within an image from single or multiple time points. The assessment of correspondence between the volumes defined by the different thresholds and methods could therefore not be performed.

The correspondence between volumes has been evaluated in a study of 78 patients with stage II to IV SCCHN. Four separate segmentation methods (visual interpretation, SUVCO [2.5g/ml], PTSUVmax [40% and 50%], and an adaptive threshold (used by Daisne et al [13])) were reviewed. Patients underwent separate CT and ¹⁸FDG PET imaging 0 to 10 days prior to the start of RT. The image sets were co-registered by an iterative algorithm. The ¹⁸FDG PET volumes delineated by the 50% of the SUVmax, and the signal to background ratio based thresholds over-lapped, and had greatest correspondence compared to volumes defined by the other methods [14]. The FV defined by the 2.5g/ml SUVCO threshold was at least 300cm³ greater than those defined by the other methods (mean volume: visual interpretation 21.5cm³, 40% of the SUVmax 16.5cm³, 50% of the SUVmax 10.5cm³, adaptive threshold 11.2cm³) [14]. Similar to Daisne et al [15], this group also reported that the PET volume extended outside the volume defined on conventional CT imaging. The volume difference noted when the SUVCO threshold was used was not corroborated by the results from this chapter.

Greco et al [16] in 2008 compared similar ¹⁸FDG CT-PET defined FV in 12 patients with SCCHN prior to the start of RT by visual interpretation, 50% of the SUVmax, 2.5g/ml SUVCO threshold, and an iterative segmentation algorithm. These volumes were compared to those defined on the CT RT planning scan. There was no significant difference between the 2.5g/ml SUVCO volumes and the CT volume (mean 60.0ml and 75.5ml respectively). The volume defined by the PTSUVmax was 77.74%, and the iterative volume 25% smaller than the CT volume.

Volume differences between thresholds may result from imaging related factors. In 6 patients with SCCHN, FVs were defined by a 50% threshold of the

SUVmax prior to the delivery of IMRT, and were outside the CT defined GTV by 0 to 72% [17].

The separate acquisition of PET and CT imaging in delineation studies can lead to mis-registration of image sets, and suggest no overlap or an overlap between the volumes. These volume differences can result from partial volume effects, patient movement during imaging of the PET component, differences in image resolution, and user defined differences for example window level setting [17].

PET volumes defined in 8 patients with SCCHN were compared with the delineation of ^{18}F FDG filled spheres within a cylindrical phantom [18]. The information gained from this process was applied to the volumes defined in patients. Two thresholds (42% and 50% of the SUVmax) were used. The post reconstruction smoothing of the PET images affected the final FV. This was associated with a loss of signal, which reduced the SUVmax and was associated with smaller FVs. Signal loss also occurred when a wide filter was used to smooth the ROI. The contoured ^{18}F FDG PET volumes were boosted to 77Gy for the 50% volume, and 72Gy for the 42% volume. The boost dose was different because the tumour volume at 42% of the SUVmax was 111.0cm^3 , and at 50% of the SUVmax this was 37.0cm^3 . The total radiation dose received by normal structures especially the cord and mandible remained the same.

The imaging and CT-PET guided FV used for RT planning should be reviewed in conjunction with an experienced Nuclear Medicine Physician and Clinical Oncologist and the FV modulated depending on extension. Extension of the volume into normal tissue may be due to the chosen threshold, or local infiltration of metabolically active disease. Unusual uptake on the attenuation and non-attenuation corrected images may be secondary to artefacts and physiological variants. Extreme variations in volume definition may reflect inaccuracies in co-registration, calibration, and ROI placement when automated algorithms are used.

Geets et al [19] reported 10 patients with pharyngo-laryngeal cancer who underwent 7 weeks of CRT. Prior to treatment CT, MRI, static and dynamic PET

imaging were undertaken, and at the mean prescribed dose of 14, 25, 35, and 45Gy. PET volumes were delineated by the automatic gradient-based method, and TVs on other imaging modalities were delineated by visual interpretation. The PET TVs were reduced by 15 to 40% during treatment, and were significantly smaller than those defined on CT. However, there was no significant difference between the volumes defined by CT or MRI.

The primary and LN FVs vastly differ accordingly to the delineation method, threshold, and the radiation dose received. Daisne et al [15] pathologically validated the ^{18}F FDG positive ROI within laryngeal macroscopic specimens. The PET volumes when auto-segmented by an iterative algorithm based on the signal to background ratio [13], were the most representative of the pathological true volume compared to CT and MRI defined volumes.

Pathological validation is required to assess if the imaging is representative of the in-vivo biological process under investigation. Further information may be gained by using H+E, IHC, and cytogenetic information for example. The ^{18}F FDG PET FV most closely represents the pathological volume, but cannot fully define it. If the wrong threshold and delineation method are chosen to define the RT volume, then a geographical miss may occur, causing an increased risk of loco-regional recurrence.

With increasing radiation dose, other factors are also important if ^{18}F FDG PET FVs are to be used for adaptive RT planning. Partial volume effects and edge definition are complicated by reduction in tumour volume, changes in the patient's weight, oedema associated with inflammation, and organ position.

Non-rigid methods of image registration aim to overcome these problems associated with deformity, and may help the accuracy of adaptive RT planning. Twelve deformable registration methods have been assessed for this use in patients with SCCHN [20]. Registration methods that incorporated local smoothing algorithms provided the greatest benefit to the co-registration of image sets at different time points during RT. The PETVCAR software co-

registered images according to rigid methods, which had the potential to increase the volume delineated.

TVs in patients with SCCHN have been defined prior to RT with an SUVCO threshold of 2.5bwg/ml, the PTSUVmax of 40% and 50%, and an adaptive threshold. The results are shown in table 4.19 and have been compared with those from this chapter. The adaptive and SUVCO thresholds are different, but between the 50% and 40% thresholds the volumes delineated were very similar, with a 35.97% reduction between the thresholded volumes reported by Schinagl [14], and 32.32% from the results of this chapter.

Table 4.19: Delineation volumes compared from UCLH and the reported study by Schinagl et al

	Threshold			
	SUV Cut Off 2.5bwg/ml (cm ³)	40% of the SUVmax (cm ³)	50% of the SUVmax (cm ³)	Adaptive (cm ³)
Schinagl	>300.0	16.40	10.50	11.20
UCLH Patients	34.95	16.18	10.95	23.95

This illustrates the similarities and differences of volume definition depending on the threshold used. However the patient population, and adaptive threshold calculations are different. The extremely large volume gained by the use of the SUVCO threshold suggests that background uptake of ¹⁸FDG within the HN is varied. PETVCAR may have been able to segment the background from tumour ¹⁸FDG uptake better at this threshold.

It is interesting that the primary FV delineated by the IAT in the 8 patients investigated in this chapter did not show a significant reduction during RT, where as the LN volume did. This may have been due to the smaller number of FV investigated within the study. The macroscopic primary and LN FV were

within the higher radiation dose field. The effect of confluent mucositis within the pharyngeal mucosa may have had a greater impact on these volumes, but such mucositis would have been absent within the deep tissues of the neck. Hentschel et al in 2009 [3] reported that adaptive threshold defined FVs increased in size with increased radiation dose, and did not correlate with the SUVmax. The IAT method was dependent on the difference between the SUVmax and SUVmean within the ROI, as well as the background SUV. Small differences in the SUVmax and mean would potentially reduce the ability of the software to auto-segment and delineate tumour volume from the background ^{18}F FDG uptake.

It would be prudent to repeat the delineation in a prospective study using PETVCAR, and compare the volumes delineated by the IAT to those on a phantom with differing levels of known ^{18}F FDG activity. The true phantom and patient volumes could then be correlated and the differences assessed.

The results from this chapter suggest a number of dosimetric implications. The SUVCO threshold is potentially of greater benefit for dose escalated FV definition during RT.

The IAT delineation method may be more beneficial from the start of treatment rather than planning a potentially larger volume delineated by this method during treatment for use in dose escalation studies. Larger PET FVs delineated have less possibility of dose escalation due to the larger amount of normal tissue that may be irradiated as a consequence.

Tissue sparing has been shown to be possible when RT treatment is re-planned using the smaller PET defined TV [21] with no increase in spinal cord or brainstem doses [18]. However, the microscopic dose to the prophylactic areas will not change. During RT also organs such as the parotid glands move medially and enter the high dose volume contributing to late morbidity.

Madani et al [22] reported 41 patients with SCCHN treated to two dose escalated levels by an IMRT SIB technique (total dose of 72.5Gy, 2.5Gy per fraction, and

77.5Gy, 3.0Gy per fraction) for 10 fractions. The PET volume was defined on a pre-RT ^{18}F FDG PET using an automatic segmentation algorithm based on the signal to background ratio. For PET volumes greater than 10cm^3 , the central 10cm^3 with the highest SUVmax received IMRT dose escalation at 3Gy per fraction, and the remaining volume was escalated to 2.5Gy per fraction. The dose limiting toxicity was not reached in this study. One patient experienced Grade 4 skin toxicity at 59.6Gy. The commonest acute toxicities were dysphagia and mucositis, with fibrosis and dysphagia being the commonest late ones. These results should be interpreted with caution. The follow-up was only 1 year with a median survival in this group of 14 months, and no statistically significant differences were found for acute or late toxicity, or the one-year disease specific survival.

Further studies are required to assess the optimal time of imaging, and optimal method for dose escalation. It may also be possible to dose escalate both the primary and LN volumes to a different final dose either using the IAT based on the risk of the individual ROI according to the SUVmax within it or the SUVCO threshold.

The advantage of the IAT, and the PTSUVmax methods over the SUVCO method is the lack of the absolute threshold. For example an SUVCO threshold would not define a FV if the SUVmax was less than the threshold. However the other two methods take the individual SUVmax within the ROI into account during the delineation process.

The argument for the use of the SUVCO is the demarcation of benign and malignant disease by the reporting clinician. Each tumour ROI has its own biological phenotype that is distinct from another region within the patient. Its use therefore is controversial for ^{18}F FDG PET FV delineation prior to the start of treatment. We have however demonstrated that this method is influenced less by the background uptake of ^{18}F FDG and therefore is more applicable to use during RT for dose escalation strategies.

Indeed no primary ROI had an SUV of less than or equal to 2.5bwg/ml either prior to the start or during RT. Also no LN ROI had a SUV less than or equal to 2.5bwg/ml before the start of RT. From 36Gy the SUVmax within the LN FVs did in some patients fall below this value indicating reduced intra-tumoural glucose metabolism.

4.4.6 The SUV used to Define the Edge of the Functional Volume

The results from this chapter have shown that the FVs delineated by the PTSUVmax increased after 36Gy and continued to increase up to the completion of treatment. The method of volume delineation for the IAT and the potential pitfalls of an SUV within the ROI that is similar to the background uptake of ^{18}F FDG have been discussed.

The underlying cause for this increased volume after 36Gy in both the primary and LN FV is because the ^{18}F FDG uptake is the same as or less than the background uptake. This effect is less evident at higher thresholds. The PETVCAR software cannot then differentiate tumour and background ^{18}F FDG uptake, and the entire boundary box rather than any tumour present inside it is delineated.

Table 4.20 shows the calculated ratio of the SUV used to define the edge (mean primary, median LN) and the background SUV. This table shows that at 0Gy, and 8 to 18Gy the ratio in both volumes is greater than 1.0. However at 66Gy this ratio especially at the lower thresholds was less than 1.0 for the LN FV (the tumour was iso-intense or hypo-intense compared to the background uptake). This indicates the difficulty experienced by the software in defining the SUV uptake within the ROI from background uptake, resulting in the larger volumes from 36 to 66Gy.

Table 4.20: The calculated tumour edge to background ratios for the primary and lymph functional volumes delineated by the percentage threshold of the SUVmax

Threshold		Tumour to Background Ratio			
		0Gy	8 to 18Gy	36 to 50Gy	66Gy
30%	Primary	3.24	3.01	1.89	1.45
	Lymph Node	1.73	1.42	0.83	0.70
35%	Primary	3.79	3.52	2.18	1.71
	Node	2.00	1.61	1.00	0.82
40%	Primary	4.27	4.04	2.50	1.96
	Lymph Node	2.31	1.83	1.12	0.97
45%	Primary	4.83	4.53	2.80	2.23
	Lymph Node	2.50	2.11	1.24	1.03
50%	Primary	5.40	5.06	3.16	2.47
	Lymph Node	2.88	2.33	1.36	1.17

This has been confirmed by Daisne et al [13] who found FVs delineated by the PTSUVmax were more susceptible to lower tumour to background ratios, especially when less than 1.5 [19].

Other studies in SCC cervix suggested that the PTSUVmax method required a tumour to background ratio of greater than 10 to effectively delineate the PET volume prior to definitive RT [23]. The results from this chapter and also from Schinagl [14] have not supported this finding. This may be due to differences in tumour biology at different anatomical sites.

The inherent assumption of all the automatic delineation methods is that the background SUV uptake is homogenous across the patient, and therefore representative. Heterogenous background uptake is likely to occur, and the method of delineation is then dependent on the placement by the user of the ROI to define this uptake. One method to overcome this is to take a number of background values of ¹⁸FDG uptake that are representative of the area to be treated.

4.4.7 Imaging Protocol

The study was designed to image patients during radical RT or CRT at four time points 0, 10, 44, and 66Gy. These time points were selected because the curative RT for these patients at UCLH is to a total dose of 66Gy conventionally delivered.

The first two imaging points corresponded to the treatment of microscopic disease during Phase I. The third imaging point was selected because this was when the second phase of RT treatment started. The last imaging point was the completion of treatment. This time point was chosen because if ^{18}F FDG avid areas were still present with a high SUV, then this would have suggested that the metabolic response to RT had been small and loco-regional recurrence was likely at this site. This final volume could then be assessed and voxel based dose escalation strategies applied. Although it could be argued that volume delineation at this time point is too late for adaptive treatment strategies. It has been important to view the response at 66Gy in relation to the delineation method, and has indicated that adaptive CT-PET guided dose escalation strategies should be imaged between 36 to 50Gy.

The study did not incorporate CT-PET in the follow-up of patients after they completed treatment. Future studies using dose escalation techniques should incorporate this to assess ^{18}F FDG uptake, and the effectiveness of dose escalation on loco-regional control.

Further CT-PET imaging should be undertaken at a minimum of 4 months following completion [24], but also at 6, 12 and 24 months after treatment. This is because recurrence is commonest during the first 2 years after treatment.

The PETVCAR software that has been used to delineate the FVs in this chapter and would allow the post-treatment imaging to be co-registered with the pre-treatment imaging and the delineated volumes propagated as bookmarks to the same location on the subsequent scans. The volumes could then be directly measured for loco-regional control and other parameters such as SUVmax correlated with this.

4.4.8 Collaboration

All delineation methods need to be validated within departments (on individual CT-PET scanners), and between departments for collaborative studies using PET radio-nuclides. Collaboration would provide greater patient recruitment and increased validity of results. Phantom calibrations are required to assess the accuracy of edge delineation techniques to aid comparability. This is because the delineation methods are dependent on the internal hard and software calibration factors of the individual camera.

The advantage of the PETVCAR software although not commercially available yet within the UK, is that it does provide a standardised method for delineation which is transferable between institutions once availability is increased. A major criticism of PET studies to date is that patient numbers are small, but also the automatic delineation algorithms are made and adapted in-house limiting the transferability and reproducibility of data. This minimises collaboration between centres especially when adaptive thresholding methods are used.

The other advantage is the dual purpose for reporting and response assessment of CT-PET imaging with ^{18}F FDG and other radio-nuclides with the PETVCAR software. This indicates the cost-effectiveness of purchasing this software, especially as it is used in conjunction with the Advantage Workstation for Windows software that is commercially available and used by PET Centres across the UK.

4.4.9 Possible Strategies for Dose Escalation

The concept of the biological target volume derived from functional imaging, and its potential use to guide and sculpt increased radiation dose delivery was first proposed in 2000 by Clifton Ling [25].

Dose escalation strategies may be by a number of different methods including: boost towards the end or after completion of RT (high dose rate brachytherapy, IMRT, or intensity modulated arc therapy (IMAT), modulation of dose per voxel depending on the SUV within it, particle beam therapy with protons (Intensity Modulated Proton Therapy), or stereotactic radiation). Alternatively, the

escalated dose may be incorporated from the start of treatment by photons or particle therapy. Currently the optimal dose escalation method is still being debated. Proton therapy is currently not available within the UK, and stereotactic RT facilities are limited. IMRT and less commonly IMAT are the most available within RT centres.

Dose escalated IMRT or IMAT may be delivered by two techniques: either SIB to the CT-PET FV from the start or at a time point during RT treatment, or voxel-based dose painting. The SIB technique has the potential for the most widespread use as this may be implemented on current software used to plan IMRT within departments, and in centres with no experience of PET based planning. Voxel-based dose painting requires dynamic PET data to allow 4D dose modulation, and is limited by the spatial resolution of the PET voxel. This can produce partial volume effects, and the need for dynamic imaging protocols are required for this technique.

Further studies are required to assess the effect of dose escalation on normal tissue [18,22,26], function, loco-regional and survival outcome, but initial studies are promising.

4.4.10 Other Applications of CT-PET Guided Adaptive Radiotherapy

Adaptive PET guided strategies will undoubtedly lead to improvements in loco-regional control and survival. However, these improvements are of most benefit when functional outcome is not compromised.

¹⁸FDG CT-PET may be used to potentially predict the response of normal tissue to irradiation, and therefore guide dose escalation strategies.

For example a study in patients with NSCLC, found the development of acute radiation pneumonitis could potentially be predicted by the ¹⁸FDG uptake in irradiated lung during RT. The mean SUV when the mean lung dose was greater than 10Gy was 2.66g/ml after 40 to 49Gy compared to 1.89g/ml at 40 to 49Gy when the mean lung dose was less than 10Gy [27]. A similar increased risk of radiation-induced pneumonitis had been reported in patients with oesophageal

cancer [28,29]. The implication of this is not only to predict normal tissue reaction but also to guide dose escalation strategies. Patients who have a lower SUV in normal lung during RT may have a greater possibility of a dose escalated boost without increasing the risk of radiation induced pneumonitis.

This has the potential to be extrapolated to normal tissue within the HN such as the constrictor muscles of the pharynx, and parotid glands. ^{18}F FDG guided CT-PET FVs can then be dose escalated, and may also guide dose delivery to avoid normal tissue with a higher background ^{18}F FDG uptake that may be at greater risk of late radiation induced damage.

4.5 Conclusions

Early studies using ^{18}F FDG PET in SCCHN reported the potential benefit to all patients who underwent RT planning but especially those with T3 and T4 primary tumours, and N2 and N3 nodal disease [30]. Out of the published studies which evaluated the clinical impact of ^{18}F FDG PET on TV definition, imaging on combined machines was uncommon, and different thresholds using differing delineation methods at multiple time points during a course of curative RT in this group of patients was rare (no more than two threshold usually 40 and 50% of the SUVmax from same method were compared at baseline).

The results from this study suggest that the volume delineated during RT is strongly dependent on both the threshold, and method used to delineate the ^{18}F FDG positive FV. The background uptake of ^{18}F FDG within the HN has less impact on the FVs defined by the SUVCO method and may be of greater benefit when use to guided dose escalated RT during treatment. However there was a significant impact of this background uptake especially on volumes delineated by the PTSUVmax and the IAT method.

The SUVmax influences the FV when delineated by the SUVCO method, but this relationship is less clear-cut when volumes are defined according to the

PTSUVmax and the IAT methods, as other factors such as radiation-induced mucositis have an increasingly important role.

There is no clear consensus as to which method is best from the published data both in SCCHN and NSCLC. There is though a move towards the use of adaptive algorithms for volume delineation at the start of RT although these methods have little benefit during RT.

The SUVCO method may prove on larger studies to be best at delineating volumes to allow adaptive RT planning with IMRT. Even this though requires significant software availability to allow auto-contouring of normal tissue structures to aid the planning process. Regardless of which method is used either between or within institutions, a flexible, and close working relationship with the Nuclear Medicine (and CT-PET Centre) is required to aid delineation and maximise the benefit of ^{18}F FDG CT-PET imaging in the RT planning process of patients with SCCHN.

Future assessment of dose escalation to ^{18}F FDG CT-PET guided FV depends on a number of factors most importantly: the delineation method, threshold for FV delineation, time point of functional imaging, time point of dose escalation (for example simultaneous integrated boost delivered through IMRT from the start of treatment, voxel based dose painting with dose modulation at a given time point to “boost” the metabolically active FV), the method of dose escalation (IMRT, RapidArc, CyberKnife, Particle therapy), as well as intra-tumoural factors such as size, and SUV. Collaborative approaches between institutions are required to improve PET based RT planning, as well as attempting to standardise the software used for volume definition. Ultimately in combination PET guided TV delineation has the potential to improve outcome in patients with SCCHN.

4.6 References

1. Higashi K, Clavo AC, Wahl RL. In vitro assessment of 2-fluoro-2-deoxy-D-glucose, L-methionine and thymidine as agents to monitor the early response of a human adenocarcinoma cell line to radiotherapy. *J Nucl Med* 1993;34:773-779
2. Hautzel H, Muller-Gartner HW. Early changes in fluorine-18-FDG uptake during radiotherapy. *J Nucl Med* 1997;38:1384-1386
3. Hentschel M, Appold S, Schreiber A, et al. Serial FDG-PET on patients with head and neck cancer: implications for radiation therapy. *Int J Radiat Biol* 2009;85:796-804
4. Denekamp J, Stewart FA, Douglas BG. Changes in the proliferation rate of mouse epidermis after irradiation continuous labelling studies. *Cell Tissue Kinet* 1976;9:19-29
5. Handschel J, Sunderkotter C, Prott FJ, et al. Increase of RM3/1-positive macrophages in radiation-induced oral mucositis. *J Pathol* 2001;193:242-247
6. Kubota R, Kubota K, Yamada S, et al. Microautoradiographic study for the differentiation of intratumoral macrophages, granulation tissues and cancer cells by the dynamics of fluorine-18-fluorodeoxyglucose uptake. *J Nucl Med* 1994;35:104-112
7. Steel G ed. *Basic Clinical Radiobiology*. 3rd ed: Arnold 2002
8. Kubota R, Yamada S, Kubota K, et al. Intratumoral distribution of fluorine-18-fluorodeoxyglucose in vivo: high accumulation in macrophages and granulation tissues studied by microautoradiography. *J Nucl Med* 1992;33:1972-1980

9. Kazama T, Swanston N, Podoloff DA, Macapinlac HA. Effect of colony-stimulating factor and conventional- or high-dose chemotherapy on FDG uptake in bone marrow. *Eur J Nucl Med Mol Imaging* 2005;32:1406-1411
10. Ong SC, Schoder H, Lee NY, et al. Clinical utility of 18F-FDG PET/CT in assessing the neck after concurrent chemoradiotherapy for Locoregional advanced head and neck cancer. *J Nucl Med* 2008;49:532-540
11. Andrade RS, Heron DE, Degirmenci B, et al. Posttreatment assessment of response using FDG-PET/CT for patients treated with definitive radiation therapy for head and neck cancers. *Int J Radiat Oncol Biol Phys* 2006;65:1315-1322
12. Abouzied MM, Crawford ES, Nabi HA. 18F-FDG imaging: pitfalls and artifacts. *J Nucl Med Technol* 2005;33:145-155; quiz 162-143
13. Daisne J-F, Sibomana M, Bol A, et al. Tri-dimensional automatic segmentation of PET volumes based on measured source-to-background ratios: influence of reconstruction algorithms. *Radiotherapy and Oncology* 2003;69:247-250
14. Schinagl DA, Vogel WV, Hoffmann AL, et al. Comparison of five segmentation tools for 18F-fluoro-deoxy-glucose-positron emission tomography-based target volume definition in head and neck cancer. *Int J Radiat Oncol Biol Phys* 2007;69:1282-1289
15. Daisne JF, Duprez T, Weynand B, et al. Tumor volume in pharyngolaryngeal squamous cell carcinoma: comparison at CT, MR imaging, and FDG PET and validation with surgical specimen. *Radiology* 2004;233:93-100

16. Greco C, Nehmeh SA, Schoder H, et al. Evaluation of different methods of 18F-FDG-PET target volume delineation in the radiotherapy of head and neck cancer. *Am J Clin Oncol* 2008;31:439-445
17. Scarfone C, Lavelly WC, Cmelak AJ, et al. Prospective feasibility trial of radiotherapy target definition for head and neck cancer using 3-dimensional PET and CT imaging. *J Nucl Med* 2004;45:543-552
18. Ford EC, Kinahan PE, Hanlon L, et al. Tumor delineation using PET in head and neck cancers: threshold contouring and lesion volumes. *Med Phys* 2006;33:4280-4288
19. Geets X, Tomsej M, Lee JA, et al. Adaptive biological image-guided IMRT with anatomic and functional imaging in pharyngo-laryngeal tumors: impact on target volume delineation and dose distribution using helical tomotherapy. *Radiother Oncol* 2007;85:105-115
20. Castadot P, Lee JA, Parraga A, et al. Comparison of 12 deformable registration strategies in adaptive radiation therapy for the treatment of head and neck tumors. *Radiother Oncol* 2008;89:1-12
21. Geets X, Daisne JF, Tomsej M, et al. Impact of the type of imaging modality on target volumes delineation and dose distribution in pharyngo-laryngeal squamous cell carcinoma: comparison between pre- and per-treatment studies. *Radiother Oncol* 2006;78:291-297
22. Madani I, Duthoy W, Derie C, et al. Positron emission tomography-guided, focal-dose escalation using intensity-modulated radiotherapy for head and neck cancer. *Int J Radiat Oncol Biol Phys* 2007;68:126-135
23. Miller TR, Grigsby PW. Measurement of tumor volume by PET to evaluate prognosis in patients with advanced cervical cancer treated by radiation therapy. *Int J Radiat Oncol Biol Phys* 2002;53:353-359

24. Greven KM, Williams DW, 3rd, McGuirt WF, Sr., et al. Serial positron emission tomography scans following radiation therapy of patients with head and neck cancer. *Head Neck* 2001;23:942-946
25. Ling CC, Humm J, Larson S, et al. Towards multidimensional radiotherapy (MD-CRT): biological imaging and biological conformality. *Int J Radiat Oncol Biol Phys* 2000;47:551-560
26. Thorwarth D, Eschmann SM, Paulsen F, Alber M. Hypoxia dose painting by numbers: a planning study. *Int J Radiat Oncol Biol Phys* 2007;68:291-300
27. Song H, Yu JM, Kong FM, et al. [18F]2-fluoro-2-deoxyglucose positron emission tomography/computed tomography in predicting radiation pneumonitis. *Chin Med J (Engl)* 2009;122:1311-1315
28. Guerrero T, Johnson V, Hart J, et al. Radiation pneumonitis: local dose versus [18F]-fluorodeoxyglucose uptake response in irradiated lung. *Int J Radiat Oncol Biol Phys* 2007;68:1030-1035
29. Hart JP, McCurdy MR, Ezhil M, et al. Radiation pneumonitis: correlation of toxicity with pulmonary metabolic radiation response. *Int J Radiat Oncol Biol Phys* 2008;71:967-971
30. Rahn AN, Baum RP, Adamietz IA, et al. [Value of 18F fluorodeoxyglucose positron emission tomography in radiotherapy planning of head-neck tumors]. *Strahlenther Onkol* 1998;174:358-364

Chapter 5

Hypoxic Imaging in Squamous Cell Carcinoma of the Head and Neck with ^{64}Cu -ATSM

5.1 Material and Methods

5.1.1 Patient Recruitment

Patients were recruited according to the eligibility criteria in table 5.1 from UCLH.

Table 5.1: Inclusion and exclusion criteria

Inclusion Criteria	Exclusion Criteria
Primary surgical resection for locally advanced SCCHN	Impaired renal function (serum creatinine greater than 200)
Histo-pathological or cytological confirmation of SCCHN	Severely impaired liver function
Age 50 years or older	Urinary or faecal incontinence
ECOG Performance Status 0 to 2	Uncontrolled psychiatric disturbance
Life expectancy greater than 12 weeks	ECOG performance status greater than 3
Adequate organ function Absence of other major concomitant illness	Second primary tumour within the HN to be treated by modality other than primary surgery

Eligible patients were identified at the multi-disciplinary team meeting and all relevant investigations reviewed. Patients were recruited in the Ear, Nose and Throat, and Oral and Maxillo-Facial clinics, and given verbal and written

information concerning trial participation. Recruitment was according to GCP guidelines. Written consent was obtained from all patients prior to participation.

Patients could withdraw from the study on request, or were withdrawn if there was non-compliance, significant patient co-morbidity, inter-current illness, or difficulty with the production of ^{64}Cu -ATSM at St Thomas' Hospital.

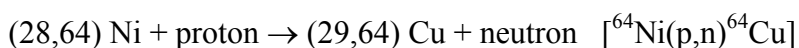
5.1.2 Trial Arm Allocation

Patients were allocated to 3D dynamic CT-PET imaging of the HN only, 3D dynamic CT-PET of the HN followed by DCE-CT, and 3D dynamic CT-PET, DCE-CT with delayed static CT-PET 18 to 24 hours after the injection of ^{64}Cu -ATSM.

5.1.3 ^{64}Cu -ATSM Production at St Thomas' Hospital

^{64}Cu -ATSM was produced and purified according to McCarthy et al [14, 15] to good manufacturing practice standards, by Dr Rowena Paul at the Clinical PET Centre, Guy's and St Thomas' Hospital, London.

In summary ^{64}Ni was electroplated onto a gold target. The electroplated target was loaded and rotated into the line of the cyclotron (CTI RDS 112 11MeV model, positive ion machine). The target was bombarded with 11MeV protons for 5 to 8 hours for batches of 1GBq depending on the activity required. Operating parameters during irradiation were: beam current 20 to 30 μA +/- 5 μA .



Eluting with hydrochloric acid purified the ^{64}Cu to produce $^{64}\text{CuCl}_2$. Purified H_2ATSM was dissolved in dimethyl-sulphoxide, and added to the $^{64}\text{CuCl}_2$ to produce ^{64}Cu -ATSM. This was then Sep –Pak conditioned, purified with ethanol, and combined with ascorbic acid to a concentration of 1mg of ascorbic acid per ml of ^{64}Cu -ATSM solution.

This solution was chemically stable for over 24 hours, and the addition of ascorbic acid prevented radio-lysis. Quality assurance procedures including pH analysis and isotope identity testing were then completed prior to the release of the radio-nuclide for clinical use.

Appendix 4 contains the production process of ^{64}Cu -ATSM in detail.

5.1.4 Administration of ^{64}Cu -ATSM

The ^{64}Cu -ATSM was transported from St Thomas' Hospital to UCLH in a lead container. The activity in MBq was calculated and calibrated on arrival by Physicist Dr J Dickson at UCLH and stored until required (1Bq = 1 disintegration per second). This activity was compared to the activity on the quality assurance certification. The patient's height (cm) and weight (Kg) were recorded, and details re-confirmed. The ^{64}Cu -ATSM was drawn-up by the Superintendent Radiographer (Miss Caroline Townsend), immediately prior to the start of imaging, into a 5ml sterile syringe encased in a lead syringe holder.

Patients were positioned supine, with their arms by their sides. Their head was placed in the head holder on the couch of the CT-PET machine and secured in place with a Velcro attachment. A scout CT of the HN was undertaken to ensure the patient was in the correct position to encompass the entire ROI.

The patient then underwent the defined CT HN. The couch was then advanced into the PET section of the scanner. The ^{64}Cu -ATSM was intra-venously injected into a cannula in the patient's forearm, and the dynamic imaging started at the time of injection.

5.1.5 Imaging Protocols

Patients underwent all imaging on the GE Discovery DVCT-64 CT-PET machine (64 slice combination volumetric CT and PET imager). The Nuclear Medicine Department staff completed all imaging procedures. The imaging protocols, and radiation exposure are illustrated in table 5.2a to c. Only the protocols used for the patients enrolled have been included.

Table 5.2a: Acquisition protocol for the immediate 3D dynamic Head and Neck CT-PET

Parameter	Acquisition
CT	Scout 120 kVp, 10mA CT 140 kVp, 80 mA, 0.8s, Pitch 1.75 CT slice thickness 3.75mm
PET	3D, 1 hour List Mode Dynamic Frames : 30 x 2 sec, 12 x 10 sec, 6 x 20 sec, 5 x 60 sec, 10 x 300 sec
PET Reconstruction	Iterative (3D-OSEM) 20 subsets, 2 iterations Post-Filter 6.00mm Full Width Half Maximum Slice Thickness 3.27mm Reconstruction diameter 70cm
Radiation Exposure	PET: 21.6mSv (based on a dose of 600MBq of ⁶⁴ Cu-ATSM) CT: 3.4mSv Total: 25.0mSv

Table 5.2b: Acquisition protocol for the 3D static Head and Neck CT-PET 18 to 24 hours after ⁶⁴Cu-ATSM injection

Parameter	Acquisition
CT	Scout 120 kVp, 10mA CT 140 kVp, 80 mA, 0.8s, Pitch 1.75 CT Slices 3.75mm
PET	3D for 20 Minutes single static random frame 3D for 40 Minutes single static random frame Both protocols are imaged in List Mode to help assess image quality.

PET Reconstruction	3D Iterative (OSEM) Filtered back projection 20 subsets, 2 iterations Post-Filter 6.00mm Full Width Half Maximum Slice Thickness 3.27mm Reconstruction diameter 70cm
Radiation Exposure	Immediate dynamic CT-PET: 25.0mSv Late static CT-PET: 3.4mSv Total: 28.4mSv

The DCE-CT was started after completion of the CT-PET. First, the 4cm region within the tumour was chosen in conjunction with the Nuclear Medicine Consultant (Dr I Kayani), and the scan extent programmed into the software. A 50ml sterile saline (0.9%) intra-venous infusion (4ml/sec) was administered to assess and ensure venous patency. Finally, 50ml of Omnipaque 350 (4ml/sec) was remotely administered, and the dynamic CT obtained 35 seconds after this. Table 5.2c illustrates the acquisition protocol for the DCE- CT.

Table 5.2c: Acquisition protocol for the dynamic contrast-enhanced CT

Parameter	Acquisition
CT	Scout 120 kVp, 10mA Scan Delay (after contrast): 35 seconds CT: 100 kVp, 100 mA, Axial 1.0s, Duration: 60 seconds 8 images per rotation, 1 second scan, inter-scan delay of 2.5 seconds and 5mm collimation of detectors Reconstruction: 5mm (Standard), diameter of the field of view 50cm
Radiation Exposure	8.9mSv Immediate CT-PET and DCE-CT: Total: 33.9mSv Immediate CT-PET, DCE-CT, and late imaging at 18 to 24 hours: Total 37.3mSv

5.1.6 Administration of Pimonidazole

Pimonidazole (HypoxyprobeTM, NPI Inc., Masschusettes, USA) was administered to all patients intra-venously at least 16 hours prior to surgery. The freeze-dried product was stored at 4°C in the Pharmacy Department of UCLH, and supplied (Natural Pharmacia International, Inc., Massachusetts, USA) in 1g vials.

The vial was brought to room temperature by warming in the hands, and reconstituted in 10ml of sterile 0.9% normal saline (concentration of 0.1g/ml). Pimonidazole was administered at a dose of 0.5g/m² in 100ml of 0.9% normal saline over 20 minutes, via a light protective infusion set and filter. The dose was capped at a BSA of 2.0m², and the BSA calculated according to the equation below.

$$\text{BSA (m}^2\text{)} = ([\text{Height(cm)} \times \text{Weight(kg)}] / 3600)^{1/2} [1]$$

5.1.7 Time of Surgery

Surgical teams and theatre staff were informed of each recruited patient. Patients underwent a general anaesthetic, and were positioned on the operating table according to the preparation for the surgical procedure to be carried out.

Photographs were taken intra-operatively, using a Cannon G9 Powershot (12.1 mega pixel, product code 2082B001) camera, to aid orientation and co-registration of the histological specimen with the CT-PET. The specimen was sutured onto a plastic template if required, to aid orientation by the reporting Pathologist. Figure 5.1 illustrates the template.

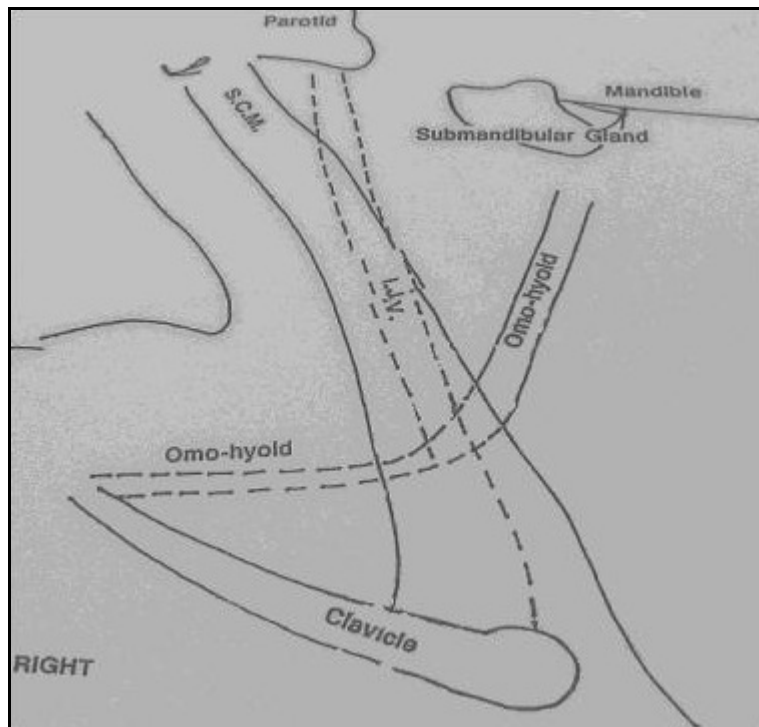


Figure 5.1: Surgical template for neck dissection specimens

The surgeon indicated critical margins, and identified general territories of nodal groups with sutures. Additional macroscopic specimens were sent in separate pots to the Pathology Department depending on the intra-operative findings. Surgical surfaces were inked to aid orientation and co-registration with CT-PET data if there were no defining features. India inks were used on discussion with the Pathology Department, and were standard colours for mastectomy specimens. These were: red (superior margin), green (inferior), medial (yellow), blue (anterior), black (posterior), and lateral (no ink). Prior to inking, the surgical surface was wiped dry with 100% alcohol by volume.

All specimens were placed in specimen pots containing 10% neutral buffered formalin with the volume of fixative ten times the volume of the tissue.

Specimens were immediately taken to the Nuclear Medicine Department, once they were signed out from theatre. The specimen was removed from the pot, placed on a tray, and a CT scan undertaken on the same CT-PET machine the patient was scanned on to aid the co-registration process. Following this, the specimen was returned to the specimen pot, taken directly to the Pathology

Department, signed in, and immediately reviewed by the Duty Pathologist. The specimen remained in 10% neutral buffered formalin for a minimum to 24 to 48hrs prior to macroscopic dissection.

Initially a CT-PET scan was planned of the specimen. However because of the timing of surgery, the specimen would needed to be scanned for a minimum of 12 hours (depending on residual activity) over night. This was not possible because the specimen needed to be logged into Pathology Reception the same day as the procedure according to local Standard Operating Procedures.

5.1.8 Preparation of Macroscopic Specimen Following Formalin Fixation

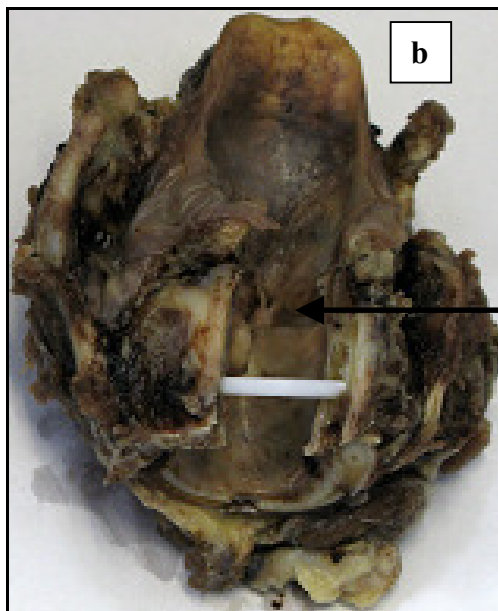
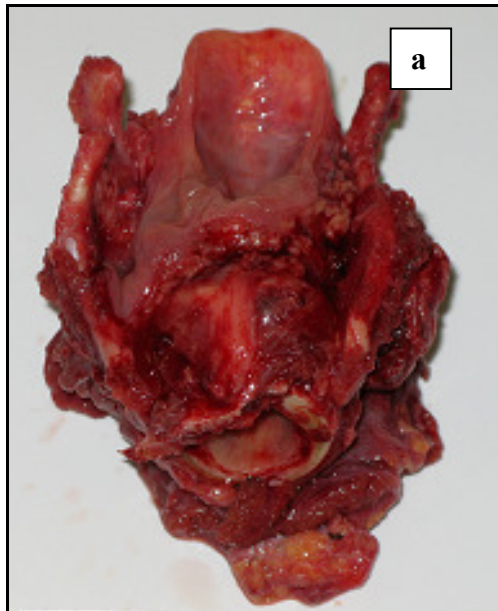
Macroscopic examination was according to the Royal College of Pathologists and undertaken by Dr Amrita Jay (Consultant Pathologist) at UCLH.

The specimen was removed from the specimen pot, further photographs taken, and diagrams annotated to aid future specimen orientation. Specimens were orientated, inspected, and dimensions recorded.

For ND specimens, surrounding structures were reviewed from the outer aspect, and the internal jugular vein was identified on the deep aspect to aid orientation. Lymph nodes were identified by inspection and palpation to the appropriate anatomical level. Each discrete node was dissected out with the attached pericapsular adipose tissue by scalpel. Larger nodes were bisected through the hilum or sliced according to the plane of orientation. The extent of extra-capsular spread was assessed by further dissection along the nodal capsular edge, together with the peri-nodal tissues. Small or flat nodes were processed whole. Tissue was placed in cassettes prior to automated wax embedding.

Laryngeal specimens were macroscopically reviewed, and sectioned through the posterior wall in the cranio-caudal direction to expose the mucosal surface. The specimen was then placed in formic acid for a minimum of 5 days depending on the extent of calcification. After this the larynx was either sectioned using a scalpel into axial rings or longitudinally. Figure 5.2a to c illustrates the fresh

laryngeal sample intra-operatively a), the sample after formalin fixation and posterior dissection b), and finally after axial dissection c). The area of squamous cell cancer is visible on each axial section as a creamy pale area indicated by the arrow.



**Tumour ulcer
on mucosal
surface**

Figure 5.2a and b: Fresh macroscopic larynx a) and formalin fixed larynx b)

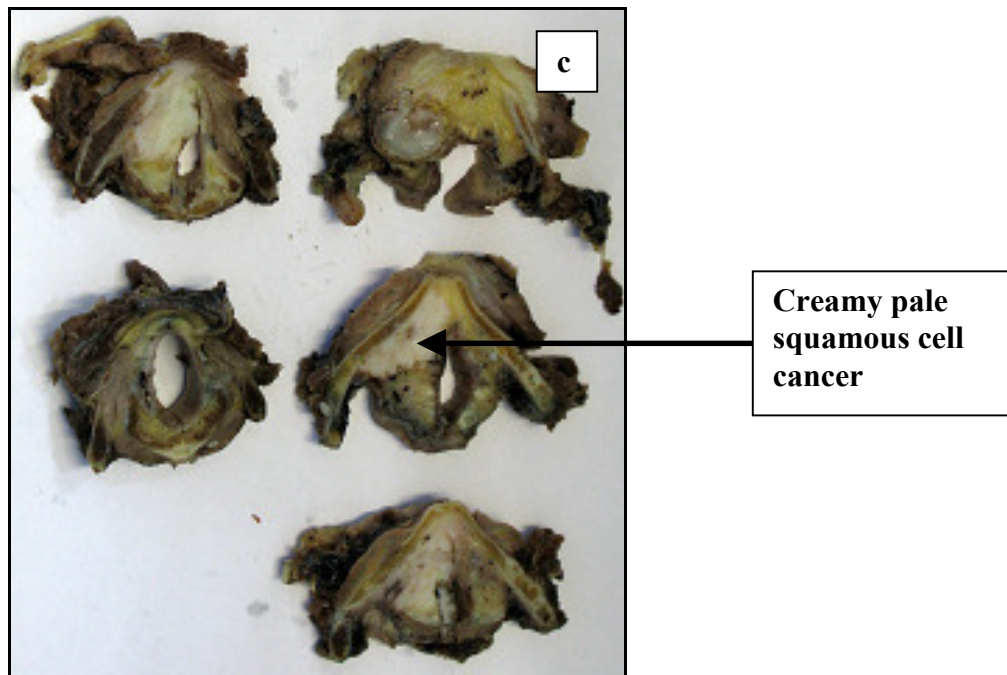


Figure 5.2 c: Formalin fixed axially sectioned larynx

5.1.9 Preparation of the Microscopic Specimen

The formalin fixed dissected specimen was processed automatically overnight within the Pathology Department. In summary, first graded alcohols were used to dehydrate the specimen. The alcohol was cleared with xylene. The specimen was infiltrated and embedded with liquid paraffin wax, and cooled. An example of the fixed wax embedded tissue is shown in figure 5.3. The arrow indicates the area of SCC.

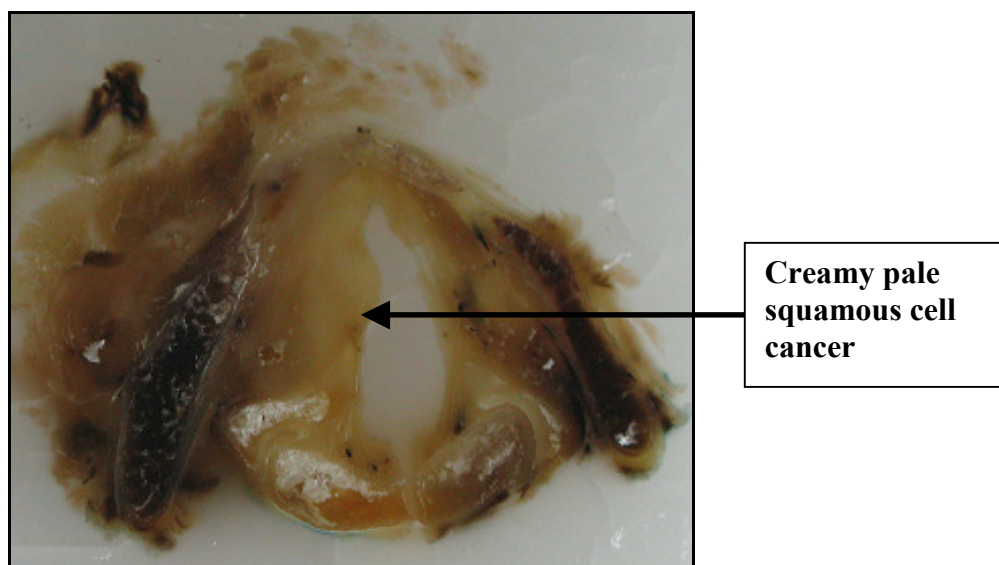


Figure 5.3: Wax embedded laryngeal specimen

The specimen block was cut into 4µm thick sections using a microtome. Tissue slices were floated on a water bath, and then captured on a glass slide and baked in an oven at 56°C for 30minutes. The resulting slides were H+E stained. The Medical Laboratory Scientific Officers within the Pathology Department completed this process. Dr A Jay then reported the H+E stained specimen.

5.1.9 Immuno-Histochemical Staining of Specimens

The IHC staining procedure was similar for all antigens. It has been explained for pimonidazole only. Antibody dilutions, and any deviations from this process are indicated for each IHC stain.

5.1.9.1 Pimonidazole

Pimonidazole adducts were detected by a two-step immuno-histochemical procedure using a primary fluorescein (FITC)-conjugated mouse monoclonal antibody (Mab) directed against the pimonidazole protein adducts and a secondary mouse anti-FITC Mab conjugated to horseradish peroxidase. Human bladder SCC was used as a control, and had previously stained positive for pimonidazole.

Four-micron wax-embedded sections were dewaxed in xylene for five minutes, and then rehydrated through graded alcohols (100, 90, and 70%) to water. Antigen retrieval was then performed. The slides were placed in a bath of 10mM citric acid pH 6.0 and boiled for 8 minutes using an 800W microwave oven (2450MHz Panasonic NN-6453BBPQ). The volume of fluid was topped up to its original level if it had evaporated to maintain the pH. The slides were left to stand for 20 minutes at room temperature and then washed in running tap water.

Slides were rinsed in Tris Buffered Saline (TBS) (Dako A3536), and Dako Peroxidase block was applied for 5 minutes. They were then rinsed with TBS, and Dako protein block (DakoCytomation Ely Cambs X0909) was applied for 5 minutes. The excess was removed, and hypoxypore-1 antibody (Chemicon Europe Ltd Hamps HP2-100) applied diluted in 1 in 100 in antibody diluent (Dako Catenation S2022) for 60 minutes.

Slides were washed for 3 minutes in TBS, and covered in Anti-fluorescein isothiocyanate (Anti-FITC) Mab (Chemicon Europe Ltd) diluted 1 in 100 in Dako antibody diluent (EnvisionTM HRP Rabbit polymer Dako K4010) for 30 minutes. Slides were washed again for 3 minutes in TBS, and then covered in 3,3'-diaminobenzidine DAB substrate (DakoCytomation K3467) for 5 minutes. Slides were rinsed with TBS, washed under running tap water, and counter stained with Meyer's haematoxylin (Surgipath Europe Ltd Peterborough UK Cat No 01582E) for 10 to 60 seconds. The slides were washed again in running tap water, dehydrated through graded alcohols, cleared in xylene, and mounted in DPX (Surgipath Europe Ltd 08600E).

5.1.9.2 GLUT1

The GLUT1 antibody (Abcam 40084) was diluted to 1 in 200 in antibody diluent and applied for 60 minutes. Then EnvisionTM HRP Rabbit polymer was applied for 30 minutes followed by washing in TBS for 3 minutes. DAB substrate was then applied for 5 minutes followed by a further TBS wash and counter staining with Meyer's haematoxylin. The control was germinal centres of reactive lymphoid tissue.

5.1.9.3 CAIX

Antigen retrieval did not require microwave heating. The CAIX antibody (Professor Pastorek, University of Bratislava) was applied diluted to a concentration of 1 in 50. Following this the process was the same as GLUT1 staining. The control tissue was bladder SCC.

5.1.9.4 HIF 1a

The HIF1a antibody (Abcam, ab8366) was applied diluted to a 1 in 8000 concentration. Following this the process was the same as GLUT1 staining. The control was human bladder SCC.

5.1.9.5 Modifications to Slide Preparation

During the process of antigen retrieval, tissue would lift off the slide due to the boiling process, shown in figure 5.4 a) H+E and b) the GLUT1 stained slide.

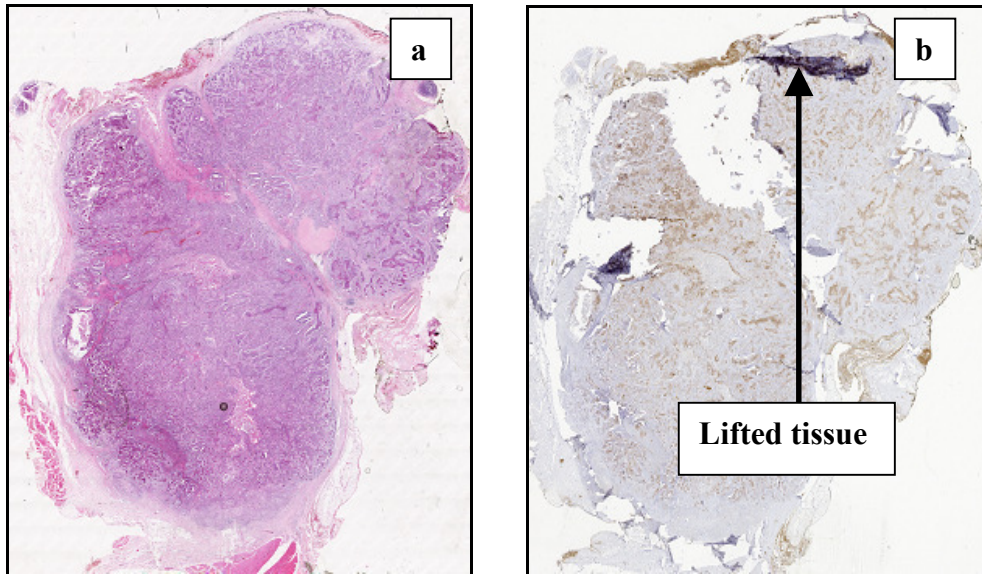


Figure 5.4a and b: Haematoxylin and eosin stained specimen from patient 1 a), and GLUT1 immuno-histochemical stained specimen with folded tissue secondary to antigen retrieval

To overcome this recurrent problem, glass slides were coated in vector bond (Vector Laboratories, USA, SP-1800) prior to tissue capture, and the slides and tissue were then heated overnight at 56°C.

5.1.9.5.1 Vector Bonding Slides

Clean glass slides were placed in metal racks, rinsed in water, and soaked in acetone for 5 minutes. Vector bond (7ml) was mixed with 350ml of acetone and stirred for 5 minutes. The acetone cleaned glass slides were placed in this solution for 5 minutes. Excess reagent was removed by dipping the slides in deionised water. The slides were air dried at room temperature, and stored until required.

5.1.9.6 Haematoxylin and Eosin Staining

Although H+E slides were prepared for diagnostic purposes, these were not removed from the Pathology Department.

Slides were dewaxed through xylene, followed by graded alcohols to water, stained in Meyer's haematoxylin for 5 minutes, and rinsed in running water. Slides were then immersed in 70% alcohol for 10 seconds, followed by counter

staining for 2 minutes in eosin (Surgipath Europe Ltd, Peterborough, UK 01600) and further washed in tap water. The stained tissue was dehydrated through graded alcohol, cleared in xylene and mounted in DPX.

5.10 Digitisation of Immuno-Histochemical Slides

All specimen slides were digitised into an ICS image format by mounting on a Nikon eclipse TE2000-E microscope. A JVC colour camera using software designed at the Gray Cancer Institute, Mount Vernon Cancer Centre, Northwood Middlesex was used at the Guy's Hospital Campus of Kings College, London.

Slides once cleaned of dust and debris were placed face down on the slide mount within the microscope. The settings were: projection x 40 (x 4 objective lens and x 10 eye piece), shutter speed 1/30sec, white balance to manual, and the shading was turned off.

The background was corrected for both black and whites averages to compensate for debris on the lens and colour changes on the slide. The light source was blocked, and the black average taken. The white average was from a clean area of the slide next to the edge of the specimen.

X and Y co-ordinates defined the ROI. The focal plane was defined by three x and y co-ordinates randomly selected by the computer, accounting for changes in thickness of the specimen. If the computer chose a position on the slide with no specimen, then the co-ordinates were altered to ensure that the focal plane included tissue.

Images were taken using a computer-controlled motorised microscope stage according to the defined co-ordinates. An overlap of 10% ensured all areas of the specimen were imaged.

Once the individual ICS images were acquired, they were stitched together using Image Stitching software designed at the Gray Cancer Institute. The image overlap was removed during this process. The final image was stored in a tiff file format.

The information within the image was stored as an 8-bit format. The value ranged from 0 to 255 for each red, green and blue colour. Total colour absence gave a value of 0, and total saturation a value of 255. This quantified the colour in each image.

5.1.11 Linear Unmixing and Calculation of the Hypoxic Fraction

Using the TRI2 software developed at the Gray Cancer Institute, the intensity and percentage of the IHC staining was assessed by a linear unmixing process, which separated the brown horseradish peroxidase stain from the other background colours within the tissue.

The digitised image was re-sampled to between 50 to 100% of the standard format otherwise the software could not deal with the size of the tiff file. The ROI was outlined to include all the histological area. Necrosis, connective tissue, stroma, and acellular regions [2,3] were excluded. The mask generated from this process was reviewed and edited accordingly. Positively stained cells were identified under the microscope, and reference colours were selected both for this, and the background haematoxylin. The H+E stained sections were reviewed at the HN multi-disciplinary team meeting at UCLH, and the tumour containing areas noted. At the time of linear unmixing, the H+E section was recalled and reviewed next to the IHC image to further aid delineation. Concerns regarding the tumour delineation were discussed with the Dr A Jay.

Reference maps were generated through the linear unmixing process separating the brown (horseradish peroxidase), and blue (haematoxylin) colours within the stained tissue.

The positively stained brown IHC image was processed further. A colour intensity histogram was generated following re-application of the mask to the excluded region and the total area calculated through histogram normalisation. Upper and lower limits were altered to exclude non-specific staining due to artefact and background. The stained area was noted, and used to calculate the hypoxic fraction. Analysis of colour intensity through computer software has been reported by other groups [4,5].

Figure 5.5 a to d illustrates this process. Figure 5.5.a the IHC stained specimen for pimonidazole with no staining within the necrotic region, b) with the ROI masked in green, c) with the unmixed brown image (pre threshold) with the mask applied in red, and d) the final unmixed thresholded stain for pimonidazole.

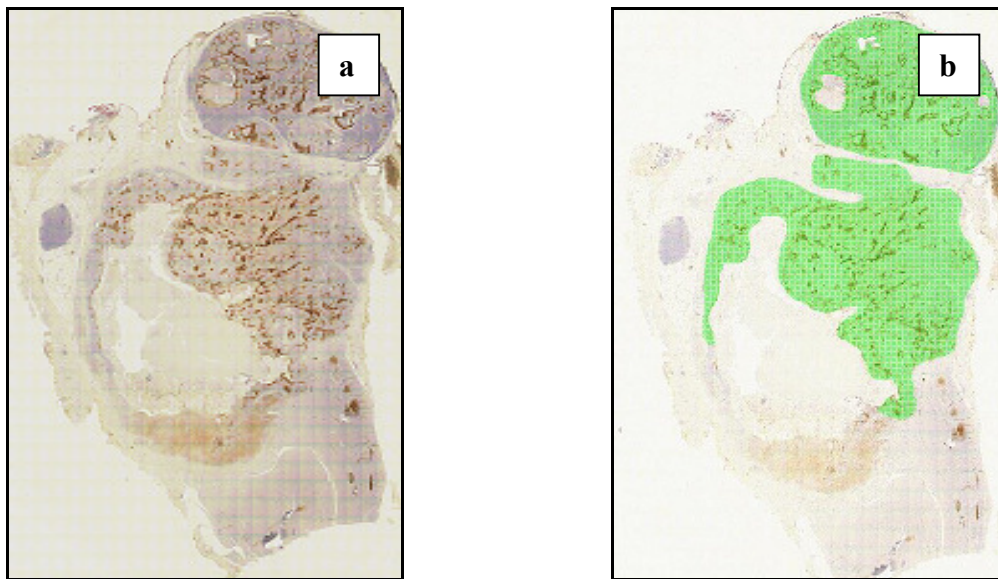


Figure 5.5a and b: The immuno-histochemically stained specimen with pimonidazole from patient 1 a), and the image with mask applied b)

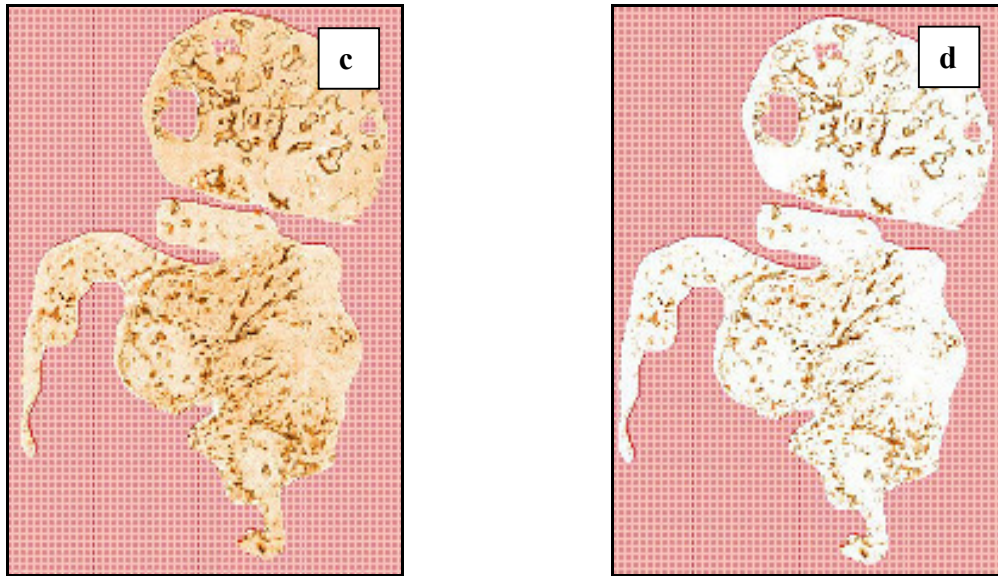


Figure 5.5c and d: The unmixed pre-thresholded image c) and the final thresholded unmixed image for pimonidazole staining d)

The equation used to calculate the area hypoxic fraction is shown.

$$\text{Hypoxic fraction} = \left(\frac{\text{Thresholded stained area}}{\text{Total stained area}} \right) \times 100$$

5.1.12 Grid Calculation of the Hypoxic Fraction and Correlation between Hypoxic Markers

The thresholded linear unmixed image was then further assessed to calculate the hypoxic fraction to corroborate the first method. Hypoxic stains are positive when the pO₂ is less than 10mmHg. Negative staining acted as an internal control.

The linear unmixed images were orientated using Adobe Photoshop Elements 8. Then the image was loaded into the TRI2 software, resampled and binned. The images were re-aligned (if required), and scaled to ensure that the size of each stained specimen corresponded. A 10 x 10 (whole mount) or a 6 x 6 grid (standard histological sized slides) was placed over each image, and the grids linked so that adjustment occurred in unison. The edge of the grid was placed

against the edge of the specimen, and the grid size was adjusted to encompass the image. The percentage staining was calculated within each grid as well as the mean intensity of staining. Only grids 100% encompassed within the specimen were used rather than grids that crossed the edge of the specimen. Pimonidazole was compared and correlated with GLUT1, CAIX, and HIF1a, as well as GLUT1 with CAIX, and HIF1a, and CAIX with HIF1a. Figure 5.6 a to d illustrates this process.

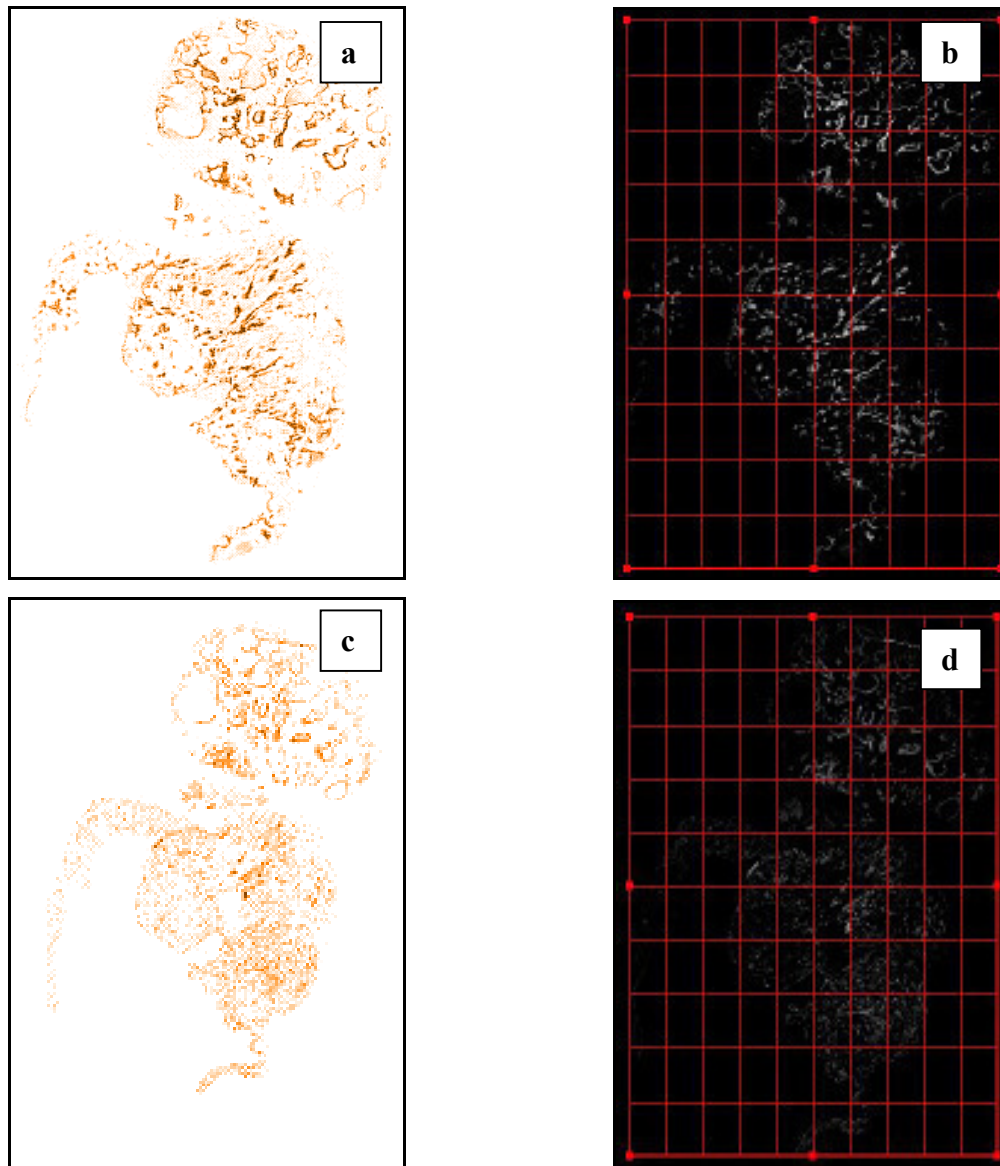


Figure 5.6a to d: The unmixed and thresholded immuno-histochemical stained specimen for patient 1 for pimonidazole a), the corresponding grayscale image with grid placement b), the unmixed, thresholded image for GLUT1 c), and the corresponding grayscale image d)

Figure 5.6 a) illustrates the aligned unmixed and thresholded stain for pimonidazole a), the image converted to grayscale b) with a 10 x 10 grid placement. Figure 5.6c) aligned unmixed and thresholded GLUT1 stained image, and d) the corresponding grayscale image with grid placement for one of the wax embedded blocks from patient 1.

5.1.13 Time-Activity Calculation

The uptake of ^{64}Cu -ATSM in Bq/ml was calculated using the Xeleris (GE Healthcare Medical Systems, WI, USA) software in the Nuclear Medicine Department.

The patient data was retrieved from optical archive, and imported into the software. The 3D PET AC data set was selected. The images were summed by location to plot the uptake of ^{64}Cu -ATSM with time. The window was adjusted to view the uptake. The tumour, necrosis, IL and CL salivary glands (submandibular, +/- parotids), carotid artery, posterior neck, and the CL SCM were outlined as ROI. The plot icon was selected, and a text file created for the uptake of ^{64}Cu -ATSM within each ROI for each image frame. The screen-capture showing the ROI panel on the left and colour outlined ROI on each frame in the top right of the image is shown in figure 5.7.

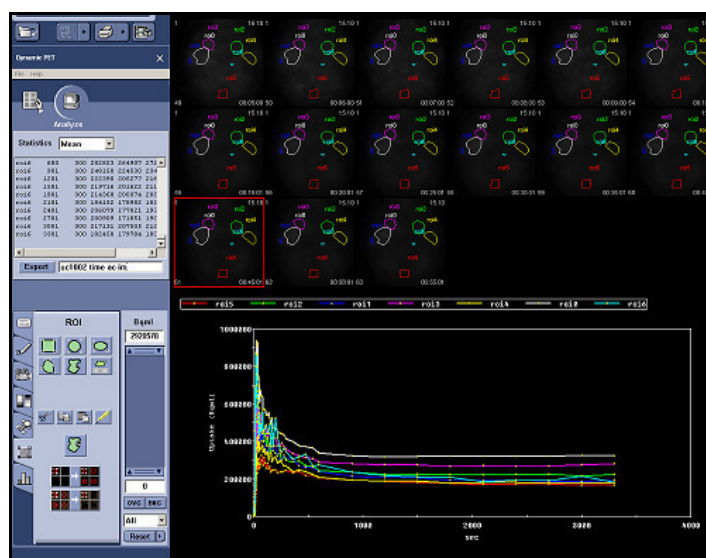


Figure 5.7: The screen capture from the Xeleris software indicating the delineation panel and outlined regions of interest

5.1.14 Tumour Ratio Calculation

This uptake of ^{64}Cu -ATSM was reviewed over time. The first 5 minutes after injection indicated fluctuant uptake, and from 5 to 60 minutes this stabilised and plateaued. Figure 5.8 illustrates the fused coronal CT-PET frame at 1-minute after injection with activity in the bilateral vasculature of the neck.

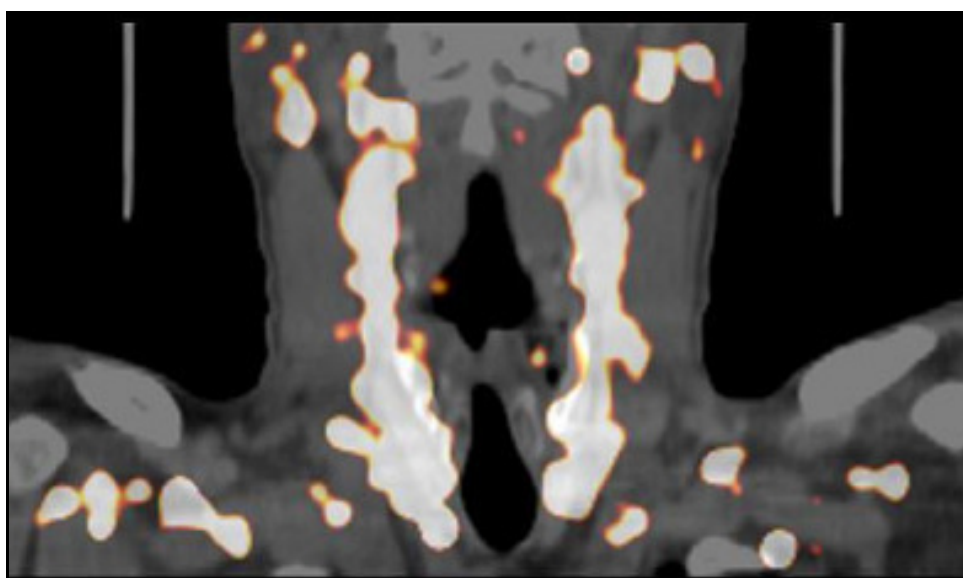


Figure 5.8: Fused coronal CT-PET frame at 1 minute with ^{64}Cu -ATSM activity in the bilateral vasculature of the neck

Tumour ratios were calculated at 5 to 20 minutes and 40 to 60 minutes for the dynamic list modes image sets. The 18-hour uptake ratio was calculated for the entire 1-hour imaging as the frames were acquired statically and could not be re-binned.

The image sets were again retrieved for each patient from optical archive, and transferred to the Xeleris Workstation. The PET AC frames were loaded, and those of interest were selected. For example: 5, 6, 7, 8, 9, 10 and 15 minutes frames for the 5 to 20 minute images, and 40, 45, 50 and 55 minute frames for the 40 to 60 minutes images.

The selected PET frames were loaded into the Xeleris Dynamic PET application. The images were summed by time, saved and re-archived. Next, the data sets were transferred to the Advantage Workstation (Advantage Windows 4.2, GE

Healthcare Medical Systems, WI, USA) along with the CT HN. These data sets were loaded into the PET/CT Review application of this software. This was because the Xeleris software was required to re-bin the required frames, and Advantage Workstation software allowed the ratio calculation per axial image.

The CT, PET, and fused images were reviewed in the axial, coronal and sagittal planes, slice by slice. The images were thresholded to remove the saturation and aid delineation of the ROI. The display icon was selected, and a sphere drawn and placed within the ROI. Each sphere was edited to ensure that it did not extend outside the ROI. The maximum value within the sphere was noted. This process was repeated for each slice. The minimum sphere size of 97mm^3 was used in the carotid artery. This is shown in figure 5.9 with the spheres numbered and delineated in red in the coronal a), and axial b) planes. The numbers on the image correspond to the sequential placement of each ROI to calculate the ratio

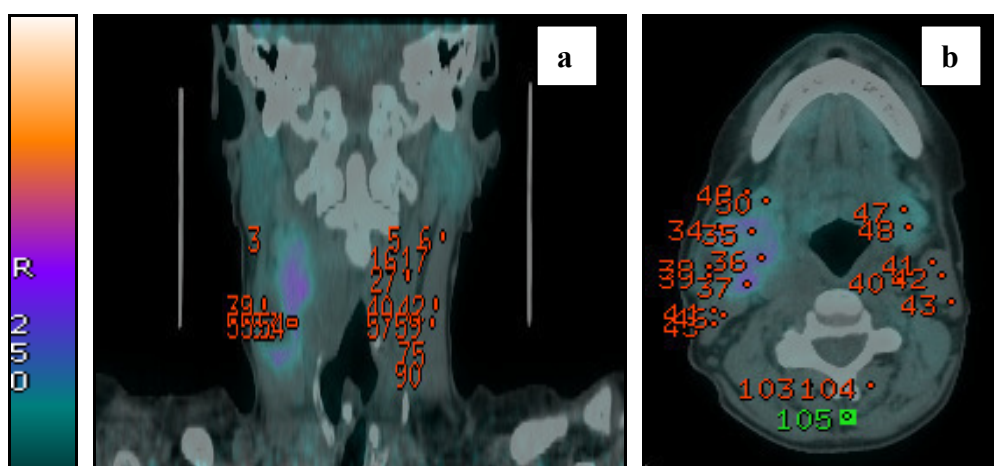


Figure 5.9: The coronal a), and axial b) image of the fused CT-PET with the spheres sequentially numbered and delineated in red

Following this, the ratio was calculated for each point on each axial image, and then averaged. This method produced a more representative indication of ^{64}Cu -ATSM uptake because each axial slice was reviewed rather than the whole volume as a single ROI.

5.1.15 Correlation of Immuno-Histochemical Staining with ^{64}Cu -ATSM Uptake

The IHC unmixed and thresholded images were aligned and a grid correlation undertaken to assess the mean grayscale intensity in each image.

The fused CT-PET, and IHC unmixed thresholded images were converted to grayscale using Adobe Photoshop Elements 8. The fused CT-PET image was used rather than the PET alone because this provided anatomical information so the uptake within the tumour ROI of ^{64}Cu -ATSM could be accurately delineated. The grayscale conversions ensured that the same intensity score was used for each image.

The information gained during the pathological dissection was reviewed. The specimen size was noted along with the dimensions of the macroscopic specimen. The distance from the edge of the tumour (anterior to posterior, superior to inferior, and medial to lateral) to the cut surface at the time of dissection was evaluated. The reconstructed CT-PET slices were 3.27mm in thickness, and each CT-PET image was reviewed to ensure the CT-PET slice visually corresponded to the fresh and formalin fixed specimen. Then the appropriate CT-PET image was selected, which corresponded with the IHC specimen.

The images (CT-PET and unmixed thresholded IHC) were aligned and loaded into the TRI2 software. Any further alignment (rotation, size scaling) to ensure that the images were the same size was done at this stage. Next a 10 x 10 (whole mount) or a 6 x 6 grid (standard histological slides) was placed onto the corresponding images. The grid was adjusted so the edge of the grid was on the edge of the CT-PET volume or IHC image. The mean intensity per grid was calculated by the TRI2 software and exported into an excel spreadsheet. Only the grids that were 100% inside the ROI were used in the analysis.

Next the mean intensities gained were at opposite ends of the grayscale spectrum. The IHC image intensity was inverted (255 - mean intensity) for each grid. The CT-PET image had a background grayscale due to the enhancement of

normal tissue when imaged by CT. The grids containing normal tissue were reviewed, and for example if the mean intensity in the grid was 80, then 80 was subtracted from the mean grid intensity to ensure that the measured value only represented ^{64}Cu -ATSM uptake.

This process was repeated for each IHC stained specimen from each block for each patient, as well as for each stain on the CT-PET images at 5 to 20 minutes, 40 to 60 minutes, and at 18 hours after ^{64}Cu -ATSM injection. Figure 5.10a and b illustrates the grid placement on the grayscale IHC image of pimonidazole a), and grayscale fused CT-PET image at 40 to 60 minutes b). The threshold has been adjusted on the pimonidazole image for reproduction purposes.

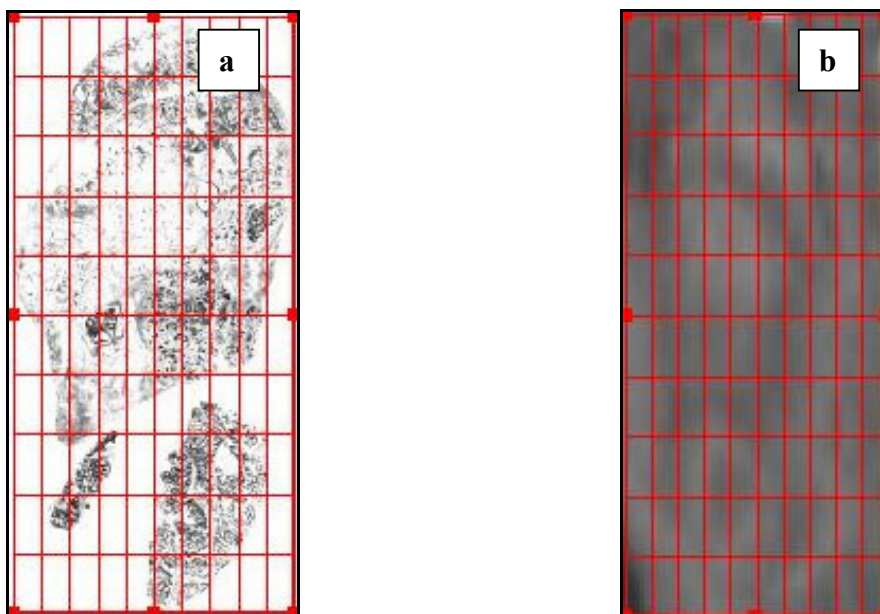


Figure 5.10a and b: Pimonidazole stained grayscale image with grid placement (10 X 10) a), and the grayscale fused CT-PET image at 40 to 60 minutes b)

5.1.15 DCE-CT Parameter Calculation

Two separate software packages were used within the Nuclear Medicine Department for analysis of the DCE-CT data.

5.1.15.1 WinFun

Firstly, WinFun (Cambridge Computed Imaging, Bourne, UK) is a validated [6] functional image analysis software package for Windows. This is based on the

information from time-density data from a single location DCE-CT sequence through a pre-determined ROI. The tissue perfusion is determined from the maximum gradient of the tissue time-density curve divided by the peak enhancement within an arterial vessel. Data is gained from the curve because changes in the CT x-ray beam attenuation reflect changes in the iodinated contrast concentration in the ROI with time. A calibration factor can be added to the algorithm within the software (from phantom studies) and is related to the iodine concentration within the contrast and the attenuation within the CT-PET camera [7].

All 88 DCE-CT images for the ROI were loaded into the software. There were 8 image sets, each with 11 frames that represented the 4cm scanned section (0.5cm per image set). The pre-contrast to post-contrast frames were reviewed and selected so that the images were all from the same axial slice. Using the DICOM (Digital Imaging and Communications in Medicine) 3.0 protocol the unwanted images were deleted.

The first pre-contrast frame was selected. The images were then reviewed within that 8-frame set to assess for mis-selection of pre, peri and post contrast images due to patient movement. The tumour and IL carotid artery were delineated on the contrast-containing image. The arterial ROI allowed the calculation of the AIF, and so the maximum enhancement within the tumour. The process icon box was selected, and the window width was set at 400, and window level at 40. The software calculated the dynamic parameters of: AIF, CP, BV and perfusion. The CP was calculated by Patlak analysis. This process was repeated to analyse all 11 frames.

5.1.15.2 Advantage WorkStation for Windows

Secondly, the CT perfusion 4 application was used on the Advantage Workstation. This application has previously been validated in DCE-CT perfusion studies in patients with SCCHN [8] and uses a deconvolution algorithm. Deconvolution techniques in SCCHN are the most widely used to assess perfusion parameters [9-11] because they are independent of cardiac

output and the possible delay in the passage of intra-venous bolus contrast in the vascular pathways above the aorta. This software defined the following terms:

BF:

The volume flow rate of blood through the vasculature in the define ROI. This was calculated as BV/MTT .

BV:

The volume of blood within the vasculature of the ROI that flowed and did not stagnate. This was calculated by the area under the tissue enhancement curve divided by the area under the arterial enhancement curve.

MTT:

The average time taken by the blood to traverse the vasculature from the arterial to the venous end of the bed. This was calculated from the deconvolution of the arterial and tissue enhancement curves.

Permeability Surface Area/Capillary Permeability:

Total surface area of capillary endothelium in a unit mass of tissue representing the total diffusional flux across all capillaries ($=1 - BF[\ln(1-E)]$, E is the fraction of contrast that leaks into the extra vascular space from the intra-vascular space (extraction fraction)).

The DCE-CT was selected and loaded into the application. The body tumour protocol selected, and the HU set at -50 to 150. The ROI was drawn over the IL carotid artery, ensuring the boundary was within the vessel wall, and the ROI locked. The last pre and post contrast images were selected and then computed by the software. The tumour ROI was drawn on each axial image. The software numbered the ROI from 3 to 10 from superior to inferior. The BF, PS, MTT, BV parameters were automatically calculated by the software.

5.1.16 Correlation of Perfusion with ^{64}Cu -ATSM Uptake

The axial CT-PET fused images were reviewed, and saved for patient 5 at 5 to 20 minutes, 40 to 60 minutes, and at 18 hours after ^{64}Cu -ATSM injection. The ROI

outlined using the Advantage GE Healthcare CT Perfusion 4 software was also reviewed, and the corresponding axial CT-PET and BF images selected.

Using Adobe Photoshop Elements 8, the images were converted to grayscale, and assessed for alignment, as before. The images were converted to grayscale to allow the uptake of ^{64}Cu -ATSM, and perfusion to be assessed for mean intensity because otherwise the correlation would not have been representative due to the different colour scales used (Blue perfusion, and rainbow for CT-PET). The grayscale perfusion and corresponding CT-PET axial images were loaded into the TRI2 software. Alignment was re-assessed, and images scaled and rotated to correspond if required. A 10 x 10 grid was placed over each image with the edges of the grid aligned to the edges of the ROI. As before the mean intensity of the grayscale was assessed per grid for each image.

Figure 5.11a to f illustrate this process. Figure 5.11a and b show the fused CT-PET, and corresponding grayscale axial images for ROI 5 from patient 5. Figure 5.11c and d illustrate the blood flow for this ROI and the corresponding grayscale image. Figures 5.11e and f illustrate the aligned grayscale blood flow and fused CT-PET images with a 10 x 10 grid placement for analysis of the mean grayscale intensity.

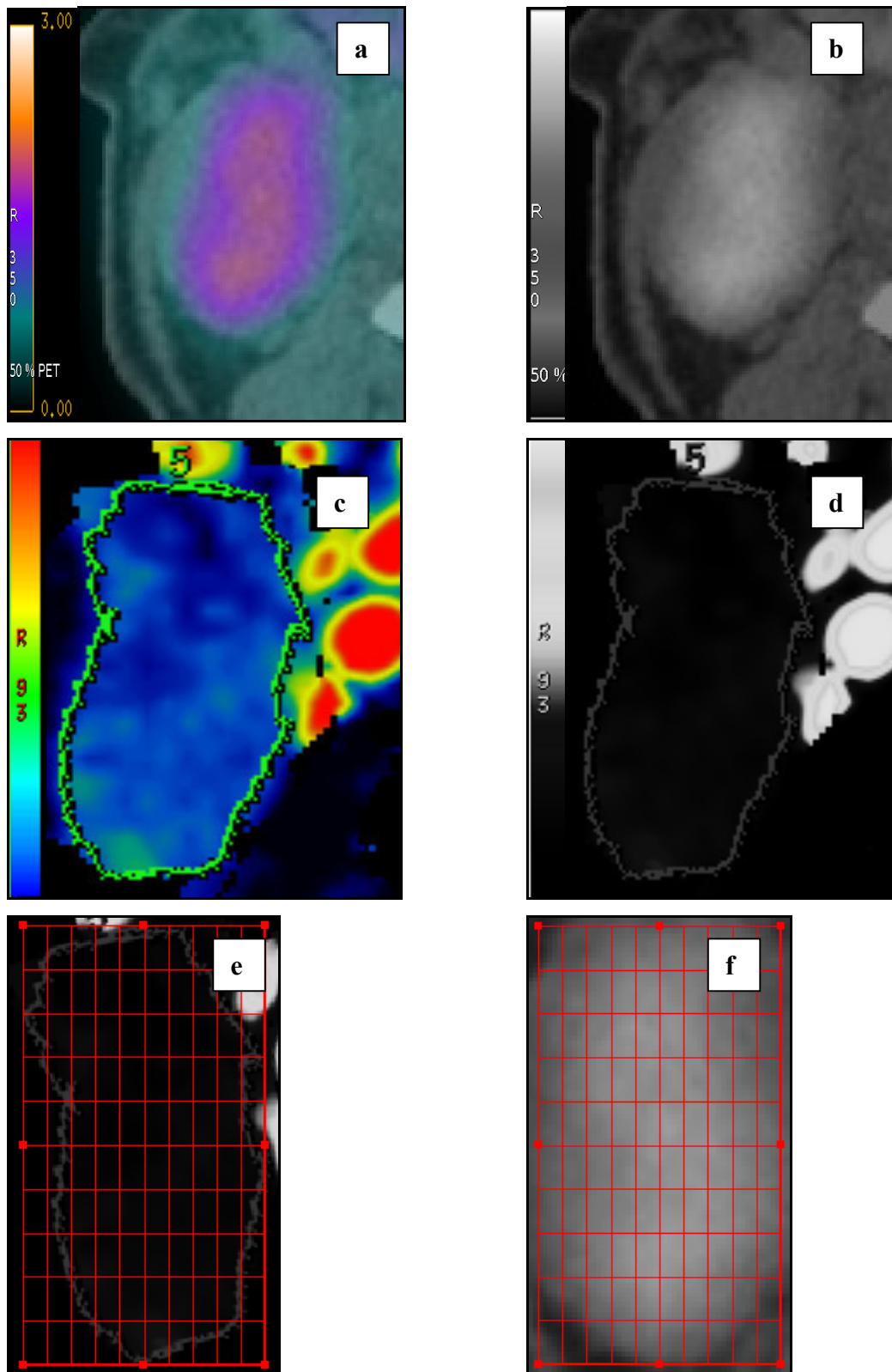


Figure 5.11a to f: Aligned axial fused CT-PET a), corresponding grayscale b), blood flow c), corresponding grayscale image d), grayscale blood flow image aligned with grid e), and grayscale CT-PET image aligned with grid f) and of ROI 5

5.1.16 Hypoxic Volume Calculation on CT-PET

The use of SUV as a semi-quantitative measure of uptake has only been validated in ^{18}F FDG clinical imaging. The hypoxic FV has been calculated as a tumour to muscle, tumour to background, and tumour to blood ratio.

Currently four clinical studies have used of these ratios. These include tumour to muscle ratios greater than or equal to 2 (CL SCM) [12], greater than or equal to 3.0 (SCM) [13], greater than or equal to 3.5 (gluteal) ratio [14], or greater than or equal to 2.6 (internal pelvis) [15].

5.1.17 Hypoxic Functional Volume Delineation

The hypoxic FV was delineated from the calculated tumour to muscle, background, and blood ratios. The CT HN and the summed PET images at 5 to 20 and 40 to 60 minutes, and those from the late imaging were selected and individually loaded into the single visit application of the PETVCAR software. A bookmark was placed in the ROI as previously described in Chapter 4, and the threshold was individually calculated from the values gained from the CL SCM, carotid artery and posterior neck. This ensured that the FV was delineated and calculated according to a ratio of 2.0, 2.5, 3.0, 3.5, and 4.0. This thresholding process was repeated for each ratio value.

5.2 Statistical Analysis

The distribution of the data was measured for normality by the Shapiro Wilks test.

The tumour ratios on each axial slice were normally distributed, and were compared at 40 to 60 minutes, and 18 hours post ^{64}Cu -ATSM injection to 5 to 20 minutes using the paired t-test.

All the other data was not normally distributed and was assessed by non-parametric methods. The uptake of ^{64}Cu -ATSM within the tumour ROI and other

ROIs measured during dynamic acquisition according to time on the Xeleris workstation was directly compared by the WCSRT.

The percentage staining of pimonidazole, GLUT1, CAIX, and HIF1a per grid was assessed by the WCSRT to evaluate the differences between percentage staining, and Kendall's correlation co-efficient to investigate the presence and strength of a relationship between two variables.

The mean grayscale intensity in each grid measured on the aligned CT-PET and DCE-CT axial images, and the IHC unmixed stained specimens and CT-PET images as 5 to 20 minutes, 40 to 60 minutes and at 18 hours after ^{64}Cu -ATSM injection were evaluated by the WCSRT, and Kendall's correlation co-efficient.

5.3 Results

5.3.1 Patient Characteristics

Forty-four patients were screened, and six patients consented. Table 5.3 shows the patient characteristics and table 5.4 the presenting symptoms, smoking and alcohol history.

Patients 3 and 6 highlighted in blue did not enter the study. Patient 3 could not be imaged because the cyclotron at St Thomas' Hospital flooded preventing isotope production. Patient 6 failed on two occasions because initially the target did not move into the beam of the cyclotron, and then the isotope failed post-production quality assurance due to radio-lysis. Patient 2 indicated in violet was only imaged for 25 minutes.

Table 5.3: Patient characteristics

Patient	Age	Gender	Primary Site	TNM Classification	Planned Surgery
1	65	Female	Unknown	Tx N2b M0	Modified right radical Neck dissection
2	73	Male	Transglottic	T4 N2c M0	Laryngectomy and nodal sampling
3	62	Male	Transglottic	T4 N0 M0	Laryngectomy
4	63	Male	Transglottic	T4 N0 M0	Laryngectomy
5	54	Male	Unknown	Tx N3 M0	Modified right radical Neck dissection
6	63	Male	Transglottic	T4 N0 M0	Laryngectomy

Table 5.4: The presenting symptoms, smoking and alcohol history

Patient	Presenting Symptoms	Pack Year History	Units of Alcohol Per Week
1	Right neck mass for 2 months	50	0
2	3 months hoarse voice and local discomfort	120	10
3	Shortness of breath, stridor and 3 months hoarse voice	80	0
4	6 months hoarse voice	23	10
5	Right neck mass for 3 months	50	10
6	4 months hoarse voice and shortness of breath	68	20

5.3.2 Protocol Adherence

5.3.2.1 Imaging

Out of the 4 patients imaged, patient 1, 4, and 5 completed the imaging protocol as planned.

Patient 1: 1 hour 3D dynamic CT-PET only

Patient 4: 1 hour 3D dynamic CT-PET, followed by a DCE-CT

Patient 5: 1 hour 3D dynamic CT-PET followed by a DCE-CT, and late static 1-hour CT-PET 18hours after ⁶⁴Cu-ATSM injection

Patient 2 was unable to tolerate lying on the scanner couch because of longstanding lumbar spondylosis, and the development of claustrophobia. The scanning protocol was terminated 25 minutes after injection. This patient was imaged 24 hours after injection with analgesia.

All patients were injected with 505 to 595MBq of ^{64}Cu -ATSM. Following injection the syringe was placed under a Geiger counter and the residual activity within the syringe calculated by the Superintendent Radiographer. This was 12.9 to 18.6MBq. There were no adverse reactions with ^{64}Cu -ATSM. Late imaging was completed 18hours after injection of ^{64}Cu -ATSM, and was the first imaging appointment of the day within the department.

5.3.2.2 Pimonidazole Administration

All patients received 0.5g/m^2 of pimonidazole intravenously a minimum of 18 hours prior to surgery with no adverse reactions.

5.3.2.3 Pathological Review

The specimens from all patients underwent standard pathological assessment by a single pathologist in 3 cases. The specimen was reviewed by the Pathologist and macroscopic dissection guided by the primary site and the appearance. For example to establish the presence of extra-capsular spread.

Figure 5.12a to d illustrates a specimen from patient 1. Figure 5.12a shows the formalin-fixed inked macroscopic specimen on the surgical template, with a visible gelatinous area of necrosis within the matted LN. The specimen was dissected cranio-caudally in the coronal plane. Figure 5.12b shows the specimen after this dissection process in plastic cassettes prior to wax embedding, and c) the final processed wax embedded tissue blocks. Arrows indicate areas of necrosis and SCC within the specimen.

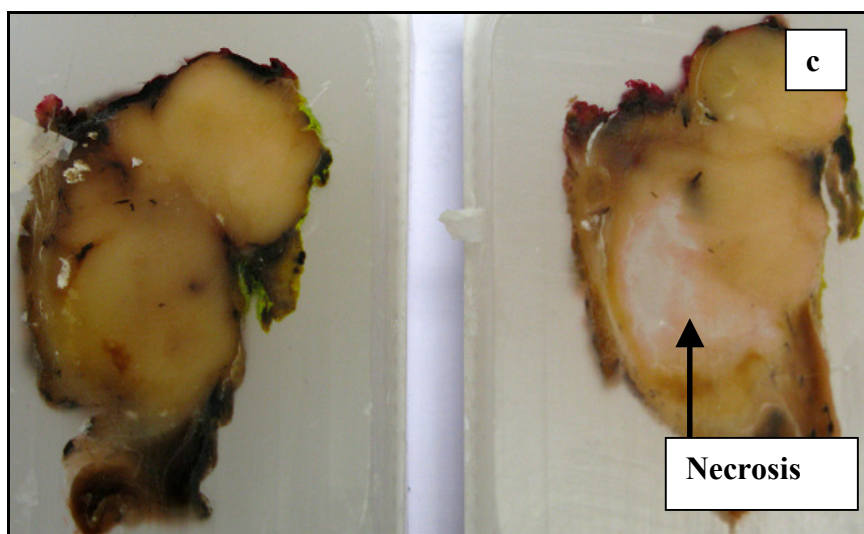
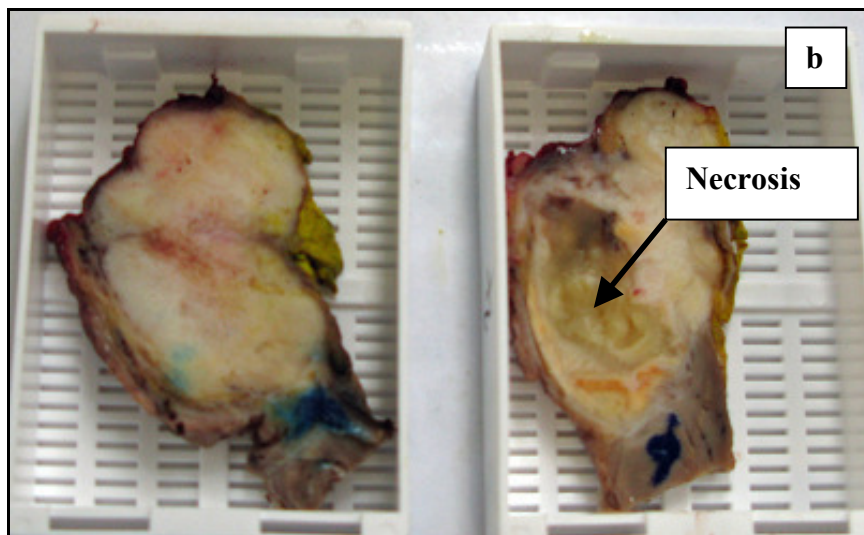
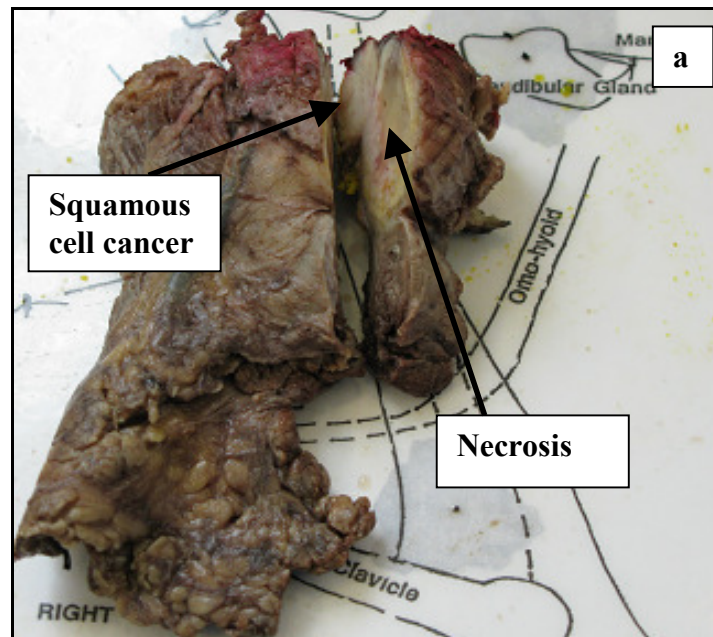


Figure 5.12a to c: The macroscopic pathological dissection of the specimen from patient 1.
a) formalin fixed, b) dissected, and c) wax embedded specimen

5.3.3 Uptake of ^{64}Cu -ATSM Within Regions of Interest During Dynamic Imaging

The uptake of ^{64}Cu -ATSM within the tumour was assessed as well as in the CL SCM, posterior neck (post neck), the CL carotid artery, and the salivary glands (CL and IL). In patients 1 and 5, this has also been expressed in relation to the uptake of ^{64}Cu -ATSM in the regions of necrosis within the tumour.

Unfortunately due to the premature termination of imaging for patient 2, uptake was not able to be assessed in this format, and could only be expressed as a ratio at 5 to 20 minutes after injection. This was because after 5 minutes of imaging when the patient developed back pain, and Dr Kayani decided to statically image the patient instead.

The maximum tumour uptake of ^{64}Cu -ATSM peaked at 30 seconds and ranged between 1,207,190 and 1,914,251 Bq/ml. This compared to the peak in the carotid artery of activity between 2,424,634 and 6,427,844 Bq/ml. The maximum activity in the CL SCM was between 430,758 and 531,687 Bq/ml at 1-minute after injection. The maximum activity within the posterior neck was between 295,997 and 668,346 Bq/ml at 1-minute. Similarly, the maximum activity within the CL salivary glands was 378,219 and 817,097 Bq/ml, and 592,680 to 919,363 Bq/ml in the IL salivary glands at 1-minute. Within areas of intra-tumoural necrosis the maximum activity was between 506,632 and 616,086 Bq/ml at 1-minute. In all patients the maximum activity within these regions had plateaued at 5 minutes after the injection of ^{64}Cu -ATSM. Table 18 in Appendix 1 indicates the maximum activity of ^{64}Cu -ATSM with time between 0 and 60 minutes after injection.

Figures 5.13a to e illustrate the time-activity curves for patient 1. Figure 5.13a) illustrates the activity in tumour and necrotic regions, tumour and the CL SCM b), tumour and the carotid artery c), tumour and the posterior neck d), and tumour and the CL and IL salivary glands e). The time-activity curves of patients 4 and 5 are in figures 16 and 17 of Appendix 2. The uptake within the tumour (Bq/ml) has been expressed as a line graph with the corresponding standard

deviation at each image frame during the 1-hour dynamic imaging process immediately following the injection of ^{64}Cu -ATSM.

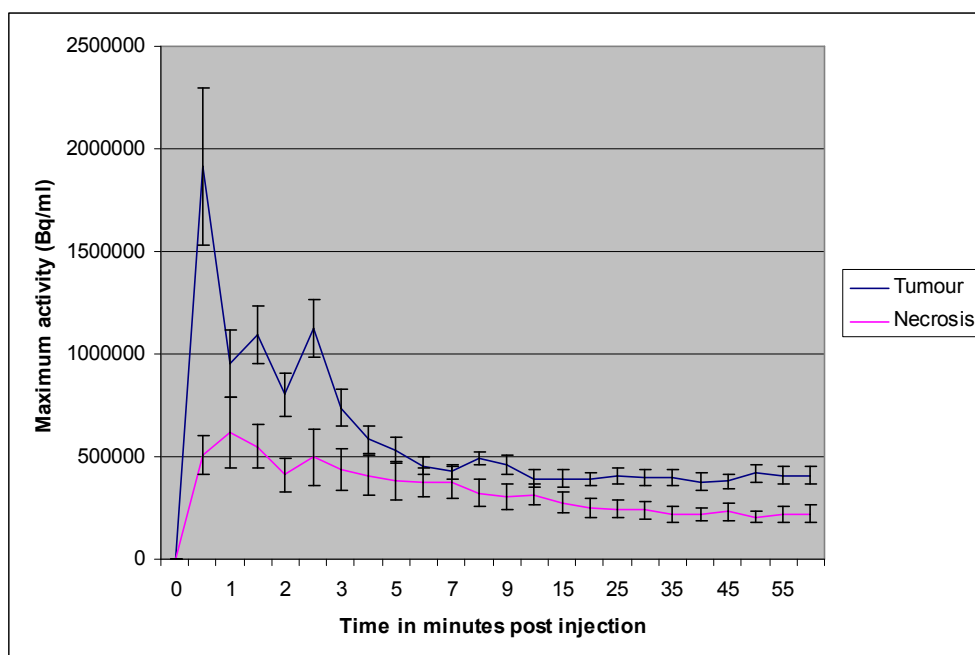


Figure 5.13a: Uptake of ^{64}Cu -ATSM within the tumour and intra-tumoural necrotic region of patient 1

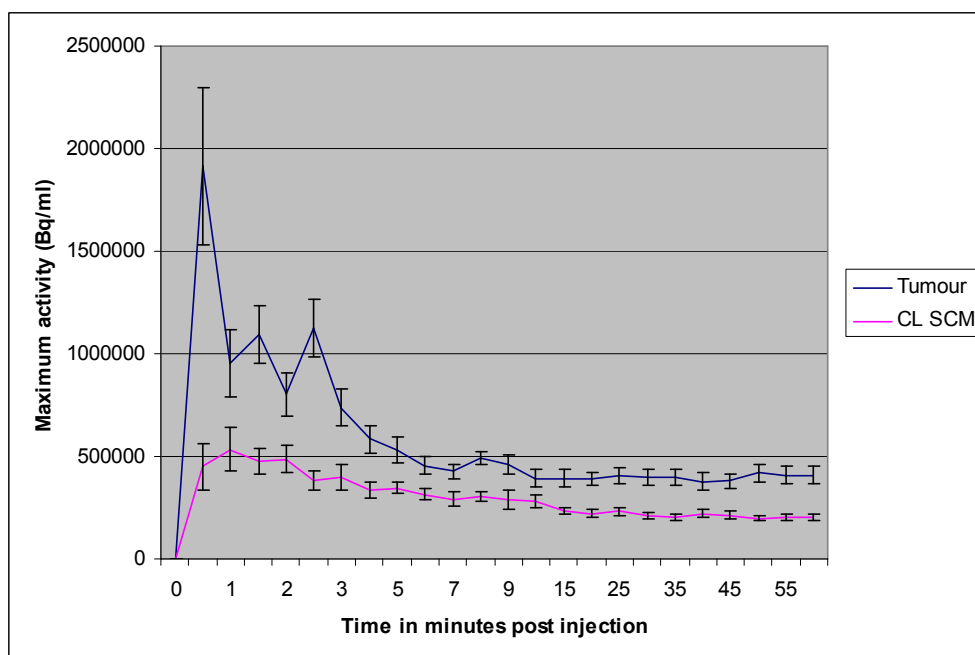


Figure 5.13b: Uptake of ^{64}Cu -ATSM within the tumour and contra-lateral sternocleidomastoid muscle of patient 1

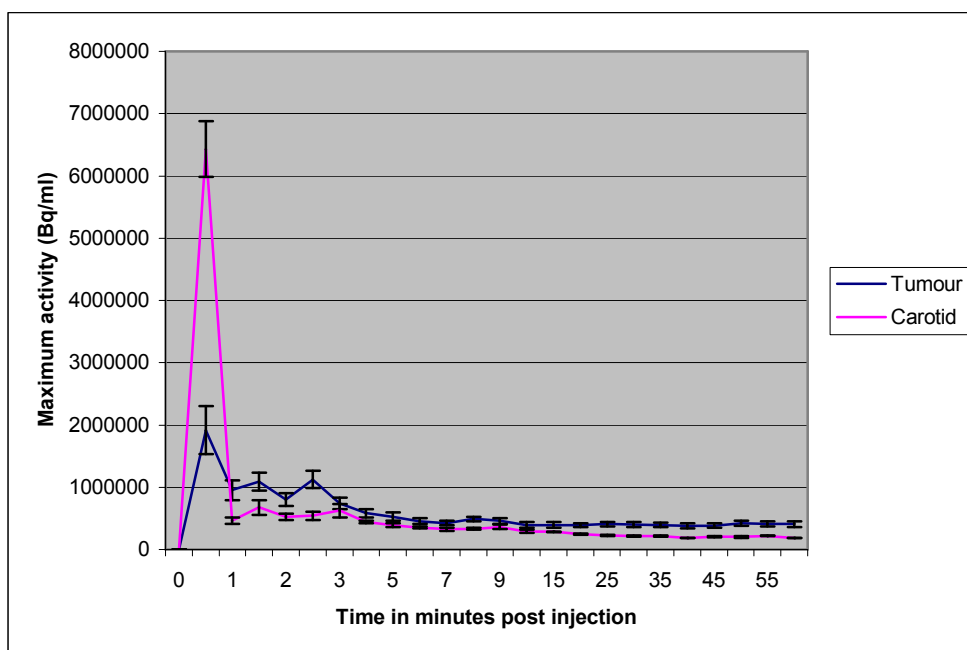


Figure 5.13c: Uptake of ^{64}Cu -ATSM within the tumour and within the contra-lateral carotid artery of patient 1

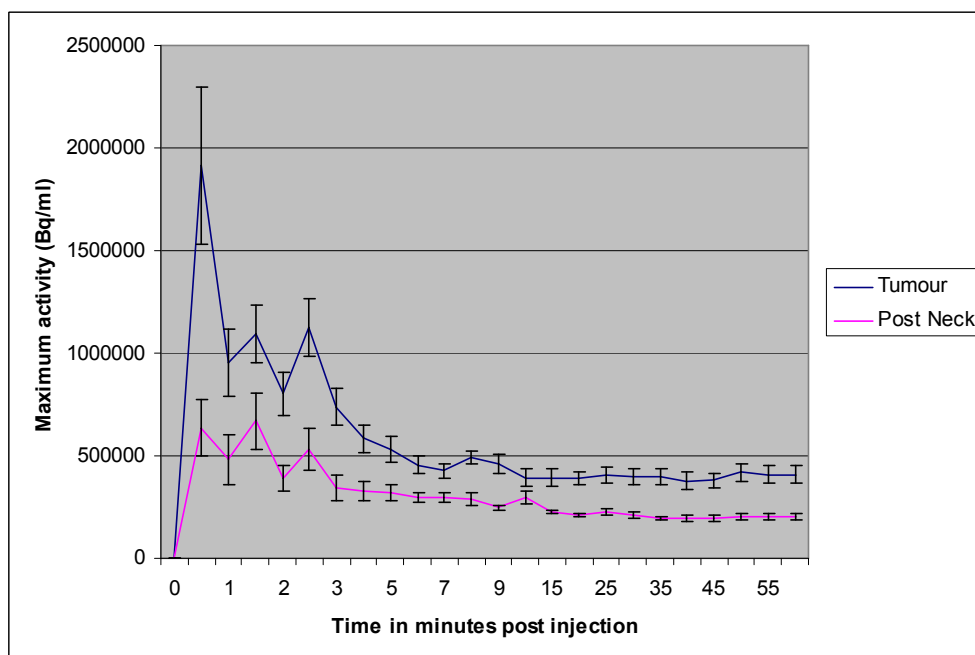


Figure 5.13d: Uptake of ^{64}Cu -ATSM within the tumour and posterior neck of patient 1

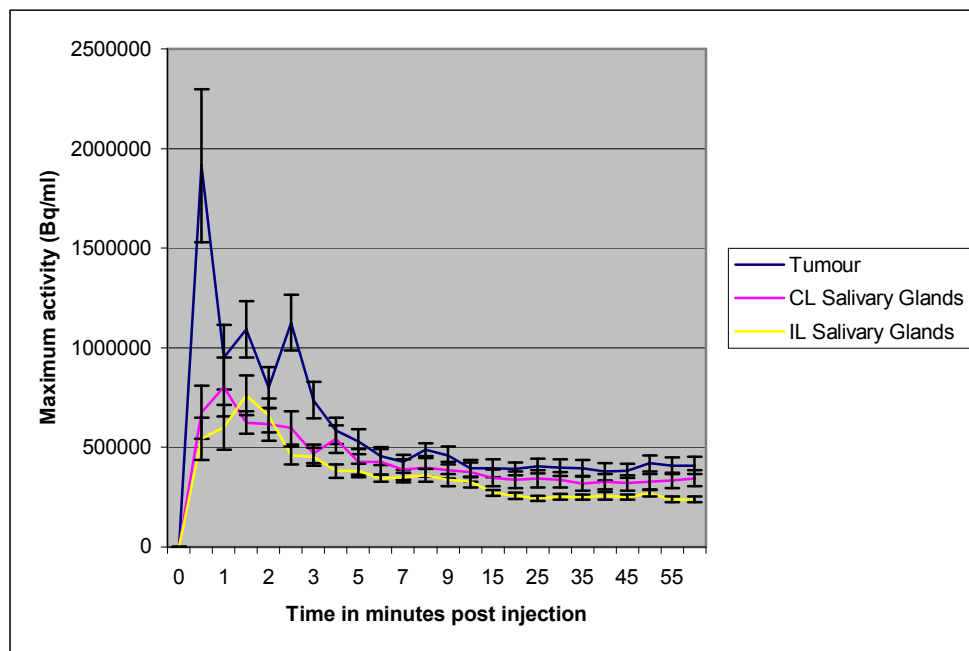


Figure 5.13e: Uptake of ^{64}Cu -ATSM within the tumour and salivary glands of patient 1

The tumour uptake ranged at 5 to 60 minutes between 228,291 to 425,795 Bq/ml, with the greatest activity in the tumour from patient 1.

The uptake of ^{64}Cu -ATSM was significantly greater in the tumour between each frame for the posterior neck ($p=0.004$, median difference 75,116Bq/ml, 95% CI 182,335 to 146,231Bq/ml), intra-tumoural necrotic region ($p=0.0002$, median difference 87,828Bq/ml, 95% CI 47,277 to 117,851Bq/ml), and the CL salivary glands ($p=0.017$, median difference 74,771Bq/ml, 95% CI 9,452 to 126,393 Bq/ml). There was no significant difference in the uptake between the tumour and IL salivary glands, carotid artery, and contra-lateral SCM.

5.3.4 Tumour Ratios

The tumour ratio of ^{64}Cu -ATSM uptake was calculated within each axial CT-PET slice and other regions of interest at 5 to 20 minutes, 40 to 60 minutes, and 18 hours after injection. The range of values for each patient across the ROI are illustrated in table 5.5a to c for 5 to 20 minutes, 40 to 60 minutes and the 18 hour time points respectively. Tumour to muscle represents the tumour uptake

compared to that within the CL SCM, tumour to blood compares the uptake to that within the carotid artery, and the tumour to background compares the uptake of ^{64}Cu -ATSM to that within the posterior neck.

Table 5.5a: The ratio of ^{64}Cu -ATSM uptake compared to that within other regions of interest 5 to 20 minutes after injection

Patient	Range of Ratios					
	Tumour to Muscle	Tumour to Blood	Tumour to Background	Tumour to Necrosis	Tumour to CL Salivary Gland	Tumour to IL Salivary Gland
1	2.39 to 5.22	1.57 to 3.68	2.08 to 4.38	3.13 to 3.33	1.17 to 1.38	1.14 to 1.65
2	2.32 to 7.82	2.55 to 4.97	3.06 to 7.02	-	1.76 to 2.57	1.76 to 2.66
4	1.80 to 6.10	1.35 to 5.23	2.16 to 6.88	-	1.72 to 2.30	1.79 to 2.82
5	1.62 to 3.40	1.24 to 2.95	1.86 to 4.64	2.43 to 2.92	0.95 to 1.33	0.91 to 1.39

In all patients, the tumour uptake was greater than the uptake in the CL SCM muscle, blood, posterior neck and necrosis at 5 to 20 minutes, 40 to 60 minutes, and 18 hours after ^{64}Cu -ATSM injection.

The ratio of ^{64}Cu -ATSM uptake within the intra-tumoural necrotic region was also compared to the uptake within the CL SCM, carotid artery and posterior neck at the three points of interest. At 5 to 20 minutes the intra-tumoural necrosis to CL SCM uptake ratio was 0.94 to 1.29, the necrosis to blood ratio was 0.67 to 1.10, and the necrosis to background ratio was 0.94 to 1.25.

For all the patients combined at 5 to 20 minutes the mean tumour to muscle ratio was 2.98 (SEM 0.19), the mean tumour to blood ratio was 2.32 (SEM 0.16), and

the mean tumour to background ratio was 3.22 (SEM 0.19). The mean tumour to IL salivary gland ratio was 1.68 (SEM 0.12), the tumour to CL salivary gland ratio was 1.61 (SEM 0.10), and the mean tumour to intra-tumoural necrotic region ratio was 2.88 (SEM 0.12).

Table 5.5b: The ratio of ^{64}Cu -ATSM uptake compared to that within other regions of interest 40 to 60 minutes after injection

Patient	Ratio					
	Tumour to Muscle	Tumour to Blood	Tumour to Background	Tumour to Necrosis	Tumour to CL Salivary Gland	Tumour to IL Salivary Gland
1	3.64 to 6.48	2.08 to 5.38	2.67 to 5.71	3.56 to 5.73	1.31 to 1.83	1.66 to 2.03
2	-	-	-	-	-	-
4	2.93 to 3.94	2.44 to 3.94	2.65 to 3.15	-	1.51 to 2.16	1.47 to 2.16
5	2.13 to 2.78	2.13 to 2.93	3.08 to 4.78	2.60 to 2.67	0.50 to 2.01	1.34 to 2.10

The dash line indicates no imaging at that time point available to calculate the ratio.

The ratio of ^{64}Cu -ATSM uptake within the intra-tumoural necrotic regions at 40 to 60 minutes post injection was 0.97 to 1.31 when compared to the uptake in the CL SCM, 0.667 to 1.10 compared to the blood within the carotid artery, and 0.70 to 1.38 when compared to the uptake within the posterior neck.

The mean tumour to muscle ratio for all the patients combined at 40 to 60 minutes was 4.02 (SEM 0.30), tumour to blood was 3.24 (SEM 0.23), and tumour to background was 3.84 (SEM 0.22). The mean complied tumour to IL salivary gland ratio was 1.73 (SEM 0.06), and the ratio with the CL salivary

gland was 1.66 (SEM 0.10), while the mean ratio to the intra-tumoural necrotic region was 4.21 (SEM 0.44).

Table 5.5c: The ratio of ^{64}Cu -ATSM uptake compared to that within other regions of interest 18 hours after injection

Patient	Ratio					
	Tumour to Muscle	Tumour to Blood	Tumour to Background	Tumour to Necrosis	Tumour to CL Salivary Gland	Tumour to IL Salivary Gland
1	-	-	-	-	-	-
2	3.30 to 6.75	2.33 to 5.07	3.50 to 7.00		2.02 to 3.03	2.32 to 3.75
4	-	-	-	-	-	-
5	3.33 to 6.56	1.67 to 5.46	3.33 to 6.61	4.91 to 6.54	2.00 to 3.42	1.89 to 3.22

The mean ratio for tumour to muscle for the two patients was 4.73 (SEM 0.39), tumour to blood was 3.35 (SEM 0.32), tumour to background 5.06 (SEM 0.48).

Table 5.6 illustrates the p-values, mean difference and 95% CI for the paired t-test for the ratios at 40 to 60 minutes compared to 5 to 20 minutes a), late 18 hour imaging compared to 5 to 20 minutes, and late imaging compared to 40 to 60 minutes c).

Table 5.6a: Statistical results for the paired t-test comparing the uptake ratio at 40 to 60 minutes to the ratio at 5 to 20 minutes

Ratio	p-value	Mean Difference	95% CI
Tumour to muscle	0.001	1.10	0.66 to 1.55
Tumour to blood	0.003	1.02	0.47 to 1.45
Tumour to background	0.004	0.70	0.20 to 1.20
Tumour to necrosis	0.004	2.22	1.42 to 3.01
Tumour to CL salivary gland	0.287	-0.07	-0.33 to +0.19
Tumour to IL salivary gland	0.214	-0.12	-0.41 to +0.18

There was a significant increase in the ratios at 40 to 60 minutes compared to 5 to 20 minutes. This was most significant for the tumour to muscle ratio. However there was no significant difference when the tumour to salivary gland ratio was compared.

Table 5.6b: Statistical results for the paired t-test comparing the uptake ratio at 18 hours after injection to the ratio at 5 to 20 minutes

Ratio	p-value	Mean difference	95% CI
Tumour to muscle	0.001	0.91	1.02 to 2.45
Tumour to blood	0.004	0.99	0.36 to 1.32
Tumour to background	0.001	1.86	1.06 to 2.67
Tumour to necrosis	0.001	2.46	1.87 to 3.05
Tumour to CL salivary gland	0.001	0.87	0.55 to 1.19
Tumour to IL gland	0.008	1.02	0.51 to 1.53

There was a significant increase in the tumour ratio 18 hours after injection compared to 5 to 20 minutes for all the regions investigated, although this was most significant for the tumour to muscle, tumour to necrosis, and tumour to CL salivary gland regions.

Table 5.6c: Statistical results for the paired t-test comparing the uptake ratio 18 hours after injection compared to 40 to 60 minutes

Ratio	p-value	Mean difference	95% CI
Tumour to muscle	0.070	0.63	-0.23 to +1.49
Tumour to blood	0.477	0.02	-0.74 to +0.79
Tumour to background	0.015	1.16	0.25 to 2.02
Tumour to necrosis	0.055	0.91	-0.26 to +2.08
Tumour to CL salivary gland	0.001	0.84	0.56 to 1.13
Tumour to IL salivary gland	0.001	1.03	0.69 to 1.38

There was a significant mean difference in the ratios between each axial slice for tumour to background, and tumour to salivary glands only. The difference in uptake with time is illustrated on the coronal fused CT-PET images from patient 5 in figure 5.14a) at 5 to 20 minutes, b) at 40 to 60 minutes and c) 18 hours after injection. Uptake is heterogeneous, and minimal uptake is seen within the region of necrosis. However the reduction in uptake within the salivary glands can be visualised with time.

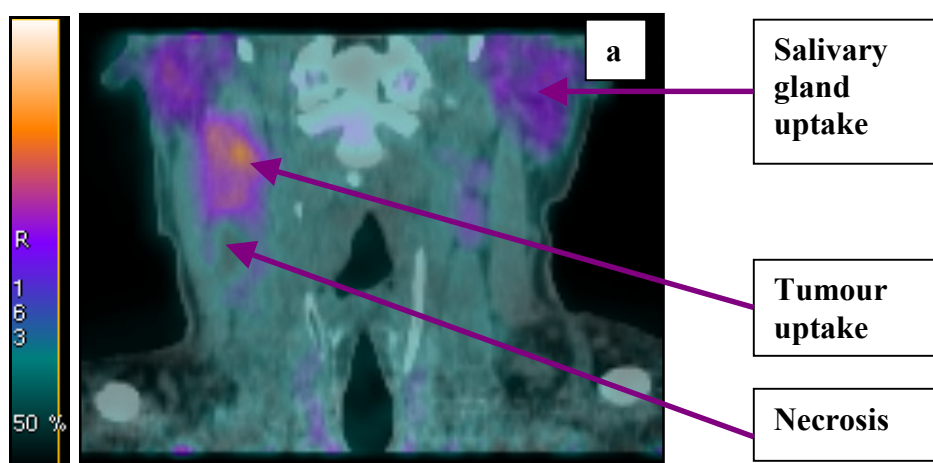


Figure 5.14 a: The uptake of ^{64}Cu -ATSM within the tumour, salivary glands, and necrotic regions at 5 to 20 minutes

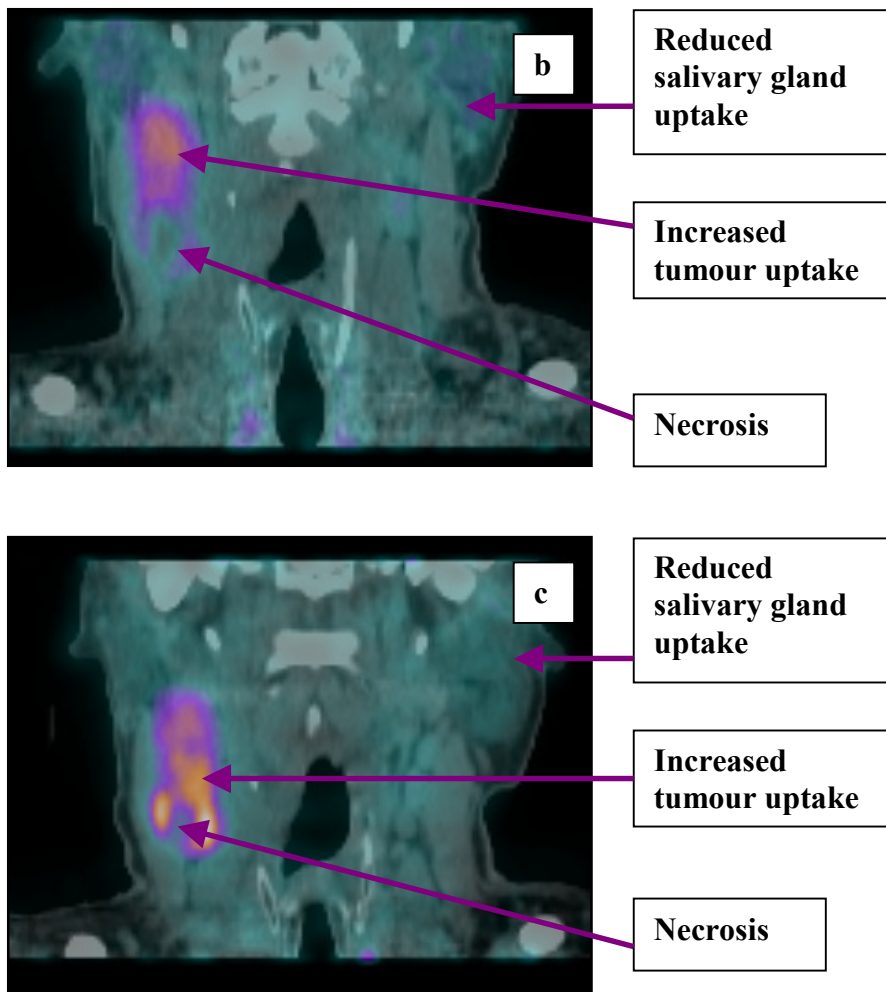


Figure 5.14 b and c: The uptake of ^{64}Cu -ATSM within the tumour, salivary glands, and necrotic regions at 40 to 60 minutes b) and 18 hours after injection c)

5.3.4.1 Other Ratios

Abnormal uptake of ^{64}Cu -ATSM was noted in 2 patients.

5.3.4.1.1 Mandible

The uptake of ^{64}Cu -ATSM was noted in the body of the left mandible in patient 2. This is shown at 5 to 20 minutes and at 18 hours after injection in figure 5.15a and b respectively, and the corresponding uptake on ^{18}F FDG CT-PET 24 hours after ^{64}Cu -ATSM injection c). The tumour to mandible uptake ratio at 5 to 20 minutes was 0.87 to 1.44. The ratio was 3.39 to 4.15 when the uptake in the mandible was compared to the CL SCM, 2.71 to 3.66 compared to the blood, and 3.02 to 3.93 when compared to the uptake in the posterior neck.

When this patient was imaged at 18 hours after the injection of ^{64}Cu -ATSM the ratio with the muscle had reduced to 1.08 to 1.00, and that with the blood had reduced to 0.52 to 0.67, and that with the background had also reduced to 0.71 to 1.17. The tumour to mandible uptake had increased with a ratio of 5.63 to 6.26. ^{18}F FDG CT-PET showed no FDG uptake within the region.

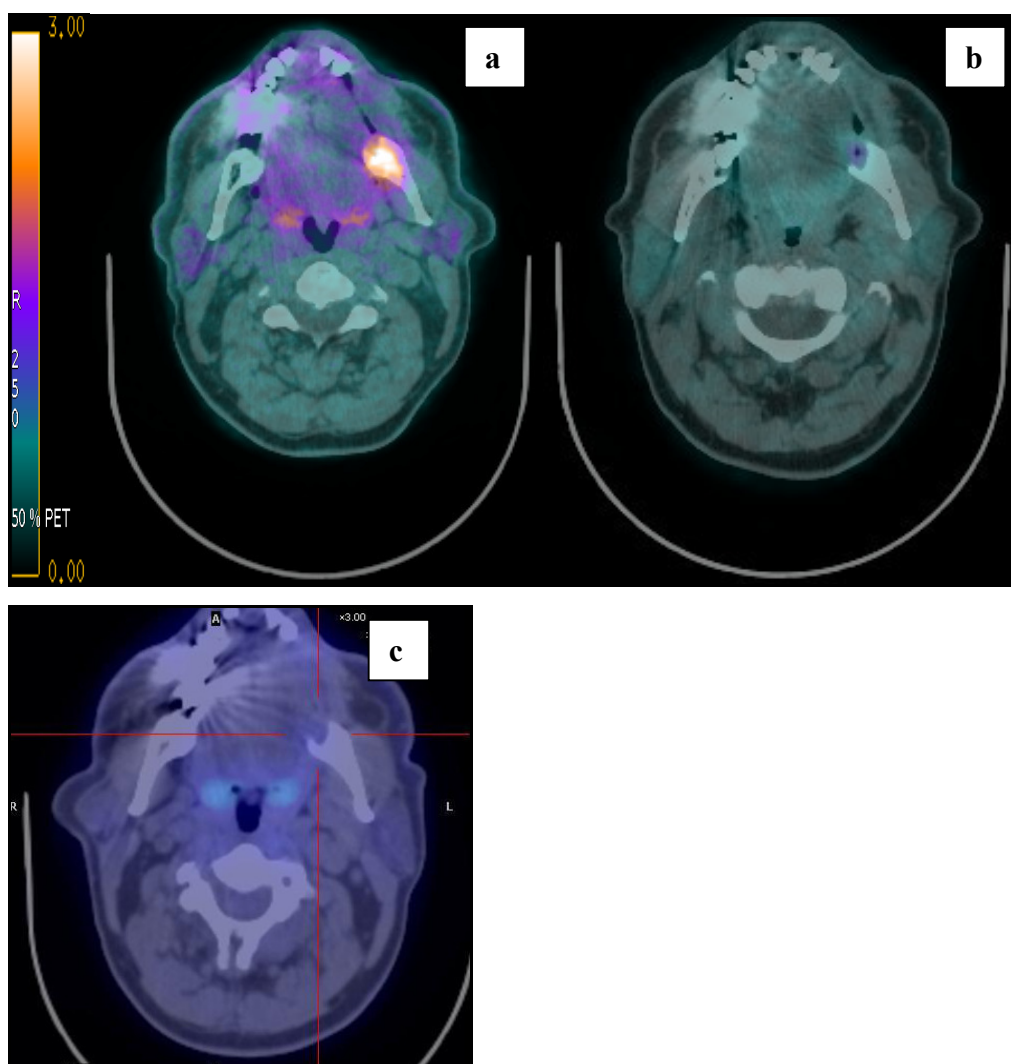


Figure 5.15a to c: Fused CT-PET axial image with increased ^{64}Cu -ATSM uptake within the left mandible at 5 to 20 minutes a), reduced uptake at 18 hours after injection b), and no uptake on ^{18}F FDG CT-PET c)

5.3.4.1.2 Right Shoulder

Increased uptake of ^{64}Cu -ATSM was noted in the right shoulder of patient 4. The ratio of ^{64}Cu -ATSM uptake within the tumour and the right shoulder was 2.13 to 2.57 at 5 to 20 minutes. The ratio of uptake during this time period within the

right shoulder was 2.66 to 3.42 when compared to that in the CL SCM, 1.55 to 2.50 compared to the blood within the carotid artery, and 2.43 to 2.73 when compared to the uptake within the posterior neck.

At 40 to 60 minutes the tumour to right shoulder ratio was 1.401. The ratio to the uptake in the CL SCM was 2.63, the blood was 2.10, and to the background was 1.86. The change in ^{64}Cu -ATSM uptake with time in this region is shown in figure 5.16a) at 5 to 20 minutes and b) at 40 to 60 minutes after injection.

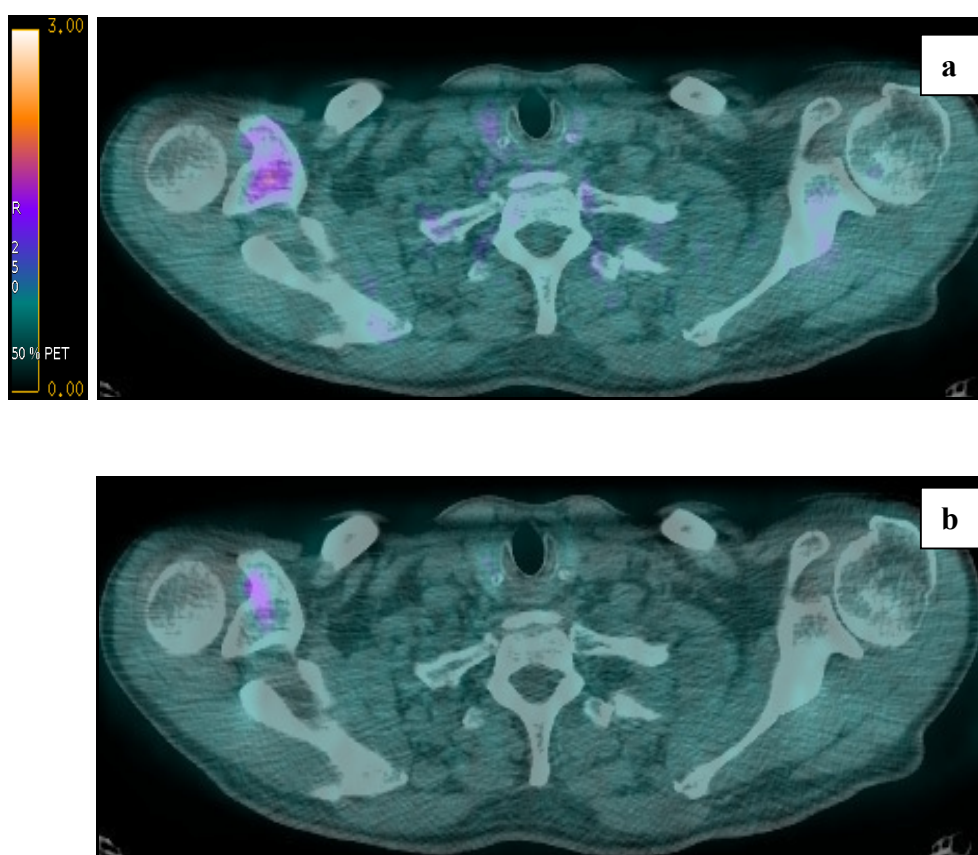


Figure 5.16a and b: The increased uptake of ^{64}Cu -ATSM within the right shoulder at 5 to 20 minutes a), and 40 to 60 minutes after injection b)

5.3.5 Hypoxic Fraction

Figures 5.17a to d show the wax embedded specimen a), and corresponding H+E staining b), and IHC pimonidazole staining c), and the corresponding fused CT-PET image d). In figure 5.17a the necrotic region is indicated with an arrow and

appears white. Creamy yellow SCC replaces the entire node, and skeletal muscle appears dark brown at the bottom of the specimen. These regions are both indicated by arrows.

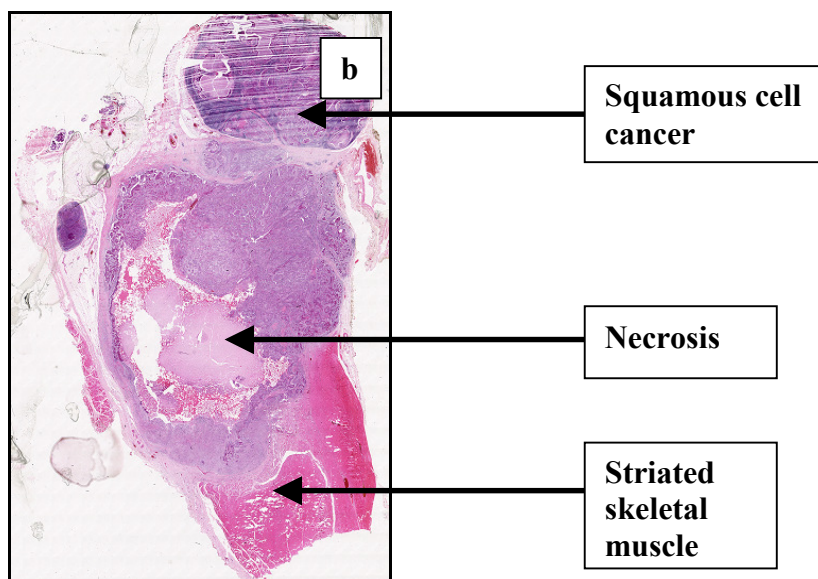
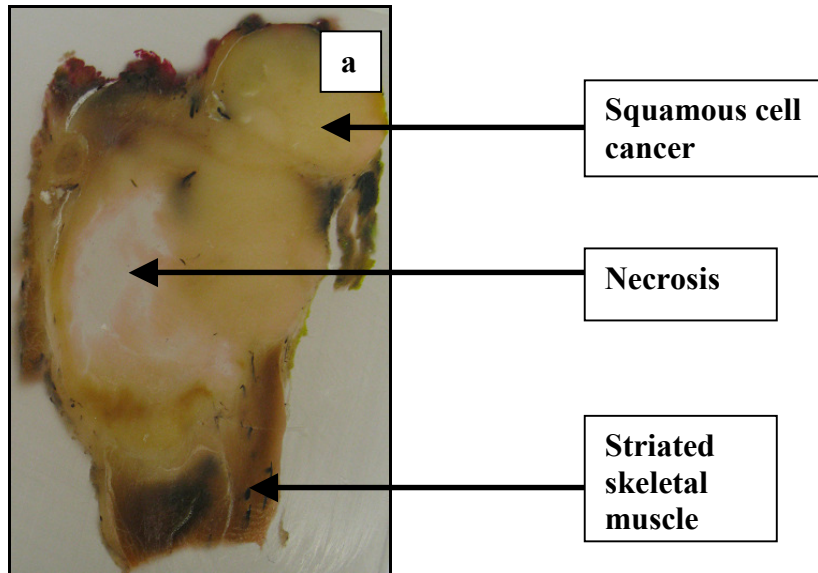


Figure 5.17a and b: The wax embedded tissue specimen a), and haematoxylin and eosin stained section from the corresponding wax block b)

Figure 5.17b illustrates intense nuclear staining (haematoxylin – purple) within the tumour (arrowed). The eosin counter stain (pink) highlights this and also is positive for striated skeletal muscle. This stains gives a colloid appearance for the region of necrosis.

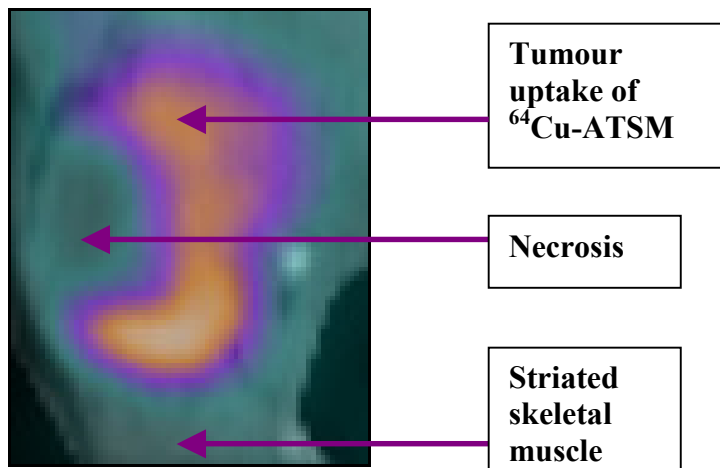
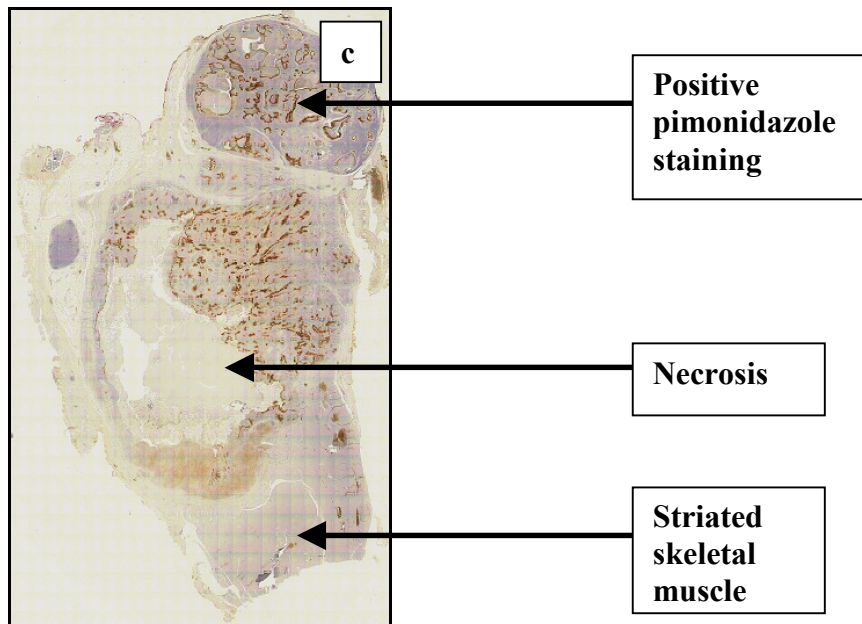


Figure 5.17c and d: The pimonidazole staining for the corresponding wax block a) for patient 1, and the CT-PET fused image d)

Figure 5.17c shows the positive pimonidazole adduct staining (brown horseradish peroxidase) within the specimen. There was no pimonidazole staining within the corresponding area of necrosis. There is generalised pimonidazole staining across the specimen, rather than focal staining suggesting the entire volume of tumour has a pO_2 less than 10mmHg. Figure 5.17d) indicates the tumour uptake and retention at 40 to 60 minutes of ^{64}Cu -ATSM. There is a clear demarcation between reduced uptake within the necrotic region and tumour uptake. Pimonidazole staining and ^{64}Cu -ATSM uptake and retention are absent in corresponding areas.

5.3.5.1 Calculated Hypoxic Area

Table 5.7 illustrates the mean thresholded hypoxic fractional area for each IHC stain. The values for each specimen block were combined to gain the mean.

Table 5.7: Mean hypoxic area fraction per block calculated from the linear unmixed image

Patient	Hypoxic Immuno-histochemical Stain	Hypoxic Fractional Area (%)
1 (2 Tissue Blocks)	Pimonidazole	34.75
	GLUT1	29.22
	CAIX	10.90
	HIF1a	8.54
2 (4 Tissue Blocks)	Pimonidazole	28.78
	GLUT1	34.33
	CAIX	21.44
	HIF1a	11.56
4 (5 Tissue Blocks)	Pimonidazole	33.73
	GLUT1	36.78
	CAIX	31.01
	HIF1a	20.59
5 (4 Tissue Blocks)	Pimonidazole	38.38
	GLUT1	56.26
	CAIX	22.78
	HIF1a	15.91

The mean hypoxic fraction for the combined patients was: pimonidazole 33.82%, GLUT1 43.85%, CAIX 23.01%, and HIF1a 14.39%.

5.3.5.2 Calculated Percentage Staining per Grid

Table 5.8a shows the median percentage staining per grid for each hypoxia IHC stain and the IQR for the combined specimen blocks for each patient, and table 5.8b shows the data combined for all 4 patients.

Table 5.8a: Median percentage immuno-histochemical staining within each grid for each patient and the corresponding inter-quartile range

Patient	Stain	Median Percentage Staining per Grid	25th Centile (%)	75th Centile (%)	Inter-quartile range (%)	Range (%)
1	Pimonidazole	44.58	28.37	59.92	31.55	6.31 to 84.87
	GLUT1	49.26	31.35	53.71	27.36	6.35 to 87.26
	CAIX	26.20	15.28	38.06	22.78	0.83 to 70.35
	HIF1a	8.348	3.65	15.21	11.56	0.70 to 65.04
2	Pimonidazole	35.19	14.81	48.64	33.83	1.02 to 87.00
	GLUT1	46.01	25.12	63.93	38.81	3.06 to 90.28
	CAIX	27.59	13.21	48.08	34.87	0.25 to 98.43
	HIF1a	11.96	3.41	23.70	20.29	0.11 to 79.32
4	Pimonidazole	54.26	29.44	71.43	41.98	1.29 to 97.68
	GLUT1	58.78	34.24	74.51	40.27	5.72 to 100.0
	CAIX	47.21	26.79	68.93	42.14	2.14 to 99.51
	HIF1a	22.69	10.00	36.54	26.54	0.00 to 90.00
5	Pimonidazole	27.72	15.42	40.91	25.48	1.03 to 78.40

	GLUT1	58.09	39.02	74.09	35.07	2.00 to 97.98
	CAIX	10.20	3.85	28.28	24.43	0.00 to 93.16
	HIF1a	14.48	4.28	28.38	24.09	0.00 to 87.29

Table 5.8b: Median percentage immuno-histochemical staining within each grid and the corresponding inter-quartile range for all the patients combined

Stain	Median Percentage Staining per Grid	25th Centile (%)	75th Centile (%)	Inter-quartile range (%)	Range (%)
Pimonidazole	38.19	22.38	80.83	58.46	1.02 to 100.00
GLUT1	54.43	33.40	72.06	38.66	2.00 to 100.00
CAIX	24.06	8.35	48.08	39.73	0.00 to 90.00
HIF1a	14.12	4.32	28.32	24.00	0.00 to 90.00

The two methods used have produced similar results for the hypoxic fraction calculation and corroborate the findings.

5.3.6 Immuno-Histochemistry Correlation

There was a significant positive correlation for pimonidazole staining with GLUT1 ($p < 0.0001$, correlation co-efficient 0.450, 95% CI 0.437 to 0.583), CAIX ($p < 0.0001$, correlation co-efficient 0.584, 95% CI 0.535 to 0.629), and HIF1a ($p < 0.001$, correlation co-efficient 0.297, 95% CI 0.231 to 0.360), when the IHC specimens were aligned and correlated for the area stained per grid and combined

for all the blocks for all 4 patients. On an individual basis, the positive correlation was greatest for patient 4 for pimonidazole and GLUT1 ($p < 0.0001$, correlation co-efficient 0.708, 95% CI 0.640 to 0.765), pimonidazole and CAIX ($p < 0.0001$, correlation co-efficient 0.695, 95% CI 0.623 to 0.754), and pimonidazole and HIF1a ($p < 0.0001$, correlation co-efficient 0.475, 95% CI 0.371 to 0.506).

There was also a significant positive correlation when GLUT1, CAIX and HIF1a were aligned and correlated with each other and this is shown in table 5.9. However this correlation was much weaker, especially for GLUT1 and HIF1a.

Table 5.9: The correlation of GLUT1, CAIX and HIF1a immuno-histochemical stains of all block from the 4 patients

Correlated Stain	p-value	Correlation Co-Efficient	95% CI
GLUT1 and CAIX	0.001	0.423	0.36 to 0.43
GLUT1 and HIF1a	0.02	0.107	0.04 to 0.18
CAIX and HIF1a	0.001	0.237	0.13 to 0.23

An example of the correlation between pimonidazole and GLUT1 is illustrated in figures 5.18 with the line of best fit drawn in green. Each circle represents an individual grid within the specimen.

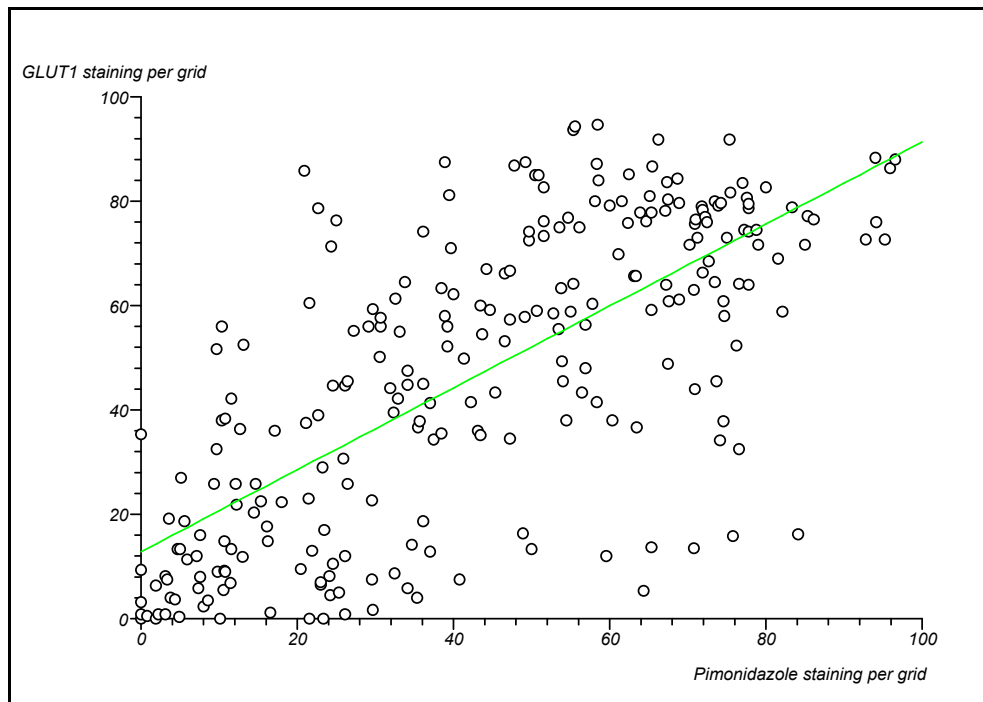


Figure 5.18: Relationship between pimonidazole and GLUT1 staining per grid

There was a significant difference in the percentage of staining within each grid when the stains were compared to each other using the WCSRT and this is shown in table 5.10. There was significantly less pimonidazole staining compared to GLUT1, and significantly greater staining of: pimonidazole compared to CAIX and HIF1a, GLUT1 compared to CAIX and HIF1a, and CAIX compared to HIF1a within the specimens.

Table 5.10: Difference in percentage staining per correlated grid

Correlated Stain	p-value	Median Difference (%)	95% CI
Pimonidazole and GLUT1	<0.0001	-10.19	-12.09 to -8.34
Pimonidazole and CAIX	<0.0001	+7.08	+5.40 to +8.76
Pimonidazole and HIF1a	<0.0001	+17.41	+15.60 to +19.23
GLUT1 and CAIX	<0.0001	+19.75	+17.59 to +21.88

GLUT1 and HIF1a	<0.0001	+24.73	+22.18 to +27.21
CAIX and HIF1a	0.0002	+2.94	+1.27 to +4.73

5.3.7 Physiological Dynamic Contrast-Enhanced CT Parameters

Two patients underwent DCE-CT after the immediate CT-PET (Patient 4 and 5). Only the data from patient 5 was used because patient 4 swallowed and raised their shoulders during the imaging acquisition. The resulted in the streak artefact on the CT images shown in figure 5.19 directly through the tumour ROI. The artefact was due to the attenuation of the x-ray beam through bone and soft tissue. The tumour is outlined in green, and the carotid artery on the IL side of the tumour has a red circle within it. An arrow indicates the area of hypo-dense streak artefact.

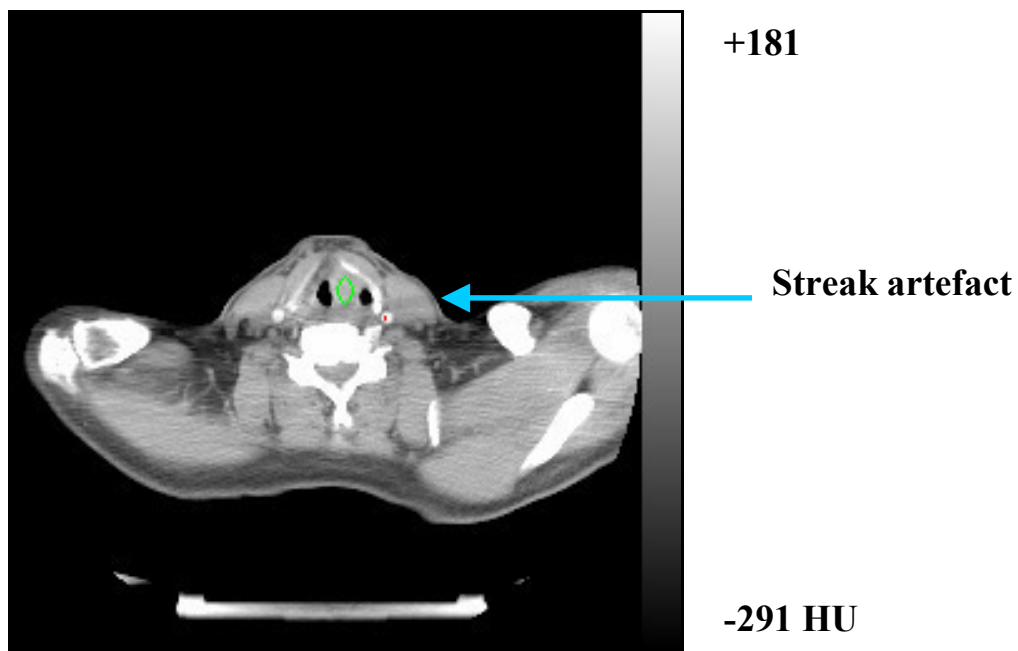


Figure 5.19: Axial CT of patient 4 with the streak artefact through the tumour region of interest

Only 7 images out of 11 did not contain streak artefact and could be analysed. There were abnormal parameters in these images of 44.62HU maximum enhancement, 1ml/min/ml perfusion, 69.11% CP and 8.19% BV which were

falsely high for patient 4. The tissue enhancement by contrast was directly related to the streak artefact and beam attenuation.

Table 5.11 illustrates the AIF, maximum enhancement in HU, perfusion, CP, and BV for each delineated ROI using the WinFun software for patient 5. Each ROI indicated corresponds to the frame number in consecutive order from the superior to inferior aspect of the tumour region. Region 9 represents the necrotic region within the most inferior ROI, 10 the CL SCM, 11 the CL sub-mandibular gland, and 12 the scalene muscle in the posterior neck

Table 5.11: Physiological parameters within the region of interest calculated by the WinFun software

Region of Interest	Arterial Input Function (HU)	Maximum Enhancement (HU)	Perfusion (ml/min/ml)	Capillary Permeability (%/min)	Blood Volume (%)
1	214.89	25.47	0.78	21.47	2.73
2	196.00	27.88	0.82	20.41	2.55
3	194.50	26.95	0.75	25.87	1.60
4	210.50	26.76	0.56	21.11	1.68
5	206.50	26.74	0.58	22.68	1.28
6	212.82	22.89	0.51	19.13	1.03
7	217.08	25.47	0.44	19.53	0.90
8	212.64	18.15	0.38	12.99	0.80
9	218.80	3.57	0.11	3.46	0.25
10	196.00	6.75	0.31	6.17	0.60
11	196.00	23.48	0.63	25.39	3.66
12	196.00	5.56	0.28	3.36	0.60

The maximum enhancement within the necrotic region was 85.74% less than the combined maximum enhancement of ROI 1 to 7. This reduction was 73.04% in

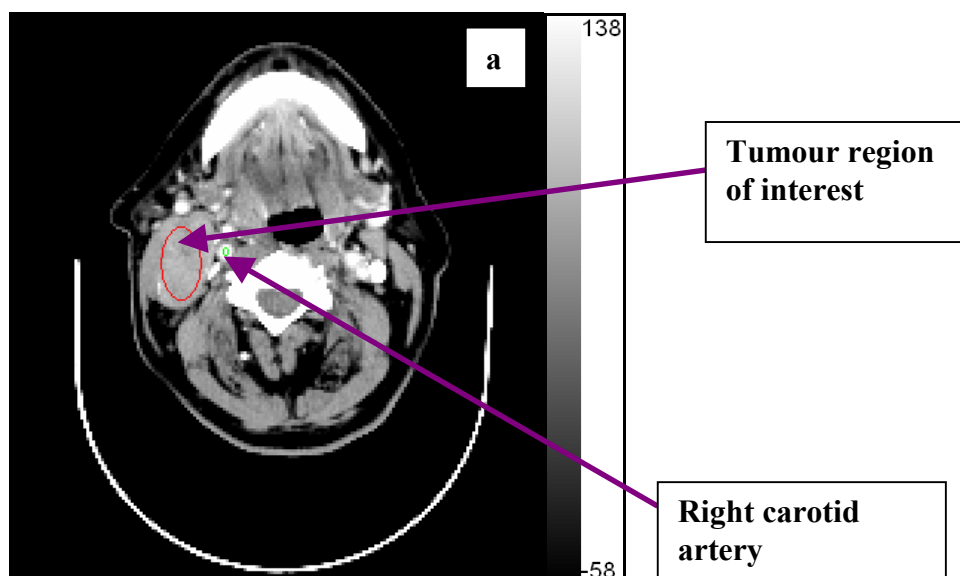
the CL SCM, 6.23% within the CL submandibular gland, and 77.79% in the posterior neck.

The perfusion within the necrotic region was 78.21% less than that within the combined tumour ROI, and 39.22%, and 45.09% less within the CL SCM and posterior neck. The perfusion within the submandibular gland was 23.53% greater than the tumour perfusion.

The CP within the necrotic region was 83.04% less than that within the tumour. This compared with a 69.21% reduction in the CL SCM and 83.23% within the posterior neck. The CP within the salivary gland was also 26.69% greater than that within the tumour.

The BV within the necrotic region was 84.08% less than that within the tumour, and 61.78% less within the CL SCM and posterior neck. However the BV within the CL submandibular gland was 133.12% greater than that within the tumour.

Figure 5.20 a to c illustrates ROI 3 delineated by the WinFun software. Arrows indicate the tumour ROI delineated in red and the carotid artery in green. Contrast is present within the carotid artery and appears white. The scale is in HU. Image b shows the maximum enhancement following contrast administration which is colour mapped, and image c the CP in %/min.



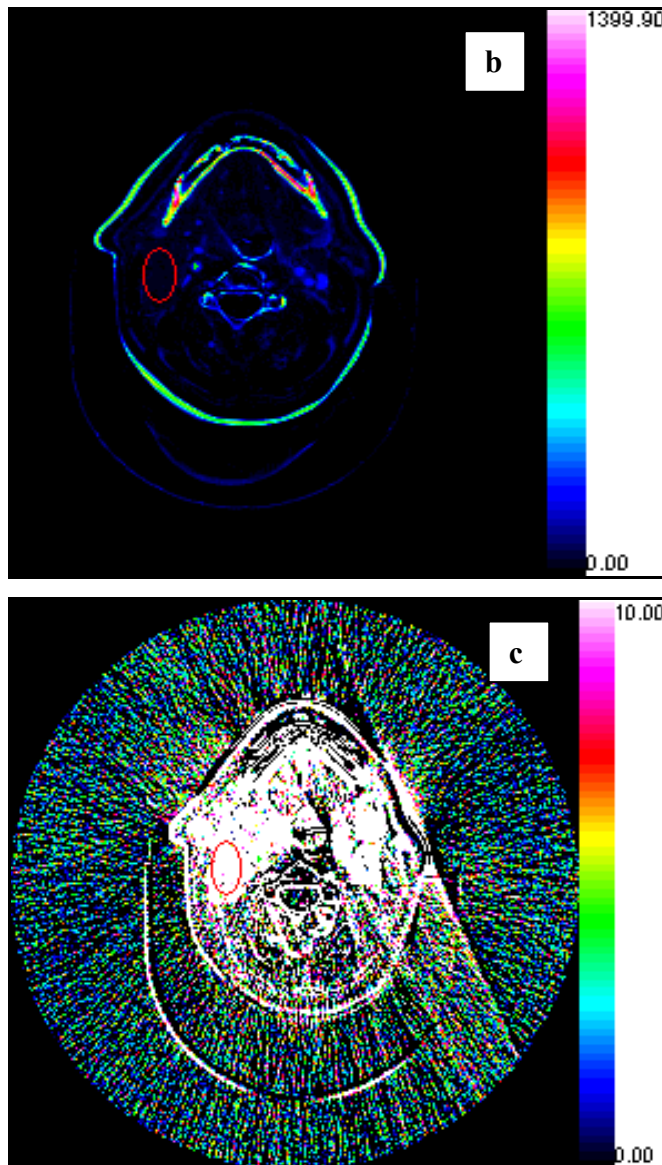


Figure 5.20a to c: Delimited region of interest a), maximum enhancement b), and permeability c) using the WinFun software

Table 5.12 illustrates the physiological parameters defined by the CT Perfusion 4 GE Healthcare software. The mean value for the ROI is shown. Region 1 represents the carotid artery, and region 9a necrosis within ROI 9. The other indicated ROI are in consecutive order from the superior to inferior aspect of the tumour region. Regions 10, 11, and 12 represent the CL SCM, CL sub-mandibular gland, and scalene muscle of the posterior neck respectively. The values for ROI 9 are lower than the other tumour values because this contained the necrotic region and lowered all the calculated parameters.

Table 5.12: Physiological parameters within the region of interest calculated by the CT Perfusion 4 GE Healthcare software

Region of Interest	Blood Flow (ml/min/100g)	Blood Volume (ml/100g)	Mean Transit Time (seconds)	Permeability Surface Area (ml/min/100g)
1 (Artery)	1000	65.70	1.94	0.00
2	186.86	6.38	2.30	4.68
3	169.52	5.69	2.18	9.81
4	168.51	5.52	2.01	10.84
5	159.23	5.67	2.54	9.75
6	172.71	5.89	2.22	6.31
7	142.45	5.02	2.49	5.04
8	114.60	4.45	3.72	8.45
9	129.90	4.54	3.01	2.78
9a (Necrosis)	15.04	0.80	11.26	0.61
10 (CL SCM)	14.18	1.54	4.94	1.25
11 (CL Salivary Gland)	87.02	6.15	5.20	0.64
12 (Posterior Neck)	7.75	0.38	8.69	0.71

The mean perfusion values across the tumour ROI were: BF 155.47 ml/min/100g, BV 5.40ml/100g, MTT 2.56 seconds, and PS 7.21 ml/min/100g.

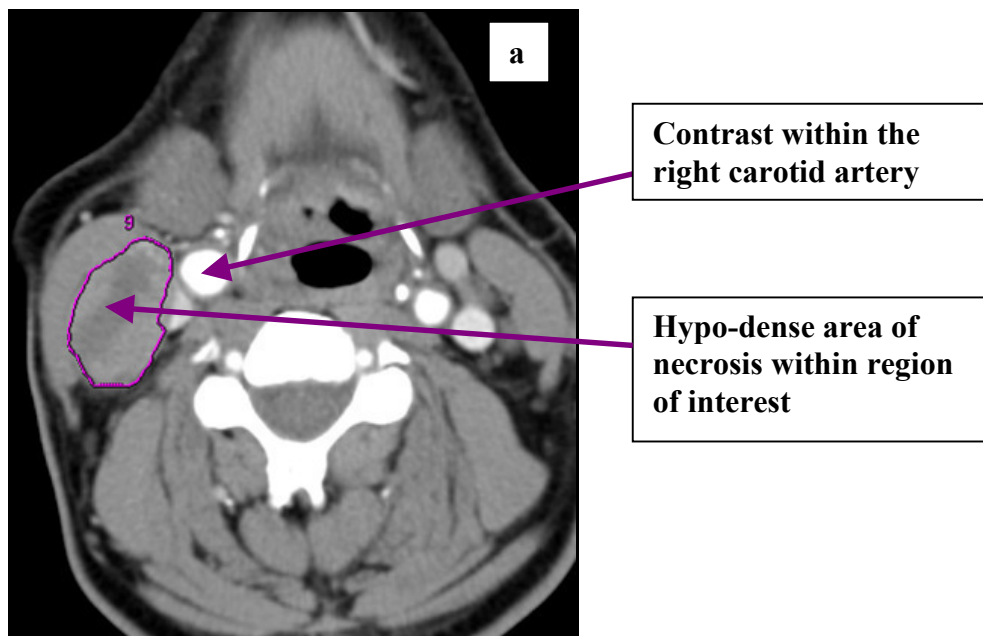
The mean BF within the necrotic region was 90.32% less than the maximum BF within the combined tumour ROI. The CL SCM muscle BF value was 90.88% of that within the tumour, the CL submandibular gland was 44.03% and posterior neck was 95.01% of that within the tumour.

The mean BV within the necrotic region was 85.17% less than that within the tumour. The BV within the CL SCM, and posterior neck was 71.45% and 92.96% less than that within the tumour respectively, and the CL submandibular gland was 13.97% greater than the tumour.

The maximum MTT was 341.18% greater in the necrotic region than in the tumour. This was 93.12%, 103.28%, and 239.72% greater in the CL SCM, CL submandibular gland, and posterior neck respectively.

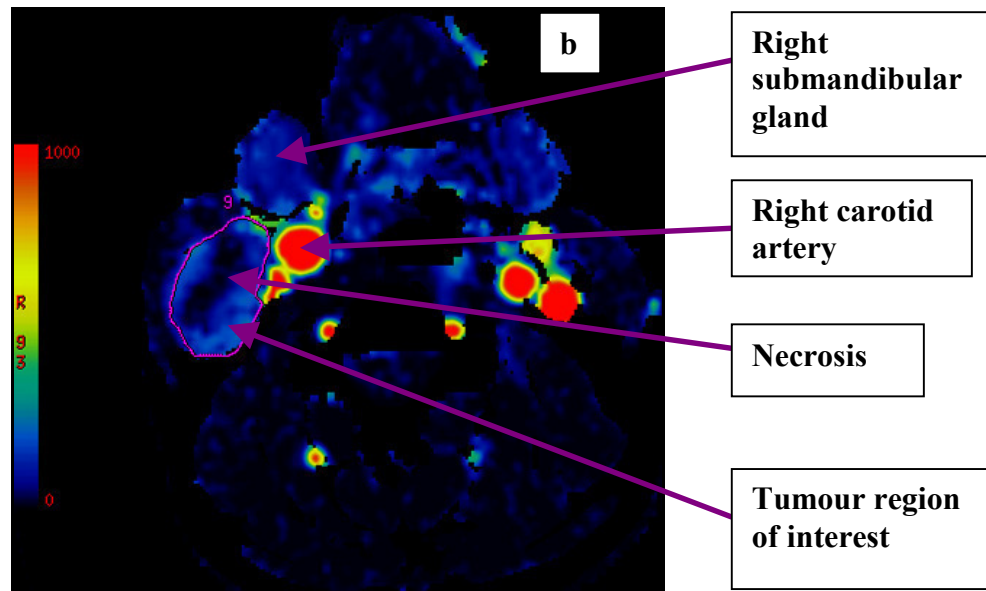
The maximum PS was 90.71% less in the region of necrosis than in the tumour, and 82.66%, 91.12%, and 90.15% less in the CL SCM, CL submandibular gland, and posterior neck respectively than the tumour.

Figure 5.21 illustrates the corresponding axial images for ROI 9 defined by the GE Healthcare software. Figure 5.21a) is the DCE-CT axial image, b) the BF, c) the BV, d) the MTT and e) the corresponding PS for the axial image. Purple arrows indicate the hypo-dense region of necrosis within the ROI, and contrast within the carotid artery in figure 5.21a).



In Figure 5.21b) BF across the image is low, but is greater within the ROI than the surrounding muscle. There is no BF within the necrotic region compared to

the surrounding tumour. The carotid artery due to the high velocity of BF is bright red with values of 1000ml/min. An arrow indicates the submandibular gland and BF within this region is similar to that within the tumour region.



The arrows in figure 5.21c) indicates the right carotid artery, region of necrosis, and tumour. The BV within the arterial vessel is greatest. The rim of tumour has a higher BV than the central area of necrosis. Similarly, the submandibular gland has a BV greater than the tumour.

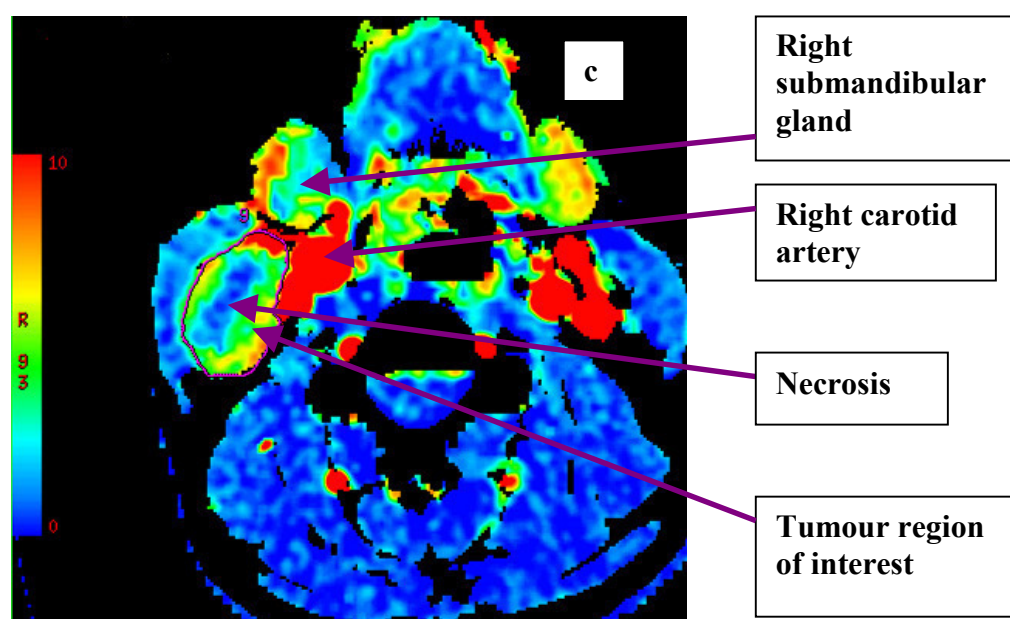
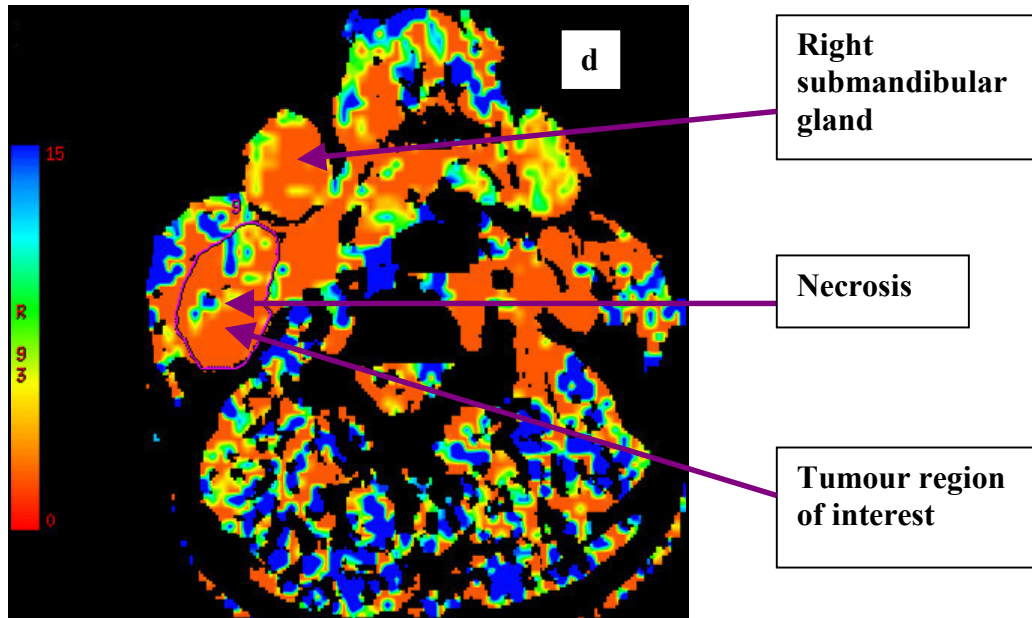


Figure 5.21d) illustrates the colour map for the MTT. The MTT is fastest through the tumour region, and is slowest within the area of necrosis. The MTT within the submandibular gland is slower than that within the tumour.



Lastly Figure 5.21e) illustrates the PS. This is heterogeneous across the tumour region. The arrow indicates the lower PS within the region of necrosis.

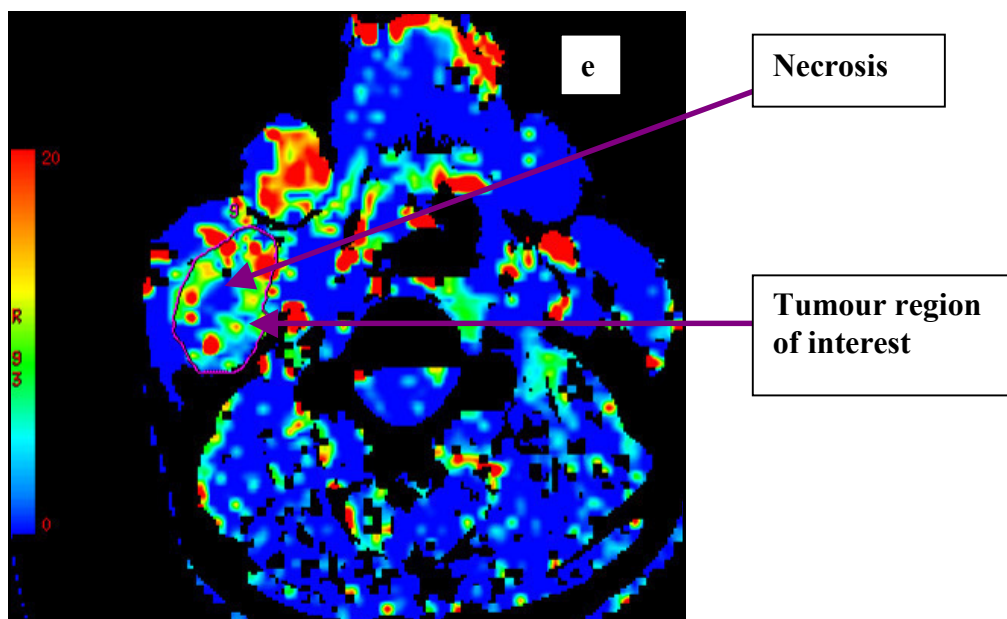


Figure 5.21a to e: Axial images for region of interest 9 defined by the CT Perfusion 4 GE Healthcare software. The colour maps are: dynamic contrast-enhanced CT a), blood flow b), blood volume c), mean transit time d), and permeability surface area e)

5.3.8 Correlation of Blood Flow and ^{64}Cu -ATSM Uptake

There was a significant median difference between the grayscale intensity for BF measured by the DCE-CT and ^{64}Cu -ATSM uptake within the tumour region at 5 to 20 minutes ($p < 0.0001$, median difference 63.30, 95% CI 56.24 to 62.30), 40 to 60 minutes ($p < 0.0001$, median difference 48.53, 95% CI 46.37 to 50.66), and at 18 hours ($p < 0.0001$, median difference 54.71, 95% CI 53.05 to 56.28) after ^{64}Cu -ATSM injection. This showed that the ^{64}Cu -ATSM uptake was significantly greater than the BF within the region.

At 5 to 20, 40 to 60 minutes and late imaging of 18 hours there was no significant correlation between these two variables within the tumour region.

However when the necrotic region was analysed separately, there was no significant correlation at 5 to 20 minutes, but there was a positive correlation at 40 to 60 minutes ($p = 0.001$, correlation co-efficient 0.343, 95% CI 0.25 to 0.43) and at 18 hours post injection ($p = 0.001$, correlation co-efficient 0.288, 95% CI 0.18 to 0.40). The correlation was weaker at 18 hours post injection compared to 40 to 60 minutes. This showed that in necrotic regions when there was no BF there was minimal or no ^{64}Cu -ATSM uptake.

5.3.9 Correlation of Immuno-Histochemistry and ^{64}Cu -ATSM Uptake

There was a significant correlation of pimonidazole, GLUT1, CAIX, and HIF1a IHC staining with the uptake and retention of ^{64}Cu -ATSM at 5 to 20 minutes, 40 to 60 minutes, and at 18 hours after injection for the combined grid data (all blocks for all patients). Table 5.13 illustrates these results.

The correlation was most significant, and the co-efficient strongest for GLUT1 at 5 to 20 minutes, pimonidazole at 40 to 60 minutes, and HIF1a 18 hours after the injection of ^{64}Cu -ATSM.

Table 5.13: The correlation between the hypoxic immuno-histochemical staining and the ^{64}Cu -ATSM uptake and retention

Time after injection	Stain	p-value	Correlation Co-efficient	95% CI
5 to 20 minutes	Pimonidazole	<0.0001	0.513	0.45 to 0.57
	GLUT1	<0.0001	0.527	0.45 to 0.59
	CAIX	<0.0001	0.452	0.37 to 0.52
	HIF1a	0.001	0.363	0.28 to 0.44
40 to 60 minutes	Pimonidazole	<0.0001	0.606	0.54 to 0.66
	GLUT1	0.001	0.225	0.12 to 0.33
	CAIX	0.01	0.122	0.04 to 0.20
	HIF1a	0.01	0.120	0.12 to 0.28
18 hours	Pimonidazole	<0.0001	0.504	0.41 to 0.59
	GLUT1	0.001	0.391	0.28 to 0.49
	CAIX	<0.0001	0.471	0.41 to 0.53
	HIF1a	<0.0001	0.538	0.48 to 0.60

Figure 5.22a to c illustrate the spread of the data for the mean grayscale intensity of pimonidazole compared to the mean grayscale intensity of ^{64}Cu -ATSM uptake on the fused CT-PET images at 5 to 20 minutes, 40 to 60 minutes, and at 18 hours after the injection of ^{64}Cu -ATSM. The line of best fit is drawn in green. Again each circle represents an individual correlated grid.

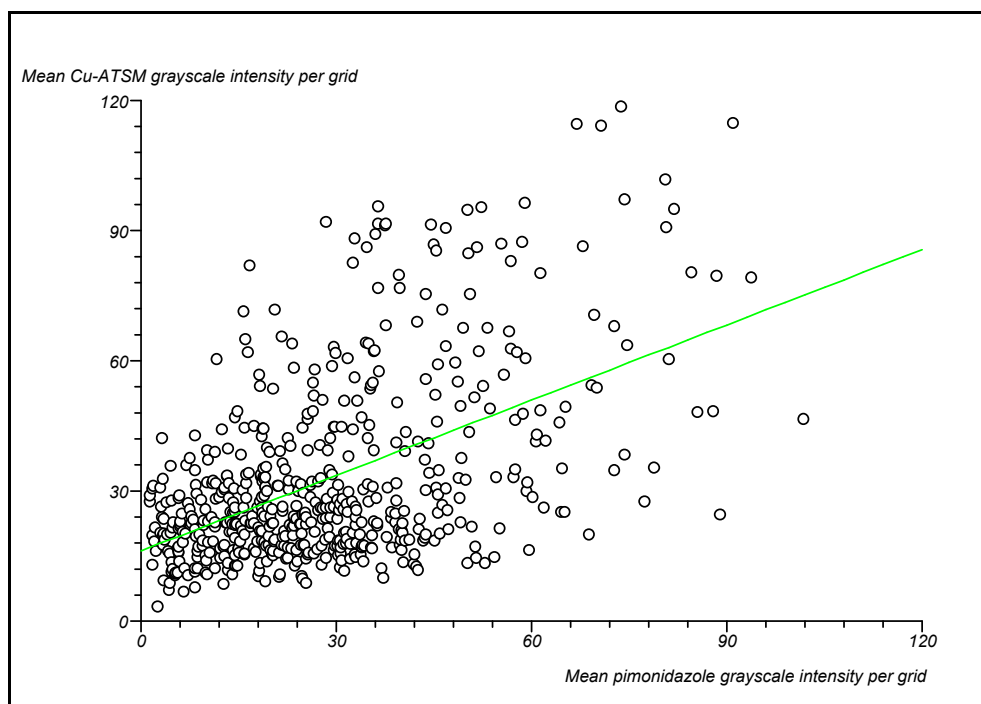


Figure 5.22a: The mean grayscale intensity of pimonidazole staining and ^{64}Cu -ATSM uptake at 5 to 20 minutes after injection

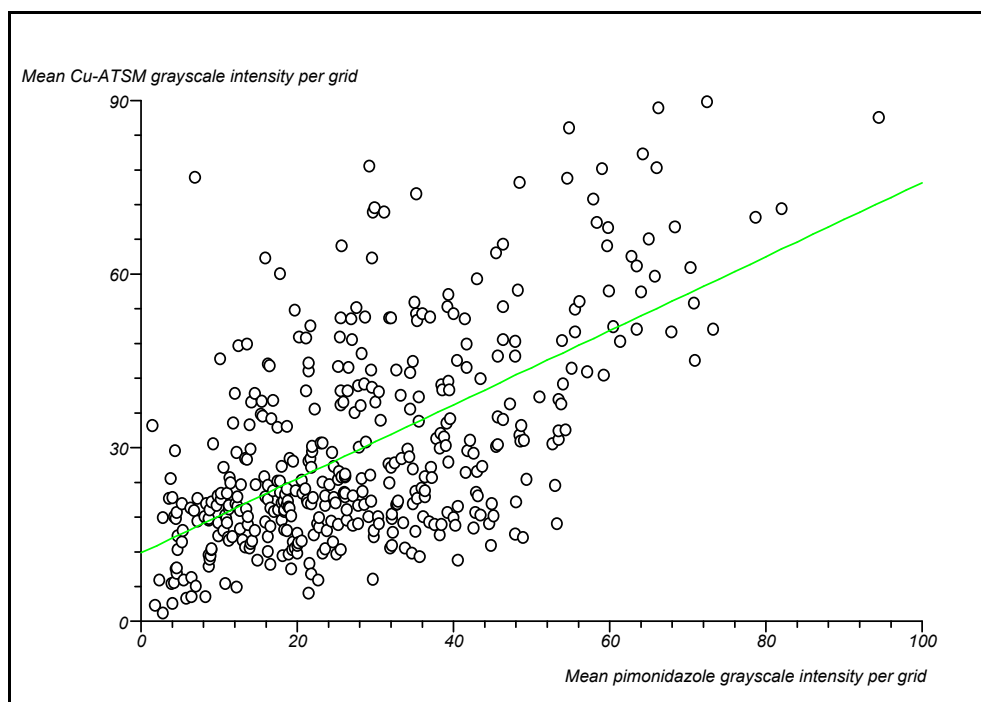


Figure 5.22b: The mean grayscale intensity of pimonidazole staining and ^{64}Cu -ATSM uptake at 40 to 60 minutes after injection

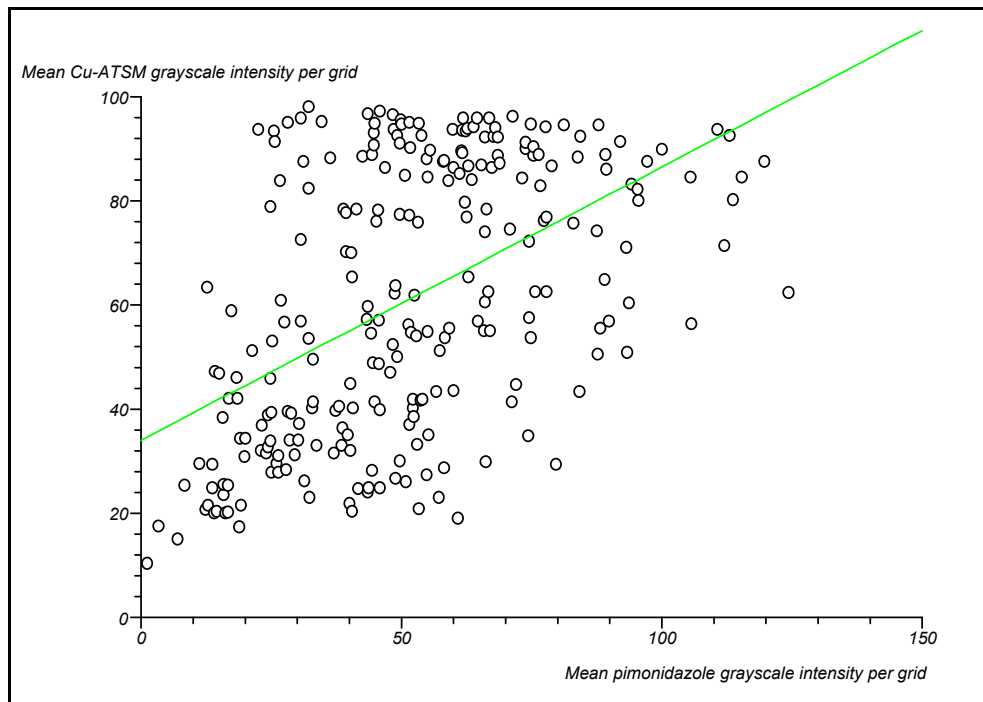


Figure 5.22c: The mean grayscale intensity of pimonidazole staining and ^{64}Cu -ATSM uptake at 18 hours after injection

5.3.10 Hypoxic Functional Volume Delineation

The hypoxic FV was delineated and calculated according to the tumour to muscle, tumour to blood and tumour to background ratios using the PETVCAR software.

Figures 5.23 illustrates the delineated FVs according to the tumour to muscle ratios of: 2.0, 2.5, 3.0, 3.5, and 4.0 at 5 to 20 minutes, 40 to 60 minutes and 18 hours after ^{64}Cu -ATSM injection for patient 5 as an example. As previously shown, as the ratios increased with increasing time after injection of ^{64}Cu -ATSM, and the defined FV increased accordingly.

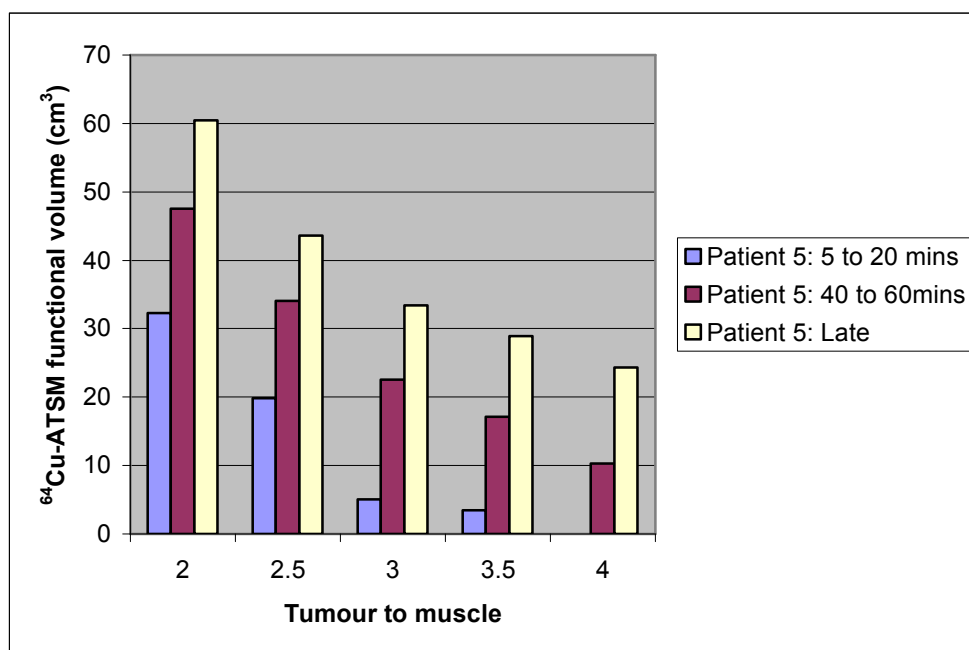


Figure 5.23: ^{64}Cu -ATSM defined hypoxic functional volume for patient 5 according to the tumour to muscle ratio

Figure 18 a to c in Appendix 2 illustrates these defined hypoxic FV according to the tumour to muscle ratio for the other patients.

Figure 5.24a and b illustrates the changes in FV delineated for patient 4 when defined by the tumour to muscle ratio of 2.5. The FV is delineated in green surrounded by a green boundary box. The red box indicates the reference region in the SCM muscle. The delineated hypoxic FV is greater at 40 to 60 minutes than at 5 to 20 minutes after injection.

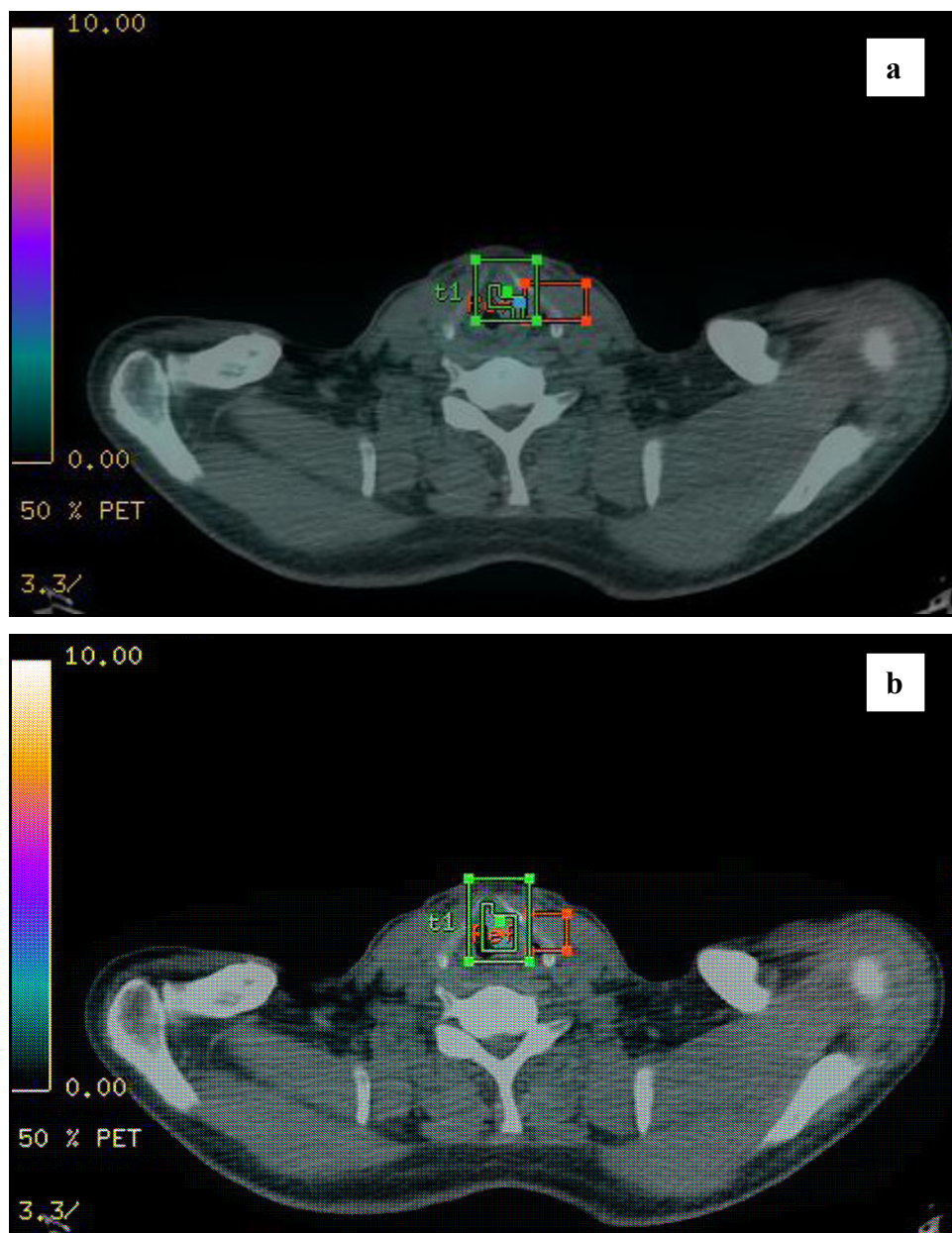


Figure 5.24a and b: The delineated hypoxic functional volume and the reference region at 5 to 20 minutes a) and 40 to 60 minutes b) after the injection of ^{64}Cu -ATSM

Table 5.14 indicates the actual hypoxic FV delineated for each tumour to muscle ratio. The hypoxic FV reduced as the defining ratio increased, and the volumes increased with time after the injection of ^{64}Cu -ATSM.

At 5 to 20 minutes there was a 50.96% to 100% reduction between the FV delineated by the 2.5 ratio, and that at the 4.0 ratio. This reduction was 53.27% to 97.03% at 40 to 60 minutes, and 59.83% to 63.5% 18 hours after injection.

Table 5.14: The hypoxic functional volume defined by the tumour to muscle ratio after the injection of ^{64}Cu -ATSM

Patient		Hypoxic Functional Volume (cm^3) Defined by the Tumour to Muscle Ratio				
		2.0	2.5	3.0	3.5	4.0
1	5 to 20 minutes	51.8	43.5	34.6	30.6	25.4
	40 to 60 minutes	61.2	49.1	40.9	36.4	32.6
2	5 to 20 minutes	25.9	19.8	15.9	11.2	9.5
	Late	28.5	21.0	15.6	12.3	10.4
4	5 to 20 minutes	3.1	1.2	0.0	0.0	0.0
	40 to 60 minutes	10.0	6.6	2.6	1.1	0.3
5	5 to 20 minutes	32.3	19.8	5.1	3.5	0
	40 to 60 minutes	47.5	34.1	22.6	17.1	10.3
	Late	60.5	43.6	33.4	28.9	24.3

The hypoxic FV defined according to the tumour to blood, and tumour to background ratios were smaller than those defined by the tumour to muscle ratio and are shown in table 5.15 and 5.16 respectively. Similarly the volumes defined reduced with each increase in the defining ratio.

Table 5.15: The hypoxic functional volume defined by the tumour to blood ratio after the injection of ^{64}Cu -ATSM

Patient		Hypoxic Functional Volume (cm³) Defined by the Tumour to Blood Ratio				
		2.0	2.5	3.0	3.5	4.0
1	5 to 20 minutes	25.4	19.2	13.5	4.4	1.1
	40 to 60 minutes	40.9	21.9	8.1	4.6	2.6
2	5 to 20 minutes	22.1	15.9	11.2	8	5.7
	Late	15.6	9.9	7.0	4.6	3.2
4	5 to 20 minutes	1.6	0.0	0.0	0.0	0.0
	40 to 60 minutes	7.3	3.5	1.4	1.3	0.0
5	5 to 20 minutes	23.4	5.1	3.5	0.0	0.0
	40 to 60 minutes	30.1	17.1	4.9	1.2	0.0
	Late	35.7	26.3	21.7	13.9	6.2

The percentage reduction in the FV defined by the tumour to blood ratio of 2.5 and 4.0 at 5 to 20 minutes was 74.21% to 100%. At 40 to 60 minutes this reduction was 93.64% to 100%, and at 18 hours after injection this was 79.47% to 82.63%.

Table 5.16: The hypoxic functional volume defined by the tumour to background ratio after the injection of ^{64}Cu -ATSM

Patient		Hypoxic Functional Volume (cm³) Defined by the Tumour to Background Ratio				
		2.0	2.5	3.0	3.5	4.0
1	5 to 20 minutes	43.5	34.6	25.4	19.2	13.5
	40 to 60 minutes	49.1	40.9	21.9	8.1	1.4
2	5 to 20 minutes	26.7	22.1	18.1	14.0	10.8
	Late	23.3	16.9	13.2	11.0	8.8
4	5 to 20 minutes	4.5	1.6	0.5	0.0	0.0
	40 to 60 minutes	7.3	3.5	1.4	0.3	0.0
5	5 to 20 minutes	47.7	32.3	19.8	10.2	3.0
	40 to 60 minutes	47.5	34.1	22.6	17.1	10.3
	Late	60.5	43.6	33.4	28.9	24.3

Lastly, the FV delineated by the tumour to background ratio at 2.5 and 4.0 reduced by 59.55% to 100%. At 40 to 60 minutes this reduction was 78.31 to 100%, and at 18 hours after injection this was 37.76% to 59.83%.

5.4 Discussion

The uptake of ^{64}Cu -ATSM significantly increased with time after injection within the tumour compared to other ROI such as the CL SCM. Hypoxia IHC staining for pimonidazole was generalised across the tumour volume, and correlated with the other endogenous stains. The uptake and retention of ^{64}Cu -ATSM on the fused CT-PET images at 5 to 20 minutes, 40 to 60 minutes and 18 hours after injection significantly correlated with all IHC hypoxia markers. There was no correlation on each axial image when this uptake was compared to BF. The hypoxic FV was greatest when defined by the tumour to muscle ratio, and reduced as the defining ratio increased.

These results suggest that ^{64}Cu -ATSM is retained within hypoxic tumour regions after injection, and may potentially act as a surrogate hypoxic radio-nuclide in CT-PET imaging.

5.4.1 Uptake of ^{64}Cu -ATSM on 3D Dynamic Imaging

The activity of ^{64}Cu -ATSM peaked within the arterial vessel at 30 seconds to 1 minute after injection. This was associated with the bolus injection of ^{64}Cu -ATSM into the venous network. It is assumed that during the first 5 minutes after injection, ^{64}Cu -ATSM moved from the intra-vascular to intra-cellular compartment, and may have equilibrated with the intra-cellular copper pool.

In EMT6 tumour bearing mice, and rat xenograft models, ^{64}Cu -ATSM was rapidly cleared from the blood pool within 5 minutes, and remained up to 4 hours after injection, at 2.22% to 7.88% of the injected dose [16,17]. This data from arterial sampling has the advantage of allowing the rate constant calculation for the transfer of the radio-nuclide between compartments.

In patients with NSCLC the organ residence time was calculated by an analytical integration method, and standardised for a 70Kg adult male. Arterial samples were also taken prior to ^{64}Cu -ATSM injection, and then at 5, 15, 30, 60, and 90 minutes. The activity at 5 minutes within the arterial blood pool was 12%, and at

90 minutes this had reduced to 8% of the injected dose. The calculated residence time within the blood pool was 1.25 ± 0.37 hours [18].

The detected activity of ^{64}Cu -ATSM in the results from the chapter plateaued within all regions between 5 to 60 minutes after injection on dynamic image assessment. This gave a global evaluation of uptake over the ROI. Delineation of these ROI was on the PET only image and was open to error because of the lack of CT anatomical data to clearly define the edge of the region.

The analysis of blood samples was possible within the study protocol due to the debate in the literature over the intra-cellular retention pattern both of ^{64}Cu -ATSM, ^{64}Cu , and the ATSM ligand. However, due to poor patient accrual blood samples were not taken. This was then planned for patients recruited at the Guy's site. The venous samples would have been taken at 0, 2, 4, 6, 8, 10, 20, 30, 40, 50, and 60 minutes after ^{64}Cu -ATSM injection. Sample analysis would be able to calculate the percentage of the injected activity within the blood pool at later time points such as: 4, 6, 12, and 24 hours. The disadvantage of this sampling was patient inconvenience, potentially limiting compliance within the study.

5.4.1.1 ^{64}Cu -ATSM uptake within the Salivary Glands

Uptake was noted in the salivary glands at 5 to 20, 40 to 60 minutes and at 18 hours after ^{64}Cu -ATSM injection. This was unusual and unexpected. There currently is no published data on the bio-distribution of any Cu isotope within the salivary gland. The uptake of ^{64}Cu -ATSM within the salivary glands may be a combination of incorporation into the copper intra-cellular pool, utilisation in normal salivary function, and a correlation with the injected dose.

In the rat SCCVII tumour model ^{64}Cu -ATSM uptake was noted in the fronto-nasal sinus, abdomen, and nasal cavity [19]. The salivary glands arise from ectodermal mesenchyme, and may impact ^{64}Cu -ATSM uptake within the salivary glands. Human foetal studies have suggested increased CAIX expression continues into adult life in areas containing adult stem cells originating from embryonic coelom and mesenchyme [20].

Pimonidazole and misonidazole positively stain the intra-lobular ducts of the parotid gland on IHC [21,22]. This may be related to a lower pO_2 and high levels of NADH reductase within the major and minor salivary glands. Under conditions of acute hypoxia, salivary flow increases in patients [23], and the serum amylase is also raised [24]. This will promote electron reduction of nitro-imidazoles to a pimonidazole adduct for example.

The normal copper retention and metabolism within the salivary glands may be implicated in the increased uptake of ^{64}Cu -ATSM. A positive correlation exists between the amount of copper within the saliva and plasma [25]. This may suggest a large bolus of radio-nuclide in the blood increased the copper content within the salivary glands.

Copper binds to salivary amylase at two metal binding sites [26], and is found in high concentrations within the rat submandibular gland in copper containing super-oxide dismutase [27]. Also Menkes protein (copper export pump) is located within acinar cells, further suggesting a role for copper secretion within the saliva [28].

This interesting phenomenon could be further explored by correlating the uptake of ^{64}Cu -ATSM in the blood with that in saliva samples after injection. Whole body CT-PET imaging was planned within the study reported in this chapter but not undertaken due to poor patient accrual. It would be important to incorporate this into further studies using copper isotopes to assess the whole body bio-distribution of Cu-ATSM.

5.4.2 Uptake of ^{64}Cu -ATSM According to the Calculated Tumour Ratios

The Xeleris software was used to calculate the dynamic uptake of ^{64}Cu -ATSM within a whole region. The disadvantage of this was that the activity could not be calculated for static images because dynamic data was required per frame, and that the activity was calculated over the entire ROI rather than per axial slice.

SUV has been validated as a semi-quantitative tool for uptake assessment of ^{18}F FDG, but this cannot be used in uptake evaluation of other radio-nuclides. The

ratios were calculated to represent the uptake within the tumour compared to other ROI. The uptake within the shoulder of patient 4 and mandible of patient 2 could not be calculated by the Xeleris software because the uptake could not be cleared visualised on the PET only image.

An important point is the tumour ratios are significantly different at 5 to 20 minutes and 40 to 60 minutes compared to the uptake activity measured on dynamic imaging. The measurement methods and software applications are different therefore it is difficult to compare these results, and the differences in uptake and retention assessed by the Xeleris software are difficult to appreciate.

5.4.2.1 Tumour to Muscle Ratio

The calculated ratios have allowed the uptake of ^{64}Cu -ATSM to be quantified in relation to normal tissue. These results are similar to those in animals where the uptake of ^{64}Cu -ATSM was 4 times greater than or equal to normal tissue [16,29].

The data suggested the retention of ^{64}Cu -ATSM increased with time after injection. The statistical difference in the tumour to muscle ratio was greatest at 40 to 60 minutes rather than 18 hours after injection when compared to the uptake at 5 to 20 minutes. Even though only two patients were imaged 18 hours after injection there was still a significant difference in these ratios at this time point within each axial image. This variation suggests that hypoxia selectivity increases with time, and this may be due to the incorporation of ^{64}Cu -ATSM into the intra-cellular copper pools. Also as the retention within the tumour increases, the ratio will increase accordingly. The long half-life of ^{64}Cu -ATSM has enabled these differences to be seen. In NSCLC patients [18], tissue retention was greater than 8 hours in organs such as the liver when computer generated. Prolonged blood sampling and kinetic analysis would allow further evaluation of this.

In the published clinical studies, tumour to muscle ratio's have varied in patients with rectal cancer between 1.0 and 3.7 [15], in NSCLC between 1.2 to 4.8 [13], and in cervical cancer between 1.2 to 12.3 [14]. All these patients were imaged with ^{60}Cu -ATSM, and these ratios corresponded to the uptake in the summed images at 30 to 60 minutes after injection.

5.4.2.2 Tumour to Blood Ratio

The mean tumour to blood ratio at 5 to 20 minutes was only 2.32, but it significantly increased to 3.24 at 40 to 60 minutes, and 3.35 at 18 hours compared to this initial time point. On closer inspection the lowest ratio at 5 to 20 minutes was 1.57. It would be assumed that initial difference between these two regions should have been greater. This may indicate that ^{64}Cu -ATSM is rapidly and non-selectively distributed after injection, producing a reduction in the activity within the intra-vascular compartment. This may be followed by a more selective retention pattern. The time-activity also showed that there was minimal difference initially with time. As the uptake within the tumour increases, and the uptake within the blood reduces due to the $t_{1/2}$, metabolism and excretion. This leads to an increase in the calculated ratio.

5.4.2.3 Tumour to Background Ratio

Similarly, the tumour to background ratio significantly increased with time after injection. The uptake within the scalene muscle compared to the CL SCM was not appreciably different. Although the difference was greatest at 18 hours with only two patients imaged at this time point further studies are required to assess if this is true or not. The mechanism of uptake and retention within the background is likely to be similar to that within the muscle as previously discussed due to the incorporation into the intra-cellular Cu pool.

5.4.2.4 Tumour to Necrosis Ratio

The increased uptake in the tumour compared to regions of necrosis suggests hypoxic but viable tissue is required for the retention of ^{64}Cu -ATSM. In necrotic tissue the uncoupling of oxidative phosphorylation inhibits the uptake of Cu-ATSM due to the lack of functioning mitochondria. In dogs, 24hour imaging after the injection of ^{64}Cu -ATSM showed no Cu-ATSM in necrotic regions in this canine myocardial perfusion model [30-32]. The examples shown in this chapter corroborated this by the lack of IHC pimonidazole staining and ^{64}Cu -ATSM uptake in the same necrotic regions. The uptake and retention of ^{64}Cu -ATSM was lower within the intra-tumoural necrotic regions than the surrounding normal tissue for example CL SCM. Even though a region is necrotic, uptake at

the periphery may lead to partial volume effects, which increase the uptake noted within the necrotic region on CT-PET imaging.

5.4.2.5 ⁶⁴Cu-ATSM Uptake in Other Sites

5.4.2.5.1 Mandible and Right Shoulder

Abnormal uptake was noted within the mandible of patient 2 and the shoulder of patient 4. The tumour to ROI ratio was greater at 18 hours compared to 5 to 20 minutes in patient 2. This suggested an initial non-selective uptake and wash out of ⁶⁴Cu-ATSM in these regions with time. However, in patient 4 this uptake increased at 40 to 60 minutes in the shoulder because the calculated ratio reduced with time. In both patients the uptake within the ROI was greater than that in the CL SCM, blood, and posterior neck. The changes in the tumour to blood and background ratios for both patients also reflected these findings.

This may suggest that ⁶⁴Cu-ATSM was retained due to a hypoxia related mechanism or copper dependent physiological pathway.

Copper ions are pro or anti-oxidant depending on intra-cellular conditions. For example ions catalyse the conversion of superoxide to hydrogen peroxide and hydroxyl radicals leading to oxidative DNA damage [33]. Alternatively, they can act as an anti-oxidant through Cu/Zinc superoxide dismutase and free radical production is reduced. Raised C-reactive protein has been positively correlated with the serum copper concentrations in patients [34]. Ceruloplasmin, is the main copper transport protein within the blood, and an acute phase protein. Inflammatory conditions, and infections for example are associated with an increased level of this protein, and increased copper concentrations within the blood [35,36].

Both of the patients in this study had inflammatory conditions. Patient 2 had undergone a dental extraction 2 weeks prior to imaging, and patient 4 was diagnosed with an inflammatory peripheral neuropathy of unknown cause. The increased ⁶⁴Cu-ATSM uptake in both sites may be secondary to inflammation.

Dental extraction may be associated reactive inflammatory change within the tooth socket and even resolving local hypoxia.

Metallothioneins bind heavy metals including copper, and mop up hydroxyl free radicals. The greater the percentage of metallothioneins present within the tumour, the poorer the outcome and reduced survival in SCC of the oral cavity when treated by surgery and PORT [37]. This is due to reduced free radical double stranded DNA damage by ionising radiation. Increased metallothionein expression has been positively correlated with the progression of oral cavity SCC [38]. ^{64}Cu -ATSM uptake may also be associated with the increased metallothionein expression in areas of inflammation through the increased regional copper carrying and utilisation capacity.

Lastly, in conditions of peripheral nerve demyelination, associated with inflammatory neuropathy, copper uptake and lipid oxidation within the nervous system precedes demyelination [39]. In human prostate cancer cell lines treated with a fatty acid synthase inhibitor, the retention of ^{64}Cu -ATSM was positively correlated with the inhibition of fatty acid synthase [40]. Patient 4 was diagnosed with a demyelinating inflammatory disease, and this may have been associated with the increased uptake of ^{64}Cu -ATSM within the right shoulder.

5.4.2.5.2 Salivary Glands

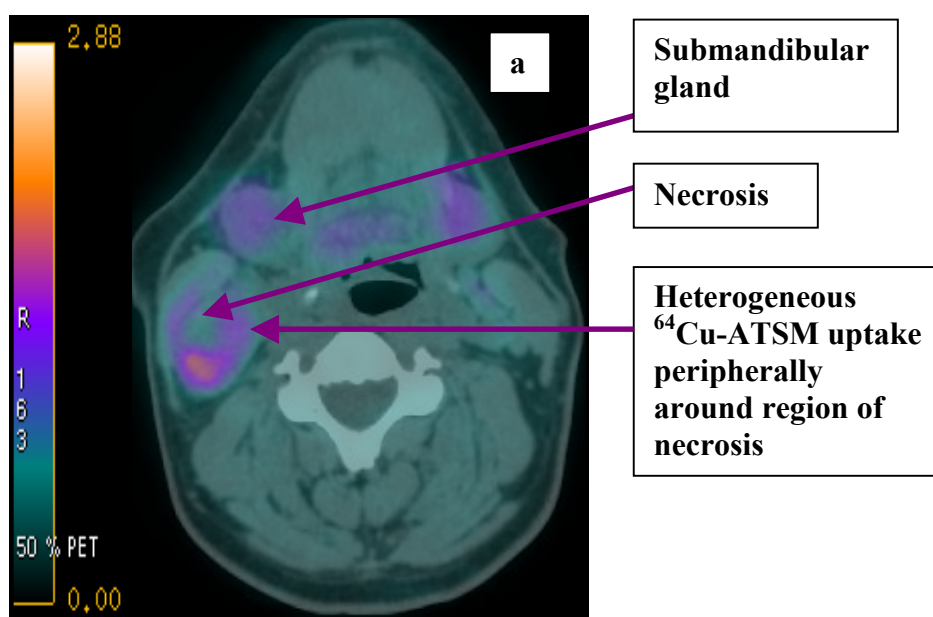
The tumour to salivary gland ratio was only significantly increased at 18 hours when compared to 5 to 20 minutes and not at 40 to 60 minutes. This suggests the salivary gland uptake and retention reduces with time after the injection of ^{64}Cu -ATSM. The involvement of copper within the salivary glands has previously been discussed (section 5.4.1.1) and the increased ratio may be associated with the increased retention within the tumour that is more evident at the later time period.

5.4.2.6 Uptake and Retention Pattern of ^{64}Cu -ATSM

Previous dual tracer studies have demonstrated the uptake of ^{64}Cu -ATSM was heterogeneous compared to the homogeneous pattern of ^{18}F FDG [30,32]. ^{18}F FDG imaging was not incorporated into the study due to excess radiation dose

exposure and the risk of a radiation induced cancers. Two patients did however have an ^{18}F FDG examination up to 4 weeks prior to the ^{64}Cu -ATSM imaging as part of their diagnostic investigations for carcinoma of unknown primary. The ^{18}F FDG image acquisition was not in the same position as the ^{64}Cu -ATSM imaging, and therefore has not been directly correlated. In these patients the ^{18}F FDG uptake was intense and homogeneous.

Figure 5.25 a) illustrates the 40 to 60 minute axial immediate 3D dynamic ^{64}Cu -ATSM CT-PET image, and b) the corresponding ^{18}F FDG CT-PET axial image. There was intense ^{18}F FDG avidity across the tumour (SUVmax 31.2bwg/ml) compared to a maximum tumour to muscle ratio of 3.755 in patient 5. The uptake of ^{64}Cu -ATSM is in the outer rim of tissue and an area of necrosis has developed within the centre of the region between the imaging points. Uptake is also noted in the bilateral submandibular glands. Intense ^{18}F FDG avidity is seen within the base of the tonsils due to prior biopsy.



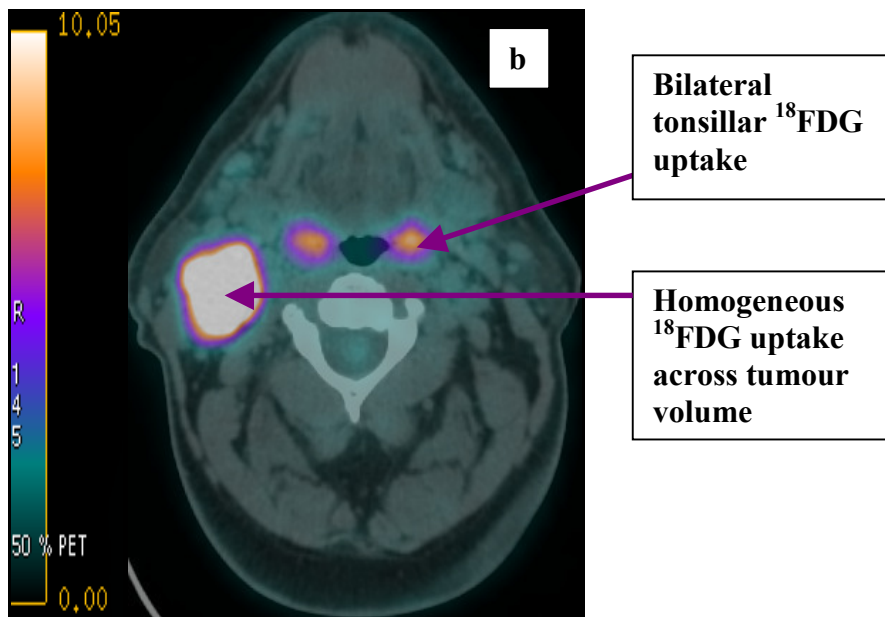


Figure 5.25a and b: The axial images of ^{64}Cu -ATSM a), and ^{18}F FDG b) representing the uptake differences of the two radio-nuclides

5.4.3 Immuno-Histochemical Hypoxic Fraction

The median hypoxic fractions for pimonidazole (38.194%), GLUT1 (54.43%), CAIX (24.06%), and HIF1a (14.12%) from this chapter are consistent with previously published data for example pimonidazole 0 to 79% [2,3,5,41-51]. Such IHC techniques are highly likely (70 to 90%) to be within 0.1% of the true labelled fraction on IHC [52].

The hypoxic fraction calculated from the median staining per grid was slightly higher than the total stained area calculation method. Percentage and intensity staining were assessed because the timing of surgery was unpredictable. Patients were allocated the start of the operating list but this changed because of the emergency procedures, and unforeseen circumstances. This can affect the intensity of pimonidazole adduct detection.

The intensity of the staining is also dependent on the antibody dilution, method of staining, pO_2 gradient within the tumour, the absolute amount of bound antigen/pimonidazole, and the kinetics and clearance of pimonidazole [41]. The fraction of HIF1a was at the lower end of the spectrum in this study at 14.12%. The dilution used was 1 in 8,000, because more concentrated dilutions saturated

the specimen with excess non-specific binding. Alternatively there may have been minimal up regulation of HIF1a expression depending on the intra-tumoural hypoxia. HIF1a up-regulation occurs at higher pO₂ levels than are required for pimonidazole binding [51]. Necrosis with the specimens suggests an increasingly hypoxic environment.

The linear unmixing and thresholding method of IHC staining is user dependent. The TRI2 software was set to ensure the colour range was the same for each patient, and each block was reviewed to assess the positive and non-specific staining. By increasing the lower staining threshold this potentially reduced the sensitivity, as some cells that stained positive would have been excluded.

There were a number of problems with the IHC staining process discussed in the section 5.1 that potentially affected the antigen retrieval due to antigen degradation. Factors include: delayed fixation that can lead to antigen proteolysis and increased non-specific antibody binding, prolonged fixation (greater than 48 hours) which increases the hydroxymethylene crossbridge formation and reduces the staining intensity, impure graded alcohols and xylene can produce inadequate tissue dehydration [53]. These factors may have influenced the hypoxic fraction calculation because the laryngeal specimens were fixed for a minimum of 5 to 7 days or longer, and there may have been impurities in the system during automated processing. Also, the day of surgery was a Thursday, and so the earliest macroscopic dissection occurred 90 hours later on the Monday.

Most importantly, this study did not interfere with the pathological diagnosis from the surgical specimen or patient treatment. Sampling a single large node prior to fixation or taking the central slice through a fresh laryngeal specimen would have enabled auto-radiography to occur but jeopardised the pathological diagnosis with regard to tumour invasion into surrounding tissue, and extra-capsular nodal extension. Auto-radiography would have corroborated the uptake and retention of ⁶⁴Cu-ATSM [54].

5.4.4 Correlation of Immuno-Histochemical Hypoxic Fractions

All the endogenous markers of hypoxia positively correlated with pimonidazole, as well as GLUT1 with CAIX and HIF1a, and CAIX with HIF1a. Published studies have found similar correlations. For pimonidazole and CAIX the correlation is strongest at distances greater than 100µm from the blood vessel [44]. This is in agreement with Koukourakis et al [48] who reported CAIX positivity was greatest in low micro-vessel density areas. CAIX positivity was also greatest in regions of pimonidazole adduct formation, as CAIX up-regulation is initiated by the HIF1a activation of the CAIX promoter region on the hypoxia response element [55]. CAIX and HIF1a expression in patients with SCCHN are associated with a poorer outcome when co-expressed [49].

Pimonidazole co-localised with HIF1a but this correlation was weaker. HIF1a is mainly a nuclear stain, whereas pimonidazole adducts are detected within the entire cell. Pimonidazole staining increases with increasing distance from the blood vessel and peaks at 80 to 100µm, and HIF1a at 40 to 50µm, reflecting the differing oxygen dependencies [5]. GLUT1 expression was correlated in SCC of the cervix with pimonidazole and CAIX [46]. In transitional carcinoma of the bladder, pimonidazole staining positively correlated with GLUT1, CAIX, and CAIX and GLUT1 with each other [47].

These results suggest that the intra-tumoural oxygen gradients accounted for differences in antigen detection. The correlation reported from the results in this chapter between pimonidazole and GLUT1 would suggest that the tumours are hypoxic, with an increased rate of glucose metabolism. This may promote a more aggressive tumour that may be more likely to locally recur because of radio-resistance and genotypic changes.

5.4.5 Haemo-dynamic Parameters Assessed by Dynamic Contrast Enhanced-Computed Tomography

It is difficult to draw any conclusions from the single patient in this chapter. The perfusion parameters from patient 5 are within the range of the current published data.

5.4.5.1 WinFun Software

Perfusion data in 9 patients with breast cancer assessed by the WinFun software has been published [56]. This indicated that the mean tumour perfusion was 0.41ml/min/ml (range 0.19 to 0.59ml/min/ml), and the mean CP was 15.0%/min (range 9 to 30%/min). The perfusion parameters gained from patient 5 using the WinFun software are in concordance with the data from these breast cancer patients. The perfusion is slightly higher and this can occur if the arterial input function is underestimated. This method is highly dependent on cardiac output, and delay in the passage of contrast through the vasculature within the neck will affect the results. This could be overcome by standardising the values for cardiac output.

5.4.5.2 GE Healthcare Software

A number of studies have investigated DCE-CT perfusion parameters in patients with SCCHN using the CT Perfusion application from GE Healthcare [8,9,57-60]. The published data is summarised in table 5.17.

Table 5.17: Perfusion parameters in patients with squamous cell carcinoma of the head and neck from DCE-CT images measured using the CT Perfusion application from GE Healthcare

Region of interest	Blood Flow (ml/min/100g)	Blood Volume (ml/100g)	Mean Transit Time (seconds)	Permeability Surface Area (ml/min/100g)
Primary and Metastatic Lymph Node	54.6 to 105.9 [1.7 to 226.9]	3.75 to 44.0 [0.5 to 12.3]	3.3 to 9.01 [3.4 to 17.1]	13.33 to 23.2 [0.1 to 39.1]
CL SCM	4.3 to 16.4 [4.03 to 10.1]	1.4 to 1.95 [0.58 to 0.7]	5.5 to 15.97 [4.37 to 5.1]	1.01 to 5.4 [1.42 to 4.0]
CL Salivary Gland	51.7 [39.7]	4.2 [1.9]	8.2 [4.1]	37.9 [12.6]
Posterior Neck	4.7 to 10.67 [2.7 to 7.06]	1.1 to 1.14 [0.6 to 0.67]	13.27 to 20.8 [5.32 to 6.8]	1.22 to 6.5 [0.81 to 5.3]

The range of mean values is shown with the standard deviation in brackets. In these studies the para-spinal muscles were used to assess the uptake in the posterior neck.

BV is difficult to measure in SCCHN because the surface mucosal epithelium is well perfused. This increases the BV within the ROI [9] as it is difficult to exclude the mucosa from the final calculated volume.

Longer MTT within tumours is associated with high interstitial pressure and blood flow through the region. The leaky endothelium allows the contrast to extravasate and blood to pool within the region. Deconvolution algorithms include the intra-vascular and extra-vascular spaces in the calculation, preventing over estimation. The prolongation of the MTT is also related to the presence of necrosis, which increases the BV and so the MTT [8,58].

The CL SCM, and posterior neck have lower BF, BV, and PS, but longer MTT than tumour regions. The salivary glands had a greater PS and a longer MTT. This has been confirmed by a single study [9]. Salivary glands have been excluded from all other published analyses but are specifically reviewed in this chapter because of the uptake of ^{64}Cu -ATSM within the region. It is uncertain why the salivary glands have such different values compared to other normal tissue, but there is an overlap with the BV in these and tumour regions.

Perfusion parameters vary throughout the ROI as shown in patient 5 and are heterogeneous depending also on the presence of necrotic regions. Necrotic regions must be excluded from the tumour calculation to gain a reliable result. BF, and so perfusion are dynamic and only reflect the intra-tumoural changes at the time of imaging. The results gained from the ROI from this patient were assumed to be representative of the entire tumour volume, but variation is present on each axial image.

Serial imaging is required to assess changes with time. Potentially the dual use of ^{62}Cu -ATSM and PTSM may allow this in future studies. Movement artefact will still be a problem on DCE-CT imaging especially in the base of tongue and

larynx due to swallowing and respiration, and the attenuation of the x-ray beam in regions of dense bone such as the clavicle and shoulders [9,60]. These both produce poor tissue enhancement curves.

5.4.6 Correlation of ^{64}Cu -ATSM Uptake and Blood Flow

Two studies have been published which correlate perfusion in ischaemic myocardial animal models with Cu-ATSM.

Fujibayashi compared ^{62}Cu -ATSM uptake with $^{201}\text{Thallium}$. In areas of very low perfusion, ^{62}Cu -ATSM uptake was low. In perfused but hypoxic areas, myocardium $^{201}\text{Thallium}$ uptake was low and ^{62}Cu -ATSM uptake was high. Auto-radiographic studies have shown ^{64}Cu -ATSM uptake is greatest in areas with a low micro-vessel density [32].

Secondly, in rats the uptake of ^{64}Cu -ATSM and ^{11}C labelled acetate was assessed. ^{11}C labelled acetate has previously been reported to be proportional to BF [61]. There was a negative correlation between the two PET radio-nuclides. In areas of low BF, there was no uptake of ^{64}Cu -ATSM, when the BF was less than 20% [62].

Overall these suggest that BF is required to deliver the tracer to the hypoxic region, and accumulation selectively occurs in hypoxic but perfused regions [63].

There was no correlation of ^{64}Cu -ATSM uptake at 5 to 20 minutes, 40 to 60 minutes or at 18 hours after injection with the BF on the DCE-CT for patient 5. No correlation of BF within the tumour is encouraging but not conclusive. The DCE-CT data is most representative of the 40 to 60 minute ^{64}Cu -ATSM uptake. Ideally multiple DCE-CT scans would be undertaken in future to assess changes in blood flow and ^{64}Cu -ATSM uptake with time.

The mean grayscale intensities for BF versus ^{64}Cu -ATSM uptake were: 0.0 to 29.74 vs. 0.0 to 79.21 at 5 to 20 minutes, 0.0 to 30.55 vs. 3.93 to 98.77 at 40 to 60 minutes, and 0.0 to 28.50 vs. 4.202 to 121.98 at 18 hours after injection. These raw mean intensity values suggest the uptake of ^{64}Cu -ATSM was greater

than the BF through the ROI within the tumour. Larger patient numbers would have allowed conclusions to be drawn from the perfusion results in this chapter. Further studies may conclude a negative or positive correlation depending on the tumour or necrotic region.

5.4.7 Correlation of ^{64}Cu -ATSM Uptake and Hypoxic Immuno-Histochemical Staining

There was a positive correlation of all exogenous and endogenous markers of hypoxia with the uptake of ^{64}Cu -ATSM at 5 to 20, 40 to 60 minutes and 18 hours after the injection. This was greatest for GLUT1 at 5 to 20 minutes, pimonidazole at 40 to 60 minutes, and HIF1a at 18 hours.

The expression of endogenous markers of hypoxia will depend on the intra-tumoural pO_2 . The IHC expression is also most representative of the 18hour imaging point and chronic hypoxia. Pimonidazole forms adducts when the pO_2 is less than 10mmHg, but ^{64}Cu -ATSM may preferentially bind at lower O_2 tensions and in conditions of anoxia, which would account for its heterogeneous distribution.

Human and animal studies have assessed the IHC correlation of hypoxia markers with ^{64}Cu -ATSM uptake. Correlation was dependent on the tumour model. The hypoxic distribution of ^{64}Cu -ATSM on auto-radiography was positively correlated with EF5, pimonidazole and CAIX expression in the mammary and 9L gliomas models only [64]. SCC models have suggested the positive correlation of Cu-ATSM uptake with pimonidazole that was not dependent on the time after injection. The vascular marker Hoechst 33342 negatively correlated with pimonidazole binding [54]. In the SCCVII murine tumour model, the positive pimonidazole fraction was 36.0% +/- 7%. The uptake of ^{64}Cu -ATSM and pimonidazole binding was greatest when these animals were exposed to hypoxic conditions [19].

Auto-radiography was planned in the study protocol, but not undertaken. Large specimens require prolonged fixation, and decalcification of ossified cartilage or bone prior to macroscopic dissection for example. Detection by auto-radiography

would not be possible on fixed specimens because no isotope activity would be detected (4 days post injection of ^{64}Cu -ATSM is equivalent to 8 half-lives and only 0.391% of the original injected activity would be present).

The freshly sectioned tissue is required for auto-radiography and would need to be stored carefully to ensure exuded fluid did not affect the distribution pattern. Sampling fresh unfixed specimens was a problem because tissue planes would be difficult to interpret. Whole laryngeal specimens are difficult to cut with a band saw when fresh, and tissue from a single matted LN infiltrated with SCC may compromise formal pathological reporting if sectioned for auto-radiography studies prior to this.

The results from this chapter suggest ^{64}Cu -ATSM is a potential surrogate marker of hypoxia. It may initially be non-selectively distributed, but when it is within the intra-cellular hypoxic environment it is irreversibly trapped and accumulates with increasing time after injection. The retention may be due to its incorporation into the intra-cellular Cu pool. The correlation with pimonidazole may suggest that chronic hypoxia is imaged rather than acute hypoxia. However the lack of correlation of ^{64}Cu -ATSM uptake and retention with BF in 1 patient has not been able to confirm or refute this.

5.4.7.1 Correlation Inaccuracies

5.4.7.1.1 Macroscopic Dissection and Tissue Processing

After the dissected specimen has been wax embedded the Medical Laboratory Scientific Officers would cut the wax block to ensure that the full surface of the specimen was level to allow even microtome sectioning. The position of tissue within the wax block was dependent on placement and movement during automated processing.

This reduced the amount of tissue available for IHC, as blocks were only received after full pathological diagnosis was completed. Ideally serial tissue sections would allow correlation at multiple levels within the same block and

specimen. There was no opportunity for this given the type of cases recruited and storage of fixed specimens (incinerated 28 days after receipt).

5.4.7.1.2 Alignment of tissue and imaging

The correlation achieved was regional, rather than per cell or pixel. The stained section was 4µm in thickness compared to 3.27mm for the fused reconstructed CT-PET, leading to spatial registration difficulties. Measurements taken at the time of surgery, and macroscopic dissection could not be used alone for alignment and correlation when choosing the most appropriate CT-PET slice. Visual inspection was most important as the specimens contracted during the fixation process.

Shrinkage of HN specimens has been assessed in a number of studies. Tissue shrinkage immediately after excision from standardised mucosal specimens in dogs was between 3.0 to 4.8 mm (20.9 to 38.3%) prior to fixation. After formalin fixation this was 0.3 to 1.4mm (32.4 to 48.8%), and a total shrinkage was 3.7 to 5.7mm (30.7 to 47.3%) for a 12mm long specimen. The variation in shrinkage was greatest for buccal mucosa and base of tongue specimens [65]. The vocal cords within laryngeal specimens shrank by 9 to 24% from excision to the immersion in 10% buffered formalin, and a further 0 to 14% after formalin fixation. This was greatest at the medial and free edge of the cord [66]. In patients with SCCHN, the mean shrinkage between pre and post processing was up to 60% [67]. Specimens containing bone and cartilage shrank less.

The volume shrinkage between excision and fixation was 19.05 to 38.46% for the ND samples, and 3.84 to 6.66% for the whole larynx specimens from patients reported in this chapter. There was a further 4.83 to 10.0% shrinkage during the paraffin wax embedment for the LN samples, and 8.94 and 10.0% for the laryngeal samples.

These factors all influence and reduce the accuracy of alignment and correlation.

5.4.7.1.3 Other Methods of Registration

The method used to align the IHC specimen and CT-PET in this study was Adobe Photoshop, and the aligned grids were compared using the TRI2 software. This was the only method and software available for use within the department.

Other rigid or non-rigid registration methods have been reported which use complex mathematical algorithms.

Rigid registration uses 6 degrees of freedom (3 translational points: x, y, z, and 3 rotational points: roll, pitch and yaw). The two images are assumed to be objects and are rotated around these points in relation to one and other until they are aligned. This method can incorporate scale factors, affine registration, and partial correction for calibration differences. For example the co-registration of CT and MRI images within the brain.

Non-rigid methods have improved on this technique due to changes in shape or anatomy. For example an element of stretching or warping is required to overlay and register one image with another (deformable transformation model). These models take account of changes in position, structure, and size during the registration process [68].

One of the most relevant methods of registration to this chapter was by Boisd'Aische et al [69]. This study developed the registration process used by Daisne et al [70]. This used a non-rigid method through a constrained dense displacement field to account for changes in the histology image due to freezing, fixation, cryotoming and staining. This model used elastic based deformation with a linear elastic regularisation constraint to optimise the registration. The thicker specimen sections used by the group aided this registration process.

The availability of such registration methods would have increased the accuracy of registration and correlation in the results from this chapter.

5.4.8 Hypoxic Functional Volume Delineation

The hypoxic FV delineated according to the tumour to muscle, blood and background ratios increased at 40 to 60 minutes for patient 1, 4, and 5, and these volumes had increased further at 18 hours after the injection of ^{64}Cu -ATSM in patient 5 when compared to the volume at 5 to 20 minutes. However the FV delineated for patient 2 were similar at 5 to 20 minutes and at 18 hours after the administration of ^{64}Cu -ATSM. The volumes defined reduced with each increase in the delineating tumour ratio above the baseline of 2.0. The tumour to muscle ratio produced the most statistically significant results and would suggest that this ratio should be used to aid the delineation of ^{64}Cu -ATSM hypoxic FVs.

These results are interesting given the implications for use in RT planning. Firstly the time point of imaging is extremely important. Although only 4 patients were imaged in this study, it does suggest that the uptake of ^{64}Cu -ATSM at 40 to 60 minutes and at 18 hours after injection would be appropriate rather than at 5 to 20 minutes as these may be more representative of the true hypoxic volume within the tumour. It would be interesting to assess the differences between these two time points in a larger study, and specifically evaluate how this affects both the final delineated volume, and the dose distribution to adjacent organs at risk during dose escalation. ^{64}Cu -ASTM does allow this flexibility given its half-life. Other isotopes such as ^{62}Cu would allow this to be assessed immediately after administration, and also at other time points during treatment. The lower emitted radiation dose may allow imaging during RT in conjunction with Cu-PTSM to assess hypoxia and perfusion using dual tracer kinetics.

A study with 3 healthy human volunteers and 3 dogs, the time, and order of injected radio-nuclides were assessed in a dual tracer study with Cu-PTSM and Cu-ATSM according to the generated time-activity curves. Identification of the individual tracers was greatest when ^{62}Cu -PTSM was injected first, followed by a time delay of 20 minutes before ^{62}Cu -ATSM was injected. The total dynamic PET scan duration was 50 minutes (30 minutes for assessment of ATSM) [71]. Such a study would also be feasible if ^{18}F -fluoro-3'-deoxy-3'-thymidine was used as a dual tracer with ^{64}Cu -ATSM to assess proliferation and hypoxia within the same tumour, ^{64}Cu -ATSM would need to be injected second because of its

longer half-life, and ^{18}F Fluorine has a higher positron emission rate. The higher rate of emission would saturate the camera and prevent detection of the second radio-nuclide. By delaying the administration of ^{64}Cu -ATSM by 24 hours, ^{18}F activity would have been reduced by 8 half-lives and so the two tracers could be identified separately.

Given the paucity of data, the defining ratio should be between 2.6 and 3.5, as these have been used with other Cu-ATSM isotope studies [13-15]. Higher ratios will be associated with smaller volumes and will be more amenable to dose escalation than for example a ratio of 2.0.

The pimonidazole staining would suggest the entire tumour volume would need to be dose escalated by RT, as the antigen detection was generalised rather than localised. This ultimately suggests that in the 4 patients imaged with ^{64}Cu -ATSM the majority of the tumour volume was hypoxic to less than 10mmHg, and at a greater risk of local recurrence.

5.4.9 Patient Recruitment

Patient recruitment was unfortunately poor. When the ^{64}Cu -ATSM study was initially developed, recruitment was planned at two sites. Following the favourable ethics opinion by NRES (National Research Ethics Service) in April 2007. Local approval was sought at UCLH, and recruitment started in May 2008. There was a 13-month period while the study was set up and sponsorship agreement negotiated. This delay was compounded by the need to produce ^{64}Cu -ATSM to good manufacturing practice standards.

Patient recruitment was also planned at Northwick Park Hospital. The site-specific local approval for Northwick Park, and Mount Vernon Cancer Centre was sought (imaging at Mount Vernon, and surgery at Northwick Park). The application was submitted to Northwick Park in February 2008, and to date local approval has not been given. Despite a number of meetings, assurances, and negotiations with all the stakeholders, different issues were raised including: the sponsorship and indemnity agreement between the sponsor UCLH, Mount

Vernon Cancer Centre, and Northwick Park Hospital, and Pathology Service requirements. These unfortunately could not be overcome.

This impacted the potential patient recruitment. However to improve recruitment a substantial amendment was submitted to NRES to open Guy's and St Thomas' Hospital as a second site for the study. This request was submitted in December 2008. Recruitment would have been through the Oral and Maxillo-Facial Surgical Department with imaging at the Clinical PET Centre at St Thomas' Hospital. The advantages included on-site production of ^{64}Cu -ATSM. Following submission, and then study presentation to the local Research and Development board at Guy's Hospital in April 2009, approval was only gained in October 2009, 10 months later. Only one patient per month could have been recruited from this site because of the stipulation from the Environment Agency that no more than 600MBq of waste could be discharged into the environment. This quota included waste from other radio-nuclides such as ^{18}F FDG. No patients were recruited from this site because of time constraints but it is hoped that the study will continue to recruit at Guy's and St Thomas' Hospitals over the coming months.

At UCLH 44 patients were screened, and only 6 recruited into the study. Patients were screened as eligible from the MDT, but due to inter-current illness and smoking related co-morbidities their treatment plan changed from curative to palliative, or from surgery to RT or CRT. This was most commonly due to the individual's fitness for surgery.

Patients also were not able to participate even though willing because of other commitments within UCLH. For example appointments with the Clinical Nurse Specialist, Speech and Language team, and Dieticians in the days leading up to their planned surgical treatment. Patients approached were overwhelmed by their diagnosis, and had great difficulty coming to terms their planned treatment. This was especially the case for laryngectomy patients.

A further substantial amendment was submitted to NRES for favourable opinion to provide a one-page summary patient information leaflet for each study arm.

This aimed to reduce the information given to potential participants, and then those who were considering participation were given a full information sheet. These were submitted in June 2008, and final favourable opinion was granted 5 months later.

Eligible study patients were also lost to recruitment if they were brought to the MDT either a few days prior to their surgery, or close to a treatment target date [72,73].

The production of ^{64}Cu -ATSM was a significant problem. Only one cyclotron and radio-chemist produced the ^{64}Cu -ATSM. Unfortunately this radio-chemist was abroad between May and September 2008, with no replacement for production. Production was not automated, which increased the radiation exposure for the individual limiting the amount of isotope that could be produced. Two patients recruited could not be imaged. One because of burst copper piping within the cyclotron, which flooding the unit. The other patient could not be imaged because the nickel target did not move into the beam of the cyclotron. This patient's surgery was then delayed, and they agreed to continue in the study. Unfortunately again the ^{64}Cu -ATSM could not be released as it failed quality assurance testing. A minimum of 2 weeks notice was required for production, and this was not always possible as previously explained.

Lastly, treatment has moved towards primary RT or CRT with surgery reserved for advanced disease, and at the time of recurrence for salvage. This change in practice impacted on recruitment.

5.4.9.1 Eligibility Criteria for Patient Recruitment

The age of patient recruitment was determined due to the emission of ionising electrons during electron capture (41%) and negatron decay (40%). These electrons cause a cascade reaction and the production of auger electrons. These all have significant ionisation potential and damage DNA in areas of ^{64}Cu -ATSM uptake.

The International Commission of Radiological Protection, published guidance in 1991 [74](ICRP 60) on the risk of lifetime mortality from cancer, and updated their guidance in 2008 (ICRP 103) [75]. The ICRP 60 has data for cancer mortality between 1950 and 1987 based on survivors from the atomic bomb explosion in Japan in 1945. The later publication has incidence data for the 47 years following this event.

The ICRP 60 publication suggested the probability of death was 0.0921 at the age of 25 for men and 0.1178 for women per mSv of whole body radiation exposure, compared to 0.0258 for men, and 0.0275 for women per mSv at the age of 75. This equated to an increased lifetime risk of 1.9763 per 10,000 population (sex-averaged, age at exposure) at 18 to 40 years of age. The ICRP 103 publication suggested this figure was lower at 1.103 per 10,000 population per mSv for men and 1.242 per mSv for women per 10,000 population aged between 18 and 64 years of age.

The probability of increased death due to radiation exposure from the imaging protocol was for example 3.435 for a 25 year old man compared to 0.962 for a 75 year old man who underwent a dynamic immediate CT-PET, DCE-CT, and a late 18 to 24 hour static CT-PET.

The use of 60 and 62 Cu-ATSM may reduce this risk given the higher positron emission rate, and so lower doses could be injected. An on-site cyclotron would be required for production of Cu isotopes with a short $t_{1/2}$.

A substantial amendment submission for the study was considered to allow recruitment of patients with recurrent disease who were to be treated by salvage surgery, and also patients between the age of 40 and 50. Unfortunately, this was not possible due to the time constraints on recruitment, and gaining favourable opinion from NRES.

5.5 Conclusions

The uptake and retention of ^{64}Cu -ATSM was assessed in four patients with SCCHN, and correlated in surgical specimens with exogenous and endogenous IHC surrogate markers of hypoxia in these patients.

The uptake and retention of ^{64}Cu -ATSM stabilised 5 minutes after injection, and then increased with time following injection. The uptake when compared to surrounding normal tissue was most significant at 40 to 60 minutes on each axial CT-PET slice according to the tumour to muscle ratio. Increased uptake was seen in the salivary glands, and this may have been due to the physiological pathway of copper in saliva. Unusual uptake was noted in the mandible and right shoulder, which may have been secondary to inflammation.

Perfusion imaging was only completed in one patient and the lack of correlation between ^{64}Cu -ATSM uptake and retention and BF especially at 40 to 60 minutes cannot conclude no association. The haemo-dynamic parameters assessed by the DCE-CT were consistent with those from other published studies in SCCHN.

The hypoxic antigen detection of GLUT1 and pimonidazole had the most significant positive correlation. CAIX and HIF1a hypoxic fractions were significantly smaller than those defined by the other two antigens.

The distribution pattern of pimonidazole and the other antigens positively correlated with the retention pattern of ^{64}Cu -ATSM at 5 to 20 minutes, 40 to 60 minutes, and 18 hours after injection. The most significant correlation of the uptake and retention of ^{64}Cu -ATSM at 40 to 60 minutes was with pimonidazole.

The hypoxic FV delineated by the tumour ratios increased with each increase in the ratio threshold. The volumes increased in size with time after injection of ^{64}Cu -ATSM, and were largest when defined by the tumour to muscle ratio.

These results are encouraging and suggest a possibility that ^{64}Cu -ATSM retention and uptake is hypoxia selective according to the distribution of the

hypoxic IHC antigens investigated. Further validation of ^{64}Cu -ATSM and investigation is warranted. In future, the FV delineated by this radio-nuclide on CT-PET imaging (if confirmed to be hypoxic in larger studies) may allow dose escalation strategies to be developed to improved loco-regional control to these hypoxic radio-resistant tumour volumes.

5.6 References

1. Mosteller RD. Simplified calculation of body-surface area. *N Engl J Med* 1987;317:1098
2. Varia MA, Calkins-Adams DP, Rinker LH, et al. Pimonidazole: a novel hypoxia marker for complementary study of tumor hypoxia and cell proliferation in cervical carcinoma. *Gynecol Oncol* 1998;71:270-277
3. Raleigh JA, Chou SC, Calkins-Adams DP, et al. A clinical study of hypoxia and metallothionein protein expression in squamous cell carcinomas. *Clin Cancer Res* 2000;6:855-862
4. Wijffels KI, Kaanders JH, Rijken PF, et al. Vascular architecture and hypoxic profiles in human head and neck squamous cell carcinomas. *Br J Cancer* 2000;83:674-683
5. Janssen HL, Haustermans KM, Sprong D, et al. HIF-1A, pimonidazole, and iododeoxyuridine to estimate hypoxia and perfusion in human head-and-neck tumors. *Int J Radiat Oncol Biol Phys* 2002;54:1537-1549
6. Miles KA. Measurement of tissue perfusion by dynamic computed tomography. *Br J Radiol* 1991;64:409-412
7. Miles KA, Young H, Chica SL, Esser PD. Quantitative contrast-enhanced computed tomography: is there a need for system calibration? *Eur Radiol* 2007;17:919-926
8. Bisdas S, Konstantinou GN, Lee PS, et al. Dynamic contrast-enhanced CT of head and neck tumors: perfusion measurements using a distributed-parameter tracer kinetic model. Initial results and comparison with deconvolution-based analysis. *Phys Med Biol* 2007;52:6181-6196

9. Rumboldt Z, Al-Okaili R, Deveikis JP. Perfusion CT for head and neck tumors: pilot study. *AJNR Am J Neuroradiol* 2005;26:1178-1185

10. Gandhi D, Chepeha DB, Miller T, et al. Correlation between initial and early follow-up CT perfusion parameters with endoscopic tumor response in patients with advanced squamous cell carcinomas of the oropharynx treated with organ-preservation therapy. *AJNR Am J Neuroradiol* 2006;27:101-106

11. Gandhi D, Hoeffner EG, Carlos RC, Case I, Mukherji SK. Computed tomography perfusion of squamous cell carcinoma of the upper aerodigestive tract. Initial results. *J Comput Assist Tomogr* 2003;27:687-693

12. Chao C, Bosch WR, Mutic S, et al. A novel approach to overcome hypoxic tumour resistance: Cu-ATSM-guided intensity modulated radiation therapy. *Int J Radiation Oncology Biol Phys* 2001;49:1171-1182

13. Dehdashti F, Mintun MA, Lewis JS, et al. In vivo assessment of tumor hypoxia in lung cancer with ⁶⁰Cu-ATSM. *Eur J Nucl Med Mol Imaging* 2003;30:844-850

14. Dehdashti F, Grigsby PW, Lewis JS, et al. Assessing tumor hypoxia in cervical cancer by PET with ⁶⁰Cu-labeled diacetyl-bis(N4-methylthiosemicarbazone). *J Nucl Med* 2008;49:201-205

15. Dietz DW, Dehdashti F, Grigsby PW, et al. Tumor hypoxia detected by positron emission tomography with ⁶⁰Cu-ATSM as a predictor of response and survival in patients undergoing Neoadjuvant chemoradiotherapy for rectal carcinoma: a pilot study. *Dis Colon Rectum* 2008;51:1641-1648

16. Lewis JS, McCarthy DW, McCarthy TJ, Fujibayashi Y, Welch MJ. Evaluation of ^{64}Cu -ATSM in vitro and in vivo in a hypoxic tumor model. *J Nucl Med* 1999;40:177-183
17. Bonnitcho PD, Vavere AL, Lewis JS, Dilworth JR. In vitro and in vivo evaluation of bifunctional bithiosemicarbazone ^{64}Cu -complexes for the positron emission tomography imaging of hypoxia. *J Med Chem* 2008;51:2985-2991
18. Laforest R, Dehdashti F, Lewis JS, Schwarz SW. Dosimetry of $^{60}/^{61}/^{62}/^{64}\text{Cu}$ -ATSM: a hypoxia imaging agent for PET. *Eur J Nucl Med Mol Imaging* 2005;32:764-770
19. Matsumoto K, Szajek L, Krishna MC, et al. The influence of tumor oxygenation on hypoxia imaging in murine squamous cell carcinoma using ^{64}Cu -ATSM or ^{18}F -Fluoromisonidazole positron emission tomography. *Int J Oncol* 2007;30:873-881
20. Liao SY, Lerman MI, Stanbridge EJ. Expression of transmembrane carbonic anhydrases, CAIX and CAXII, in human development. *BMC Dev Biol* 2009;9:22
21. Cobb LM, Nolan J, Butler SA. Distribution of pimonidazole and RSU 1069 in tumour and normal tissues. *Br J Cancer* 1990;62:915-918
22. Cobb LM, Nolan J, O'Neill P. Microscopic distribution of misonidazole in mouse tissues. *Br J Cancer* 1989;59:12-16
23. Pilardeau P, Richalet JP, Bouissou P, et al. Saliva flow and composition in humans exposed to acute altitude hypoxia. *Eur J Appl Physiol Occup Physiol* 1990;59:450-453
24. Jam I, Shoham M, Wolf RO, Mishkin S. Elevated serum amylase activity in the absence of clinical pancreatic or salivary gland disease: possible role of acute hypoxemia. *Am J Gastroenterol* 1978;70:480-488

25. Bales CW, Freeland-Graves JH, Askey S, et al. Zinc, magnesium, copper, and protein concentrations in human saliva: age- and sex-related differences. *Am J Clin Nutr* 1990;51:462-469
26. Agarwal RP, Henkin RI. Metal binding characteristics of human salivary and porcine pancreatic amylase. *J Biol Chem* 1987;262:2568-2575
27. Morita M, Kudo H, Doi Y, et al. Enhanced immunocytochemical expression of antioxidant enzymes in rat submandibular gland after normobaric oxygenation. *Anat Rec* 2002;268:371-380
28. D'Amico F, Skarmoutsou E, Sanfilippo S, Camakaris J. Menkes protein localization in rat parotid acinar cells. *Acta Histochem* 2005;107:373-378
29. Dearling JLJ, Lewis JS, Mullen GED, et al. Design of hypoxia-targeting radiopharmaceuticals: selective uptake of copper-64 complexes in hypoxic cells. *European Journal of Nuclear Medicine* 1998;25:788-792
30. Obata A, Yoshimoto M, Kasamatsu S, et al. Intra-tumoral distribution of (64)Cu-ATSM: a comparison study with FDG. *Nucl Med Biol* 2003;30:529-534
31. Lewis JS, Herrero P, Sharp TL, et al. Delineation of hypoxia in canine myocardium using PET and copper(II)-diacetyl-bis(N(4)-methylthiosemicarbazone). *J Nucl Med* 2002;43:1557-1569
32. Tanaka T, Furukawa T, Fujieda S, et al. Double-tracer autoradiography with Cu-ATSM/FDG and immunohistochemical interpretation in four different mouse implanted tumor models. *Nucl Med Biol* 2006;33:743-750
33. Bremner I. Manifestations of copper excess. *Am J Clin Nutr* 1998;67:1069S-1073S

34. Bo S, Durazzo M, Gambino R, et al. Associations of dietary and serum copper with inflammation, oxidative stress, and metabolic variables in adults. *J Nutr* 2008;138:305-310
35. Beshgetoor D, Hambidge M. Clinical conditions altering copper metabolism in humans. *Am J Clin Nutr* 1998;67:1017S-1021S
36. Lewis AJ. The role of copper in inflammatory disorders. *Agents Actions* 1984;15:513-519
37. Szelachowska J, Dziegiel P, Jelen-Krzeszewska J, et al. Prognostic significance of nuclear and cytoplasmic expression of metallothioneins as related to proliferative activity in squamous cell carcinomas of oral cavity. *Histol Histopathol* 2008;23:843-851
38. Szelachowska J, Dziegiel P, Jelen-Krzeszewska J, et al. Correlation of metallothionein expression with clinical progression of cancer in the oral cavity. *Anticancer Res* 2009;29:589-595
39. Viquez OM, Valentine HL, Amarnath K, Milatovic D, Valentine WM. Copper accumulation and lipid oxidation precede inflammation and myelin lesions in N,N-diethyldithiocarbamate peripheral myelinopathy. *Toxicol Appl Pharmacol* 2008;229:77-85
40. Vavere AL, Lewis JS. Examining the relationship between Cu-ATSM hypoxia selectivity and fatty acid synthase expression in human prostate cancer cell lines. *Nucl Med Biol* 2008;35:273-279
41. Azuma C, Raleigh JA, Thrall DE. Longevity of pimonidazole adducts in spontaneous canine tumors as an estimate of hypoxic cell lifetime. *Radiat Res* 1997;148:35-42
42. Janssen HL, Hoebbers FJ, Sprong D, et al. Differentiation-associated staining with anti-pimonidazole antibodies in head and neck tumors. *Radiother Oncol* 2004;70:91-97

43. Raleigh JA, Calkins-Adams DP, Rinker LH, et al. Hypoxia and vascular endothelial growth factor expression in human squamous cell carcinomas using pimonidazole as a hypoxia marker. *Cancer Res* 1998;58:3765-3768
44. Kaanders JH, Wijffels KI, Marres HA, et al. Pimonidazole binding and tumor vascularity predict for treatment outcome in head and neck cancer. *Cancer Res* 2002;62:7066-7074
45. Nordsmark M, Loncaster J, Aquino-Parsons C, et al. The prognostic value of pimonidazole and tumour pO₂ in human cervix carcinomas after radiation therapy: a prospective international multi-center study. *Radiother Oncol* 2006;80:123-131
46. Airley RE, Loncaster J, Raleigh JA, et al. GLUT-1 and CAIX as intrinsic markers of hypoxia in carcinoma of the cervix: relationship to pimonidazole binding. *Int J Cancer* 2003;104:85-91
47. Hoskin PJ, Sibtain A, Daley FM, Wilson GD. GLUT1 and CAIX as intrinsic markers of hypoxia in bladder cancer: relationship with vascularity and proliferation as predictors of outcome of ARCON. *Br J Cancer* 2003;89:1290-1297
48. Koukourakis MI, Giatromanolaki A, Sivridis E, et al. Hypoxia-regulated carbonic anhydrase-9 (CA9) relates to poor vascularization and resistance of squamous cell head and neck cancer to chemoradiotherapy. *Clin Cancer Res* 2001;7:3399-3403
49. Koukourakis MI, Bentzen SM, Giatromanolaki A, et al. Endogenous markers of two separate hypoxia response pathways (hypoxia inducible factor 2 alpha and carbonic anhydrase 9) are associated with radiotherapy failure in head and neck cancer patients recruited in the CHART randomized trial. *J Clin Oncol* 2006;24:727-735

50. Hoogsteen IJ, Marres HA, Wijffels KI, et al. Colocalization of carbonic anhydrase 9 expression and cell proliferation in human head and neck squamous cell carcinoma. *Clin Cancer Res* 2005;11:97-106
51. Aebersold DM, Burri P, Beer KT, et al. Expression of hypoxia-inducible factor-1alpha: a novel predictive and prognostic parameter in the radiotherapy of oropharyngeal cancer. *Cancer Res* 2001;61:2911-2916
52. Cline JM, Rosner GL, Raleigh JA, Thrall DE. Quantification of CCI-103F labeling heterogeneity in canine solid tumors. *Int J Radiat Oncol Biol Phys* 1997;37:655-662
53. Werner M, Chott A, Fabiano A, Battifora H. Effect of formalin tissue fixation and processing on immunohistochemistry. *Am J Surg Pathol* 2000;24:1016-1019
54. O'Donoghue JA, Zanzonico P, Pugachev A, et al. Assessment of regional tumor hypoxia using 18F-fluoromisonidazole and 64Cu(II)-diacetyl-bis(N4-methylthiosemicarbazone) positron emission tomography: Comparative study featuring microPET imaging, Po2 probe measurement, autoradiography, and fluorescent microscopy in the R3327-AT and FaDu rat tumor models. *Int J Radiat Oncol Biol Phys* 2005;61:1493-1502
55. Wykoff CC, Beasley NJ, Watson PH, et al. Hypoxia-inducible expression of tumor-associated carbonic anhydrases. *Cancer Res* 2000;60:7075-7083
56. Groves AM, Wishart GC, Shastry M, et al. Metabolic-flow relationships in primary breast cancer: feasibility of combined PET/dynamic contrast-enhanced CT. *Eur J Nucl Med Mol Imaging* 2009;36:416-421
57. Bisdas S, Surlan-Popovic K, Didanovic V, Vogl TJ. Functional CT of squamous cell carcinoma in the head and neck: repeatability of tumor and

muscle quantitative measurements, inter- and intra-observer agreement. Eur Radiol 2008;18:2241-2250

58. Bisdas S, Baghi M, Smolarz A, et al. Quantitative measurements of perfusion and permeability of oropharyngeal and oral cavity cancer, recurrent disease, and associated lymph nodes using first-pass contrast-enhanced computed tomography studies. Invest Radiol 2007;42:172-179
59. Bisdas S, Spicer K, Rumboldt Z. Whole-tumor perfusion CT parameters and glucose metabolism measurements in head and neck squamous cell carcinomas: a pilot study using combined positron-emission tomography/CT imaging. AJNR Am J Neuroradiol 2008;29:1376-1381
60. Hermans R, Lambin P, Van den Bogaert W, et al. Non-invasive tumour perfusion measurement by dynamic CT: preliminary results. Radiother Oncol 1997;44:159-162
61. Gropler RJ, Siegel BA, Geltman EM. Myocardial uptake of carbon-11-acetate as an indirect estimate of regional myocardial blood flow. J Nucl Med 1991;32:245-251
62. Fujibayashi Y, Cutler CS, Anderson CJ, et al. Comparative studies of Cu-64-ATSM and C-11-acetate in an acute myocardial infarction model: ex vivo imaging of hypoxia in rats. Nucl Med Biol 1999;26:117-121
63. Fujibayashi Y, Taniuchi H, Yonekura Y, et al. Copper-62-ATSM: a new hypoxia imaging agent with high membrane permeability and low redox potential. J Nucl Med 1997;38:1155-1160
64. Yuan H, Schroeder T, Bowsher JE, et al. Intertumoral differences in hypoxia selectivity of the PET imaging agent $^{64}\text{Cu}(\text{II})$ -diacetyl-bis(N4-methylthiosemicarbazone). J Nucl Med 2006;47:989-998

65. Johnson RE, Sigman JD, Funk GF, Robinson RA, Hoffman HT. Quantification of surgical margin shrinkage in the oral cavity. *Head Neck* 1997;19:281-286
66. Kimura M, Tayama N, Chan RW. Geometrical deformation of vocal fold tissues induced by formalin fixation. *Laryngoscope* 2003;113:607-613
67. Cheng A, Cox D, Schmidt BL. Oral squamous cell carcinoma margin discrepancy after resection and pathologic processing. *J Oral Maxillofac Surg* 2008;66:523-529
68. Crum WR, Hartkens T, Hill DL. Non-rigid image registration: theory and practice. *Br J Radiol* 2004;77 Spec No 2:S140-153
69. du Bois d'Aische A, Craene MD, Geets X, et al. Efficient multi-modal dense field non-rigid registration: alignment of histological and section images. *Med Image Anal* 2005;9:538-546
70. Daisne JF, Duprez T, Weynand B, et al. Tumor volume in pharyngolaryngeal squamous cell carcinoma: comparison at CT, MR imaging, and FDG PET and validation with surgical specimen. *Radiology* 2004;233:93-100
71. Rust TC, Kadrmas DJ. Rapid dual-tracer PTSM+ATSM PET imaging of tumour blood flow and hypoxia: a simulation study. *Phys Med Biol* 2006;51:61-75
72. Department of Health. The NHS Cancer Plan: a plan for investment, a plan for reform. In; 2000
73. Department of Health. Cancer Reform Strategy. In; 2007
74. International Commission of Radiological Protection. ICRP Publication 60: 1990 Recommendations of the International Commission of Radiological Protection, 60. *Annals of the ICRP* 1991;21/1-3

75. International Commission of Radiological Protection. ICRP 103: Recommendations of the ICRP. Annals of the ICRP 2008;37 (2-4)

Chapter 6

Conclusions from CT-PET Studies in Squamous Cell Cancer in the Head and Neck

The 5-year survival of patients treated for SCCHN continues at 35% even though significant improvements have been made in investigative pathways and treatment. Poor outcome is associated with the development of treatment resistance in tumour stem cells. This resistance leads to loco-regional recurrence in 50% of patients regardless of the treatment they receive.

The major contributing factors are increased intra-cellular glucose metabolism and hypoxia. These processes are non-invasively detected and visualised by CT-PET imaging. These volumes may be targeted by dose escalated RT. Effective strategies require CT-PET guided TV delineation for RT planning, using a method and software that can be transferred between institutions to allow collaboration.

The method of delineation must accurately reflect the intra-tumoural regional process and the defined volume. Volume definition in turn will guide RT planning, dosimetry, and the delivered dose to these TVs and adjacent at risk organs during the delivery of dose escalated RT.

6.1 Conclusions

6.1.1 ¹⁸Fluoro-2-deoxyglucose Target Volume Delineation

¹⁸FDG is the commonest radio-nuclide used in clinical practise, and is a surrogate marker for glucose metabolism. The methods of ¹⁸FDG TV delineation have been much debated in the literature in both NSCLC, and SCCHN.

Two fixed (SUVCO, and PTSUVmax), and 1 adaptive automatic TV delineation methods were investigated before, and at three time points during conventionally fractionated curative RT or CRT in patients with locally advanced SCCHN at UCLH, London using PETVCAR software provided by GE Healthcare.

From these three methods, 10 thresholds were directly compared: SUVCO 2.5, 3.0, 3.5, and 4.0bwg/ml; 30, 35, 40, 45, and 50% of the SUVmax; and an IAT based on the individual SUVmax, and mean within the ROI, and the background uptake of ^{18}F FDG. Each CT-PET data set during treatment was automatically and individually co-registered to the pre-treatment imaging. Every ^{18}F FDG avid ROI was selected and automatically defined.

Twelve patients were recruited, 10 completed the imaging protocol, and 8 were analysed. Patients underwent a CT-PET of the HN 72 hours prior to the start of treatment, and then at 8 to 18Gy, 36 to 50Gy, and 66Gy. Eight primary, and 20 LN avid ^{18}F FDG regions were evaluated.

6.6.1.1 SUV Cut Off

The delineated FVs significantly reduced with radiation dose at 36 to 50Gy, and 66Gy compared to the pre-treatment FV. This was most significant when the 3.0bwg/ml SUVCO threshold defined the FV. The volumes were dependent on the threshold and significantly reduced at each imaging point when the 3.0, 3.5, and 4.0bwg/ml threshold defined volumes were compared to that defined by the 2.5bwg/ml threshold. This was most significant when the FV defined at 4.0bwg/ml was compared to that at 2.5bwg/ml. The theoretical radiation dose required to reduce these FVs to zero was between 84 and 152Gy for the primary, and 60 to 68Gy for the LN sites.

The SUVmax within the FVs defined by the various SUVCO thresholds was also significantly reduced at the same dose points, and positively correlated with the size of the defined FV. There was no significant difference in the SUVmax at each imaging point within the primary FV when SUVCO thresholds were compared. However, within the LN FV, the SUVmax was significantly reduced at each imaging point. This was because the SUVmax was lower in these

volumes and therefore more affected by the absolute SUVCO threshold. The theoretical radiation dose required to reduce the SUVmax to zero within these FVs was 112 to 128Gy for the primary, and 68 to 80Gy for the LNs.

6.6.1.2 Percentage Threshold of the SUVmax

The FVs defined at all thresholds by this method were not significantly reduced during treatment. There was a trend to an increase in volume, especially at the primary site, but this was not significant. The defined FVs did significantly reduce at each imaging point when the volume was compared to that defined by the 30% threshold.

The SUVmax was significantly reduced in the same manner as the SUVCO threshold. There was no correlation between the defined FVs and the SUVmax by this method. The theoretical dose required to reduce the SUVmax to zero was 128Gy for the primary, and 100Gy for the LN volumes.

6.6.1.3 Individualised Adaptive threshold

Similarly, the primary FVs delineated by this method were not significantly reduced during treatment, but the LN FVs were significantly reduced (although there was no correlation between the dose and delineated FV).

The SUVmax within the primary volume was significantly reduced after 36 to 50Gy, and in the LN volume after 8 to 18Gy. The RT dose required to reduce the theoretical SUVmax within the volume to zero was 112Gy for the primary, and 80Gy for the LN sites.

6.6.1.4 Background Uptake of ¹⁸Fluoro-2-deoxyglucose

The background uptake of ¹⁸FDG did not significantly increase during treatment, and in all cases was below the SUVCO thresholds used to define the FV.

The FVs defined by the SUVCO method therefore were not influenced by background ¹⁸FDG uptake, and radiation induced-inflammation for example was excluded from the final volume.

However, the background SUV significantly influenced the FVs defined by the PTSUVmax, especially after 36Gy. The calculated SUV used to define the volume was dependent on the SUVmax within the ROI. During treatment the difference between this and the background SUV reduced especially within the LN FV at 66Gy. This suggested the increased volume towards the end of RT was purely due to the delineation method, threshold, and SUV within the ROI.

The FV delineated by the IAT method was also dependent on the difference between the maximum and minimum SUV within the ROI.

6.1.2 ⁶⁴Cu-ATSM Hypoxia Definition, and Target Volume Delineation

Cu-ATSM has been proposed as a surrogate marker of hypoxia in CT-PET imaging. The use of ⁶⁴Cu-ATSM allowed immediate and late imaging due to the prolonged half-life of 12.7 hours. The uptake and retention pattern has not previously been validated with IHC hypoxic exogenous or endogenous antigens in patients with SCCHN. The imaging of tumour hypoxia, and the resultant delineation of hypoxic FVs may potentially be incorporated into dose escalation strategies to overcome hypoxic radio-resistance in the defined FV and reduce the rate of loco-regional failure.

Six patients due to be treated by primary surgery with locally advanced SCCHN were recruited over 12 months from May 2008. Four patients were injected with 505 to 595MBq of ⁶⁴Cu-ATSM, and underwent an immediate 1 hour 3D dynamic CT-PET. Two patients were also imaged by a 1-hour 3D static CT-PET 18 hours after injection, and by a DCE-CT after completion of dynamic imaging.

Eighteen hours prior to surgery, patients received 0.5g/m² of pimonidazole. Following surgery, the macroscopic specimen was orientated and dissected, and IHC undertaken on the wax embedded tissue blocks to detect pimonidazole adducts, GLUT1, CAIX and HIF1a antigens representative of intra-tumoural hypoxia. The uptake and retention of ⁶⁴Cu-ATSM was assessed at 5 to 20 minutes, 40 to 60 minutes, and 18 hours after injection by the calculation of tumour to muscle, background and blood ratios. The IHC hypoxic fraction was defined after linear unmixing the colours of the digitised IHC specimen. These

and the fused corresponding CT-PET images were converted to grayscale and correlated with the uptake and retention of ^{64}Cu -ATSM on CT-PET imaging at these time points, and within a 4cm section of intra-tumoural BF.

The tumour to muscle, blood and background ratios at 5 to 20 minutes, 40 to 60 minutes and 18 hours after injection were used to define the FV at ratios of 2.0, 2.5, 3.0, and 4.0 using the PETVCAR software.

The uptake and retention of ^{64}Cu -ATSM within the tumour on each axial CT-PET image significantly increased at 40 to 60 minutes and 18 hours after injection when compared to the uptake at 5 to 20 minutes within the tumour and normal tissue. This was most significant for the tumour to muscle ratio at 40 to 60 minutes after injection. Initially at 5 to 20 minutes after injection, the activity within the blood was not hugely different to that within the tumour, suggesting initial non-selective uptake that becomes hypoxia selective with time.

Interestingly there was significant uptake and retention within the salivary glands in all patients. This has not formerly been published, and may highlight the use of copper in salivary amylase secretion. Two other unusual sites of retention were noted within the mandible and right shoulder. In both cases these patients were found to have a inflammatory process. The role of copper during inflammation and demyelination is recognised which may have accounted for this uptake pattern, and local hypoxia may also have been a contributing factor.

The IHC hypoxic fraction was dependent on the detected antigen of interest and ranged between 14 and 54%. Pimonidazole positively correlated with CAIX, and HIF1a, and this was most significant with GLUT1. There was no difference in the method of hypoxic fraction calculation.

On a grid by grid regional assessment, there was a significant positive correlation with the IHC exogenous and endogenous markers of hypoxia at 5 to 20 minutes, 40 to 60 minutes and 18 hours after the injection of ^{64}Cu -ATSM. This was most significant when the pimonidazole adduct staining was compared with the uptake and retention of ^{64}Cu -ATSM at 40 to 60 minutes. Eighteen hours after injection,

HIF1a, and pimonidazole correlation with ^{64}Cu -ATSM uptake and retention were most significant, and this was the case for GLUT1 at 5 to 20 minutes.

The perfusion parameters on DCE-CT from one patient were analysed. Although no conclusions can be drawn, there was no correlation of BF with the uptake of ^{64}Cu -ATSM in this patient when images were converted to grayscale, and corresponding grids correlated on each axial image of the ROI over a 4cm region of the tumour.

The hypoxic FV defined at 5 to 20 minutes, 40 to 60 minutes and 18 hours after injection, were largest for the tumour to muscle ratio of 2.5, and then reduced as the ratio increased to 4.0. The FVs were also larger at 40 to 60 minutes and 18 hours after injection compared to 5 to 20 minutes. The hypoxic FVs defined by the tumour to blood and tumour to background ratios were smaller than those defined by the tumour to muscle ratio.

The results suggest that ^{64}Cu -ATSM does image hypoxia, and hypoxic TV delineation is dependent on the time of imaging after injection, and the method of delineation. The distribution of pimonidazole adducts, and ^{64}Cu -ATSM would suggest that the entire tumour volume was hypoxic. This study also highlighted the complexity, and feasibility of early phase study design, set up, and recruitment in CT-PET imaging and the potential difficulty this can pose to researchers.

6.2 Future Directions and Applications to Clinical Practice

6.2.1 ^{18}F Fluoro-2-deoxyglucose CT-PET Guided Target Volume Delineation

^{18}F FDG CT-PET guided RT has the potential to sculpt, optimise, and deliver escalated radiation dose heterogeneously across a defined FV [1] without increasing normal tissue toxicity [2].

Effective dose optimisation and escalation strategies require a collaborative approach to CT-PET research in RT planning, definition of the timing of imaging

during treatment, and method and threshold of volume delineation. Dose escalation may adapt the dose to the shrinking FV during treatment. Alternatively an increased dose may be delivered across the pre-treatment defined FV through a SIB technique. Adaptive strategies may utilise this as well as the voxel based dose painting method.

Tumour heterogeneity and gradients of increased glucose metabolism or hypoxia across the volume, allow dose optimisation through dose painting techniques. With 3D dynamic imaging, the dose can be modulated within a CT-PET voxel depending on the uptake of the radio-nuclide which acts as a surrogate for radio-resistance. Dose adaptation and optimisation during RT also requires effective methods of auto-contouring normal tissue, and image registration to account for changes in anatomy due to nutritional deficiency, oedema, and inflammation during the radiation treatment.

6.2.1.1 Dose Escalation Study

This study has indicated that FVs delineated by the SUVCO are less susceptible to background ^{18}F FDG uptake, and thresholds of 3.0, 3.5, and 4.0bwg/ml are significantly reduced during treatment.

Dose escalation methods to ^{18}F FDG CT-PET guided volumes could incorporate a SIB technique at the start of treatment or after 36Gy of RT with voxel based dose painting through IMRT. Other methods would be IMAT, or stereo-tactic irradiation of residual volumes either during or at the end of treatment. The placement of fucidal markers may aid stereo-tactic delivery.

Commercially available software such as PETVCAR, increase the possibility of widespread CT-PET guided treatment planning, and aid collaboration in delineation studies.

RT structure sets (RTSS) were created after FV definition using an SUVCO threshold of 3.0bwg/ml by PETVCAR in patients from the study reported in Chapter 4. These were DICOM compatible, and transferable from the GE Advantage Windows Work Station to Oncentra Masterplan (Nucletron,

Veenendaal, The Netherlands), and then to Aria and Eclipse IMRT planning software (Varian Medical Systems Inc., Palo Alto, CA, USA).

The potential of dose escalation was explored in four patients using a standard 7 field IMRT technique. CT-PET RTSS and the reconstructed CT HN were used to retrospectively plan IMRT (65Gy in 30 fractions to high-risk disease, and 54Gy in 30 fractions to low-risk disease). IMRT was escalated in 5% increments of this standard IMRT high-risk dose to the CT-PET guided volume defined by the SUVCO threshold of 3.0bwg/ml. The equivalent dose in 2Gy per fraction, and the biological effective dose for each dose increment was calculated according to an α/β ratio of 10 for HN tumours. A SIB technique was used and planned from the start of treatment because dynamic imaging was not available to allow dose painting, and the aim was to demonstrate the possibility and guide future dose escalation studies.

The dose to the biological TV was optimised during the RT process and a 3mm margin was created to expand this volume to a PTV.

Figure 6.1 illustrates the standard IMRT colour washed plan with the 95% isodose shown.

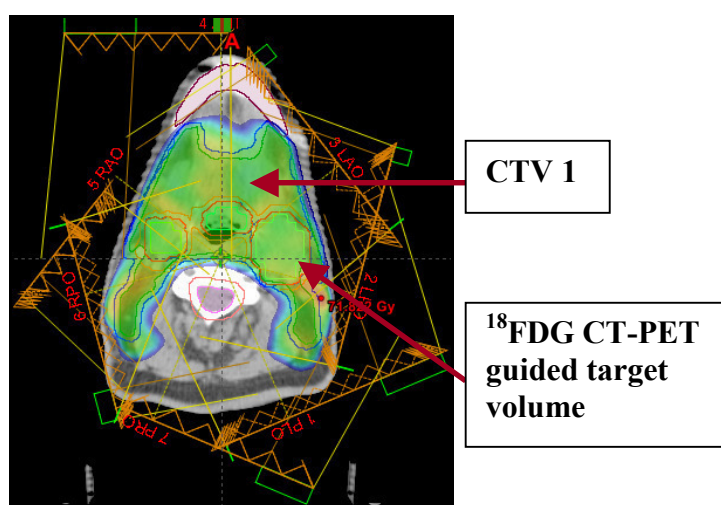


Figure 6.1: Colour washed axial image of standard Head and Neck IMRT plan

Figure 6.2a) indicates the 115% dose escalated plan. The CT-PET guided PTV was planned to receive 74.5Gy in 30 fractions, and the CTV1 65Gy in 30 fractions. A colour wash thresholded to 62Gy has been applied. In Figure 6.2b) the 95% isodose for the CT-PET guided PTV of 70.78Gy has been applied to exclude regions that would have received a lower dose from the image. The CT-PET defined PTV is indicated by an arrow. Three ^{18}F FDG CT-PET guided FVs are present on the image, two LN regions, and a primary posterior third of tongue region.

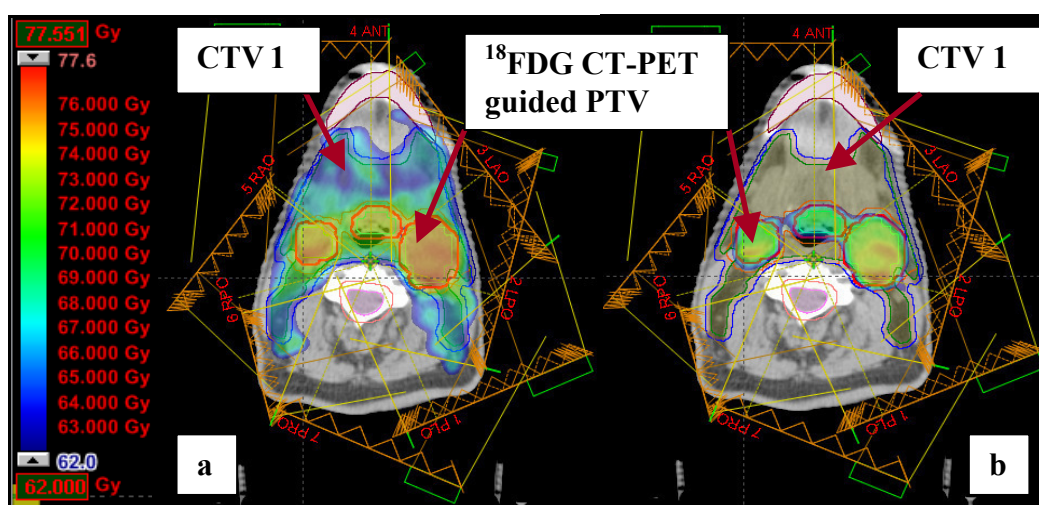


Figure 6.2a and b: Dose escalated ^{18}F FDG CT-PET guided target volume with lower threshold set at 62Gy a), and lower threshold at 70.78Gy

This planning study demonstrated the possibility of CT-PET guided dose escalation using commercially available software. In this example normal tissue constraints were not exceeded, and both primary and LN FV were escalated to the same dose.

A prospective study would examine the feasibility of both SIB and voxel based dose painting methods of dose escalation. Dose distribution across the CT-PET guided FV, and adjacent normal tissue structures would be assessed.

The PETVCAR software would allow CT-PET data sets to be co-registered before, during and after treatment and volumes reviewed according to areas of local recurrence and dose distribution within that volume. Recurrence would be

assessed voxel by voxel, and the dose received and SUVmax compared within that voxel.

Within this study design, dose levels in increments of 5% will be compared either to 65Gy in 30 fractions, or 70Gy in 35 fractions. Different FV within the patient may be escalated to different dose levels depending on the level of biological risk as shown by the theoretical dose required to reduce the SUVmax to zero in these two volumes.

Assessment of acute and late toxicity would be required to ensure patient safety, by stopping dose escalation levels if for example laryngeal necrosis develops. Standard and dose escalated IMRT continue to use tissue tolerance data published nearly 20 years ago [3]. QUANTEC (Quantitative Analysis of Normal Tissue Effects in Clinic) will guide tolerance doses for RT techniques such as IMRT that deliver a bath and shower radiation dose. The normal tissues are bathed in low dose irradiation, and the targeted disease sites are showered with high dose. This important step forward will allow CT-PET guided dose escalation studies to assess the impact on normal tissue, and functional outcome, and correlate with improvements in loco-regional control.

Normal tissue ^{18}F FDG uptake assessment within for example the pharyngeal constrictor muscles would be important. Physiological uptake in these tissues during radiation will provide valuable information to predict functional outcome after treatment. ^{18}F FDG uptake during treatment in normal tissues may also guide the total escalated dose. Increased uptake may suggest an increased likelihood of late toxicity, and so limit the total dose delivered. Alternatively reduced uptake may suggest a lower risk of toxicity, and a potential to escalate to higher doses.

6.2.1.2 Dual Radio-nuclide Studies

Tumour biology is complex and increased glucose metabolism and hypoxia may suggest a more aggressive phenotype [4].

Dual radio-nuclide imaging with ^{18}F FDG and for example Cu-ATSM would allow different intra-tumoural regions to be visualised and potentially dose optimised

and escalated by voxel based dose painting depending on the level of radio-resistance calculated from tumour probability models [5]. Such studies need to be able to identify each individual radio-nuclide, and will require a time interval between administration for example a minimum of 5 half-lives for ^{18}F FDG or 24 hours with this nuclide administered first and then Cu-ATSM.

6.2.1.3 Phantom Validation Studies

^{18}F FDG delineation methods are dependent on the calibration factors, hard and software of individual cameras. Collaborative studies would require individual centres to incorporate these into studies using commercially available software.

Adaptive thresholding methods require such knowledge. Prior to dose escalation with the IAT, further validation is required to assess the effect in larger patients numbers on FV delineation during RT. This should then be correlated in phantom studies with the true phantom edge, and that defined on CT-PET imaging in patients by the algorithm.

6.2.2 ^{64}Cu -ATSM Hypoxia Definition, and Target Volume Delineation

The results reported in chapter 5 suggested that ^{64}Cu -ATSM was a potential surrogate marker of hypoxia. However before dose escalation studies are contemplated to the defined hypoxic FV, further validation is required in larger patient numbers to confirm or refute these results.

6.2.2.1 Patient Recruitment

This study had originally planned to recruit 20 patients, and this would have provided more robust conclusions. Ideally patient recruitment will continue at UCLH and commence at Guy's and St Thomas' Hospitals NHS Foundation Trust. Other imaging arms within the protocol can then be completed including whole body CT-PET imaging, and venous blood sampling to give further information on the uptake, retention pattern, and bio-distribution of ^{64}Cu -ATSM. Also the association of ^{64}Cu , and the ATSM ligand can be closely evaluated within the blood.

6.2.2.2 Registration of Imaging and Pathological Specimens

Improved registration with non-rigid methods may allow the overlap between the CT-PET and digitised IHC image to be evaluated. Laser capture microscopy [6] on the IHC digitised images will allow antigen detection at a cellular level which may then be correlated with the retention of ^{64}Cu -ATSM within an individual voxel and provide more accurate spatial mapping of distribution. The hypoxia within the voxel would then be proportional to the number of hypoxic cells. This microscopy could also be used in conjunction with hypoxia metagene sequencing and analysis in micro-array studies because the gene sequence could be established within an individual voxel provided the tissue and imaging are accurately co-registered.

6.2.2.3 Dual Radio-nuclide and Perfusion Imaging

Dual radio-nuclide imaging using Cu-ATSM and PTSM, for hypoxia and perfusion imaging or ^{18}F Fluoro-3'-deoxy-3'-thymidine for proliferation will give further information into the complex intra-tumoural biology that is associated with loco-regional recurrence. Similarly, consideration will need to be given to the order and timing of administration of each radio-nuclide under investigation.

Perfusion within tumour and normal tissues is dynamic and temporal intra-regional variation occurs [7]. Serial imaging with DCE-CT, would provide a more representative map of these changes, and allow more extensive correlation with IHC hypoxic antigens, and ^{64}Cu -ATSM uptake and retention.

6.2.2.4 Hypoxia Imaging with other Copper Isotopes

Alternative isotopes with a shorter half-life, and a higher positron emission rate such as 60 , 61 , and ^{62}Cu will allow repeated imaging without exposing the patients to excessive radiation dose. They may also be incorporated into dual tracer studies. This will allow the imaging of chronic hypoxia, perfusion and reoxygenation during treatment to be correlated.

6.2.2.5 Correlation of Imaging with Hypoxia Metagene Sequencing

Once validated in larger numbers of patients, the uptake and retention of ^{64}Cu -ATSM may be correlated with hypoxia metagene sequences to further determine

individual risk. This will allow loco-regional recurrence to be correlated with genotype and Cu-ATSM uptake. Multiple biopsy specimens of whole specimens will give the greatest opportunity to spatially map the tumour unless used in conjunction with laser microscopy.

6.2.2.6 Hypoxic Target Volume Delineation

Hypoxic TV delineation for use in RT planning is vitally important and as shown is dependent on the method of delineation and threshold. The uptake and retention of Cu-ATSM must be defined according to the time point after injection as well. This will depend on the Cu isotope used. Later imaging time points may be more representative of chronic hypoxia. As with perfusion, this process is dynamic, and delineation on multiple hypoxia image sets may provide a more representative map of spatial distribution and ensure all the hypoxic areas are included in the volume [8].

The delineation of the FV may then be further assessed in studies specifically to evaluate the benefit of using the tumour to muscle, blood or background ratios. The threshold selected should predict the true hypoxic volume, and so the risk of loco-regional recurrence.

6.2.2.7 Dose Escalation to Hypoxic Functional Volumes

After this, dose escalation studies similar to those using ^{18}F FDG may be attempted. Serial imaging will evaluate the most representative imaging point of chronic hypoxia. Retention studies before and during treatment will evaluate when adaptive RT should be commenced, and how it should be delivered, as reoxygenation with treatment will be visualised [9].

Voxel based dose painting will give the best opportunity to modulate and optimise dose based on the individual risk within the voxel for recurrence and so mirror the heterogeneous pattern of hypoxia [10,11].

6.3 Conclusion

CT-PET guided RT planning, dose optimisation and escalation to both metabolically active and hypoxic FVs requires close collaboration with the Nuclear Medicine Department, and other institutions to provide robust delineation techniques. Accurate delineation also depends on factors related to the radio-nuclide, and camera.

The detection, visualisation, and delineation of FVs must represent the true pathological volume, and validation studies with ^{64}Cu -ATSM are vitally important.

Finally, the Clinical Oncologist must be confident when defining the CT-PET guided TVs for RT planning that the delineation method provides an accurate representation of the process under investigation. Dose escalation to targeted areas of radio-resistance will then be effective, and have the greatest impact on loco-regional control.

6.3 References

1. Ling CC, Humm J, Larson S, et al. Towards multidimensional radiotherapy (MD-CRT): biological imaging and biological conformality. *Int J Radiat Oncol Biol Phys* 2000;47:551-560
2. Madani I, Duthoy W, Derie C, et al. Positron emission tomography-guided, focal-dose escalation using intensity-modulated radiotherapy for head and neck cancer. *Int J Radiat Oncol Biol Phys* 2007;68:126-135
3. Emami B, Lyman J, Brown A, et al. Tolerance of normal tissue to therapeutic irradiation. *Int J Radiat Oncol Biol Phys* 1991;21:109-122
4. Thorwarth D, Eschmann SM, Paulsen F, Alber M. Hypoxia dose painting by numbers: a planning study. *Int J Radiat Oncol Biol Phys* 2007;68:291-300
5. Alber M, Paulsen F, Eschmann SM, Machulla HJ. On biologically conformal boost dose optimization. *Phys Med Biol* 2003;48:N31-35
6. Curran S, McKay JA, McLeod HL, Murray GI. Laser capture microscopy. *Mol Pathol* 2000;53:64-68
7. Bisdas S, Surlan-Popovic K, Didanovic V, Vogl TJ. Functional CT of squamous cell carcinoma in the head and neck: repeatability of tumor and muscle quantitative measurements, inter- and intra-observer agreement. *Eur Radiol* 2008;18:2241-2250
8. Nehmeh SA, Lee NY, Schroder H, et al. Reproducibility of intratumor distribution of (18)F-fluoromisonidazole in head and neck cancer. *Int J Radiat Oncol Biol Phys* 2008;70:235-242
9. Thorwarth D, Eschmann SM, Paulsen F, Alber M. A model of reoxygenation dynamics of head-and-neck tumors based on serial 18F-

fluoromisonidazole positron emission tomography investigations. *Int J Radiat Oncol Biol Phys* 2007;68:515-521

10. Bentzen SM. Theragnostic imaging for radiation oncology: dose-painting by numbers. *Lancet Oncol* 2005;6:112-117
11. Dirix P, Vandecaveye V, De Keyzer F, et al. Dose painting in radiotherapy for head and neck squamous cell carcinoma: value of repeated functional imaging with (18)F-FDG PET, (18)F-fluoromisonidazole PET, diffusion-weighted MRI, and dynamic contrast-enhanced MRI. *J Nucl Med* 2009;50:1020-1027

Appendix 1

Tables

Chapter 4

Table 1

The simple linear regression correlation for the defined the primary functional volume by the SUV Cut Off thresholds and radiation dose

SUV Cut Off Threshold (bwg/ml)	Correlation Co-efficient	p-value	95% Confidence Interval (cm³)
2.5	-0.274	0.135	-0.57 to -0.09
3.0	-0.374	0.038	-0.64 to -0.02
3.5	-0.438	0.014	-0.67 to -0.10
4.0	-0.468	0.008	-0.71 to -0.14

Table 2

Simple linear regression results for the primary functional volume delineated by the percentage of the SUVmax method and dose

Percentage Threshold of the SUVmax (%)	Correlation Co-efficient	p-value	95% Confidence Interval (cm³)
30	0.337	0.058	-0.01 to +0.61
35	0.326	0.068	-0.03 to +0.61
40	0.300	0.095	-0.05 to +0.59
45	0.288	0.109	-0.07 to +0.80
50	0.257	0.155	-0.10 to +0.57

Table 3

The mean percentage, actual reduction, p-values, and 95% confidence intervals for the lymph node functional volume delineated by the SUV Cut Off thresholds at each imaging point

SUV Cut Off Threshold (bwg/ml)	Imaging Point (Gy)	Median Percentage Reduction	Median Reduction (cm³)	p-value	95% CI (cm³)
2.5 to 3.0	<i>0</i>	35.85	1.10	0.0001	0.60 - 2.00
	<i>8 to 18</i>	65.22	0.60	0.001	0.30 - 1.40
	<i>36 to 50</i>	87.50	0.65	0.002	0.20 - 1.00
	<i>66</i>	-	0.20	0.007	0.00 - 0.45
2.5 to 3.5	<i>0</i>	54.72	1.65	<0.0001	0.90 - 2.12
	<i>8 to 18</i>	91.30	1.08	<0.0001	0.40 - 2.20
	<i>36 to 50</i>	100.00	0.80	<0.0001	0.20 - 2.25
	<i>66</i>	-	0.20	0.004	0.00 - 0.55
2.5 to 4.0	<i>0</i>	69.81	1.90	<0.0001	1.10 - 3.90
	<i>8 to 18</i>	95.65	1.38	<0.0001	0.50 - 2.80
	<i>36 to 50</i>	100.00	0.85	<0.0001	0.20 - 2.80
	<i>66</i>	-	0.20	0.004	0.00 - 0.55

Table 4

The median percentage, actual change, p-values and 95% confidence intervals for the lymph node functional volume delineated by the SUV Cut Off thresholds between the imaging points

SUV Cut Off Threshold (bwg/ml)	Compared Imaging Points (Gy)	Median Percentage change	Median change (cm³)	p-value	95% CI (cm³)
2.5	<i>0 to 8-18</i>	-56.60	+1.65	0.999	+0.65 to +3.25
	<i>0 to 36-50</i>	-84.91	-2.45	<0.0001	-5.30 to -1.15
	<i>0 to 66</i>	-100.00	-3.38	<0.0001	-7.05 to -1.45
3.0	<i>0 to 8-18</i>	-76.47	+0.90	0.999	+0.25 to +2.50
	<i>0 to 36-50</i>	-97.06	-1.85	<0.0001	-4.40 to -0.75
	<i>0 to 66</i>	-100.00	-3.53	<0.0001	-5.90 to -0.25
3.5	<i>0 to 8-18</i>	-91.66	+0.73	0.998	+0.20 to +2.35
	<i>0 to 36-50</i>	-100.00	-1.93	<0.0001	-4.00 to -0.45
	<i>0 to 66</i>	-100.00	-2.00	0.0001	-4.95 to -0.45
4.0	<i>0 to 8-18</i>	-93.75	+0.50	0.995	+0.05 to +2.1
	<i>0 to 36-50</i>	-100.00	-3.50	0.0002	-3.50 to -0.25
	<i>0 to 66</i>	-100.00	-2.75	0.0002	-4.35 to -0.25

Table 5

Simple linear regression results for the relationship between the lymph node functional volume delineated by the SUV Cut Off thresholds and radiation dose

SUV Cut Off Threshold (bwg/ml)	Correlation Co-efficient	p-value	95% Confidence Interval (cm³)
2.5	-0.285	0.01	-0.48 to -0.07
3.0	-0.291	0.009	-0.48 to -0.08
3.5	-0.290	0.009	-0.48 to -0.08
4.0	-0.287	0.009	-0.48 to -0.07

Table 6

The median percentage, actual reduction, p-values, and 95% confidence intervals for the lymph node functional volume delineated by the percentage thresholds of the SUVmax at each imaging point

Percentage Threshold of the SUVmax (%)	Imaging Point (Gy)	Median Percentage Reduction	Median Reduction (cm³)	p-value	95% CI (cm³)
30 to 35	<i>0</i>	-1.18	+0.90	>0.999	+0.14 to +1.70
	<i>8 to 18</i>	-18.18	-0.05	0.3529	-1.05 to +0.55
	<i>36 to 50</i>	+1.12	+0.63	<0.999	+0.01 to +0.45
	<i>66</i>	0.00	+0.20	0.999	+0.00 to +1.30

30 to 40	<i>0</i>	-10.59	-1.20	<0.0001	-3.10 to -0.70
	<i>8 to 18</i>	-26.14	-1.23	<0.0001	-2.45 to -0.60
	<i>36 to 50</i>	-11.11	-1.23	<0.0001	-2.50 to -0.25
	<i>66</i>	-2.22	-0.40	0.0005	-2.55 to -0.50
30 to 45	<i>0</i>	-25.06	-1.88	<0.0001	-3.60 to -1.10
	<i>8 to 18</i>	-34.09	-1.70	<0.0001	-3.90 to -0.55
	<i>36 to 50</i>	-23.86	-2.05	<0.0001	-3.90 to -0.55
	<i>66</i>	-13.33	-0.73	<0.0001	-3.05 to -0.20
30 to 50	<i>0</i>	-36.47	-2.55	<0.0001	-4.50 to -1.45
	<i>8 to 18</i>	-40.91	-2.23	<0.0001	-4.25 to -1.35
	<i>36 to 50</i>	-33.33	-2.63	<0.0001	-5.70 to -1.35
	<i>66</i>	-24.44	-1.45	<0.0001	-4.30 to -0.60

Table 7

The median percentage, actual change, p-values and 95% confidence intervals for the lymph node functional volumes delineated by the percentage thresholds of the SUVmax between the imaging points

Percentage Threshold of the SUVmax (%)	Compared Imaging Points (Gy)	Median Percentage Change	Median Change (cm³)	p-value	95% CI (cm³)
30	<i>0 to 8-18</i>	+2.44	+0.58	0.414	-6.67 to +5.52
	<i>0 to 36-50</i>	+17.35	+4.09	0.211	-7.26 to +15.44
	<i>0 to 66</i>	+35.73	+25.53	0.065	-9.76 to +60.82
35	<i>0 to 8-18</i>	+5.16	+0.99	0.355	-7.06 to +5.08
	<i>0 to 36-50</i>	+9.26	+1.78	0.321	-6.88 to +10.43
	<i>0 to 66</i>	+133.49	+20.41	0.071	-8.79 to +49.61
40	<i>0 to 8-18</i>	+3.54	+0.58	0.401	-5.81 to +4.66
	<i>0 to 36-50</i>	-6.34	-1.03	0.334	-6.43 to +4.38
	<i>0 to 66</i>	+116.48	+14.89	0.078	-7.29 to +37.07
45	<i>0 to 8-18</i>	+1.49	+0.20	0.453	-4.05 to +3.65
	<i>0 to 36-50</i>	-13.70	-1.837	0.165	-6.00 to +2.33

	0 to 66	+111.43	+11.79	0.091	-7.01 to +30.58
50	0 to 8-18	-0.12	+0.01	0.496	-3.17 to +3.20
	0 to 36-50	-22.49	-2.462	0.075	-6.064 to +1.139
	0 to 66	+95.82	+8.19	0.101	-5.59 to 21.96

Table 8

Simple linear regression results for the lymph node functional volume delineated by the percentage thresholds of the SUVmax and radiation dose

Percentage Threshold of the SUVmax (%)	Correlation Co-efficient	p-value	95% Confidence Interval (cm ³)
30	+0.057	0.612	-0.16 to +0.27
35	+0.073	0.519	-0.15 to +0.29
40	+0.054	0.635	-0.17 to +0.27
45	+0.073	0.515	-0.15 to +0.29
50	+0.078	0.492	-0.14 to +0.30

Table 9

Simple linear regression results for the SUVmax within the primary functional volume delineated by the SUV Cut Off thresholds and radiation dose

SUV Cut Off Threshold (bwg/ml)	Correlation Co-efficient	p-value	95% Confidence Interval (bwg/ml)
2.5	-0.447	0.012	-0.69 to -0.11
3.0	-0.483	0.006	-0.72 to -0.16
3.5	-0.435	0.014	-0.68 to -0.10
4.0	-0.384	0.036	-0.65 to -0.03

Table 10

The median percentage, actual reduction, p-values, and 95% confidence intervals for the SUVmax within the lymph node functional volume delineated by the SUV Cut Off thresholds at each imaging point

SUV Cut Off Threshold (bwg/ml)	Imaging Point (Gy)	Median Percentage Reduction	Median Reduction (bwg/ml)	p-value	95% CI (bwg/ml)
2.5 to 3.0	<i>0</i>	0.00	0.00	0.790	*
	<i>8 to 18</i>	0.00	0.00	0.875	*
	<i>36 to 50</i>	-49.18	0.00	0.063	0.0 to + 1.35
	<i>66</i>	0.00	0.00	0.895	*
2.5 to 3.5	<i>0</i>	0.00	-0.65	0.016	-1.65 to 0.0
	<i>8 to 18</i>	-43.59	0.00	0.031	-1.40 to 0.0
	<i>36 to 50</i>	-100.00	-1.35	0.008	-1.65 to 0.0
	<i>66</i>	-100.00	-1.45	0.031	-1.45 to 0.0
2.5 to 4.0	<i>0</i>	0.00	-1.55	0.003	-1.75 to 0.0
	<i>8 to 18</i>	-100.00	0.00	0.003	-1.40 to 0.0
	<i>36 to 50</i>	-100.00	-1.35	0.007	-1.65 to 0.0
	<i>66</i>	-100.00	-1.45	0.007	-1.75 to 0.0

*** Indicates no CI calculated as there was no difference between the compared groups**

Table 11

The median percentage, actual reduction, p-values and 95% confidence intervals for the SUVmax within the lymph node functional volume delineated by the SUV Cut Off thresholds between the imaging points

SUV Cut Off Threshold (bwg/ml)	Compared Imaging Points (Gy)	Median Percentage Change	Median change (bwg/ml)	p-value	95% CI (bwg/ml)
2.5	<i>0 to 8-18</i>	+36.59	+2.1	0.999	+1.15 to +3.05
	<i>0 to 36-50</i>	-50.41	-4.05	<0.0001	-7.55 to -3.85
	<i>0 to 66</i>	-100.00	-5.45	<0.0001	-7.55 to -3.85
3.0	<i>0 to 8-18</i>	+36.59	+2.18	0.997	+1.20 to +3.35
	<i>0 to 36-50</i>	-74.80	-4.30	<0.0001	-5.70 to -3.10
	<i>0 to 66</i>	-100.00	-5.68	<0.0001	-7.90 to -3.75
3.5	<i>0 to 8-18</i>	+29.26	+1.80	0.998	+0.20 to +3.05
	<i>0 to 36-50</i>	-100.00	-4.26	<0.0001	-5.80 to -2.55
	<i>0 to 66</i>	-100.00	-5.55	<0.0001	-8.00 to -3.40
4.0	<i>0 to 8-18</i>	+21.13	+1.30	0.991	+0.0 to +2.65
	<i>0 to 36-50</i>	-100.00	-3.60	0.0002	-3.60 to -5.80
	<i>0 to 66</i>	-100.00	-5.55	0.0002	-8.20 to -3.40

Table 12

Simple linear regression results for the SUVmax within the lymph node functional volume delineated by the SUV Cut Off thresholds and radiation dose

SUV Cut Off Threshold (bwg/ml)	Correlation Co-efficient	p-value	95% Confidence Interval (bwg/ml)
2.5	-0.537	<0.0001	-0.64 to -0.36
3.0	-0.517	<0.0001	-0.66 to -0.34
3.5	-0.476	<0.0001	-0.63 to -0.29
4.0	-0.476	<0.0001	-0.63 to -0.28

Table 13

The mean and standard error of the mean for the SUV used to define the primary functional volume delineated by each percentage threshold of the SUVmax

Percentage Threshold of the SUVmax (%)		SUV (bwg/ml)			
		0Gy	8 to 18Gy	36 to 50Gy	66Gy
30	<i>Mean</i>	3.73	3.15	2.33	1.73
	<i>SEM</i>	0.70	0.64	0.35	0.28
35	<i>Mean</i>	4.34	3.70	2.70	2.01
	<i>SEM</i>	0.81	0.74	0.41	0.33
40	<i>Mean</i>	4.93	4.24	3.09	2.30
	<i>SEM</i>	0.94	0.86	0.46	0.38
45	<i>Mean</i>	5.50	4.75	3.45	2.55
	<i>SEM</i>	1.05	0.96	0.53	0.42
50	<i>Mean</i>	6.20	5.31	3.88	2.90
	<i>SEM</i>	1.17	1.07	0.59	0.46

Table 14

The mean increase, p-values, and 95% confidence intervals for the SUV used to define the primary functional volume at each imaging point by the percentage thresholds of the SUVmax

Percentage Threshold of the SUVmax (%)		Mean Increase (bwg/ml)	p-value	95% CI (bwg/ml)
30 to 35	0	0.62	0.001	0.35 to 0.89
	8 to 18	0.54	0.001	0.30 to 0.78
	36 to 50	0.36	0.0004	0.21 to 0.51
	66	0.29	0.0004	0.17 to 0.41
30 to 40	0	1.20	0.0008	0.62 to 0.18
	8 to 18	1.09	0.0008	0.57 to 1.60
	36 to 50	0.76	0.0003	0.48 to 1.04
	66	0.58	0.0003	0.34 to 0.81
30 to 45	0	1.83	0.0007	0.99 to 2.67
	8 to 18	1.60	0.0008	0.85 to 2.35
	36 to 50	1.12	0.0002	0.69 to 1.55
	66	0.88	0.0001	0.57 to 1.18
30 to 50	0	2.48	0.0006	1.35 to 3.61
	8 to 18	2.15	0.0007	1.15 to 3.16
	36 to 50	1.56	0.0002	0.99 to 2.13
	66	1.16	0.0002	0.73 to 1.60

Table 15

The median increase, p-values, and 95% confidence intervals for the SUV used to define the lymph node functional volume at each imaging point by the percentage thresholds of the SUVmax

Percentage Threshold of the SUVmax (%)		Mean Increase (bwg/ml)	p-value	95% CI (bwg/ml)
30 to 35	0	0.35	<0.0001	0.20 to 0.49
	8 to 18	0.30	<0.0001	0.20 to 0.40
	36 to 50	0.20	<0.0001	0.15 to 0.25
	66	0.10	<0.0001	0.10 to 0.15
30 to 40	0	0.70	<0.0001	0.45 to 0.95
	8 to 18	0.55	<0.0001	0.40 to 0.80
	36 to 50	0.35	<0.0001	0.25 to 0.50
	66	0.25	<0.0001	0.20 to 0.30
30 to 45	0	1.05	<0.0001	0.70 to 1.40
	8 to 18	0.80	<0.0001	0.55 to 1.50
	36 to 50	0.55	<0.0001	0.40 to 0.70
	66	0.35	<0.0001	0.30 to 0.45
30 to 50	0	1.50	<0.0001	0.95 to 1.95
	8 to 18	1.05	<0.0001	0.65 to 1.55
	36 to 50	0.75	<0.0001	0.55 to 0.95
	66	0.50	<0.0001	0.40 to 0.65

Table 16

Simple linear regression relationship between the SUVmax and the primary functional volume delineated by the SUV Cut Off thresholds

SUV Cut Off Threshold (bwg/ml)	Correlation Co-efficient	p-value	95% Confidence Interval (bwg/ml)
2.5	0.618	0.0002	0.34 to 0.80
3.0	0.718	<0.0001	0.49 to 0.86
3.5	0.749	<0.0001	0.53 to 0.87
4.0	0.780	<0.0001	0.59 to 0.89

Table 17

Simple linear regression relationship between the SUVmax and the lymph node functional volume delineated by the SUV Cut Off thresholds

SUV Cut Off Threshold (bwg/ml)	Correlation Co-efficient	p-value	95% Confidence Interval (bwg/ml)
2.5	0.633	<0.0001	0.48 to 0.75
3.0	0.631	<0.0001	0.48 to 0.75
3.5	0.632	<0.0001	0.48 to 0.75
4.0	0.627	<0.0001	0.47 to 0.74

Chapter 5

Table 18

The range of activity of ^{64}Cu -ATSM with time after injection

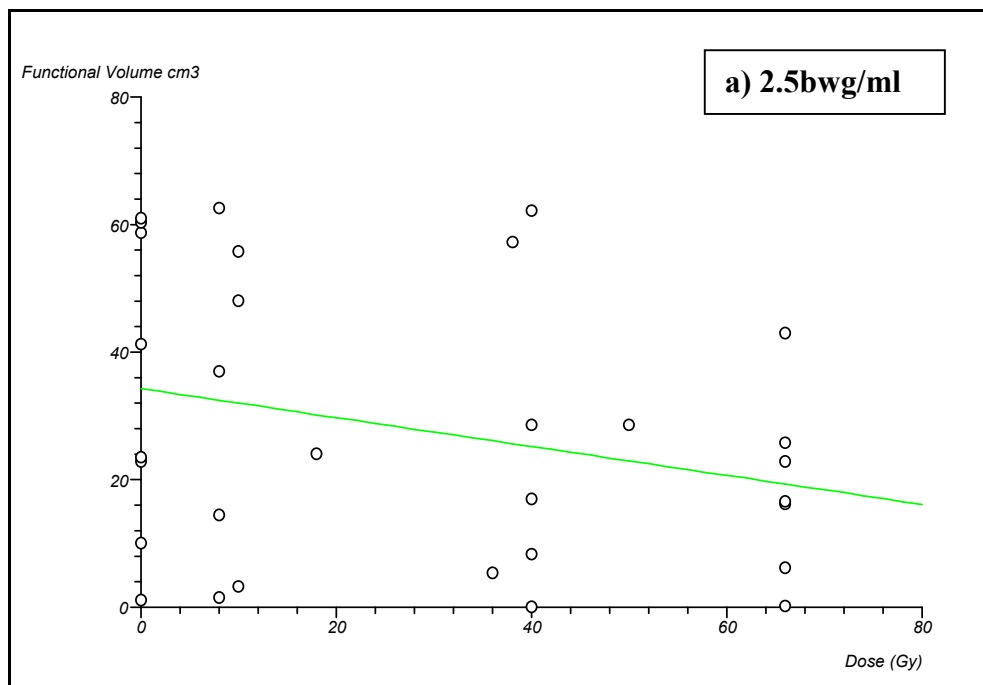
Time in minutes	Region of interest	Maximum ^{64}Cu-ATSM Activity (Bq/ml)
0	<i>Tumour</i>	0
	<i>Necrosis</i>	0
	<i>CL SCM</i>	0
	<i>Carotid</i>	0
	<i>Posterior Neck</i>	0
	<i>IL Salivary gland</i>	0
	<i>CL Salivary gland</i>	0
0.5	<i>Tumour</i>	1,207,190 to 1,914,251
	<i>Necrosis</i>	407,086 to 509,500
	<i>CL SCM</i>	222,093 to 602,272
	<i>Carotid</i>	2,524,364 to 6,427,844
	<i>Posterior Neck</i>	248,720 to 668,346
	<i>IL Salivary gland</i>	505,133 to 701,623
	<i>CL Salivary gland</i>	222,093 to 969,980
1	<i>Tumour</i>	802,635 to 952,490
	<i>Necrosis</i>	506,632 to 616,632
	<i>CL SCM</i>	430,758 to 531,687
	<i>Carotid</i>	463,499 to 934,858
	<i>Posterior Neck</i>	295,997 to 536,123
	<i>IL Salivary gland</i>	592,680 to 919,363
	<i>CL Salivary gland</i>	378,219 to 817,097
5	<i>Tumour</i>	472,078 to 528,834
	<i>Necrosis</i>	295,921 to 332,470
	<i>CL SCM</i>	235,522 to 365,885

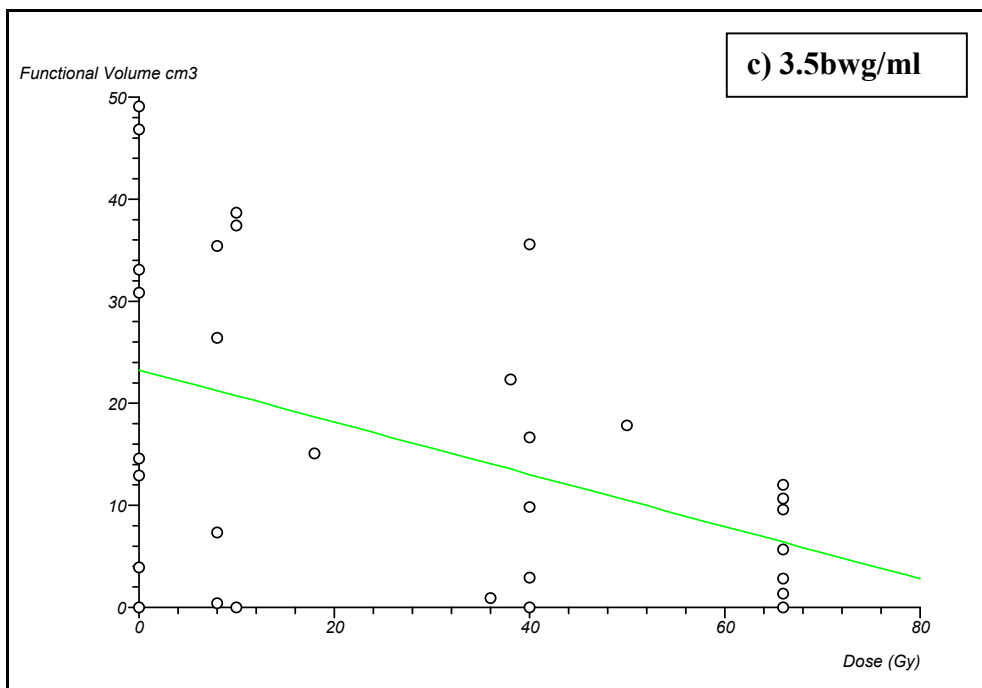
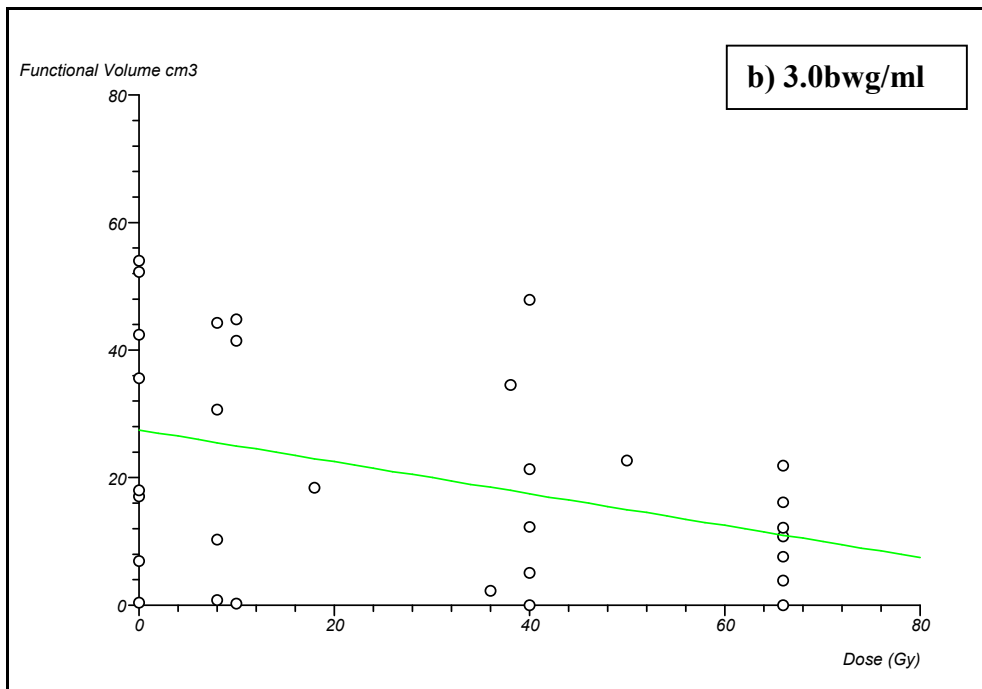
	<i>Carotid</i>	350,185 to 390,944
	<i>Posterior Neck</i>	218,572 to 488,606
	<i>IL Salivary gland</i>	383,724 to 384,385
	<i>CL Salivary gland</i>	293,257 to 449,352
10	<i>Tumour</i>	342,589 to 394,509
	<i>Necrosis</i>	213,397 to 29,3397
	<i>CL SCM</i>	188,005 to 281608
	<i>Carotid</i>	277,875 to 290,935
	<i>Posterior Neck</i>	213,776 to 332,624
	<i>IL Salivary gland</i>	237,757 to 326,410
	<i>CL Salivary gland</i>	272,016 to 375,880
60	<i>Tumour</i>	228,291 to 408,949
	<i>Necrosis</i>	95,034 to 102,034
	<i>CL SCM</i>	136,355 to 201,087
	<i>Carotid</i>	148,684 to 202,467
	<i>Posterior Neck</i>	139,776 to 200,642
	<i>IL Salivary gland</i>	192,535 to 240,687
	<i>CL Salivary gland</i>	191,850 to 238,621

Chapter 4

Figures 1a to c

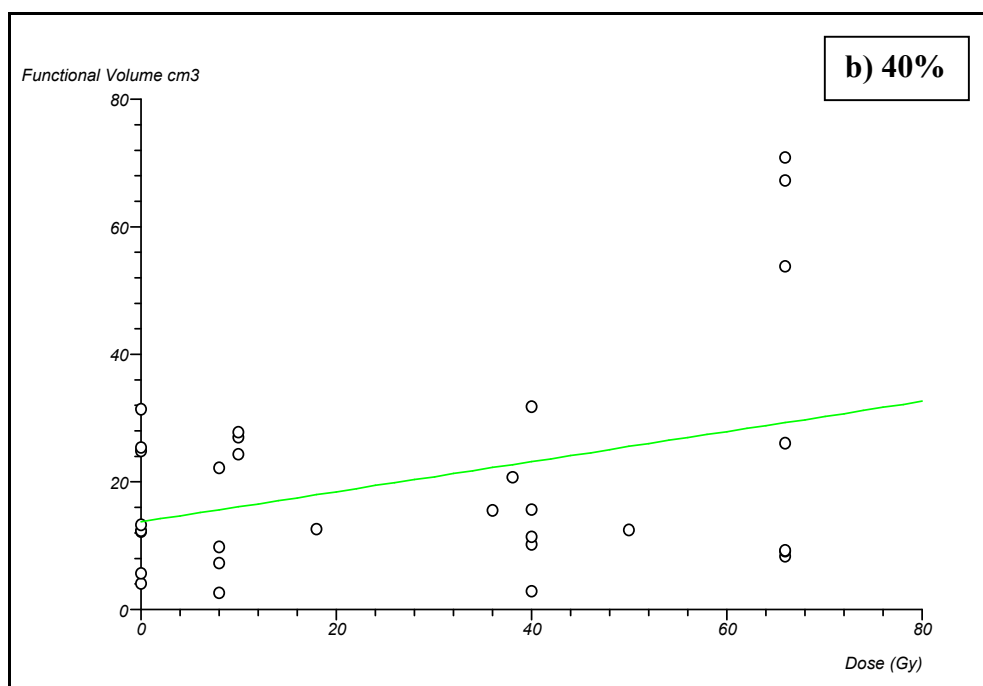
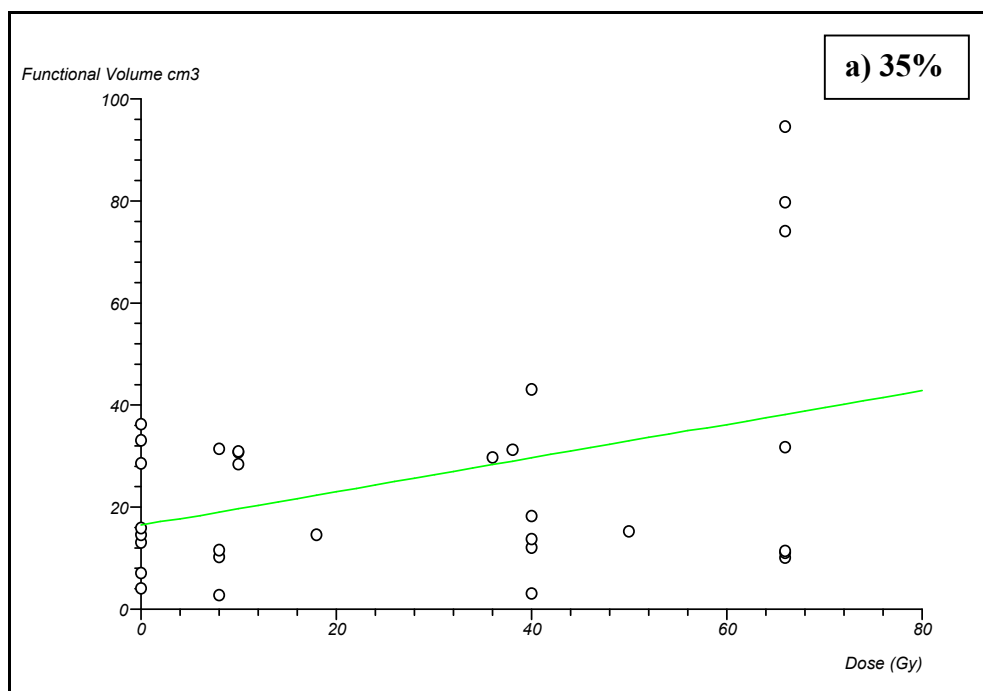
The negative correlation of the primary functional volume delineated by the SUV Cut Off thresholds of 2.5bwg/ml a), 3.0bwg/ml b), and 3.5bwg/ml c) and radiation dose





Figures 2a to d

The simple linear regression of the primary functional volume delineated by the percentage of the SUVmax thresholds of 35% a), 40% b), 45% c, and 50% d) and radiation dose



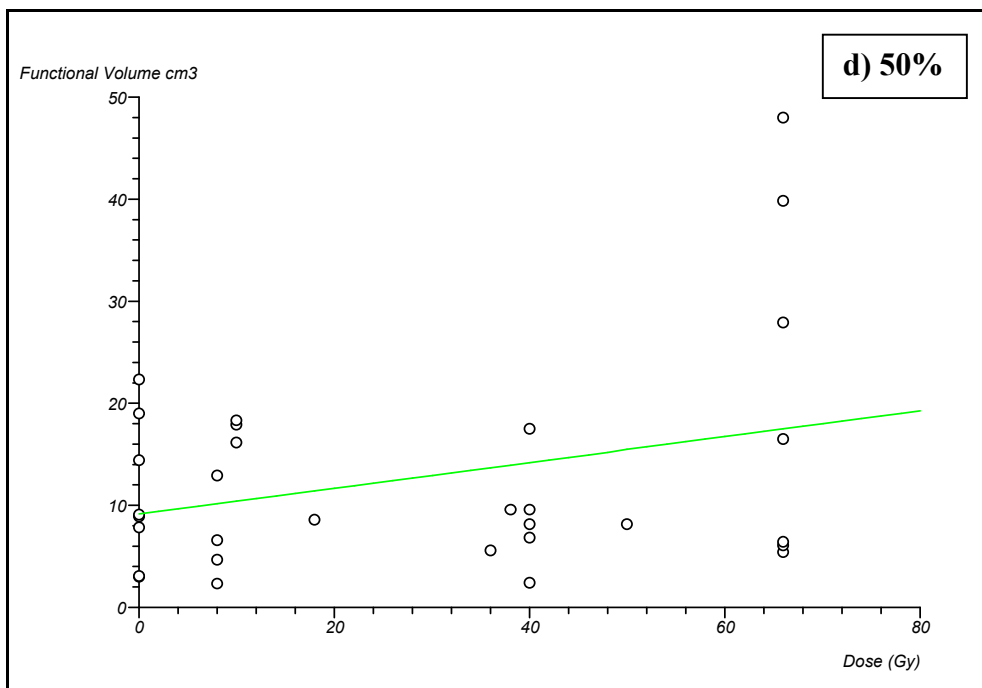
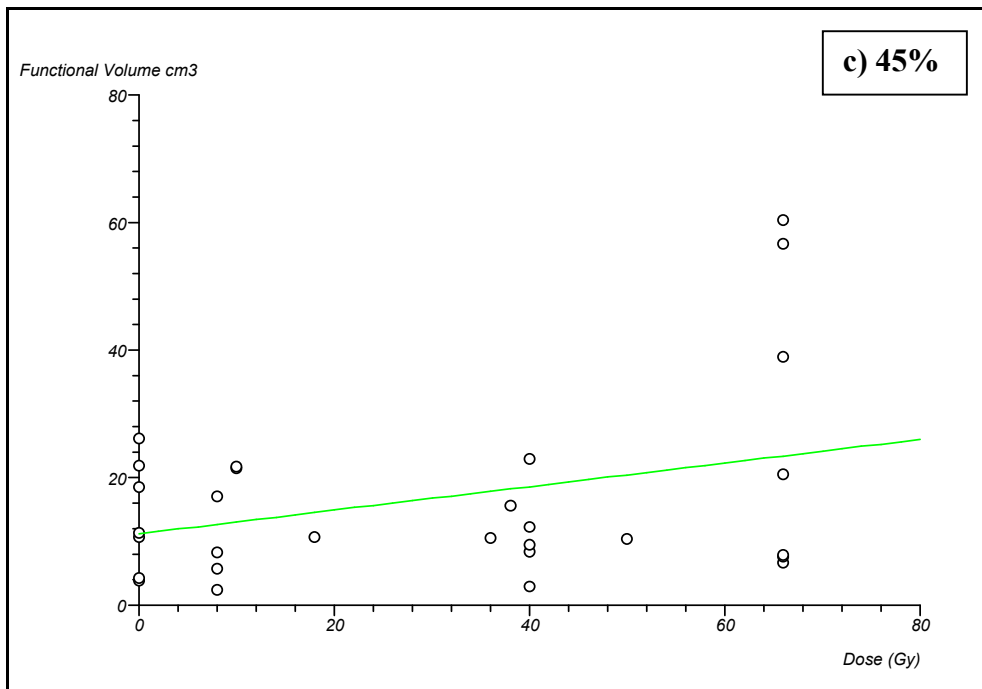
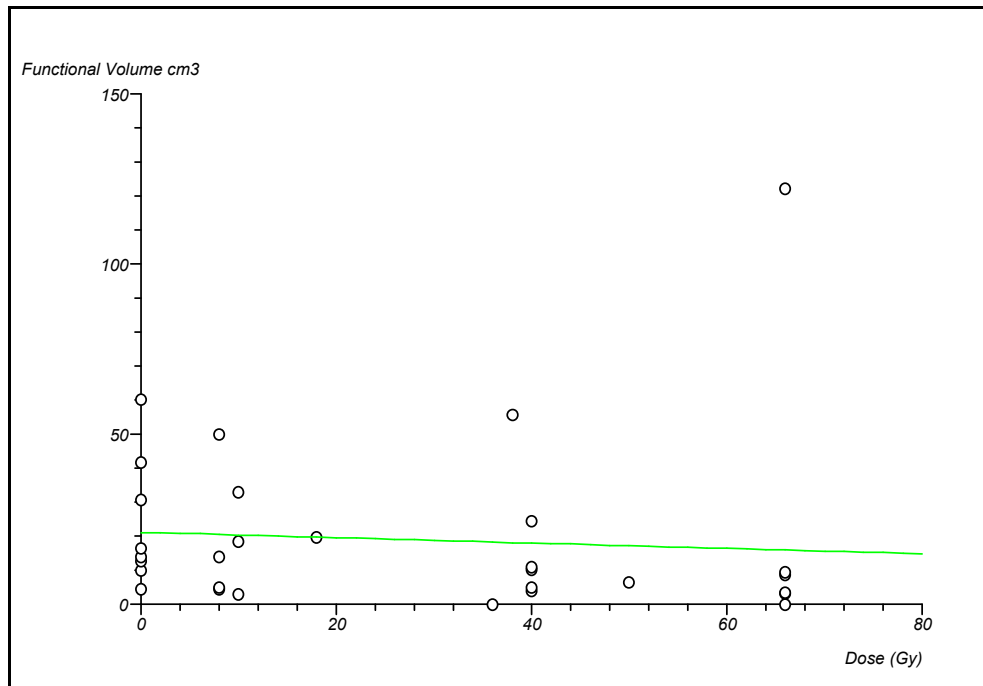


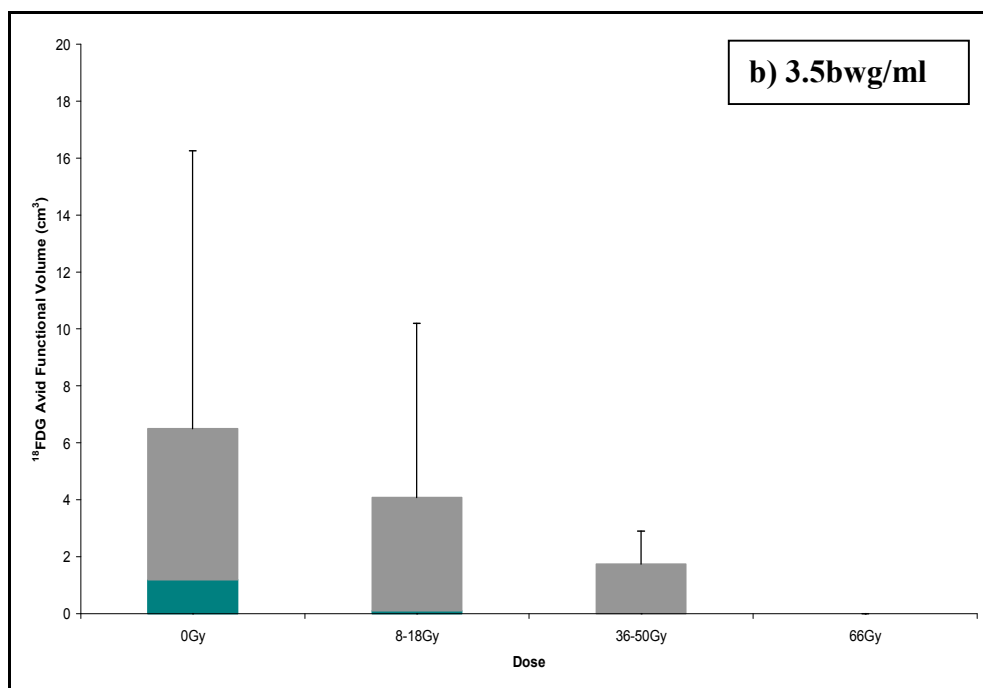
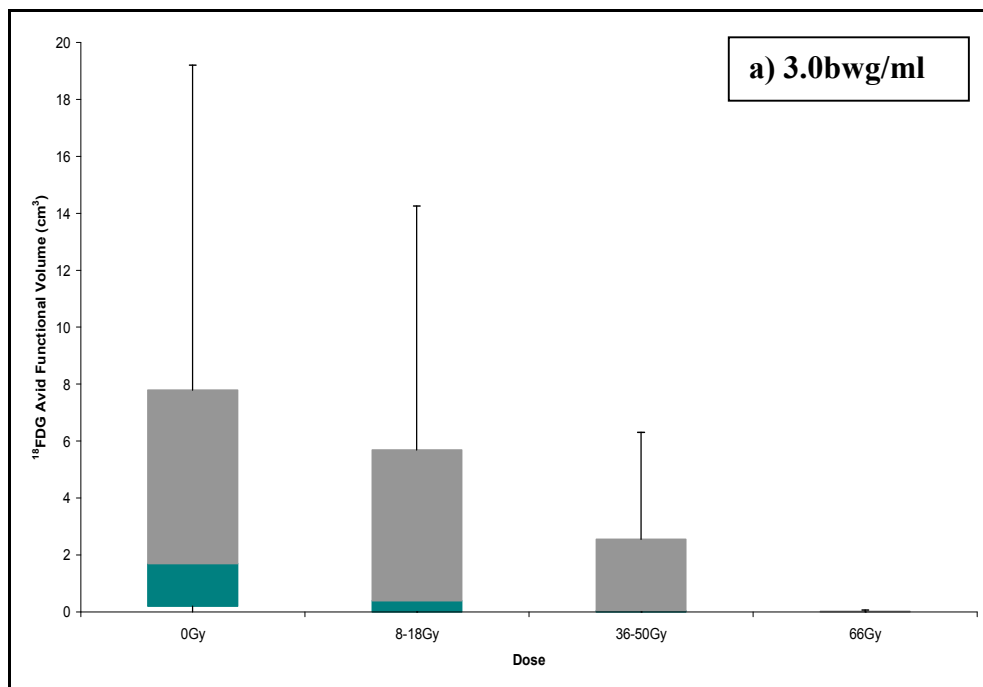
Figure 3

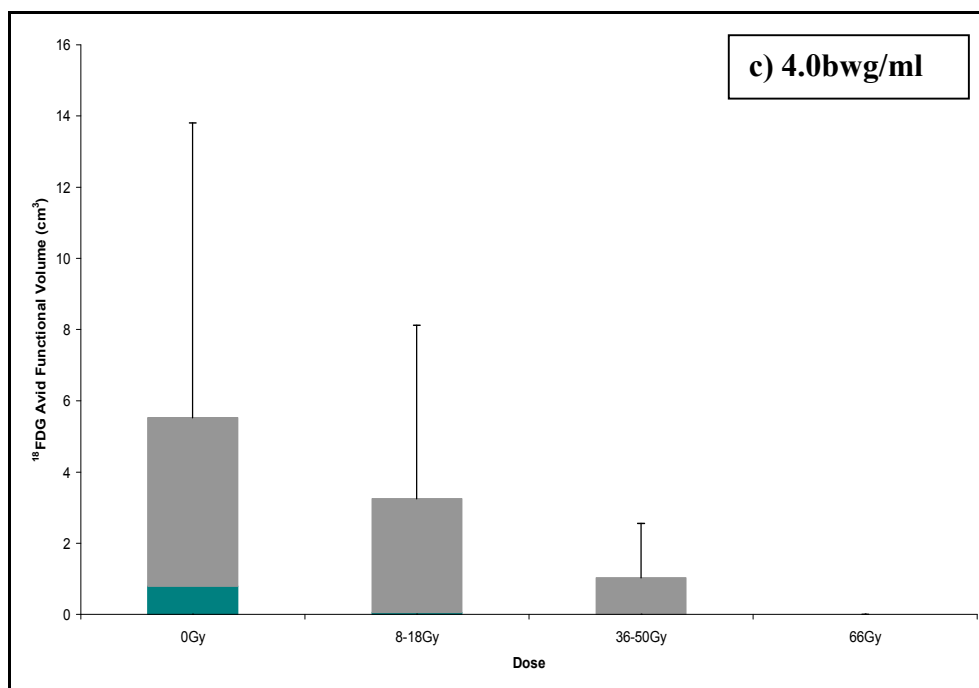
The simple linear regression relationship between the delivered radiation dose and the primary functional volume delineated by the individualised adaptive threshold



Figures 4a to c

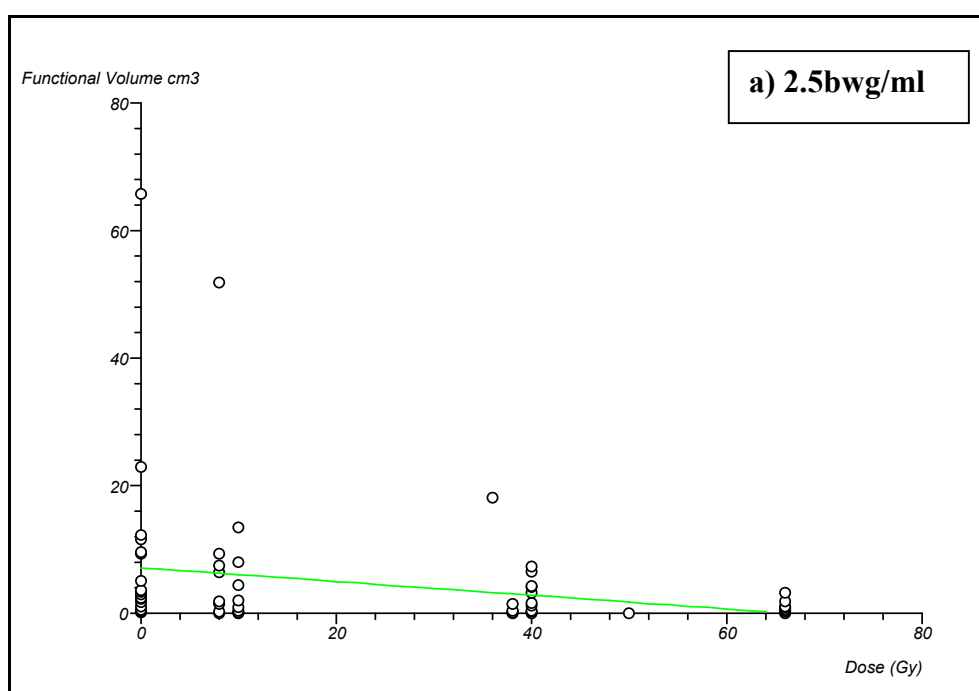
The box and whisker plots of the lymph node functional volumes delineated by the SUV Cut Off thresholds of 3.0bwg/ml a), 3.5bwg/m b), and 4.0bwg/ml c)

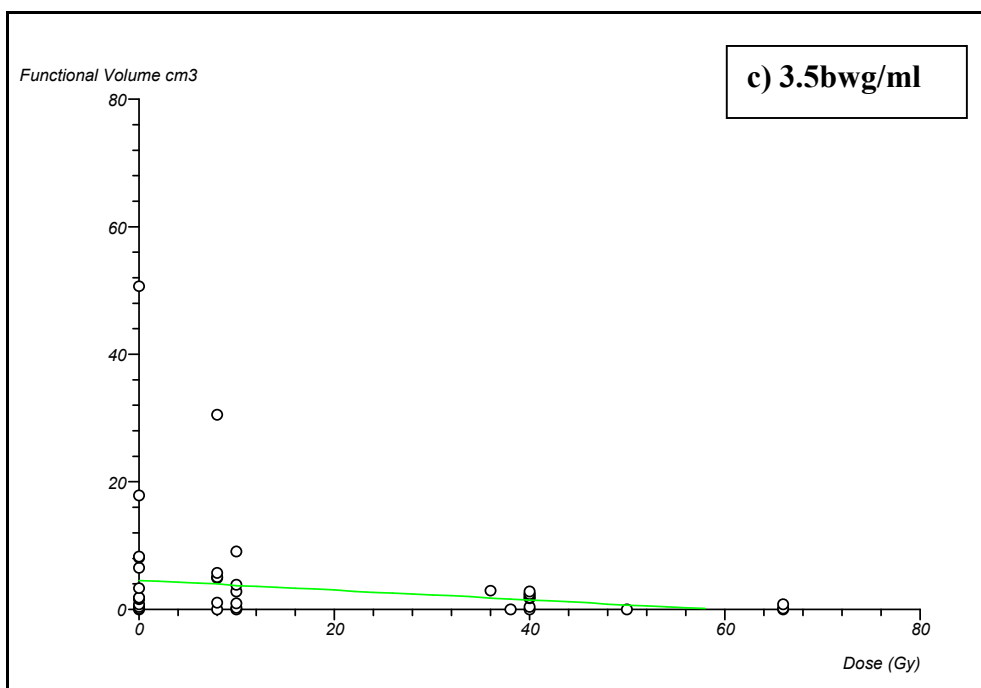
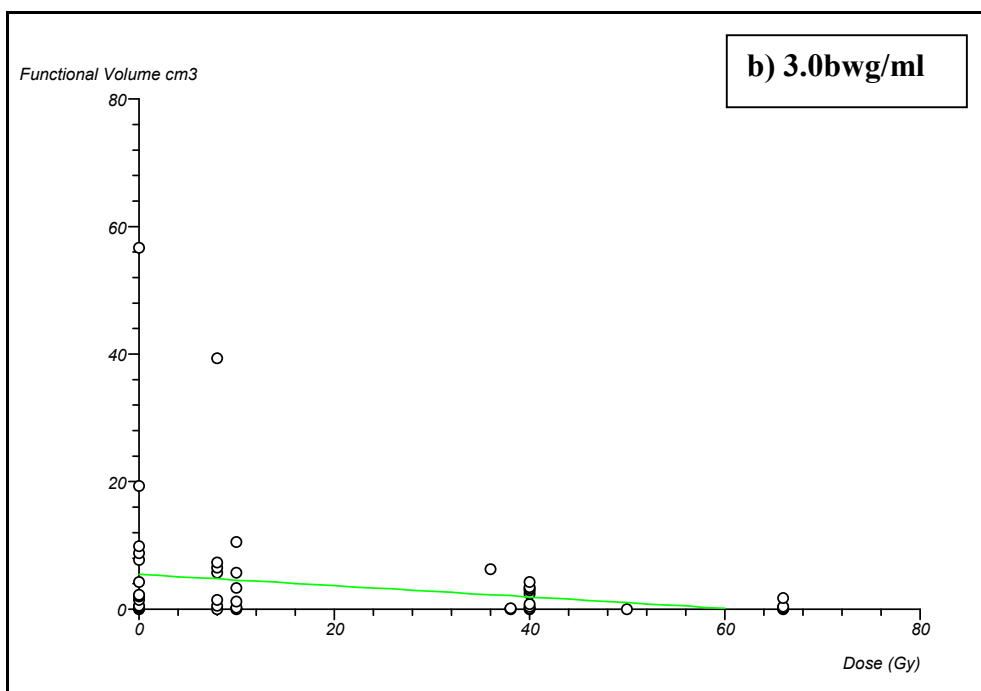


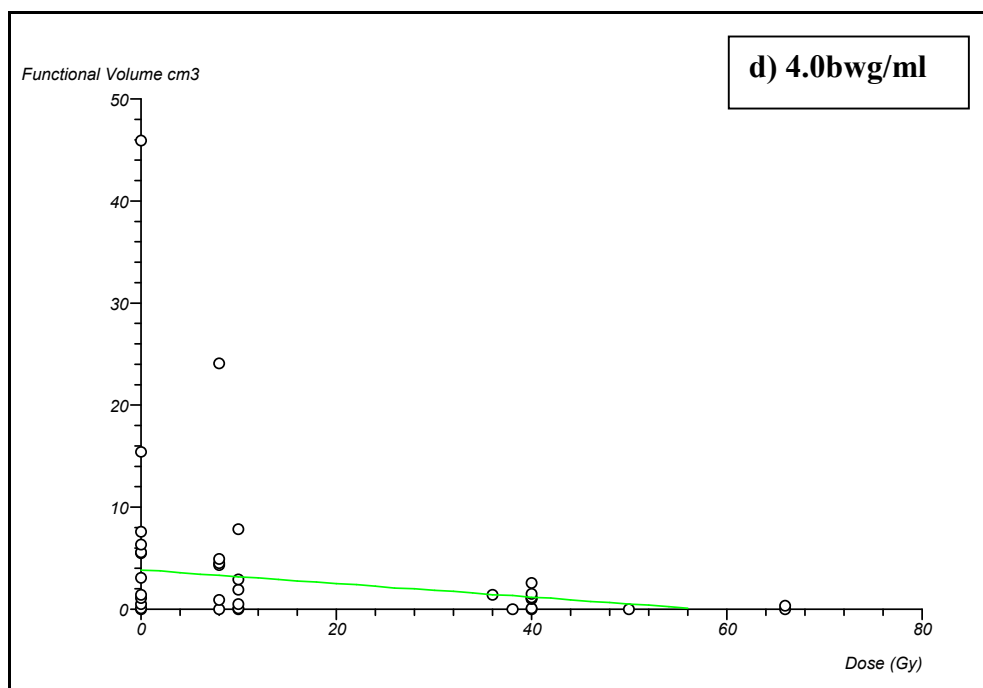


Figures 5a to c

The negative correlation of the lymph node functional volume delineated by the SUV Cut Off thresholds of 2.5bwg/ml a), 3.0bwg/ml b), and 3.5bwg/ml c), and 4.0bwg/ml d) and radiation dose

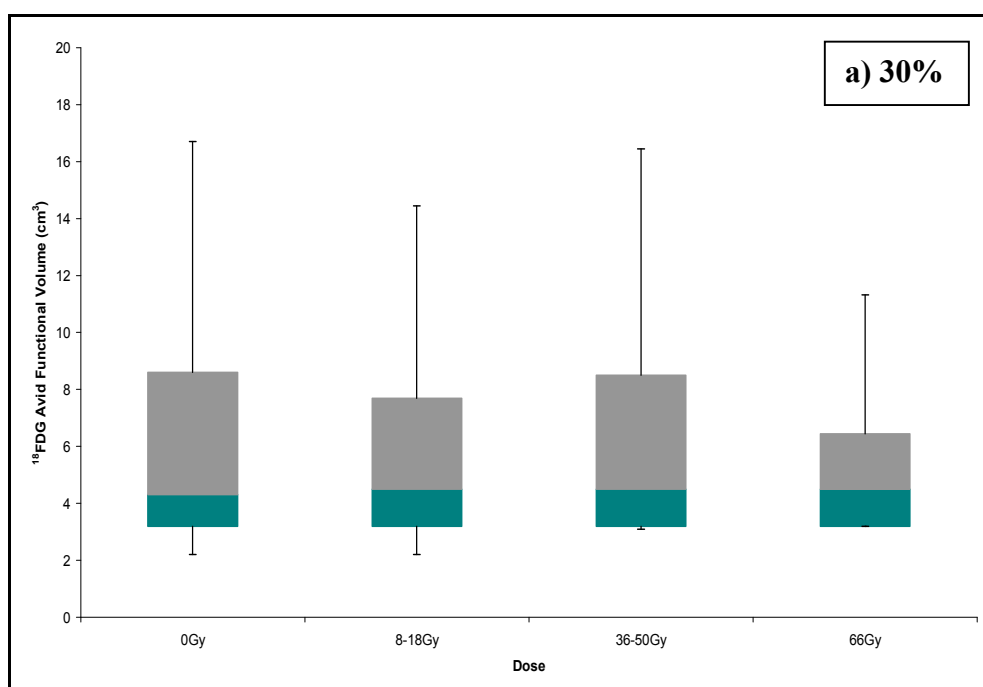


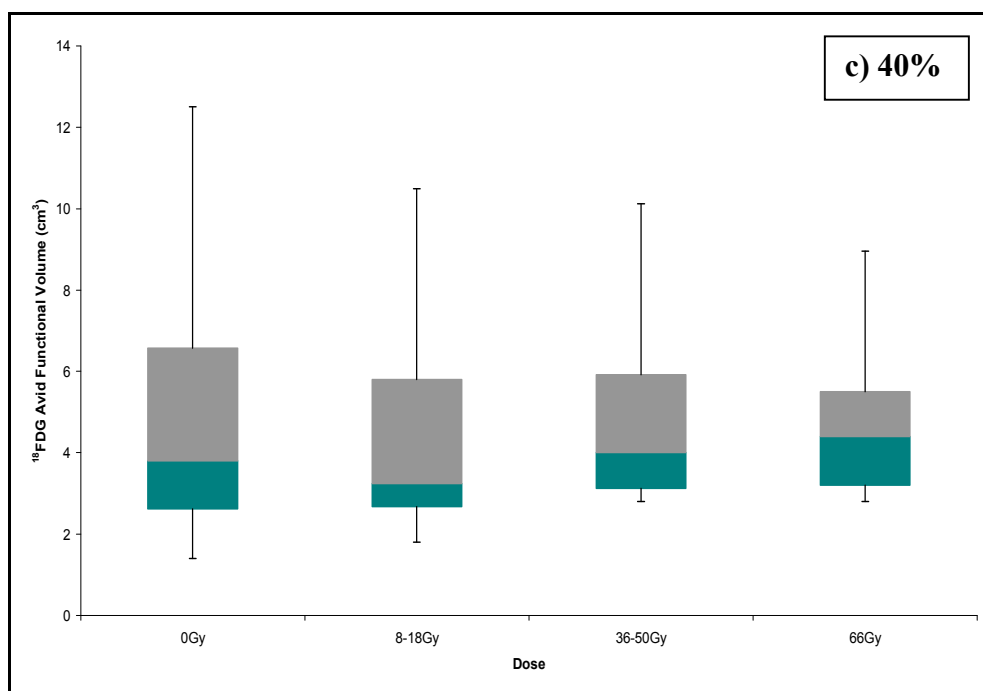
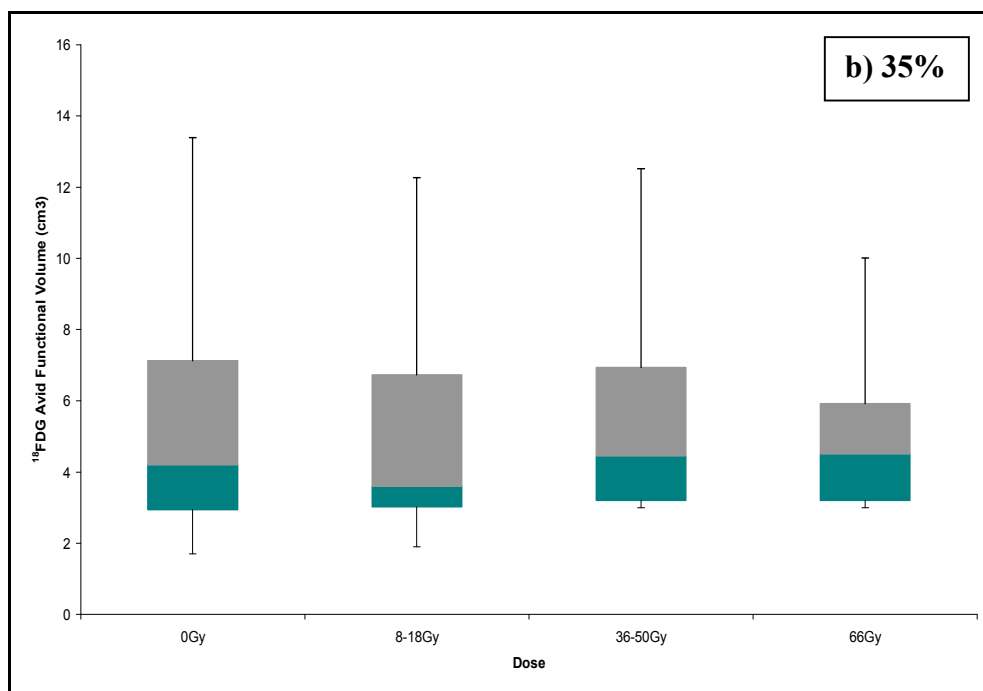


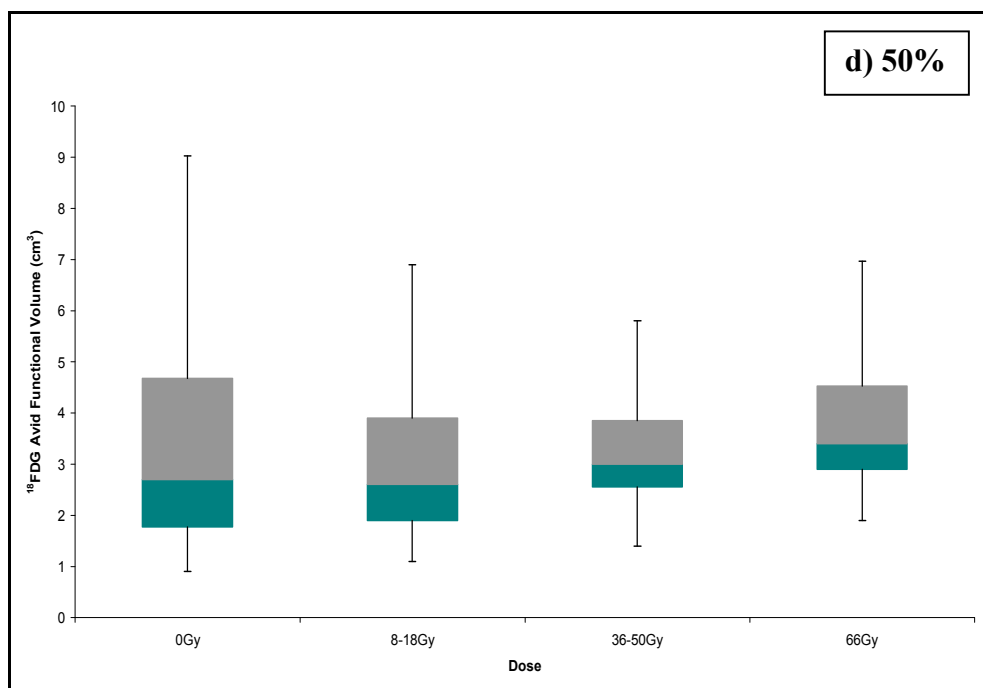


Figures 6a to d

The box and whisker plots of the lymph node functional volumes delineated by the percentage thresholds of the SUVmax 30% a), 35% b), 40% c), and 50% d)

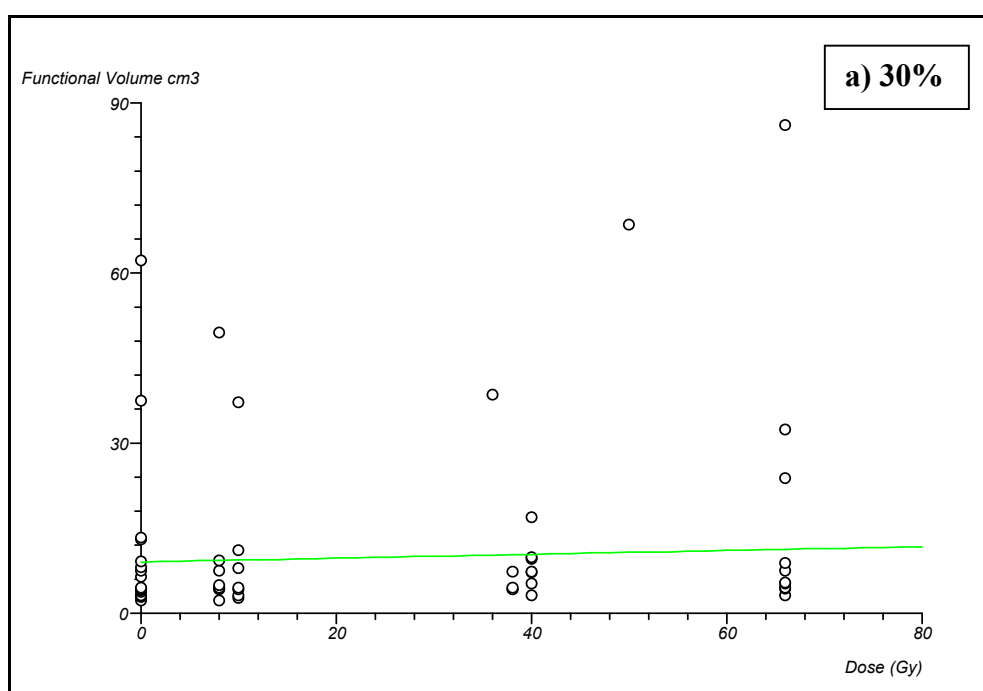


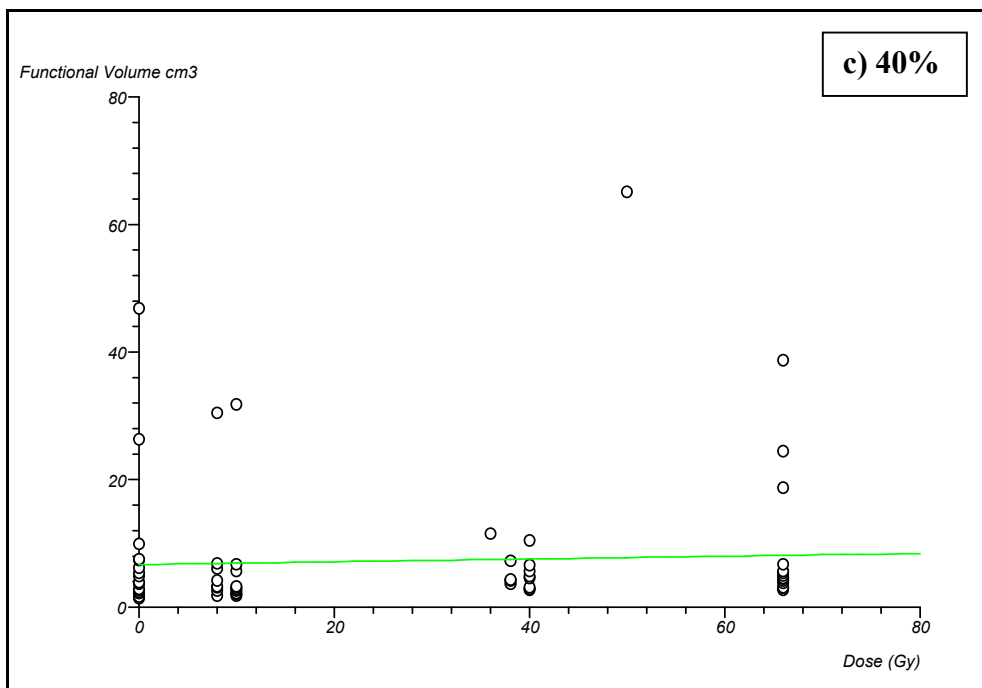
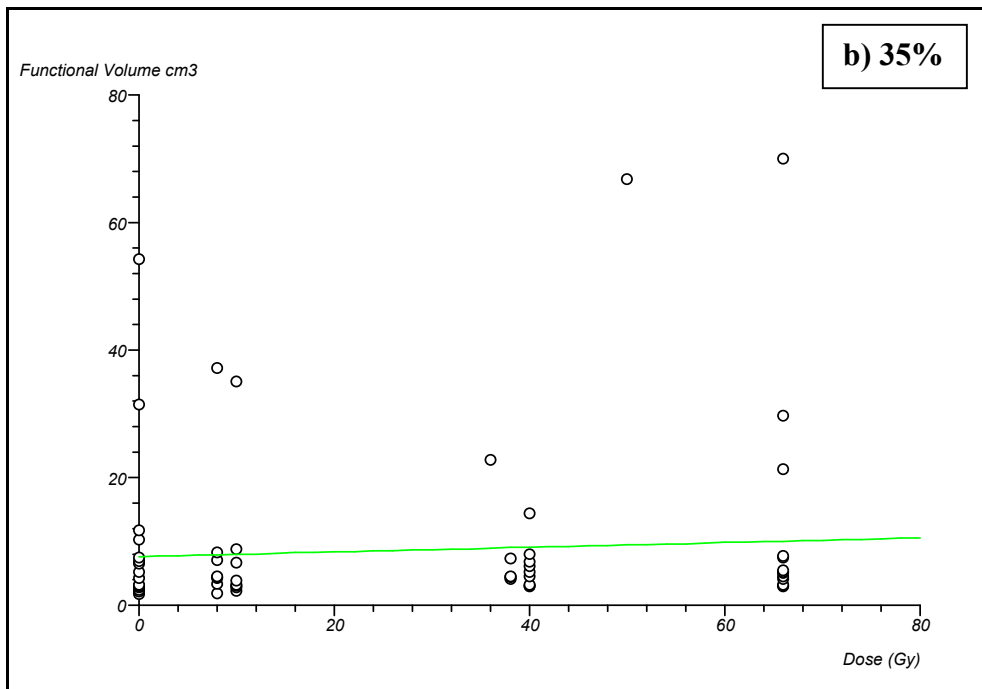




Figures 7a to d

The simple linear regression of the lymph node functional volume delineated by the percentage of the SUVmax thresholds of 30% a), 35% b), 40% c), 45% d), and 50% e)





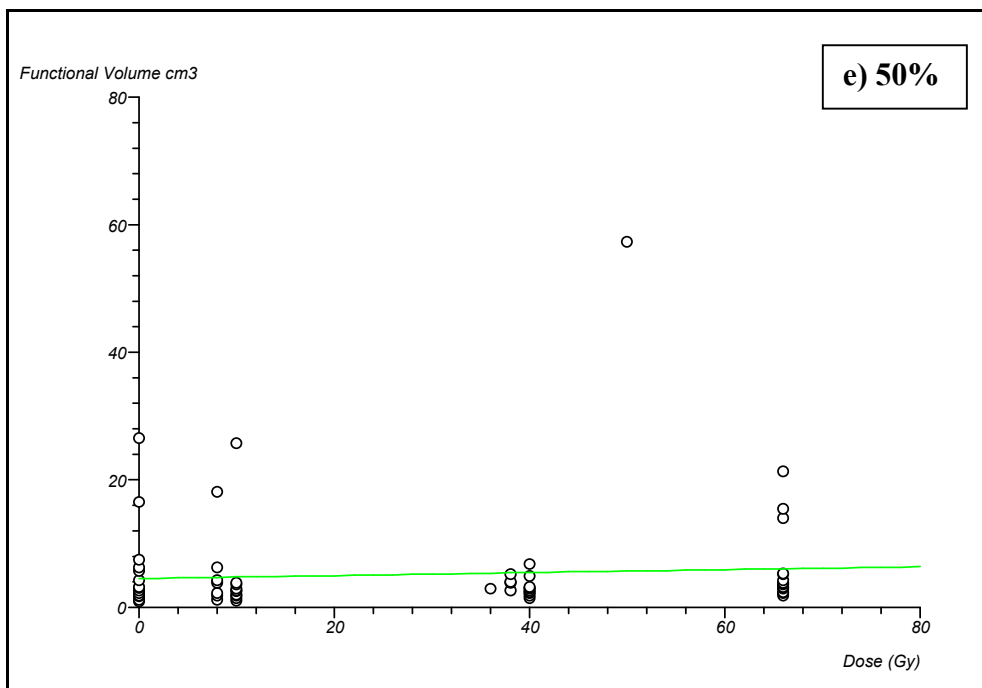
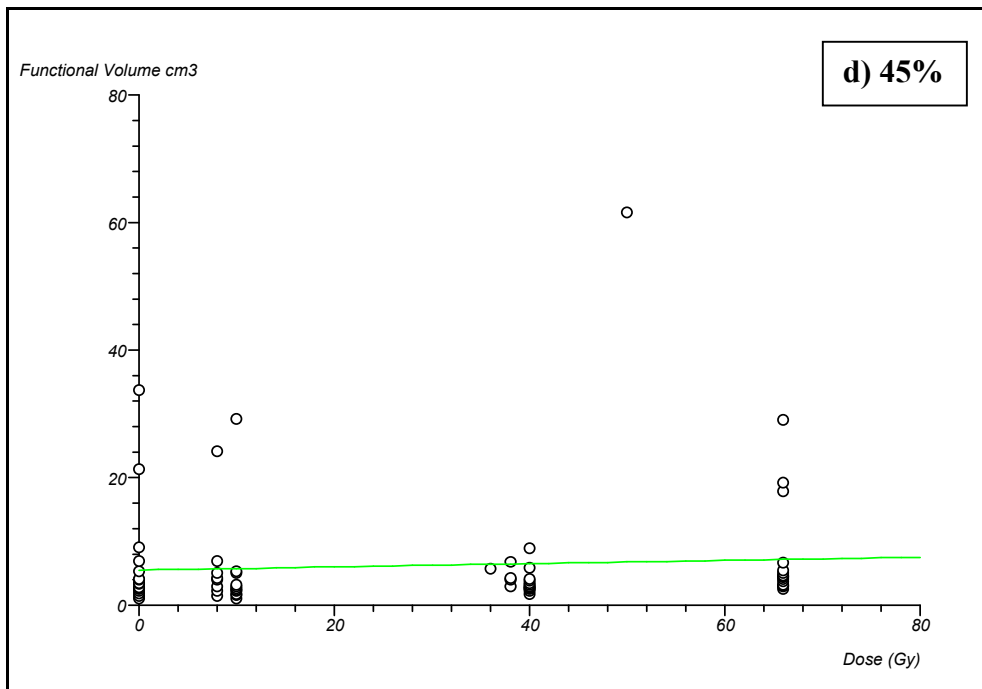
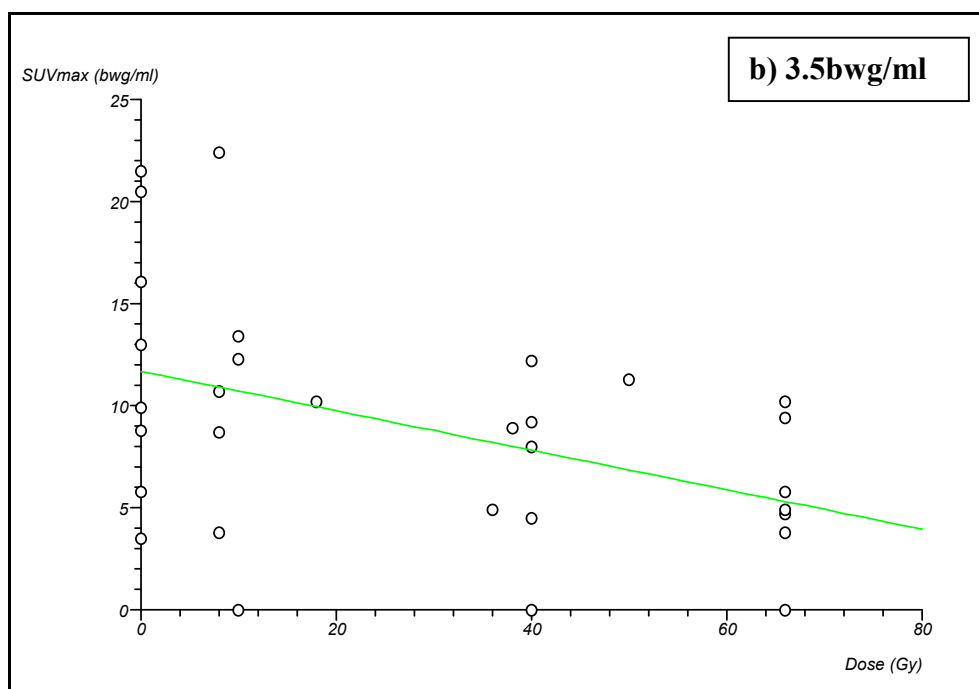
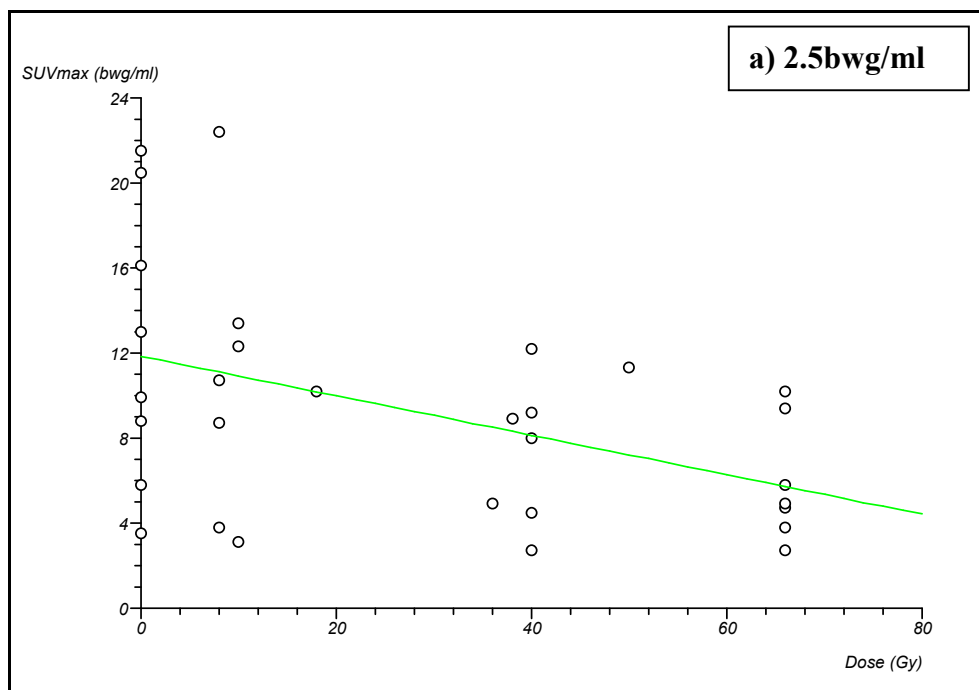


Figure 8 a to c

The negative correlation between SUVmax within the primary functional volume delineated by the SUV Cut Off thresholds of 2.5bwg/ml a), 3.5bwg/ml b), and 4.0bwg/ml c) and the radiation dose



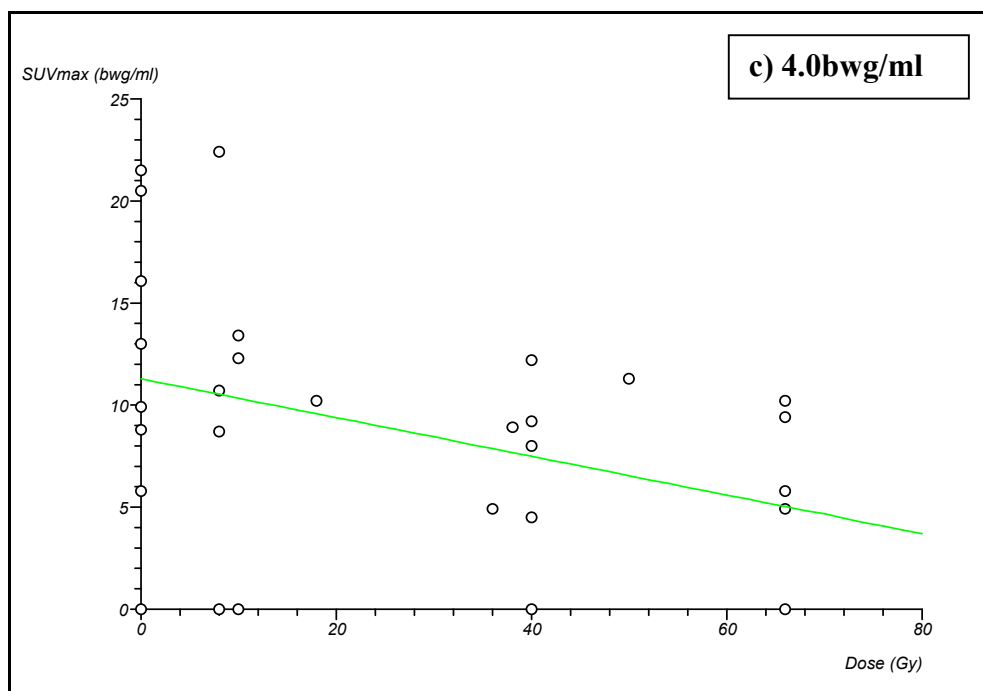
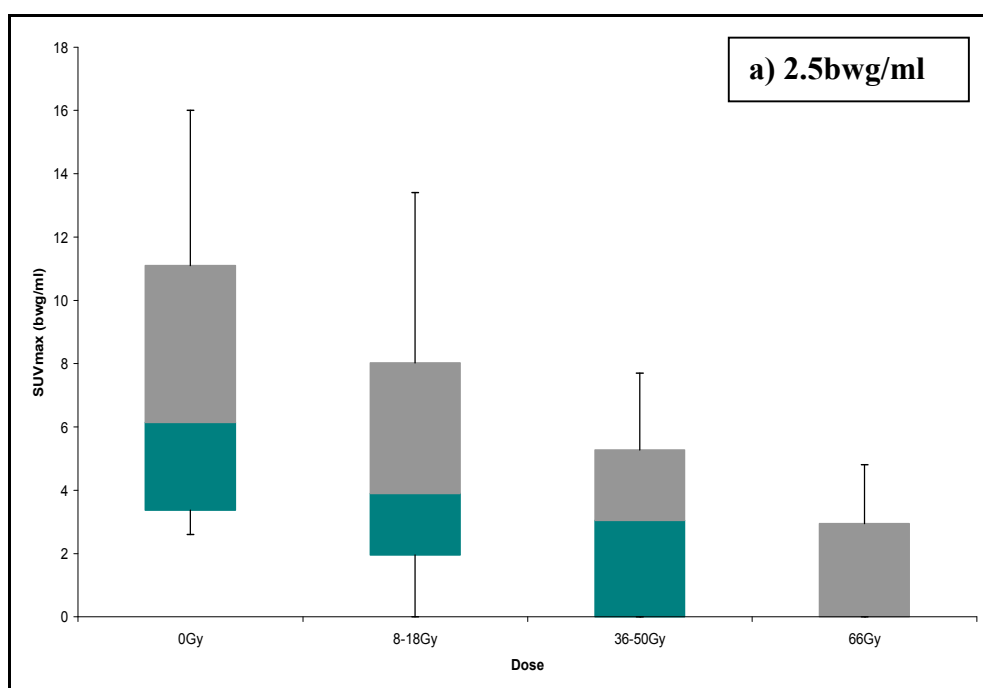


Figure 9a to c

The box and whisker plots of the SUVmax within the lymph node functional volumes delineated by the SUV Cut Off thresholds of 2.5bwg/ml a), 3.5bwg/ml b), and 4.0bwg/ml c)



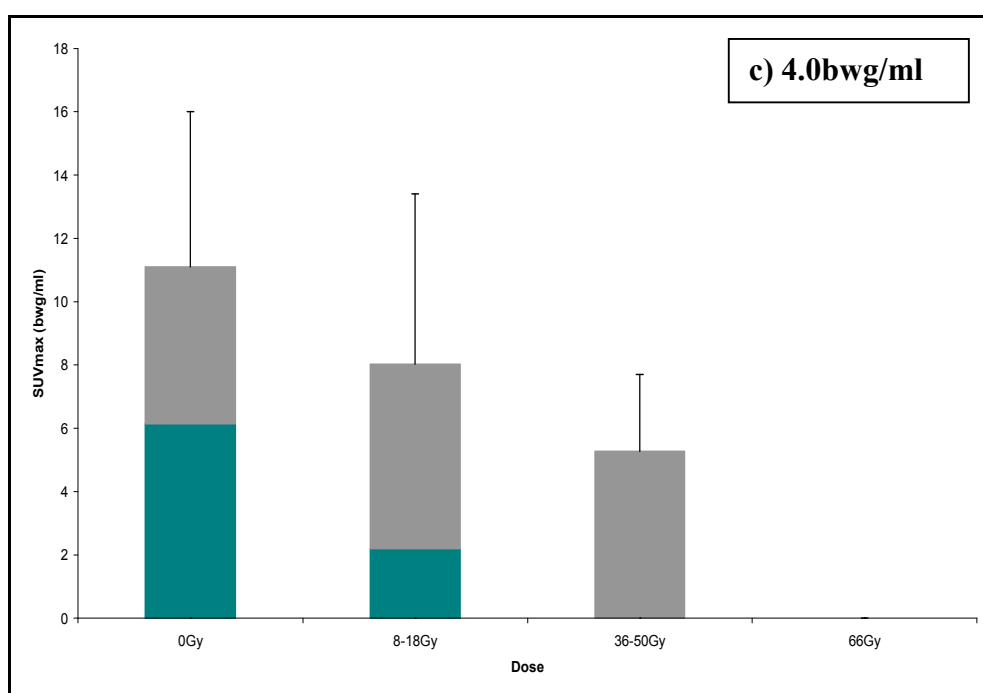
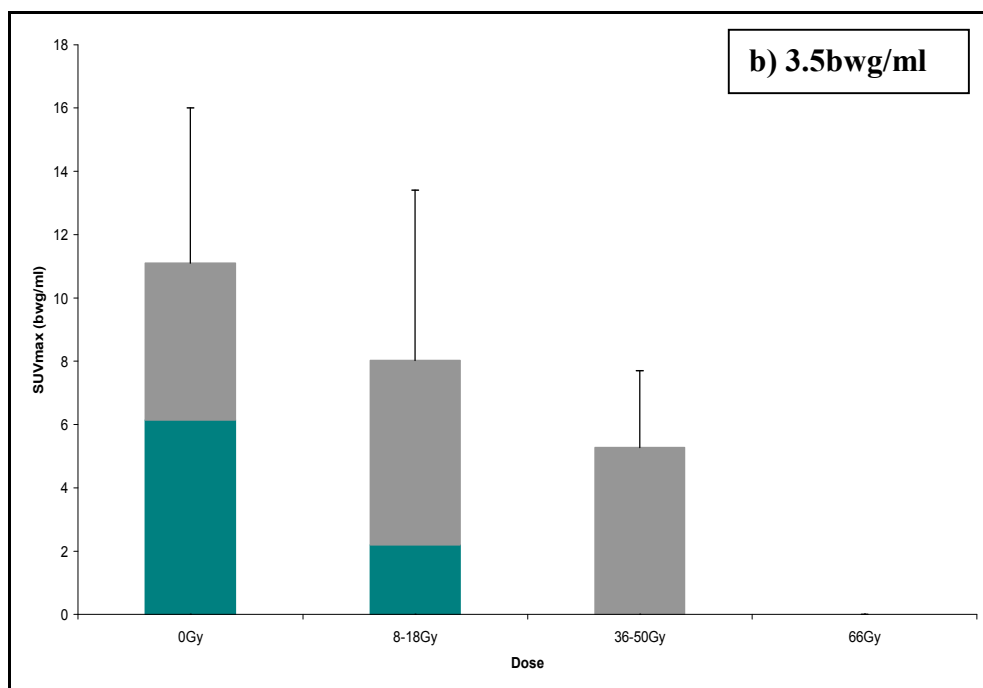
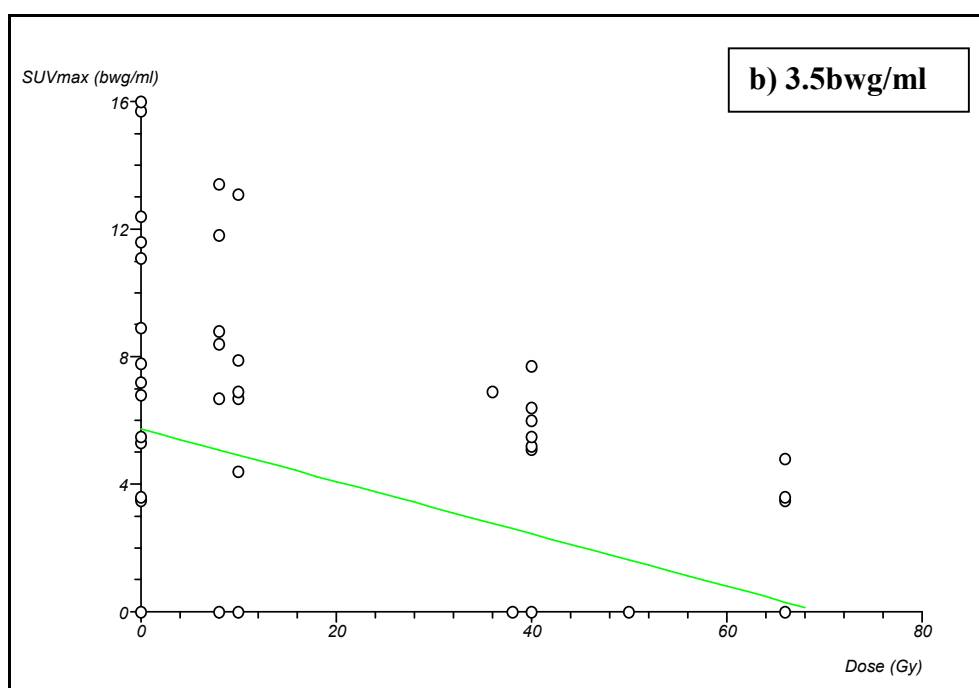
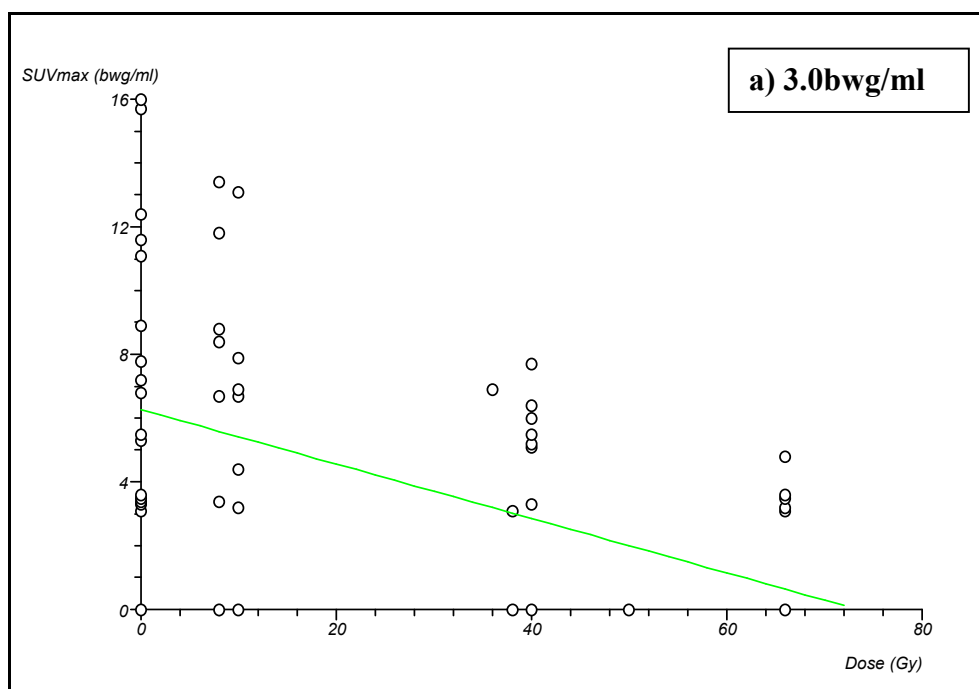


Figure 10a to c

The negative correlation between the lymph node functional volume delineated by the SUV Cut Off thresholds of 3.0bwg/ml a), 3.5bwg/ml b), and 4.0bwg/ml c) and radiation dose



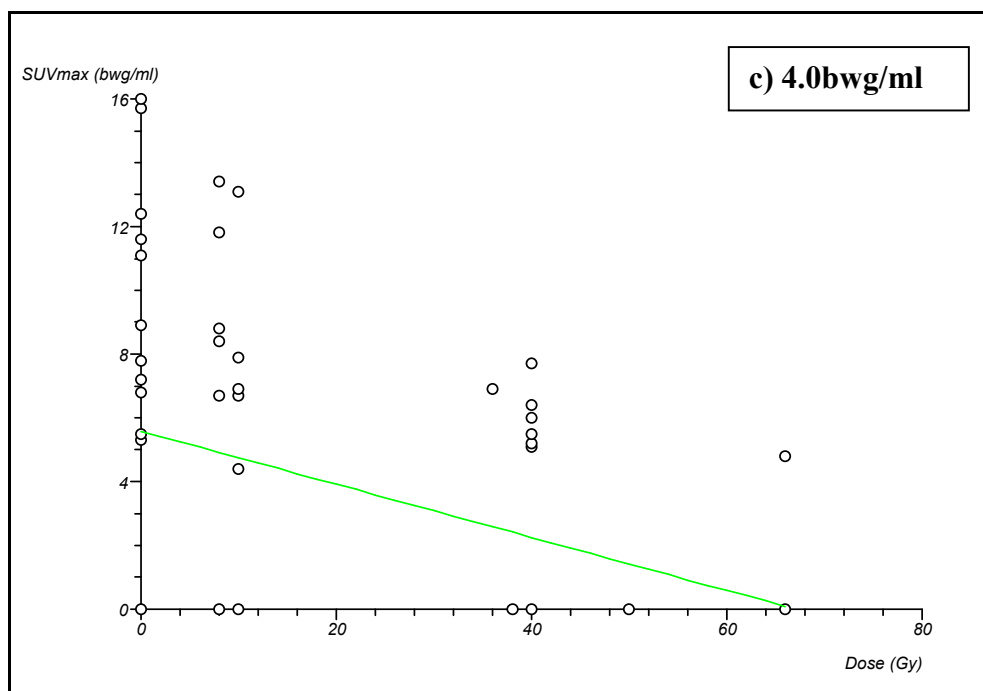


Figure 11

The negative correlation between the SUVmax within the lymph node functional volume delineated by the percentage of the SUVmax and the radiation dose

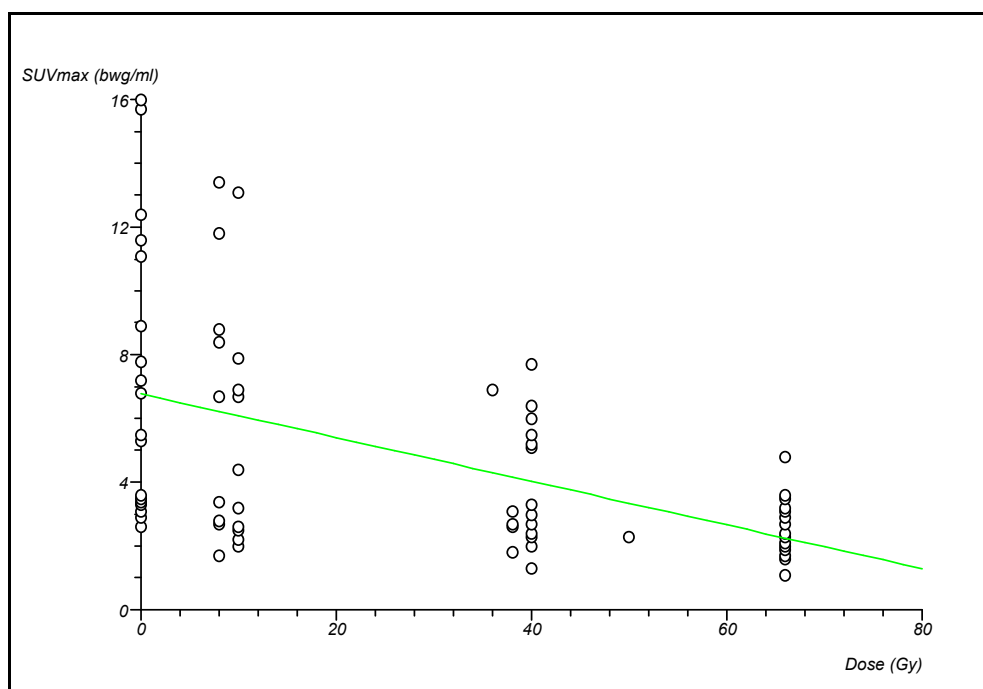


Figure 12

The SUVmax within the lymph node functional volume delineated by the individualised adaptive threshold

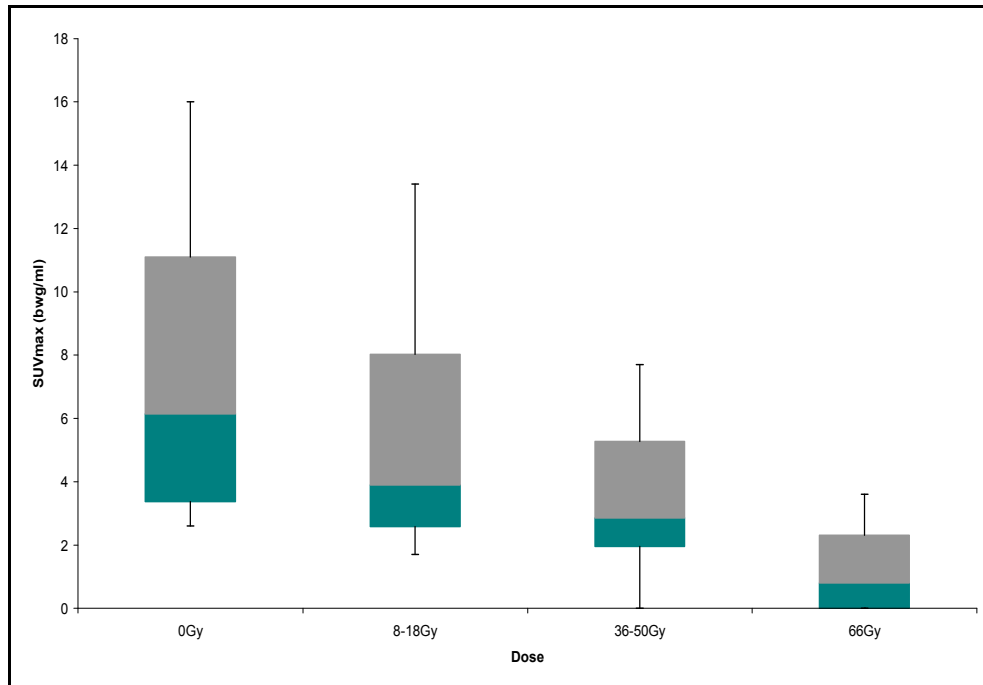


Figure 13

Simple linear regression between the SUVmax within the lymph node functional volume delineated by the individualised adaptive threshold and the radiation dose

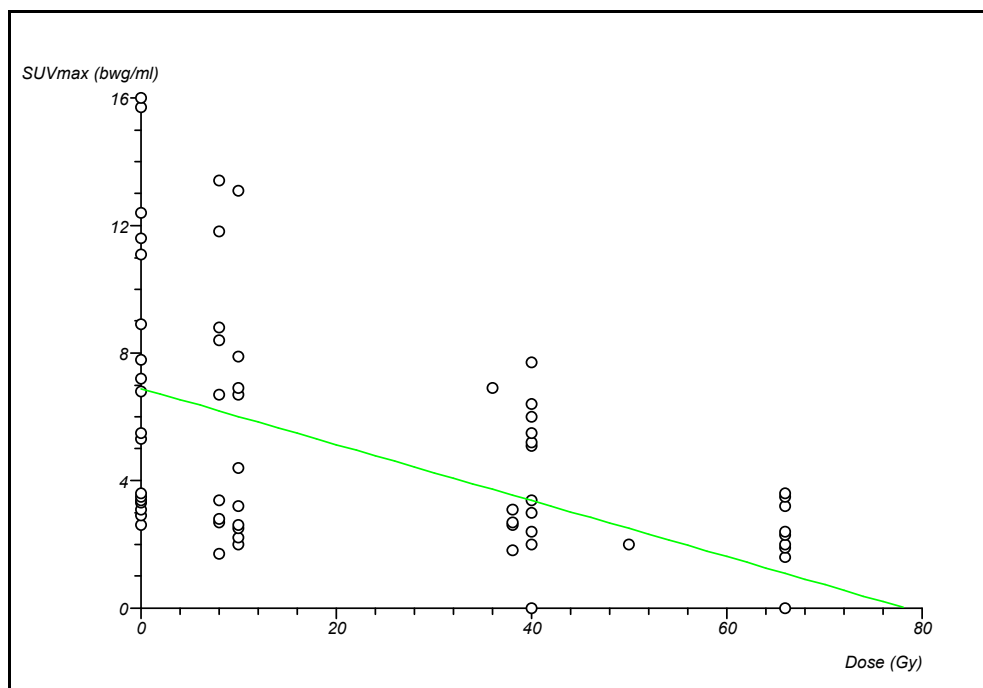
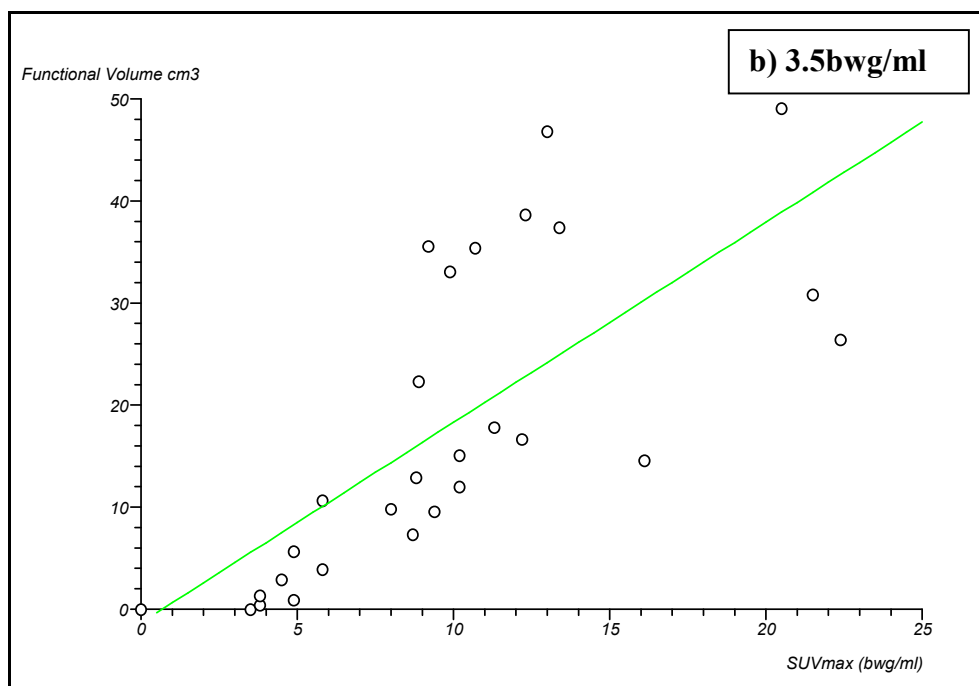
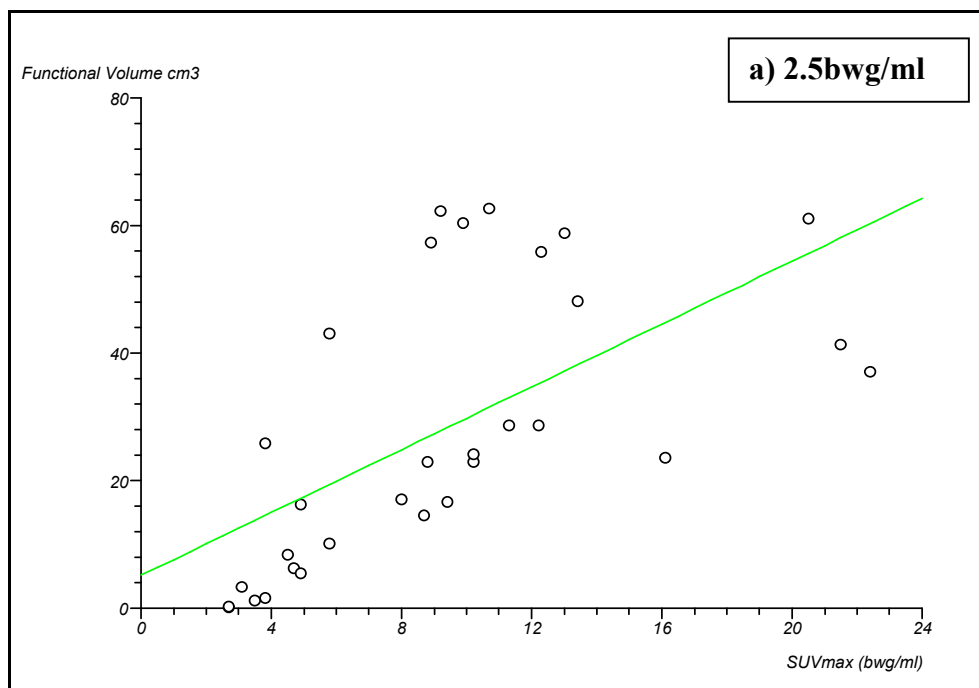


Figure 14 a to c

The positive correlation between the primary functional volume delineated by the SUV Cut Off thresholds of 2.5bwg/ml a), 3.5bwg/ml b), and 4.0bwg/ml c), and the SUVmax within the volume



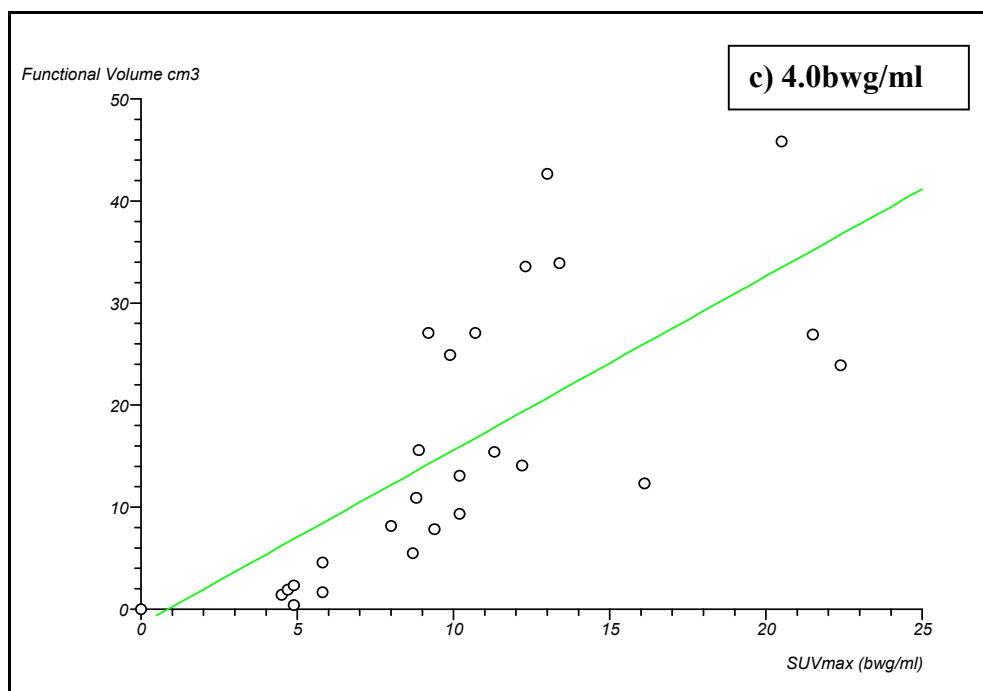
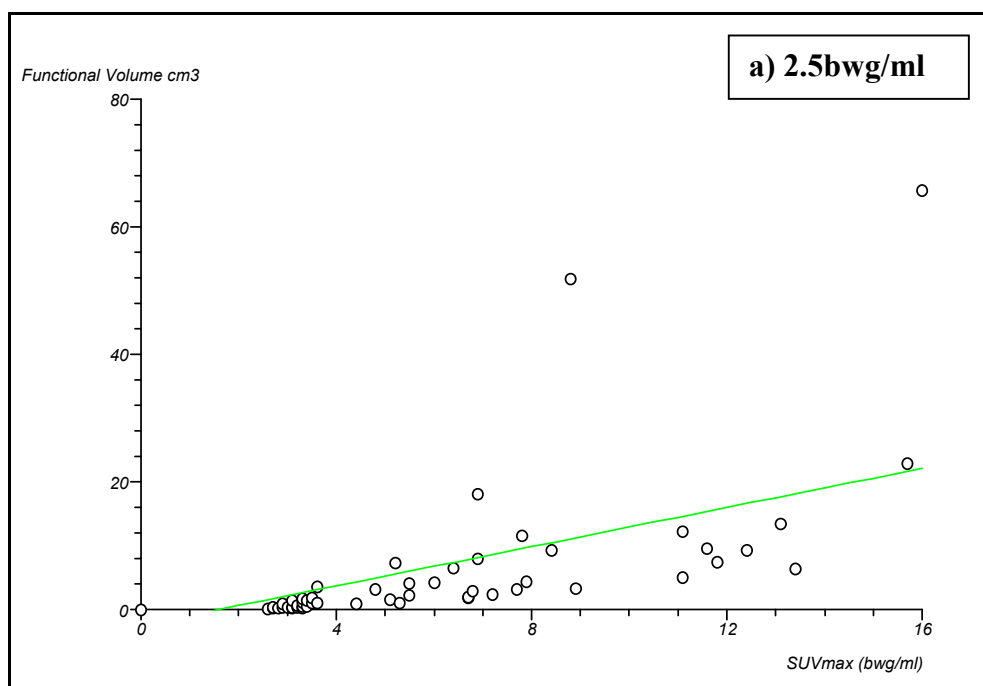
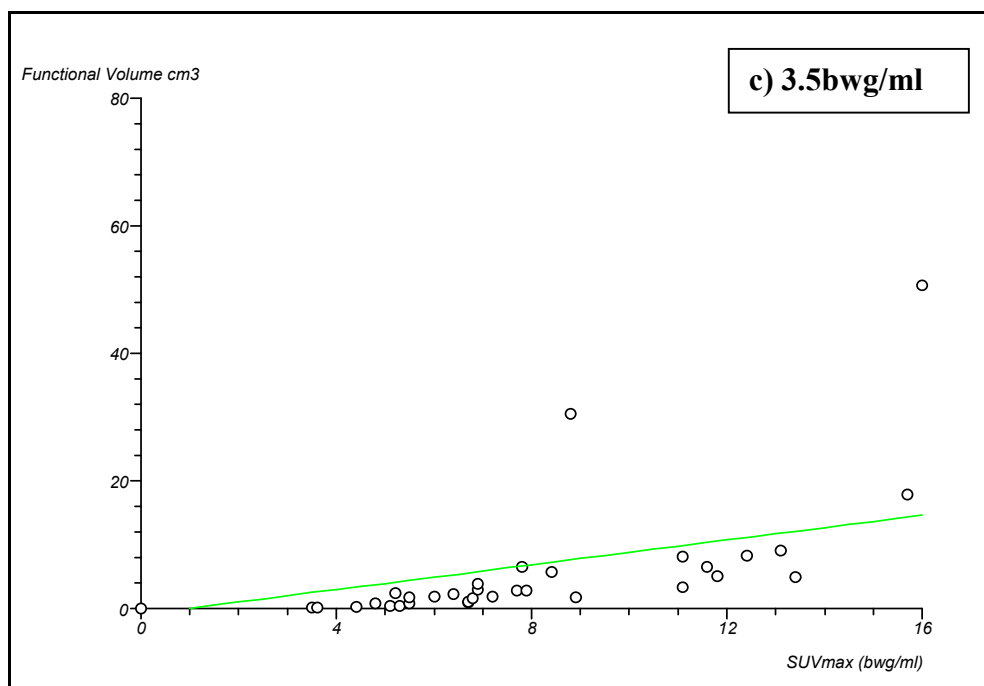
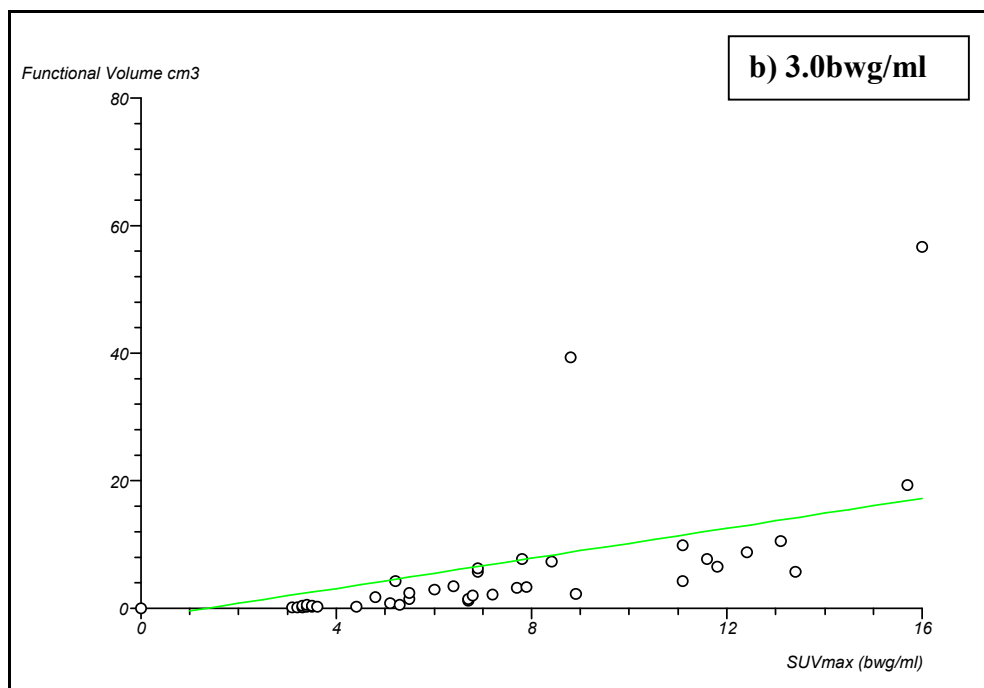
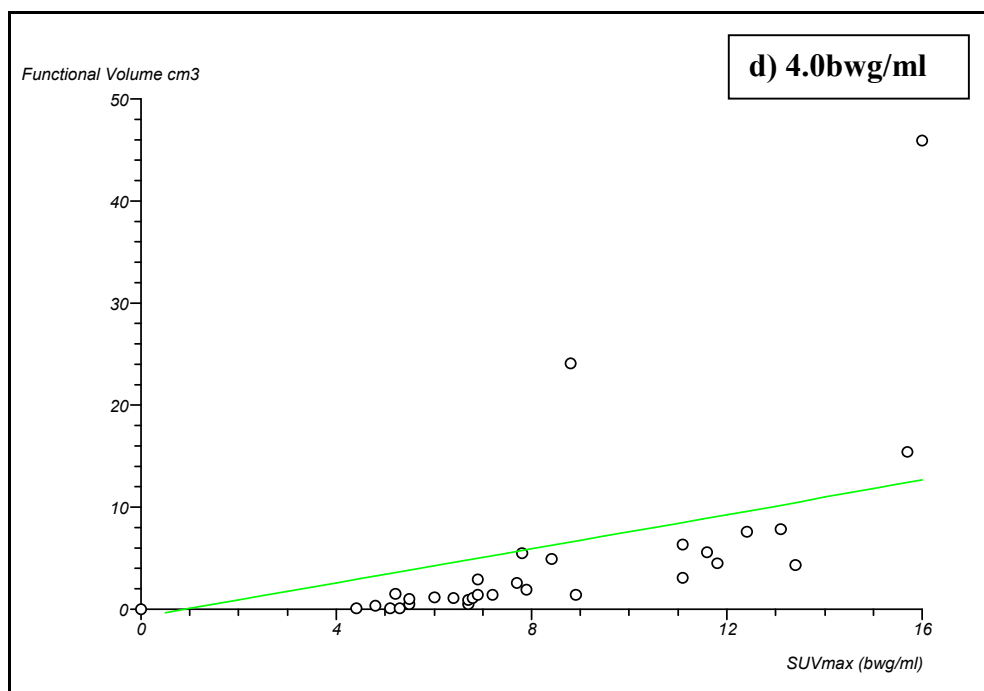


Figure 15 a to d

The positive correlation between the lymph node functional volume delineated by the SUV Cut Off thresholds of 2.5bwg/ml a), 3.0bwg/ml b), 3.5bwg/ml c), and 4.0bwg/ml d), and the SUVmax within the volume



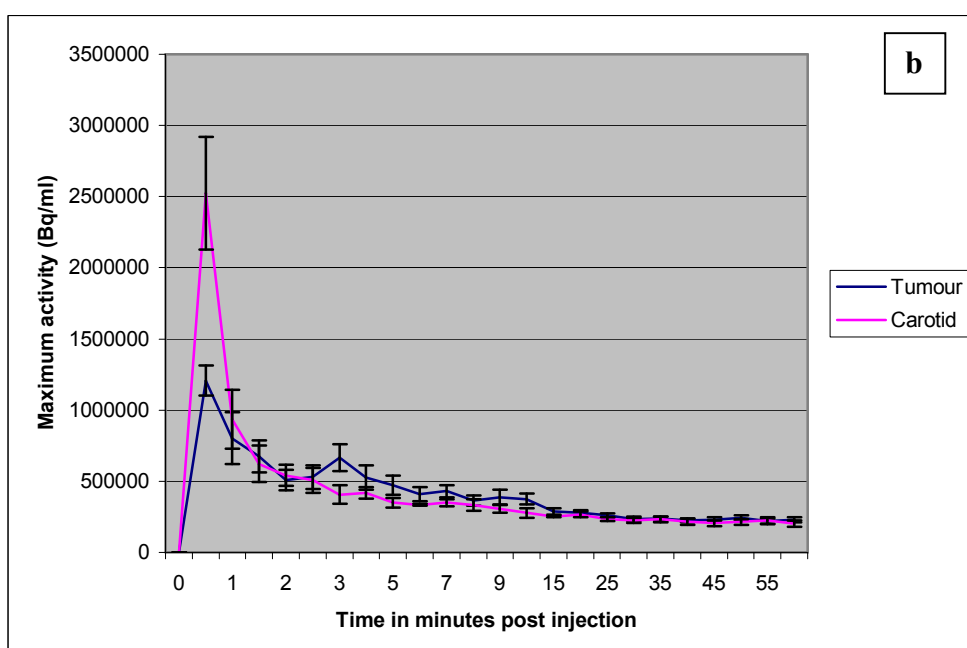
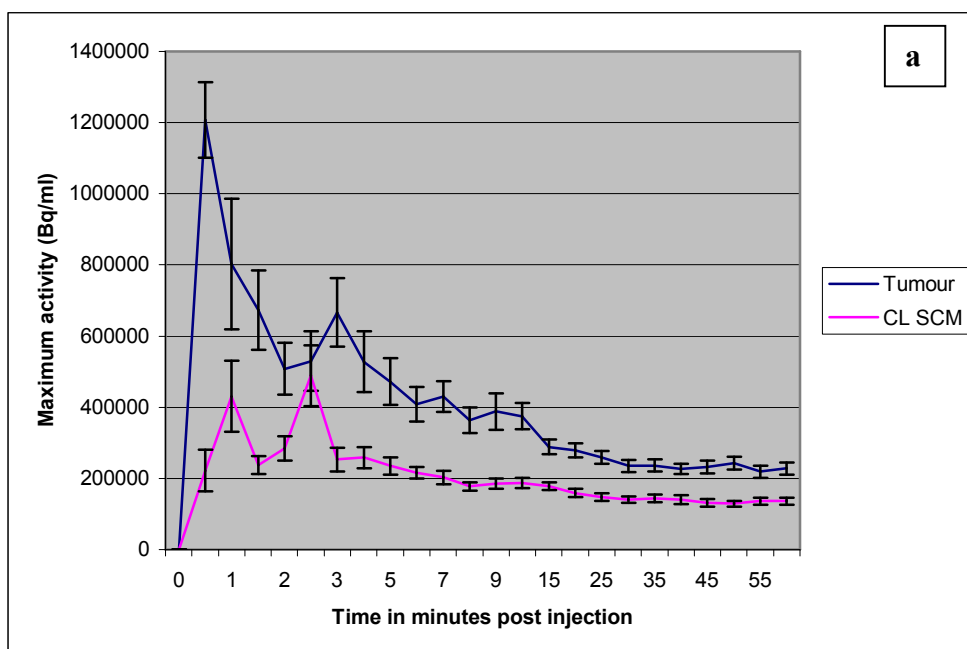




Chapter 5

Figure 16 a to d

The uptake of ^{64}Cu -ATSM within the tumour in patient 4 compared to other regions of interest. Contra-lateral SCM a), carotid artery b), posterior neck c), and salivary glands d)



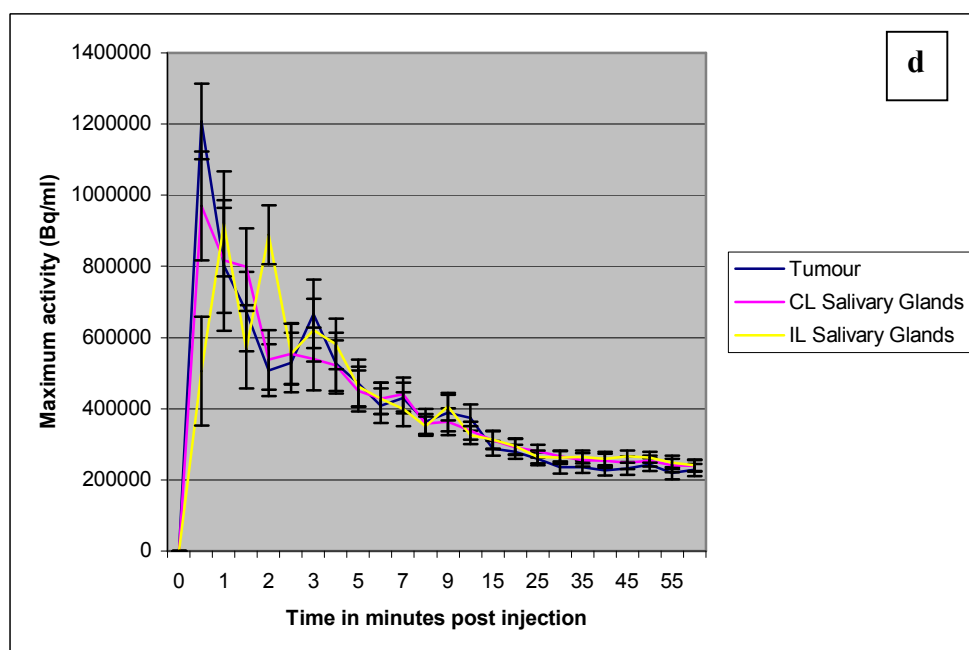
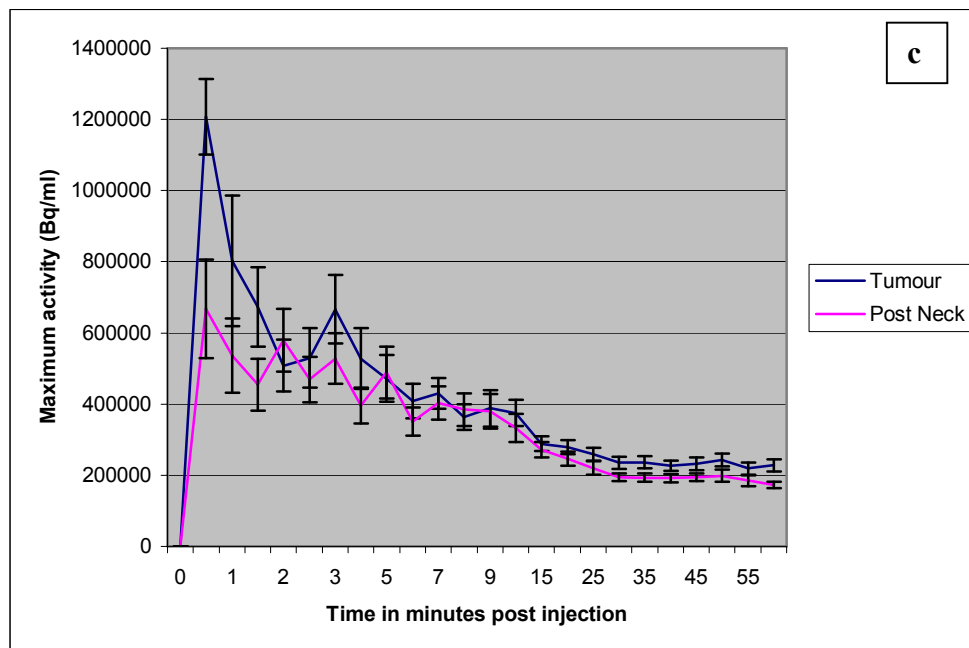
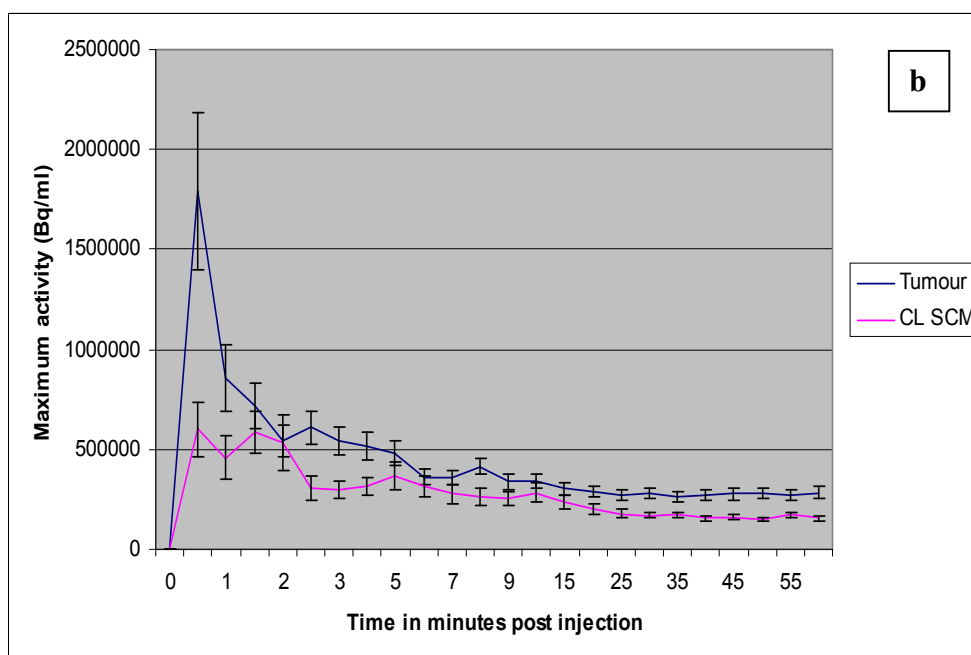
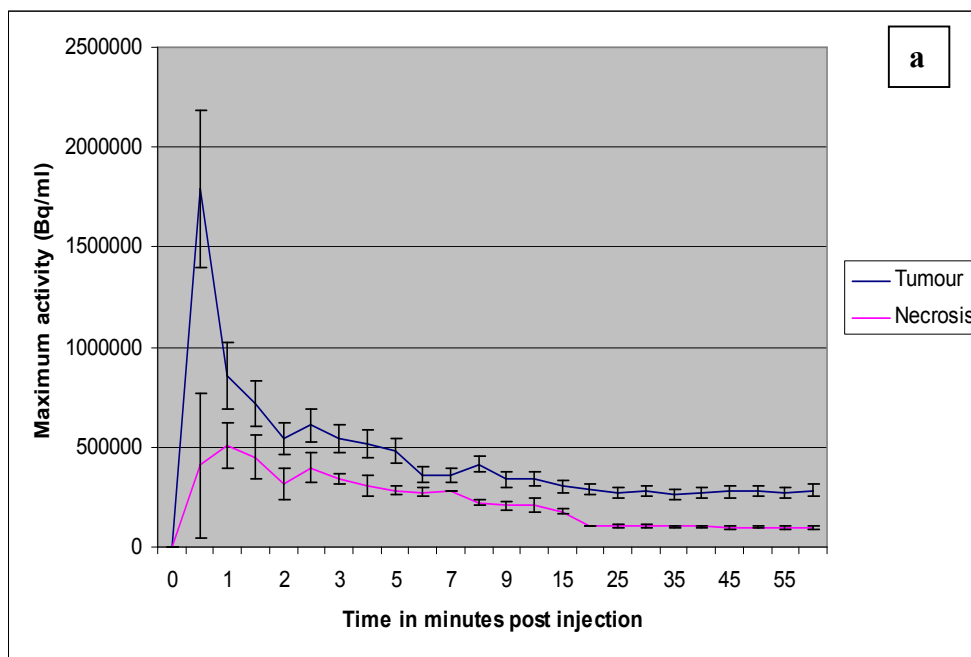
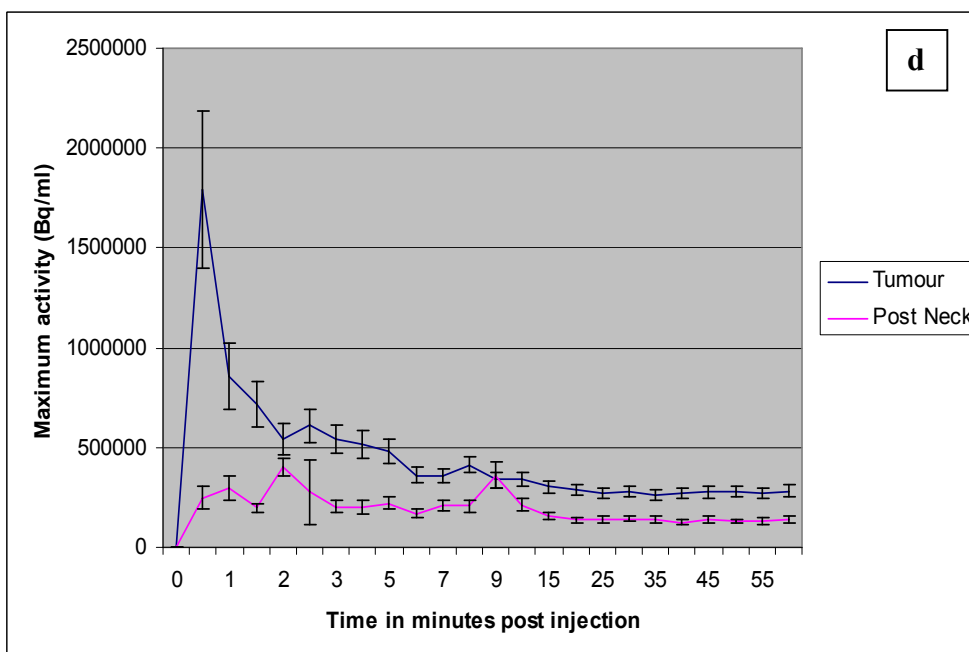
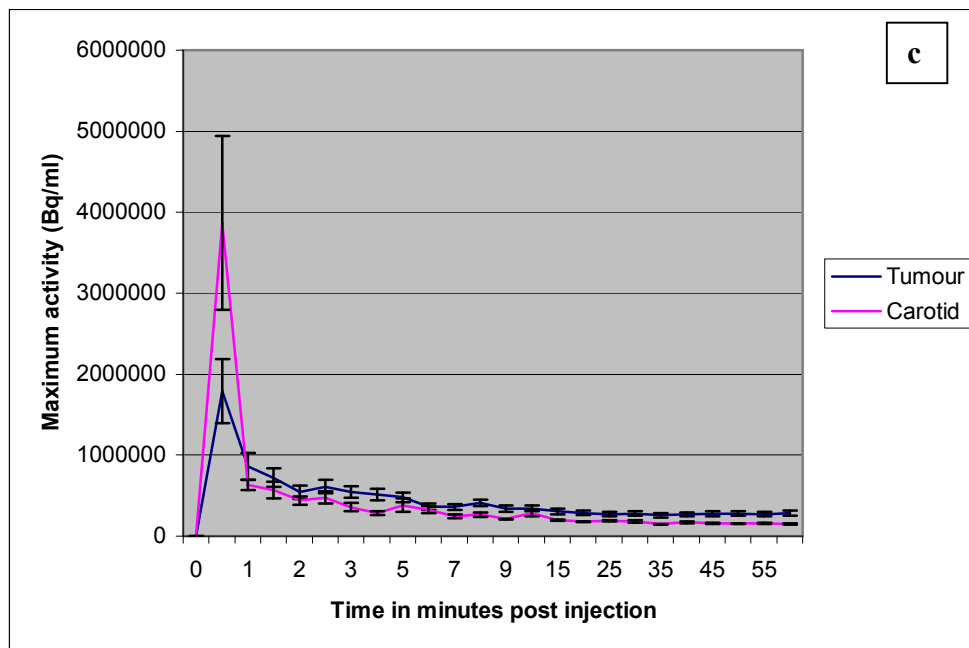


Figure 17 a to d

The uptake of ^{64}Cu -ATSM within the tumour in patient 5 compared to other regions of interest. Necrosis a), contra-lateral SCM b), carotid artery c), posterior neck d), and salivary glands e)





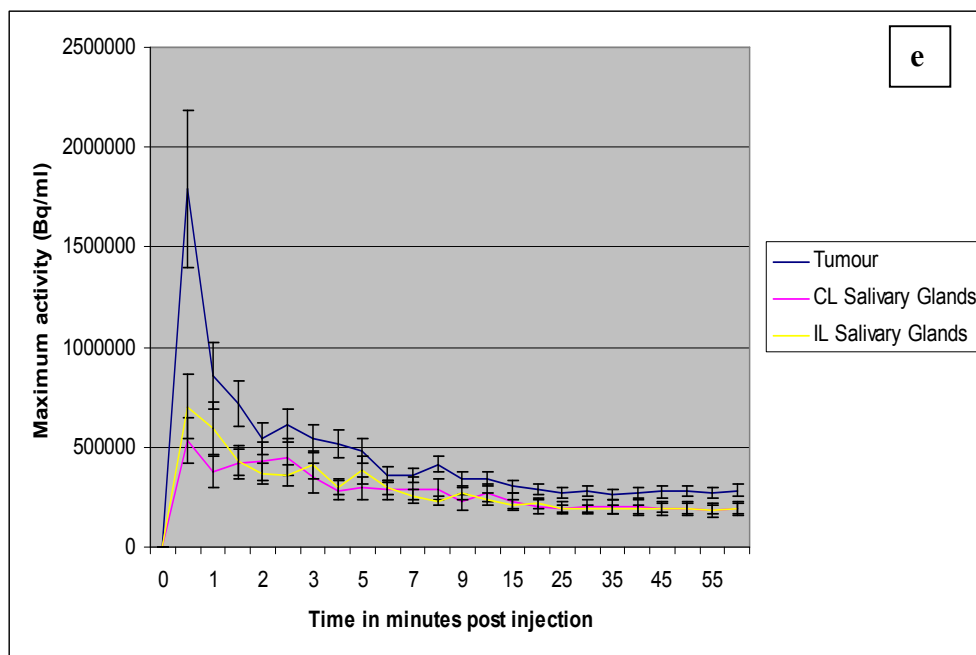
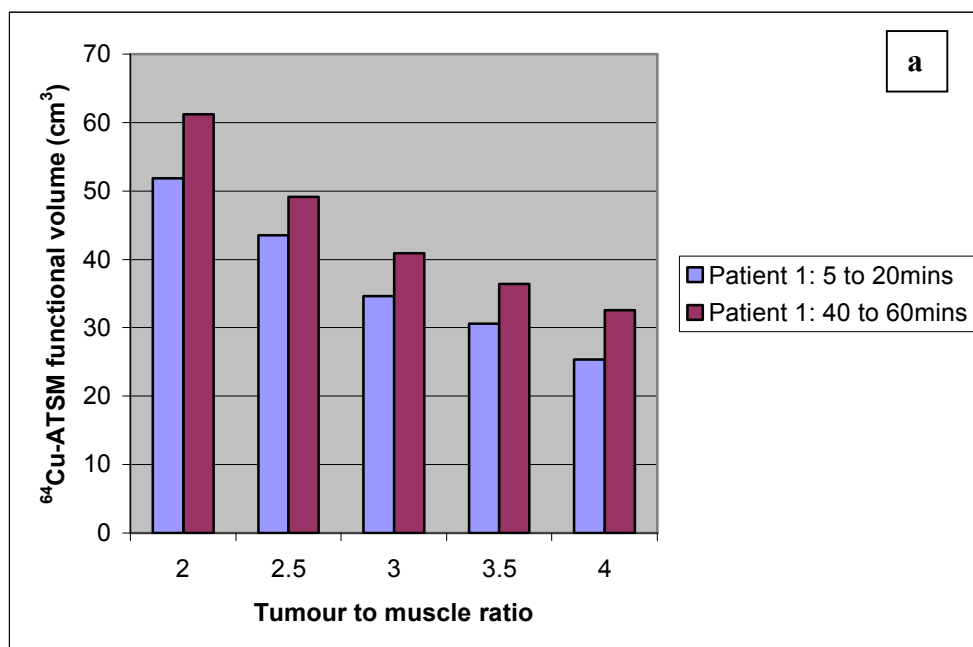
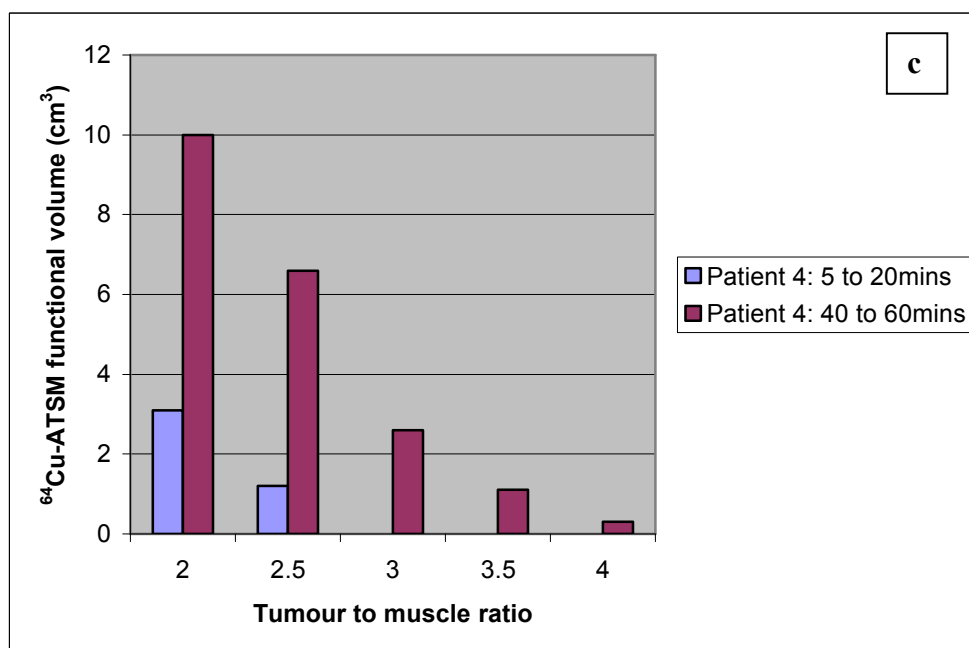
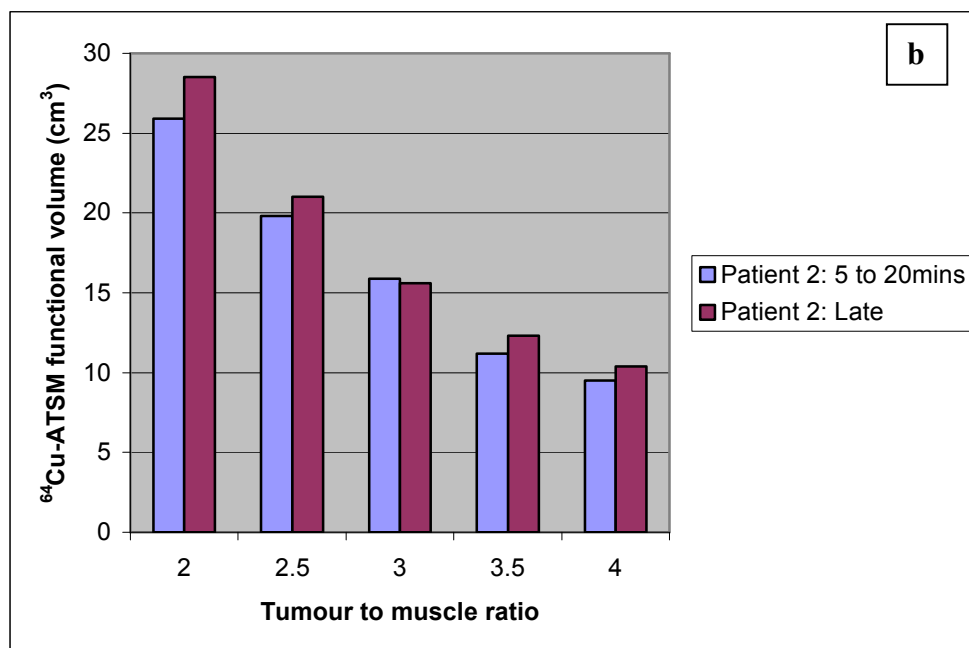


Figure 18 a to c

The defined hypoxic functional volumes in patient 1 a), 2 b), and 4 c) according to the tumour to muscle ratio





Appendix 3

Equations

Chapter 4

Equations 1 to 3

Simple linear regression modelling for the relationship between the radiation dose and the primary functional volume delineated by the SUV Cut Off thresholds

1. SUV Cut Off 2.5bwg/ml: $FV (cm^3) = -0.226Dose(Gy) + 34.273$

2. SUV Cut Off 3.0bwg/ml: $FV (cm^3) = -0.250Dose(Gy) + 27.490$

3. SUV Cut Off 3.5bwg/ml: $FV (cm^3) = -0.256Dose(Gy) + 23.284$

Equations 4 to 7

Simple linear regression modelling for the relationship between the radiation dose and the primary functional volume delineated by the percentage thresholds of the SUVmax

4. 35% of the SUVmax: $FV (cm^3) = 0.271Dose(Gy) + 17.049$

5. 40% of the SUVmax: $FV (cm^3) = 0.191Dose(Gy) + 14.205$

6. 45% of the SUVmax: $FV (cm^3) = 0.150Dose(Gy) + 11.569$

7. 50% of the SUVmax: $FV (cm^3) = 0.101Dose(Gy) + 9.421$

Equations 8 to 10

Simple linear regression modelling for the relationship between the radiation dose and the lymph node functional volume delineated by the SUV Cut Off thresholds

8. SUV Cut Off 2.5bwg/ml: $FV (cm^3) = -0.107Dose(Gy) + 7.121$

9. SUV Cut Off 3.5bwg/ml: $FV (cm^3) = -0.077Dose(Gy) + 4.552$

10. SUV Cut Off 4.0bwg/ml: $FV (cm^3) = -0.067Dose(Gy) + 3.855$

Equations 11 to 14

Simple linear regression modelling for the relationship between the radiation dose and the lymph node functional volume delineated by the percentage thresholds of the SUVmax

11. 35% of the SUVmax: $FV (cm^3) = 0.036Dose(Gy) + 7.616$

12. 40% of the SUVmax: $FV (cm^3) = 0.022Dose(Gy) + 6.688$

13. 45% of the SUVmax: $FV (cm^3) = 0.025Dose(Gy) + 5.495$

14. 50% of the SUVmax: $FV (cm^3) = 0.023Dose(Gy) + 4.527$

Equations 15 to 17

Simple linear regression modelling for the relationship between the radiation dose and the SUVmax within the primary functional volume delineated by the SUV Cut Off thresholds

15. SUV Cut Off 2.5bwg/ml:

$$SUV_{max} (bwg/ml) = -0.093Dose(Gy) + 11.848$$

16. SUV Cut Off 3.5bwg/ml:

$$SUV_{max} (bwg/ml) = -0.096Dose(Gy) + 11.683$$

17. SUV Cut Off 4.0bwg/ml:

$$\text{SUVmax (bwg/ml)} = -0.094\text{Dose(Gy)} + 11.279$$

Equations 18 to 20

Simple linear regression modelling for the relationship between the radiation dose and the SUVmax within the lymph node functional volume delineated by the SUV Cut Off thresholds

18. SUV Cut Off 3.0bwg/ml:

$$\text{SUVmax (bwg/ml)} = -0.085\text{Dose(Gy)} + 6.264$$

19. SUV Cut Off 3.5bwg/ml:

$$\text{SUVmax (bwg/ml)} = -0.082\text{Dose(Gy)} + 5.728$$

20. SUV Cut Off 4.0bwg/ml:

$$\text{SUVmax (bwg/ml)} = -0.083\text{Dose(Gy)} + 5.583$$

Equations 21 to 23

Simple linear regression modelling for the relationship between the SUVmax and the primary functional volume delineated by the SUV Cut Off thresholds

21. SUV Cut Off 2.5bwg/ml:

$$\text{FV (cm}^3\text{)} = 2.461\text{SUVmax(bwg/ml)} + 5.157$$

22. SUV Cut Off 3.5bwg/ml:

$$\text{FV (cm}^3\text{)} = 1.961\text{SUVmax(bwg/ml)} - 1.321$$

23. SUV Cut Off 4.0bwg/ml:

$$\text{FV (cm}^3\text{)} = 1.704\text{SUVmax(bwg/ml)} - 1.457$$

Equations 24 to 26

Simple linear regression modelling for the relationship between the SUVmax and the lymph node functional volume delineated by the SUV Cut Off thresholds

24. SUV Cut Off 2.5bwg/ml:

$$FV (cm^3) = 1.536SUV_{max}(bwg/ml) - 2.464$$

25. SUV Cut Off 3.5bwg/ml:

$$FV (cm^3) = 0.973SUV_{max}(bwg/ml) - 0.936$$

26. SUV Cut Off 4.0bwg/ml:

$$FV (cm^3) = 0.834SUV_{max}(bwg/ml) - 0.723$$

4.1 Preparation of ^{64}Ni Solution

^{64}Ni was transferred onto a weighing boat with a gold spatula, and placed in a 50ml beaker. Ten millilitres of high purity concentrated nitric acid was transferred to the beaker via disposable pipette, along with the same quantity of deionised water. The solution was stirred, heated and evaporated to a green film under a stream of air. High purity concentrated nitric acid (6ml) was added to the beaker, heated again and evaporated to a green film. High purity sulphuric acid (20 drops) was added once cooled, and then 10ml of deionised water. The solution was reheated to near dryness. Once cooled this was transferred to a volumetric flask, and made up with deionised water.

4.2 Electroplating of the Target

Teflon plating spacers and plating glass tubes were soaked in 50% hydrochloric acid, and rinsed with deionised water. Platinum electrodes and the gold bullet for electroplating were cleaned with 6 molar(M) hydrochloric acid. The bullet was rinsed with deionised water, oven dried, cooled, and weighed. The plating cell was then assembled.

Ammonium hydroxide was added to the ^{64}Ni solution to achieve a pH of 9.0. Ammonium sulphate was added equal to 0.1g of target. The solution was then transferred to the plating cells. The gold bullet was electroplated for a minimum of 12 hours at 3 volts, at a revolution speed of 1 revolution per second. When completed, the nickel solution was discarded. The gold bullet was removed from the teflon spacer, rinsed with deionised water, and oven dried. The dry weight of the target was noted.

4.3 Production of the H_2ATSM Ligand

4-methyl-3-thiosemicarbazide was dissolved in 50ml of 5% acetic acid solution, and heated to 60°C with constant stirring. The solution was filtered and any undissolved material removed. Over the next 45 minutes, 2,3-butanedione was added drop wise to achieve a 1:2 stoichiometry with 4-methyl-3-

thiosemicarbazone. The H₂ATSM (yellow air stable solid) precipitated out, and the mixture was stirred for an additional 30 minutes at 60°C. The solution was filtered (Buchner filter funnel and flask connected to a vacuum pump), and the crude H₂ATSM washed in two 50ml aliquots of deionised water, two 50ml aliquots of methanol, and two 50ml aliquots of diethyl ether, and then vacuum dried at 75°C overnight.

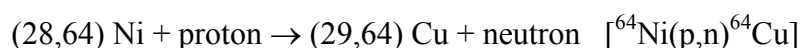
The crude H₂ATSM was suspended in dichloromethane to re-crystallise, and heated to 40°C for 30 minutes. Dimethylsulfoxide was added drop wise. The solution was cooled after the solid complex had dissolved. Methanol was added until the H₂ATSM precipitated. The solution was filtered while hot, and then refrigerated overnight. Any undissolved material was collected and dried overnight at 75°C.

The solution was then re-filtered, and washed with two 50ml aliquots of deionised water, two 50ml aliquots of methanol, and two 50ml aliquots of diethyl ether, and then vacuum dried for 1 hour.

The purified H₂ATSM was characterised by elemental analysis, nuclear magnetic resonance (¹H and ¹³C) and mass spectroscopy (molecular ion peak m/z = 2601).

4.4 ⁶⁴Copper Production and Purification

After the gold bullet target was electroplated, it was loaded and rotated into the line of the cyclotron (CTI RDS 112 11MeV model, positive ion machine). Operating parameters during irradiation were: beam current 20 to 30μA +/- 5 μA. Irradiation times of 5 to 8 hours for batches of 1GBq were used. The cold finger was inserted into the back of the bullet. The bombardment parameters were determined according to the required ⁶⁴Cu activity, and the proton beam was switched on. On completion, the cold finger was removed, and the bullet was rotated out of the line of the beam. The bullet was removed and placed in a lead pot. The copper production is shown in the equation.



4.5 Purification of the Isotope

Before the bullet was processed, the Bio-Rad column and vials were prepared. The column and tap were washed with deionised water, followed by a small volume of 6M hydrochloric acid. Bio-Rad AG 1X8 resin (2.5g) was added to 10ml of deionised water, decanted and repeated, ensuring the resin did not dry out during the process. Ten millilitres of 9M hydrochloric acid was added, and stirred until a slurry formed. The resin slurry was transferred to the column, and allowed to settle. The excess hydrochloric acid was drained, and more resin added to produce a stationary phase 6 to 8cm in length. Fifteen vials were labelled to receive the elution aliquots. The hot finger was assembled and the GE detector set up to measure the spectrum.

The unloaded bullet was placed in a 30ml syringe, and then in capintec (settings: chamber 1, calibration 015, isotope other) and the activity level recorded. The bullet was then placed on the hot finger, and a few drops of 6M hydrochloric acid added, and then evaporated at 90°C. This was repeated 3 times with 9M hydrochloric acid. The eluent within the column was drained to ensure the eluent meniscus just touched the top of the resin bed. The residue from the bullet was dissolved using 9M hydrochloric acid, and then loaded into the column. This was repeated three times. The bullet was then removed from the hot finger to the lead pot, and the activity measured.

The column tap was opened, and the column eluted into vial 1, until the solvent meniscus touched the top of the resin bed. Five millilitres of 9M hydrochloric acid was added to the column, and eluted into vial 1. The activity measured and spectral analysis performed. Twenty millilitres of 6M hydrochloric acid was added to the column, and 5mls of eluent collected into vials 2 to 5. This was repeated with 5ml of 0.5M hydrochloric acid, and 1ml eluent volumes were collected until the majority of the radio-activity was removed. Characteristic ^{64}Cu peaks were visualised at 511 and 1345KeV. The vials with the highest $^{64}\text{CuCl}_2$ activity were combined, and used to radio-label the ligand.

4.6 Preparation of ^{64}Cu -ATSM

4.6.1 Radio-labelling of ATSM

One milligram of H_2ATSM was dissolved in 1ml of dimethyl-sulphoxide, and 10 μl of this ATSM/dimethyl-sulphoxide was added to the $^{64}\text{CuCl}_2$. Once agitated the mixture was allowed to stand for 2 to 5 minutes at room temperature. The ^{64}Cu -ATSM containing solution was then transferred to the conditioned C18 SepPak Light cartridge

4.6.2 C18 Sep-Pak Conditioning

Five millilitres of sterile ethanol was passed through the C18 Sep-Pak cartridge, followed by 5ml of deionised sterilised water, and the cartridge air-dried.

4.6.3 Purification of ^{64}Cu -ATSM

Ten milligrams of ascorbic acid was dissolved in 1ml of sterile saline. The ^{64}Cu -ATSM was transferred to a sterile 30ml syringe connected to the C18 Sep-Pak cartridge via a 3-way tap. The solution was pushed through the Sep-Pak. Ten millilitres of sterile water was pushed through the cartridge, and repeated twice. The ^{64}Cu -ATSM bound to the Sep-Pak was eluted with 2ml of sterile ethanol and collected in fractions of 0.2ml. The activity was measured, and the fractions with the greatest activities combined. The dissolved ascorbic acid was combined with the ^{64}Cu -ATSM fractions to a final volume of 1mg/ml ascorbic acid. The solution was diluted with at least 20 times the ethanol volume with sodium chloride for injection (0.9%) BP. The ^{64}Cu -ATSM was then filtered through a Millipore (0.2 μm sterile membrane) filter using a shielded syringe, followed by 5ml of sterile saline. This procedure was carried in the isolator.

4.6.4 Quality Assurance

Ten millilitres of ethanol was placed in the TLC tank, and 0.2ml of ^{64}Cu -ATSM was removed from the final vial for quality assurance, and 1 μl was placed on a TLC plate. The plate was dried with compressed air, and placed in the tank. When the solvent front was 1cm away from the top of the plate, it was removed and dried. The TLC plate was placed in the TLC scanner, and a tab placed half

way through the plate width. Measurements were taken for 2 minutes with the gas turned on.

4.6.5 pH Analysis

One drop of the ^{64}Cu -ATSM sample was placed on a pH strip, and the colour compared to the scale on the dispenser cartridge.

4.6.7 Isotope Identity Testing

The sterile vial containing ^{64}Cu -ATSM was placed in front of the GE detector and activity recorded for 240 seconds.

4.6.8 Chemical Stability of the Isotope

^{64}Cu -ATSM was unstable with time as an ethanol/saline solution. The purity remained greater than 99.9% (gamma-ray spectroscopy). However, radio-chemical purity (radio-TLC) was unreliable and often less than 95% after 3 hours. Ascorbic acid as a 10mg/ml solution was added to produce 1mg of ascorbic acid per ml of ^{64}Cu -ATSM solution to prevent radio-lysis. The solution was then stable for over 24 hours.